FINAL REPORT

Understanding and Mitigating Wildfire Risk in California

Contract 19RD008

Prepared for the California Air Resources Board

Principal Investigators:

Allen Goldstein, University of California at Berkeley

E-mail: ahg@berkeley.edu

Kelley Barsanti, University of California at Riverside

E-mail: kbarsanti@engr.ucr.edu

Co-Principal Investigators:

John Battles, University of California at Berkeley

Scott Stevens, University of California at Berkeley

Robert York, University of California at Berkeley

Thomas Kirchstetter, UC Berkeley, Lawrence Berkeley National Laboratory

Nathan Kreisberg, Aerosol Dynamics Inc.

Contributing Researchers:

Dr. Deep Sengupta, Postdoc, UC Berkeley

Dr. Yutong Liang, former PhD Student, UC Berkeley

Dr. Daniel Foster, former PhD Student, UC Berkeley

James Butler, PhD Student, UC Berkeley, Lawrence Berkeley National Laboratory

Afsara Tasnia, PhD Student, UC Riverside

Guadalupe Lara, former MS Student, UC Riverside

Dr. Paul Van Rooy, former Postdoc, UC Riverside

November 30, 2023

Disclaimer

The statements and conclusions in this Report are those of the contractor and not necessarily those of the California Air Resources Board. The mention of commercial products, their source, or their use in connection with material reported herein is not to be construed as actual or implied endorsement of such products.

Acknowledgements

We thank our colleagues at the California Air Resources Board for useful collaboration in planning the prescribed burn experiments, and our contract manager Nehzat Motallebi for her many contributions to the success of this project. We thank the burn crew and staff from Blodgett Forest Research Station for performing and managing the prescribed burn experiments, and Ariel Roughton for assisting our team with housing and infrastructure support. We gratefully acknowledge Robert Weber of University of California at Berkeley, Coty Jen of Carnegie Mellon University, and CAL FIRE staff for excellent logistical and planning support.

Table of Contents

Glossary of Symbols and Acronyms

ABCD	Aerosol Black Carbon Detector
ATD	Automated Thermal Desorption
AQMD	Air Quality Management District
AQS	Air Quality Station
BB	Biomass Burning
BC	Black Carbon
BFRS	Blodgett Forest Research Station
CAL FIRE	California Department of Forestry and Fire Protection
CARB	California Air Resources Board
CO	Carbon Monoxide
CO_2	Carbon Dioxide
CWD	Coarse Woody Debris
DBH	Diameter at Breast Height
DEFCON	Direct Emission Fire Concentrator
EC	Elemental Carbon
EF	Emission Factor
FIREX-AQ	Fire Influence on Regional to Global Environments Experiment - Air Quality
FLAME-IV	Fourth Fire Lab at Missoula Experiment
FOFEM	First-Order Fire Effects Model
FWD	Fine Woody Debris
GCxGC	Two-Dimensional Gas Chromatograph
IVOC	Intermediate Volatility Organic Compound
JFSP	Joint Fire Science Program
MCE	Modified Combustion Efficiency
NASA	National Aeronautics and Space Administration
NEIVA	Next-generation Emissions InVentory expansion of Akagi
NO_x	Nitrogen Oxides
NOAA	National Oceanic and Atmospheric Administration
OC	Organic Carbon
PAH	Polycyclic Aromatic Hydrocarbons
PM	Particulate Matter
$PM_{2.5}$	Fine Particulate Matter
QA/QC	Quality Assurance-Quality Control
QMD	Quadratic Mean Diameter
RAMN	Richmond Air Monitoring Network
RH	Relative Humidity
RSC	Residual Smoldering Combustion
Rx	Prescribed Burn
SOA	Secondary Organic Aerosol
SF	San Francisco
SSP	Satelite Smoke Product
STFS	Short-Term Flaming

SVOC	Semi-Volatile Organic Compound
TD	Thermal Desorption
ToFMS	Time-of-Flight Mass Spectrometer
UC	University of California
UCB	University of California Berkeley
UCR	University of California Riverside
US	United States
UAS	Uncrewed Aerial System
UTV	Utility Task Vehicle
VOC	Volatile Organic Compound
WE-CAN	Western wildfire Experiment for Cloud chemistry and Nitrogen
WF	Wildfire

Abstract

The Forest Carbon Plan recommends seizing every opportunity to increase the rate of fuels treatment to reduce fire hazard and limit greenhouse gas emissions. Prescribed fire is an effective and efficient fuel treatment. Thus, the recent executive order (B-52-18) calls on the California Air Resources Board (CARB) to reduce barriers to prescribed fires. However, the value of increased burning must be weighed against the competing objective of maintaining air quality. Biomass burning (BB) can be a dominant source of primary carbonaceous aerosols and of non-methane organic compounds, including volatile, intermediate and semi-volatile organic compounds (I/S/VOCs). These compounds are well understood to be major contributors to secondary particle formation in the atmosphere; however, their identities and quantities (which largely control the extent of particle formation) are poorly constrained. To balance the trade-off between reducing fire hazard and limiting exposure to criteria pollutants, an accurate means to predict fire emissions from prescribed burning is essential. The contractor conducted measurements via ground- and airborne-based (drone) sampling platforms during prescribed burn activities. The ground-based systems were equipped to measure black carbon (BC), carbon dioxide (CO_2), carbon monoxide (CO), and oxides of nitrogen (NO_X) in real time while simultaneously collecting I/VOCs on sorbent cartridges and SVOCs and $PM_{2.5}$ on quartz filters. The airborne system included the capability to measure CO_2, CO, BC and collect sorbent cartridges and quartz filters to understand BB emissions that escape the canopy to the regional airshed. Gas and particle concentration data were converted to emission factors using well established carbon balance methods that account for the fraction of carbon in the fuels and assume most of the mass emitted exists as CO_2 and CO. Emission profiles were characterized from two distinct types of prescribed fires: third-entry burns (burned twice previously for management purposes) in a mature, second-growth mixed conifer forest and first-entry burns in a second-growth mixed conifer forest. These two extremes capture what will in the future become a gradient in management status. The first-entry burns are representative of the majority of burn projects that are being proposed currently- that is, introducing fire in forests that have been unburned since the policy of fire suppression was implemented a century ago. The third entry burns represent the desired future goal- that is, a forest that is being maintained with light burning in perpetuity. Emission factors were derived from emission measurements taken during the burns; carbon stocks were measured before and after the burns. The experiments occurred on University of California property at the Blodgett Forest Research Station, a mixed conifer forest representative of large regions of the western slope of the Sierra Nevada. Emission factors are reported for EC, BC, OC, $PM_{2.5}$, speciated VOCs, IVOCs, and SVOCs. The observed EFs were used to validate those used by CARB in the First-Order Fire Effects Model (FOFEM) for modeling atmospheric emissions from prescribed burns. Using time-resolved observations from the PurpleAir sensor network in California, analyses of PM2.5 indoor infiltration ratios during non-fire and wildfire days were completed.

Executive Summary

Fires can emit high levels of trace gases and primary (directly emitted) particulate matter (PM). During plume evolution, some of the gases react to form ozone and secondary PM (i.e., secondary organic aerosol, SOA), thereby degrading air quality downwind and potentially endangering human health. A recent study shows that increasing wildfires are erasing decades of air pollution gains in the Northwest, including rural parts of Northern California (McClure and Jaffe, 2018). Climate change will sharpen the problems involving wildfires in the western U.S. For example, in the Sierra Nevada, warmer and drier climate in combination with fire-control practices over the last century, have produced a developing situation with more frequent fires that are of higher severity, and thus increasing impacts on local and regional air quality. Fuel treatments, such as prescribed fire and the mechanical removal of vegetation, are often implemented to reduce the spread and intensity of large wildland fires (Fulé et al., 2012). Given its cost-efficiency, prescribed fire is often the preferred fuel treatment (Bustic et al., 2017). Yet there are critical public health and social justice concerns about the emissions associated with a greatly expanded program of prescribed fire (Roos et al., 2018). Improvements in model representation of fuels and emissions are needed to advance the scientific understanding and allow reliable predictions of the linkages between fire and land management practices and fire emissions and impacts.

The objectives of this contract were to: 1) analyze gaseous and particulate organic carbon emission samples from California wildfires collected by CARB staff using their mobile platform in coordination with the FIREX-AQ aircraft campaign; 2) evaluate biomass burning emission factors in FOFEM for climate pollutants (e.g., CO_2); criteria pollutants (e.g., NO_x, CO, and $PM_{2.5}$); and 3) quantify emission factors (EFs) of criteria pollutants, VOCs, and selected air toxics from prescribed burns. Calculated EFs were compared with those from wildfires in order to understand how reducing fire risk through prescribed burn also alters emissions. Outcomes of these objectives include improved EFs from prescribed burns of managed and previously unmanaged forest; and comparison to EFs from wildfires, including recently measured and published values.

Contractors developed datasets for use by air quality management and scientific communities by characterizing smoke emissions as a function of land management practices. First entry prescribed burns were completed in a mixed-conifer forest at the Blodgett Forest Research Station (BFRS) over four consecutive days, from 20-23 April 2021. These burns occurred during spring conditions that allowed for high fuel consumption without excessive risk of escape and with minimal smoke impacts on downwind communities. Smoke was sampled using ground- and drone-based instruments to characterize fresh gaseous and particulate emissions during several hours of each day's prescribed burn. Forest and fuel characteristics were collected in each unit from established permanent inventory plots at BFRS both before and after the prescribed burns. The field estimates of biomass provided sufficient information to quantify the variation in the structure and abundance of fuels. Fire intensity was quantified by comparing pre- and post-fire fuel loads. Measured fuel

consumption and smoke emissions were compared with predictions using the First Order Fire Effects Model (FOFEM) for prescribed fires in this common California forest type.

The UC Riverside and UC Berkeley teams successfully analyzed gaseous and particulate organic carbon emission samples, respectively, from California wildfires collected by CARB staff using their mobile platform in coordination with the FIREX-AQ aircraft campaign. The data were compared with data from BFRS (1st and 3rd entry burns) and with reported literature values. Differences in the levels and abundances of some volatile organic compounds (VOCs) and $PM_{2.5}$ speciated organics were observed between the wildfire samples and the BFRS samples. The differences in the levels of some compounds were driven by dilution and reactive losses and secondary production during plume transport. The differences in relative abundances also suggests that there were differences in the fuel consumed, as would be expected for wildfires relative to prescribed burns.

A series of FOFEM model runs were conducted to evaluate model skill in predicting climate pollutants (e.g., CO_2) and criteria pollutants (e.g., CO and $PM_{2.5}$). Predicted emission factors (EFs) were compared between model runs and with measured EFs to assess sensitivity and uncertainty in the context of fuel loading, fuel consumption, and EFs. The results of the FOFEM simulations, including comparisons with measured emissions and fuel loading and consumption will be submitted to the International Journal of Wildland Fire for publication.

Observations of gaseous and particulate compounds were used to calculate EFs for the prescribed burns at BFRS. A single compartment was burned over a period of four days and divided into three sub units. The compartment was typical of second-growth mixed conifer forests where high tree density and high surface fuel loads create high wildfire hazard. The forest structure and fuels were highly similar between the three burn units, as was reflected in the measured climate and criteria pollutants.

Using time-resolved observations outside and inside over 1400 buildings from the crowdsourced PurpleAir sensor network in California, we determined that infiltration ratios (indoor $PM_{-2.5}$ of outdoor origin/outdoor $PM_{2.5}$) reduced from 0.4 during non-fire days to 0.2 during wildfire days. Even with reduced infiltration, mean indoor concentration of $PM_{2.5}$ nearly tripled during wildfire events, with lower infiltration in newer buildings and those utilizing air conditioning or filtration. These results were published in the Proceedings of the National Academy of Sciences, PNAS (Liang et al., 2021).

The spring prescribed burns at BFRS successfully met management goals. The mass of litter and fine woody debris was reduced by 65%, total ground and surface fuel load was reduced by 53% with the lower rates of combustion (<50%) occurring in the heavy fuels (i.e., duff and coarse woody debris). Further, crown scorch never exceeded 32% and only one of the 63 trees > 50 cm

diameter breast height was killed in the fire. While surface fuel loads were meaningfully reduced, carbon loses were relatively low compared to values reported in the literature for similar treatments in comparable forests. The fires proceeded through flaming and smoldering combustion phases and smoke samples were collected from ground- and drone-based platforms. The drone generally sampled a wider range of combustion conditions, from flaming to smoldering, resulting in generally higher VOC mixing ratios and PM mass concentrations. The EFs, however, between the ground and drone samples were relatively consistent, and we recommend these data be pooled when calculating mean EFs to use in emissions modeling. Further, EFs between 1st and 3rd entry burns were also relatively consistent, suggesting that the composition of emissions was similar between these types of burns. The total emissions, however, scaled with fuel loading for these burns and that information is critical for predicting emissions from both prescribed burns and wildfires.

Task Summary and Work Described in This Project

The major objectives of this work were to develop emission factors (EFs) of fine particulate matter ($PM_{2.5}$), organic carbon (OC), elemental carbon (EC), black carbon (BC), gas phase volatile organic compounds (VOCs), and particle phase organic chemicals for prescribed burns typical of those conducted in the mixed conifer forests of the Sierra Nevada Mountains in California. The observed EFs were used to validate those used by CARB in the First-Order Fire Effects Model (FOFEM) for modeling atmospheric emissions from prescribed burns. The work done for each of the 6 tasks identified in the contract is briefly summarized below:

Task 1: Plan prescribed burns

The initial step of the project was field campaign planning which included the following:
Design experimental plan, identify appropriate plots for prescribed burns at Blodgett Forest Research Station, plan the suite of ground-based measurements and prepare required instruments, plan the drone-based measurement system and build drone sampler, perform site visits to planned measurement locations, prepare burn plan and submit to CAL FIRE for approval, and assess FOFEM model inputs and treatment of EFs, including as a function of fuel type, fuel moisture, and burn characteristics.

Task 2: Analyze FIREX-AQ samples collected by CARB from California wildfires

During the period of the FIREX-AQ field campaign, contractors provided a sampler for collection of gas- and particle-phase organic carbon to CARB staff for collection during wildfires. Wildfire smoke samples were collected from two fires in August and November 2019 by CARB using their Mobile Measurement Platform: Springs Fire (5,000 acres) and Kincade Fire (78,000 acres). VOC samples were analyzed on the TD-GCxGC-TOF instrument at UC Riverside. $PM_{2.5}$ samples were analyzed on the TD-GCxGC-TOF instrument at UC Berkeley.

Task 3: Complete prescribed burns

Prescribed burns were completed in April 2021. Three plots were successfully burned (units A, B, C), on back-to-back days with one unit (A) taking two days for burn completion. All burns were conducted during daytime. Measurements of above-ground pre-fire carbon pools were completed including detailed fuel measurements. A sampling protocol was developed and applied for above-ground biomass stocks (duff, litter, FWD, CWD, shrubs, and trees), and a field crew was trained on the sampling protocol. Smoke sampling was completed for all units (A, B, C). Samples and data were successfully collected as proposed using ground- and drone-based measurement platforms.

Task 4: Analyze prescribed burns samples and data

Analysis of samples and data from prescribed burns were completed. Contractors measured biomass in each plot before and after prescribed burns to determine amount and type of fuel consumed. Speciated particle phase organics were analyzed from filter samples at UCB and EFs were calculated for ground and drone samples. Speciated VOCs were analyzed at UCR from sorbent tube samples and EFs were calculated for ground and drone samples. Analysis of BC in smoke from prescribed burns and wildfires was completed. FOFEM model runs were completed. Calculated consumption, EFs, and total emissions from FOFEM were compared with observations. Analysis of already-collected data during 2018 and 2020 wildfires in California was completed for BC and $PM_{2.5}$. Using time-resolved observations from the PurpleAir sensor network in California, analyses of $PM_{2.5}$ infiltration ratios during non-fire and wildfire days were completed.

Task 5: Draft final report

The contractor will deliver to CARB a draft version of the Final Report detailing the purpose and scope of the work undertaken, the work performed, and the results obtained and conclusions. Specific contracted deliverables include:

1) database of chemical species collected on filters and sorbent tubes detected by GCxGC-ToFMS; compounds quantified by peak area and identified by name or by compounds class using standards as available;
2) calculated EFs for bulk gaseous and particulate compounds (e.g., total PM), for individual species and for classes of compounds (e.g., 'PAHs') in gas and particle phases; EF database include metadata to link EFs with fuel characteristics and burn conditions;
3) temporal profiles of online gaseous chemical species (e.g., CO, CO_2); and
4) pre-fire fuel characterizations including mass and moisture content by component along with burn conditions and fuel consumption for the prescribed fires at BFRS.

This report is submitted in fulfillment of Task 5.

Task 6: Amend final report

Revised final report of the project and its results will be delivered to CARB.

1. Introduction

1.1. Background

As part of a decades-long trend, wildfires in California are growing larger, burning at higher severity, and exacting greater social costs (Safford et al., 2022). From an air quality perspective, fine particulate matter ($PM_{2.5}$) and ozone formed from fires are two of the deadliest components of smoke. A recent study shows that increasing wildfires are erasing decades of air pollution gains in the Northwest, including rural parts of Northern California (McClure and Jaffe, 2018). Climate change will sharpen the problems involving wildfires in the western U.S. For example, in the Sierra Nevada, warmer and drier climate in combination with fire-control practices over the last century, have produced a developing situation with more frequent fires that are of higher severity, and thus increasing impacts on local and regional air quality.

In the dry forests of the American West, long-term policies of wildfire suppression and early harvesting practices have led to the accumulation of understory fuels in forests, including in California (Collins et al., 2011). This century-long shift in forest structure in tandem with a warming climate greatly increases the potential for destructive fires (Collins et al., 2011; Stephens et al., 2014). Fuel treatments, such as prescribed fire and the mechanical removal of vegetation, are often implemented to reduce the spread and intensity of large wildland fires (Fulé et al., 2012). Given its cost-efficiency, prescribed fire is often the preferred fuel treatment (Bustic et al., 2017). Yet there are critical public health and social justice concerns about the emissions associated with a greatly expanded program of prescribed fire (Roos et al., 2018).

Fires can emit high levels of trace gases, including NO_x, CO and CO_2; volatile, I/S/VOCs; and primary (directly emitted) PM. During plume evolution, I/VOCs react to form ozone and secondary PM (i.e., secondary organic aerosol, SOA), thereby degrading air quality downwind and potentially endangering human health. The quantities and properties of the emitted compounds are highly variable and largely dependent on fuel type and burn conditions (Akagi et al., 2011; Jolleys et al., 2012; McMeeking et al., 2009), thus differences in emissions are expected between prescribed fires and wildfires.

Through Joint Fire Science Program (JFSP) and National Oceanic and Atmospheric Administration (NOAA) funded projects, contractors demonstrated that collaborative application of advanced instrumentation can yield significantly improved estimates of gaseous and particulate compounds emitted from fires (including PM, and SOA/O_3 precursors). The lower volatility compounds, particularly those most likely to contribute to PM, were notably absent from commonly used emissions inventories (Hatch et al., 2017). For particle-phase compounds, contractors published emission factors (EFs), scalable by modified combustion efficiency (MCE), for elemental and organic carbon (EC and OC, respectively), and speciated organic compounds (and class) (Jen et al., 2019). This detailed emissions characterization was an important part of the

joint FIREX-AQ campaign (NOAA and NASA partnership), which combined in-situ surface and airborne observations with remote sensing data. The leveraging of the contractors' NOAA-FIREX efforts provided critical information to improve model predictions of the impacts of fires on chemistry and climate.

In current models used to support air quality decisions, the ability to represent air quality and climate effects of fires is severely limited. Contractors recently compared predicted emissions using the First Order Fire Effects Model (FOFEM, (Keane and Lutes, 2018)) from six wildfires in California with field data (Lydersen et al., 2014). In general, FOFEM performed reasonably well in estimating fuel consumption and relevant emissions for air quality. However, based on comparisons with pre-fire measurements of fuel loads, FOFEM got the "right" answer for the "wrong" reasons. For most fuel characterizations tested, the model underestimated flaming emissions and overestimated smoldering emissions. As noted above, the quantities and properties of the compounds emitted depend on combustion conditions (e.g., flaming versus smoldering), as well as the characteristics of the fuel (Yokelson et al., 2013; Hatch et al., 2017; Jen et al., 2019). Thus there is a critical need to link accurate measurements of pre-fire fuel conditions, post-fire fuel consumption, and gaseous and particulate emissions in order to improve predictions of fire emissions and their effects on air quality and climate.

Contractors assembled a uniquely qualified team to advance scientific understanding of the linkages between fire and land management practices and fire emissions and impacts. Characterization and quantification of biomass burning emissions are needed to improve modeling of their impact on human health and climate. Furthermore, fuel manipulation and reduction treatments are a vital tool for reducing fire severity, and likely the most effective way of reducing future biomass burning emissions in a hotter, drier, and more variable climate. Hence, there is an urgent need to reduce fuel loading in forests and to better understand the impacts of wildfire and prescribed burning on the atmosphere and climate, and for policy-relevant science to aid in the process of managing fires.

1.2. Objectives

Objectives of this research project were to: 1) analyze gaseous and particulate organic carbon emission samples from California wildfires collected by CARB staff using their mobile platform in coordination with the FIREX-AQ aircraft campaign; 2) evaluate biomass burning emission factors in FOFEM for climate pollutants (e.g., CO_2); criteria pollutants (e.g., NO_x, CO, and $PM_{2.5}$); and 3) quantify emission factors (EFs) of criteria pollutants, VOCs, and selected air toxics from prescribed burns. Calculated EFs were compared with those from wildfires in order to understand how reducing fire risk through prescribed burn also alters emissions.

This project provides emissions from a representative set of prescribed burns in a mixed conifer forest in California, and compares with emissions from prescribed fires and wildfires in the western

US. Measured EFs were used in collaboration with CARB staff to evaluate FOFEM model estimates of short-lived climate pollutants and other air pollutants and will be used to improve model estimates in the future. Outcomes include improved EFs from prescribed burns of managed and previously unmanaged forest; and comparison to emission factors from wildfires, including recently measured and published values.

1.3. Methods and Approach

The quantities and chemical composition of gases and PM emitted from fires are affected by fire intensity, combustion phase, and fuel structure. New field-based measurements are needed to support evaluation of the air quality impacts of wildfires vs. prescribed fires (under different management scenarios). These include coupled characterization of fuel characteristics and consumption, burn characteristics, and emissions as uniquely provided by this project.

Experimental Design

Contractors developed datasets for use by air quality management and scientific communities by characterizing smoke emissions as a function of land management practices. These results are meant to inform operational models, such as FOFEM, by evaluating estimates of fuel consumption and characterizing emissions as a function of established emission inventory categories, vegetation classes, and fuel components. Coupled ground- and airborne- based measurements were used to sample near-fire emissions during prescribed burns at the Blodgett Forest Research Station (BFRS) in California. Airborne measurements were needed to understand fire emissions that escape the canopy to the regional airshed, and to get a representative average of the emissions and their evolution above and downwind of the fires. The ecosystem at BFRS is a mixed conifer forest. Fire is part of the research and management plan for BFRS, which has a long history of fire management research through the Fire and Fire Surrogate Treatments study, among others (Stephens et al., 2012). Attribution of prescribed burn emissions to vegetation classes and fuel components was facilitated by leveraging NOAA-FIREX projects in which gaseous and particulate emissions were measured from combustion of relevant fuels in the Missoula Fire Lab. The detailed emissions characterization for prescribed burns are compared with similar characterization for western wildfires by analyzing samples collected by CARB staff in California during the 2019 summer wildfire season.

Prescribed Burns

A map showing the areas at BFRS identified for the 3rd and 1st entry burns is provided in **Figure 1.1**. The 3rd entry burns were completed in 2017 in Compartments 60, 340, and 400 (shaded gray). These compartments range in area from 17.3 ha to 24.0 ha. The 1st entry burns were completed in Spring 2021 in Compartment 110. As shown in the inset enlarged map and **Figure 1.2**, compartment 110 was split into three units (A, B, C) separated by fire breaks. Roads or trails that

are drivable with utility task vehicles (UTVs) surrounded all burn areas in 2021.These units range in size from 6.6 ha to 9.8 ha.

The 3rd entry burns were part of the long-term Fire and Fire Surrogate Study (2009) at Blodgett Forest (Stephens et al., 2009). The initial prescribed fire (i.e., 1st entry) was implement in 2002 with a 2nd entry burn in 2009. The 3rd entry treatment was implemented during a 3-day window in the fall (October 30 to November 1, 2017) when weather conditions met prescriptions. During the firing operations, air temperature averaged 17 °C, relative humidity ranged from 35%-45%, wind speeds from 1-2 km h^{-1}, and 10-h fuel moisture from 5-7% (Levine et al. 2020). For details regarding the sampling strategy and treatment impact see Levine et al. ((Levine et al., 2020) and York et al. (York et al., 2022).

The 1st entry prescribed fires were completed in the spring during a window that is typically targeted for weather and fuel moisture conditions that allow for high fuel consumption without excessive risk of escape. The fires occurred over four consecutive days, from 20-23 April 2021. Ground-based instruments were mounted on an UTV and placed on the west side of the burn units to maximize smoke sampling efficiency. Launch points for drones were on the side of the ground-based sampling locations. This allowed a clear line of site between the operator and the drone.

The ignitions occurred during daytime with Unit A being burned on the first two days and Units B and C being burned on the next two days. The general objectives were to consume at least 50% of fine fuels while limiting mortality of trees greater than 50 cm DBH to less than 10%. For canopy trees surviving the fire, crown damage was desired to be less than 50% on average. At the time of ignitions, 10-hour fuel moisture ranged from 11 to 15%; relative humidity ranged from 35 to 50%; and temperatures ranged from 14 to 18 °C. Strip-head fires were used with flame lengths typically less than 1.5 m. Torching of understory trees was common and torching of midstory trees occurred infrequently. Canopy trees that died were primarily killed by excessive heat scorching.

The burn window was selected based on conditions that minimized air quality impacts of prescribed fires on neighboring communities. Prevailing winds are normally chosen to move smoke away from communities and fires are burned with higher amounts of flaming combustion versus smoldering to reduce the amount of smoke and its duration. Even with these measures smoke commonly reaches communities, especially at night when downslope winds are present and smoke sometimes pools in low lying areas. As part of the required Smoke Management Plan, the contractors worked with the local air pollution control district to minimize public health impacts.

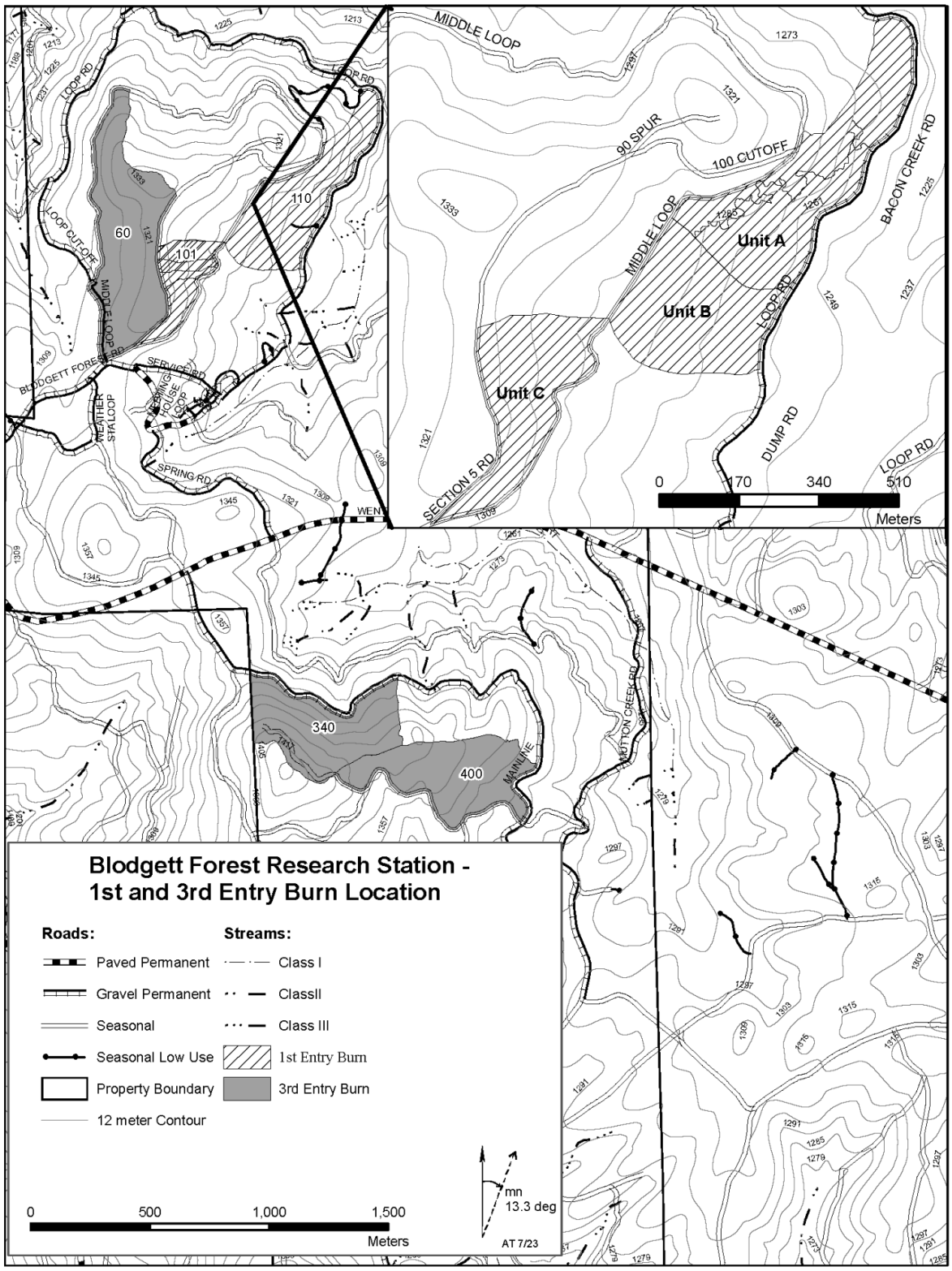

Figure 1.1 Overview of 1st (2021) and 3rd (2017) entry burn locations at Blodgett Forest Research Station. This project focusses on the 1st entry burns sampled in 2021 (see also **Figure 1.2**).

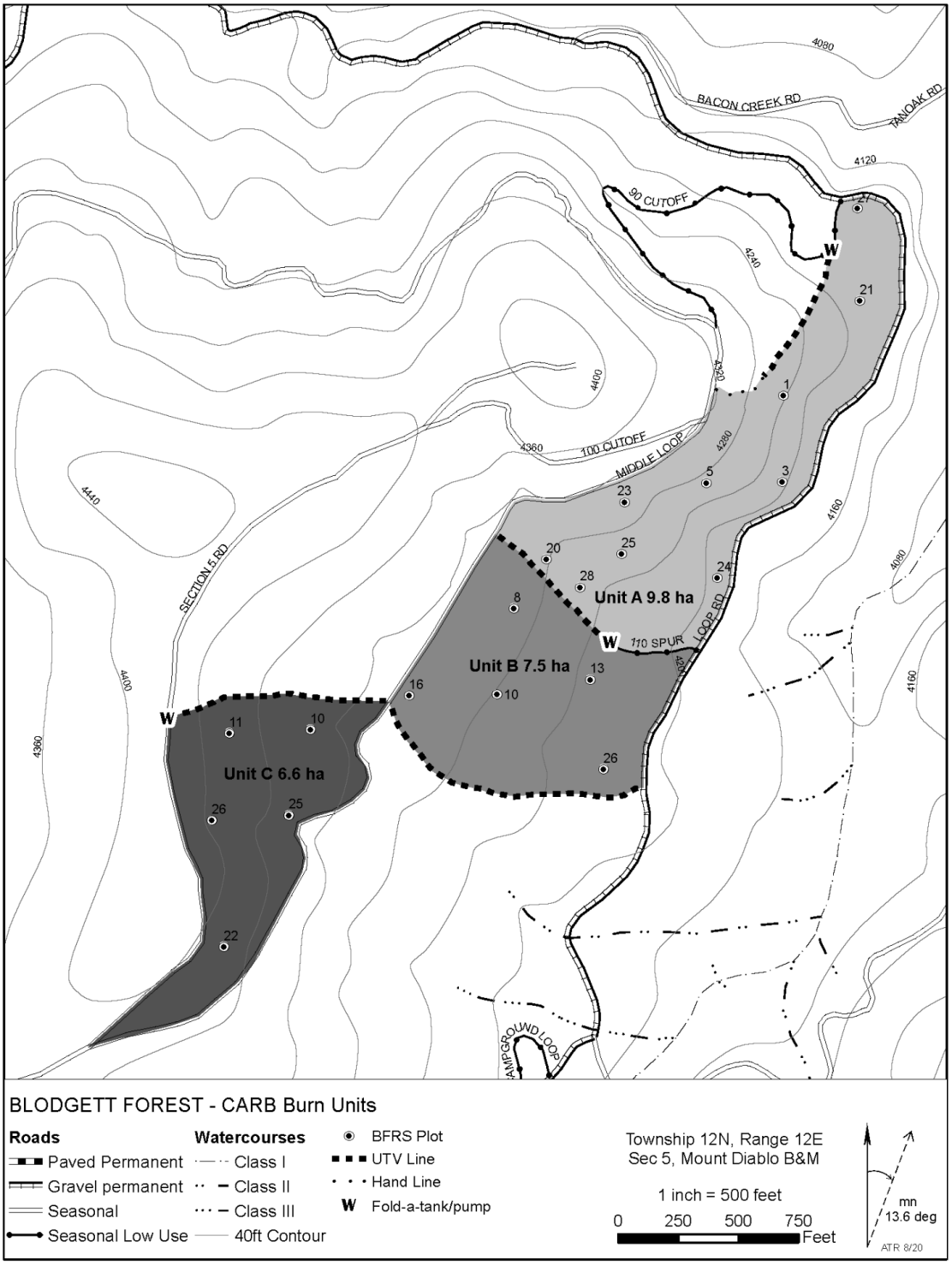

Figure 1.2 Blodgett Forest Research Station map showing location of 1st entry (no previous prescribed fire) stand, Compartment 110, divided into three burn units: A, B, and C. Existing access roads and UTV-drivable fire breaks provided access for both ground- and drone-based sampling.

Emissions Measurements

Sampling Approach. Considering the local meteorology, and in coordination with the fire management team, measurements were conducted via ground- and drone-based sampling platforms to characterize fresh gaseous and particulate emissions during several hours of each day's prescribed burn. The ground-based system was built on the bed of a UTV that included a suite of real-time online measurements (Horiba CO, CO_2, and NO_x analyzers; and a miniature aethalometer and a research-grade multi-wavelength aethalometer for BC) plus a multi-channel sequential sampler for simultaneous collections of I/VOCs on sorbent cartridges in parallel with SVOCs and $PM_{2.5}$ on quartz filters. These sample pairs were analyzed offline using two-dimensional gas chromatography coupled with time-of-flight mass spectrometry (GCxGC-ToFMS) for speciated organics. The drone platform included similar measurements of CO_2, CO, and BC; matching the ground sampling, with I/VOCs collected on sorbent cartridges and SVOCs and $PM_{2.5}$ on quartz filters for identical offline analysis. Offline OC/EC analysis was also performed using punches from filter samples taken from quartz filters collected on both platforms. This coordinated sampling and analysis of gaseous and particulate compounds allowed the contractors to determine EFs for individual compounds in the gas and particle phase, components of the particle phase (e.g., OC, EC, BC), and total $PM_{2.5}$.

The mobile ground-based sampling platform was positioned downwind of the burn unit(s) on either existing access roads or newly created firebreaks on the perimeter of the burn unit(s). The first burn (Unit A) lasted 2 days, while the second two burns (Units B and C) lasted one day each. Sampling was conducted for ~3 hours during the smoldering phase. Online instruments operated continuously during this time, while sorbent tube and filter samples were collected sequentially during this time for ~30 min/sample.

Aerial sampling using an Uncrewed Aerial System (UAS) complemented the ground sampling with an expected averaged representation of the prescribed burn emissions profile that escapes the forest canopy. Constraints related to safety and difficult terrain limited the flight plan to manual control under visual observation. The drone was therefore launched from an access road with visual lines of sight to the fires. The UAS was flown into plumes well above the canopy (20-50 m). For each flight, a single filter plus cartridge set was used to sample directly from multiple plumes during the flight.

Gaseous Organic Compounds. Adsorption/thermal desorption (TD) cartridges were used to collect gaseous I/VOCs from the ground- and drone-based platforms. Contractors found that the use of dual-sorbent bed cartridges (100 mg Tenax TA 35/60 and 200 mg Carbograph 1 TD 60/80 in series) permitted collection of compounds with a wide range of volatilities. During FLAME-4 and FIREX, compounds ranging from C3 oxygenates to C15 sesquiterpenes could be trapped and analyzed (Hatch et al., 2015). Breakthrough samples were collected to assess the trapping efficiency of the cartridges toward the most volatile compounds.

Cartridge samples were analyzed using a Pegasus 4D GC×GC-ToFMS (LECO Corp., St. Joseph, MI) equipped with a Turbomatrix 650 automated thermal desorption (ATD) system (Perkin-Elmer, Waltham, MA) at UC Riverside. The Turbomatrix 650 ATD permits multiple analyses of the same cartridge, thereby readily allowing replicate analyses for quality control, as well as application of different GC×GC-TOFMS analytical conditions (e.g., different injection split ratios to extend the range of quantification or different column sets). Selection of column sets were based on analysis of BB samples collected during FLAME-IV and FIREX, and were optimized for enhanced separation of targeted compounds. Preferred column sets for BB samples thus far include: 1) a DB-VRX primary column 30 m, 0.25 mm I.D., 1.4 μm film, Agilent, Santa Clara, CA) and a Stabilwax secondary column (1.5 m, 0.25 mm I.D., 0.5 μm film, Restek, Bellefonte, PA); and 2) a Rxi-5ms primary column (30 m, 0.25 mm I.D., 0.25 μm film, Restek, Bellefonte, PA) with a Rxi-17Sil MS (1.5 m, 0.15 mm I.D., 0.15 μm film, Restek, Bellefonte, PA) secondary column (Hatch et al., 2015, 2019).

The GC×GC-ToFMS data was processed using a combination of proprietary software from LECO (ChromaTOF) and in-house algorithms. QA/QC procedures, including calibration, were performed using ChromaTOF; sample alignment and compound identification were performed with the in-house algorithms.

Particulate Organic Compounds. Quartz filters were used on ground- and drone-based platforms to collect SVOCs and $PM_{2.5}$ emitted from fires, for analysis of OC/EC and speciated organic compounds. Samples were analyzed using thermal desorption two-dimensional gas chromatography-electron impact/vacuum ultraviolet high-resolution time-of-flight mass spectrometry (GC×GC-EI/VUV-HRToFMS) with online derivatization at UC Berkeley; a custom instrument developed in the Goldstein group (Jen et al., 2019). Small punches of each filter were thermally desorbed at 320 °C in a He flow using a Gerstel Thermal Desorption System. The He gas stream was saturated in N-Methyl-N-(trimethylsilyl) trifluoroacetamide, a derivatization agent, for online derivatization during thermal desorption. The compounds were trapped at 30 °C prior to injection onto the first column. Compounds are first separated by volatility with a Rxi-5Sil MS column then by polarity with a Rtx-200 MS column. EI-HRToFMS was then used to ionize and measure the mass fragments of the separated compounds. Though a vast number of compounds remain unidentified, the UCB team has built a mass spectral (MS) library in NIST format named University of California, Berkeley, Goldstein Library of Organic Biogenic and Environmental Spectra (UCB-GLOBES), including mass spectra from FIREX BB samples and additional relevant field samples. This MS library was used to match and keep track of compounds observed in the prescribed burn experiments.

The measurements described above generated data for combustion diagnostics including MCE (an index of smoldering versus flaming) and CO/CO_2 (similar to MCE index, smoldering/flaming

ratio). Measurements of CO_2 and CO enable calculation of EFs (in units of g (or lbs) species per kg (or ton) fuel burned) by the carbon mass balance method for all of the other co-sampled gaseous and particulate species (includes individual compounds as well as "bulk" EFs, such OC and $PM_{2.5}$). EF databases were developed for measurements made during the BFRS prescribed fires.

For both the filters and cartridges, blank and background samples were collected daily for background subtraction of the smoke samples. Calibration standards were similarly analyzed for a range of BB-relevant compounds (including aromatic/aliphatic hydrocarbons, phenol derivatives, furan derivatives, and terpenes) to positively identify and quantify such compounds. Further details on sample handling and analysis protocols, including QA/QC procedures, can be found in Hatch et al. (Hatch et al., 2015, 2019) and Jen et al. (Jen et al., 2018, 2019).

Experimental Approach. A key element of this contract was a coordinated effort to link ecosystem determinants of fire behavior with emission profiles. At BFRS, the application of prescribed fire follows typical management objectives, namely, to reduce future fire severity via the consumption of surface fuels while limiting the mortality of canopy trees (Stephens and Moghaddas, 2005a). The 1st entry burns were completed in a stand that because of its management history ((Stephens and Moghaddas, 2005b), was prioritized for fuel reduction treatments.

To incorporate fine scale heterogeneity in fuel consumption and emissions production (Hiers et al., 2020), the treatment area was divided into three burn units approximately 8 ha in area (**Figure 1.2**). Prescribed fire was applied to each unit over the course of four consecutive days.

Sampling Strategy. Forest and fuel characteristics were collected in each unit from established permanent inventory plots at BFRS both before and after the prescribed burns. Sampling methods followed established inventory protocols (e.g., Vilanova et al., 2023). However, considering the importance of ground and surface fuel characteristics in determining fire behavior and emission profiles (Weise and Wright, 2014), contractors intensified the sampling regime of fuel classes (**Figure 1.3**). Specifically, the sampling intensity of litter, duff, 1-hr and 10-hr fuels was increased by 8x; 100-hr fuels by 5x; and CWD by 3x. There were four 30-meter main transects (blue) extending from plot center at cardinal directions. Depths of duff and of litter were sampled at locations 2.0, 2.1, 2.2, 2.3, 2.4, 2.5, 3.0, 3.5, 4.0, 4.5, 5.5, 7.0, 7.5, 9.5, 19.5, and 29.5 meters from plot center along each of the four main transects. 1-hour, 10-hour, and 100-hour fine woody debris particles were tallied on 1-meter subtransects located along each main transect from 2-3, 3-4, 4-5, 7-8, 9-10, 19-20, and 29-30 meters along each main transect and orthogonal to (bisected by) the main transect and intersecting it at 2.5, 3.5, 4.5, 5.5, 7.5, 9.5, 19.5, and 29.5 meters (red). Coarse woody debris particles were inventoried (diameter, location, decay class) from 0-30 meters along each main transect, and understory vegetation intersecting the main transect from 0-15 meters was recorded using line intercept sampling. Trees ≥ 11.4 cm DBH and saplings ≥ 1.37 m height were

inventoried (species, DBH, height, height to live crown, live/dead status, and spatial location) within a 500 m^2 fixed area plot (trees; purple) or a 116 m^2 fixed area plot (saplings; green).

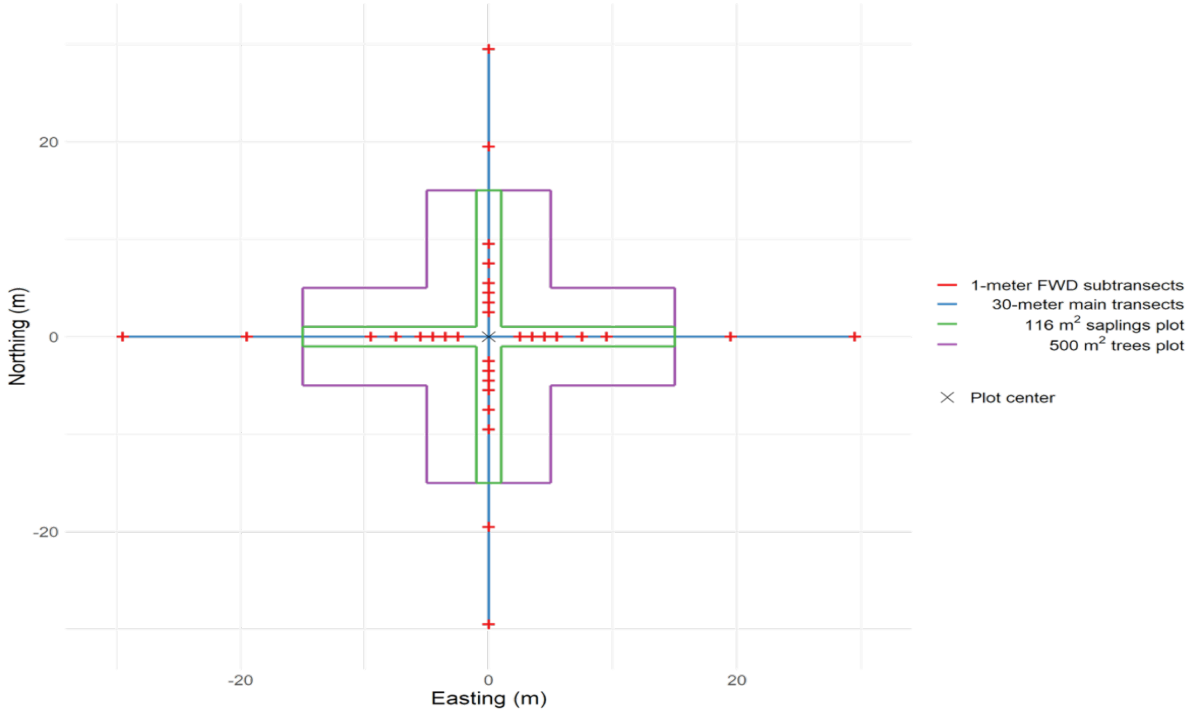

Figure 1.3 Forest and fuel plot inventory layout for the 1st entry prescribed fire at BFRS.

Prior to burning, ground and surface fuels were sampled using the line-intercept method (Brown, 1974; Van Wagner, 1982). On each of four 30-m transects arranged at cardinal directions from the plot center, the depth of litter and duff was recorded at 16 points. Fine woody debris (FWD) was measured by three diameter classes (≤ 0.64 cm diameter; > 0.64 ≤ 2.54 cm; > 2.54 ≤ 7.62 cm) that correspond to 1-, 10-, and 100-hour time lags. FWD particles were tallied by time lag class along a series of 16 subtransects (1m in length) along each transect (total FWD subtransects per plot = 16*4= 64). Coarse woody debris (CWD, woody particles > 7.62 cm in diameter at intersection) was inventoried along each transect, with the diameter at intersection and decay class of each particle recorded. Shrubs were inventoried along each 30-m transect, with crews recording the species, height, major and minor crown diameters, and (for post-burn observations) the percent crown torch of each individual shrub whose crown intersected the transect. Crews recorded an ocular estimate of percent cover of herbaceous species along each transect. Saplings (trees > 1.37 m in height but less than 11.4 cm in diameter at breast height, DBH) were inventoried within a 116 m^2 fixed area plot, with crews recording the species, live/dead status, DBH, height, height to live crown, decay class (for snags), percent crown torch (post-burn), and percent crown scorch (post-burn) for each sapling. Likewise, trees (≥ 11.4 cm DBH) were inventoried with the same information on a 500 m^2 fixed area plot.

For two weeks prior to burning, surface fuel moistures were measured. At two locations in each unit, samples of 100-hr and 1000-hr fuels were collected and sealed in metal soil sampling cans. The weight of the cans was measured (g) and placed in a drying oven at 105 °C for 24 hours, and then re-weighed to calculate moisture content on a dry weight basis.

Analysis. These intensive plot data were converted into unit-level biomass density estimates using established methods as follows. Biomass density estimates for litter, duff, fine woody debris, and coarse woody debris were calculated using species-specific coefficients given by Van Wagtendonk et al. (Van Wagdendonk et al., 1996, 1998) as described in Stephens (Stephens, 2001). Biomass was estimated for individual shrubs using the allometric equations given by McGinnis et al. (McGinnis et al., 2010) and converted to per-area biomass density using the line-intersect equations described in Battles et al. (Battles et al., 1996). Percent cover observations for herbaceous plants were converted to biomass density using the methods of Campbell et al. (Campbell et al., 2009). Crown foliage and branch biomass of saplings and trees was estimated using allometric equations aggregated by Jenkins et al. (Jenkins et al., 2003). Contractors repeated the field measurements after the prescribed fire, adding estimates of crown torching, foliage scorching, and bole char height to the live tree assessments and estimates of crown torching to live shrub estimates.

The field estimates of biomass provided sufficient information to quantify the variation in the structure and abundance of fuels. By comparing pre- and post-fire fuel loads, contractors quantified fire intensity. To inform total emission estimates, biomass was converted to carbon using a carbon-to-mass ratio of 0.5 for all pools except duff where a ratio of 0.37 was used (Penman et al., 2003).

FOFEM Integration. FOFEM is a fire effects model that estimates the immediate impacts, or first-order effects, of fire including fuel consumption and smoke emissions (Keane and Lutes, 2018)/ It forms the basis for CARB's Emission Estimation System (EES, https://www.arb.ca.gov/ei/see/see.htm) used to inventory smoke production from wild and managed fires in the state. FOFEM is national in scope. It relies on geographic region and vegetation type to select default input values and appropriate algorithms. It requires site-level fuel load inputs (biomass per unit area) of common fuel components. The components are defined as litter, duff, 1-hr fuel (wood 0-0.1 cm diameter), 10-hr fuel (wood 0.1 - 2.5 cm diameter), 100-hr fuel (wood 2.5-7.6 cm diameter), 1000-hr fuel (wood > 7.6 cm diameter), and live fuels (i.e., herbs, shrubs, and tree foliage). FOFEM includes default loadings for classes of vegetation (i.e., Ponderosa pine forest) that can be adjusted for magnitude and fuel moisture content using site-specific information.

FOFEM estimates consumption of the fuel load inputs using a variety of methods. It assumes 100% consumption of litter and herbaceous fuel types. Shrub and duff consumption are determined with empirically derived regression models based on geographic region. To estimate woody fuel consumption, FOFEM applies Burnup, a mechanistic fuel consumption model. In addition to total

fuel consumption, the fractions consumed during flaming combustion and smoldering combustion are estimated using the Burnup model. Fuel moisture levels are key determinants in modeling these combustion ratios. Smoke emissions are calculated from the combustion estimates using reported EFs (in units of mass of emissions/mass of fuel consumed). These factors are empirically derived for each pollutant and fuel component, with some components having different EFs for flaming vs. smoldering combustion. The current defaults used by EES also vary by moisture content class (i.e., dry, moderate, and wet).

This project supported the EES by evaluating the fuel consumption and smoke emissions projected by FOFEM with measurements of fuel consumption and emissions from prescribed fires in a common California forest type. The results informed a three-stage model assessment conducted in collaboration with CARB that focused on: 1) the suitability of the existing fuel models for mixed conifer forest type; 2) the accuracy of fuel consumption estimates; and 3) the sensitivity of smoke predictions to fuel consumption and the default EFs. The empirical documentation of consumption by fuel component provides the means to test and then calibrate, if needed, the performance of Burnup under novel fuel loadings. New EFs are provided that maintain existing functionality, but include EFs for individual compounds/compound classes in both the gas and particle phases that are considered important for predicting air quality impacts and are not currently included in FOFEM.

2. Description of Fuel Characteristics: Pre and Post Prescribed Burn

2.1. Pre-Fire Conditions

The 1st entry prescribed fire was conducted in a stand (Compartment 110, **Figure 1.2**) that is generally representative of the vast California mixed conifer forests (31,223 km^2) that dominate the midslope zone on the westside of the Sierra Nevada (Safford and Stevens, 2017; USDA, 2023). Prior to the fire suppression era, these forests had low to moderate severity frequent-fire regimes (i.e., < 35 years) ((North and Hurteau, 2011; Safford and Stevens, 2017)). They are dominated by a mix of tree species that include ponderosa pine (*Pinus ponderosa* Douglas ex Lawson), Douglas-fir (*Pseudotsuga menziesii* (Mirb.) Franco), incense-cedar (*Calocedrus decurrens* (Torr.) Florin), white fir (*Abies concolor* (Gord. & Glend.) Lindl. ex Hildebr.), sugar pine (*Pinus lambertiana* Douglas), and California black oak (*Quercus kelloggii* Newberry). The climate of the western Sierra Nevada is Mediterranean with cool wet winters followed by warm-to-hot, dry summers. Going forward, temperatures are expected to rise (3 to 5 °C on average by the end of the 21st century) and the summer drought period is expected to lengthen (Dettinger et al., 2018).

Compartment 110 is a second-growth forest that has experienced single tree selection harvests at approximately 10-year intervals starting in 1983. The pretreatment forest density of 377 ± 36 trees ha^{-1} (mean ± standard error) and basal area of 45 ± 8 m^2 ha^{-1} fell well within reported values for mixed conifer forests (Vaillant et al., 2009; Vilanova et al., 2023). However, given its history of sustainable harvests, tree density and basal area tended toward the lower end of the observed range. Similarly the pretreatment ground and surface fuel load of 104 ± 16 Mg ha^{-1} matched contemporary values albeit at the lower end of the range. In summary, the forest structure and fuel load of Compartment 110 prior to prescribed fire was typical of second-growth mixed conifer forests where high tree density and high surface fuel loads create high wildfire hazard (Stephens et al., 2009; York et al., 2012).

There were only modest differences in forest structure (**Table 2.1**) and composition (**Table 2.2**) among the three burn units. Unit C had the highest tree density and basal area while Unit B had the least, but the range of variation was small with Unit B having 35% less density and 29% less basal area (**Table 2.1**). The most striking difference in terms of composition was the shift in dominance between white fir and sugar pine in Unit B. While white fir accounted for more than 15% of the relative basal area in Units A and C, it was < 5% in Unit B. On the other hand, sugar pine was the second most dominant species (21%) in Unit B while sugar pine was the least dominant species (< 5%) in Units A and C (**Table 2.2**).

Table 2.1. Forest structure of the three burn units prior to the application of prescribed fire. Units located at Blodgett Forest Research Station. Results for live trees ≥ 11.43 cm in diameter at breast height; QMD - quadratic mean diameter.

Unit	Area (ha)	N (plots)	Basal Area (m^2 ha^{-1})		Density (trees ha^{-1})		Tree Height (m)		QMD (cm)
			mean	se	mean	se	mean	se	
A	9.8	9	40.9	4.7	358	30	16.8	1.0	38.2
B	7.5	5	39.4	11.2	312	27	16.2	1.7	40.1
C	6.6	5	55.9	9.0	480	56	16.2	1.2	38.5

Table 2.2. Forest composition in the three burn units prior to the application of prescribed fire. Units located at Blodgett Forest Research Station. Results for live trees ≥ 11.43 cm in diameter at breast height. Composition is reported as relative basal area (i.e., dominance).

	A		B		C	
Species	mean	se	mean	se	mean	se
incense-cedar	33.6	0.1	29.8	0.1	32.5	0.1
ponderosa pine	18.4	0.1	15.9	0.1	26.5	0.1
Douglas-fir	26.2	0.1	19.4	0.1	13.3	0.0
white fir	15.9	0.1	4.7	0.0	15.7	0.0
sugar pine	0.1	0.0	20.9	0.2	4.8	0.0
black oak	3.7	0.0	2.5	0.0	7.2	0.1

Initial fuel loads were also similar among the burn units (**Table 2.3**). Both in terms of total fuel load and distribution by class, the differences between Unit A and B were minor. However Unit C did have 24% more ground and surface fuel with most of the difference due to having nearly 60% more duff (**Table 2.3**). Not surprisingly given its greater tree density and basal area, Unit C also supported more fuel in its tree crowns.

Table 2.3. Fuel loads in the three burn units prior to the application of prescribed fire. Units located at Blodgett Forest Research Station. Means and standard errors (se) reported for each unit. CWD = coarse woody debris (i.e., 1000+hr fuels).

Class	Unit A		Unit B		Unit C	
	Mass (Mg ha^{-1})		Mass (Mg ha^{-1})		Mass (Mg ha^{-1})	
	mean	se	mean	se	mean	se
1-hr	1.3	0.1	1.3	0.2	1.0	0.2
10-hr	4.3	0.4	4.3	0.1	3.5	0.5
100-hr	9.8	1.6	8.1	1.4	9.9	5.0
CWD (1000-hr+)	17.2	2.9	21.9	5.6	16.5	2.5
Litter	34.8	1.9	27.3	5.0	38.8	2.7
Duff	34.8	5.6	29.0	5.5	50.7	9.1
Herb	0.1	0.0	0.3	0.2	0.1	0.0
Shrub	1.5	0.6	1.3	0.4	0.8	0.3
Crown (tree)	64.5	9.3	61.8	18.1	80.7	15.8

2.2. Prescribed Fire Objectives

The overall management goal was to restore fire as an ecosystem process while reducing wildfire hazard. The specific objectives were to consume at least 50% surface fuels, primarily from litter and fine woody debris (FWD, includes 1-, 10-, and 100-hour fuel categories). At the same time we wanted to manage the burn intensity to avoid either low or high intensity scenarios that would typically be undesirable for most management contexts. Specifically, the objectives were to limit the crown scorch of canopy trees surviving the fire to less than 50% on average, and to limit post-burn mortality to no more than 10% of trees greater than 50 cm DBH.

2.3. Post-Fire Conditions

The spring burns met or exceeded the management goals. Specifically, the treatments reduced the mass of litter and fine woody debris by 65% (**Figure 2.1**). Total ground and surface fuel load was reduced by 53% with the lower rates of combustion (<50%) occurring in the heavy fuels (i.e., duff and coarse woody debris). In terms of limiting burn intensity, crown scorch never exceeded 32% in any unit (**Table 2.4**) and only one of the 63 trees > 50 cm DBH was killed in the fire.

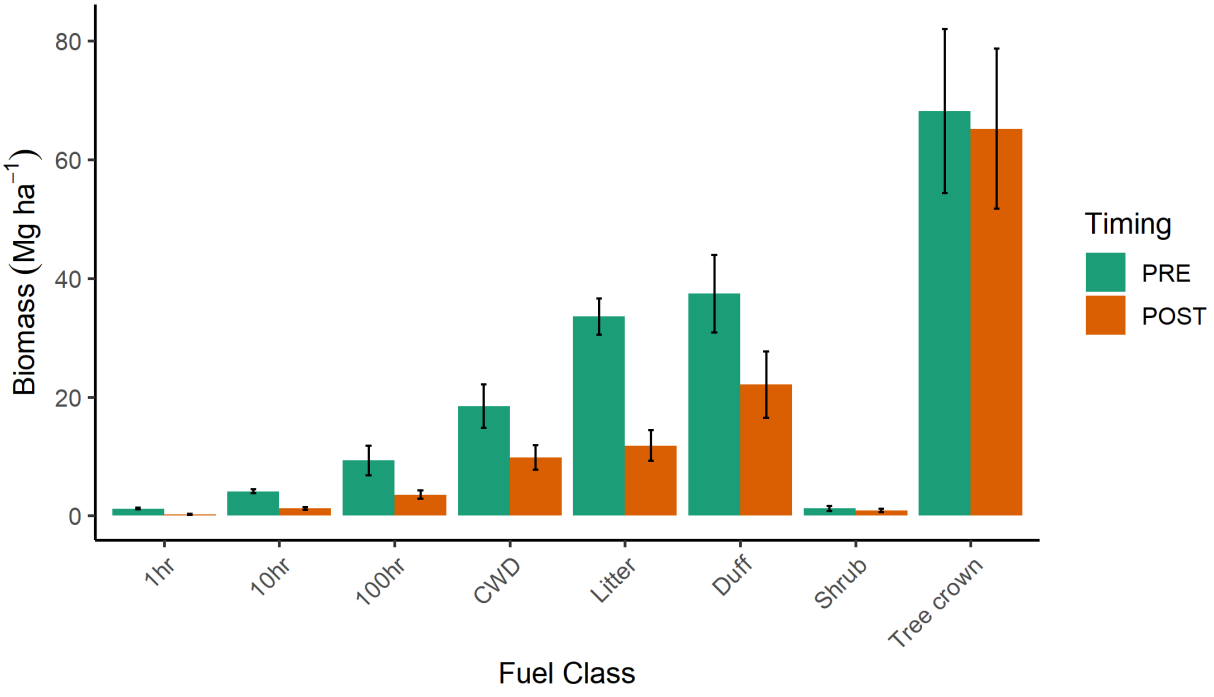

Figure 2.1 Changes in the fuel loads following 1st entry prescribed fire at Blodgett Forest Research Station. Biomass reported as the area-weighted mean and standard error from the three burn units.

Table 2.4. Fire severity statistics for the prescribed fires implemented in the three units at Blodgett Forest Research Station. Mortality is reported for trees ≥ 11.43 cm DBH. N represents the number of trees that survived the fire. Means and standard errors (se) reported for each unit.

Unit	Mortality (%)	N (tree)	Torch (%)		Scorch (%)		Char (%)		Char Height (m)
			mean	se	mean	se	mean	se	mean
A	12.4	141	0.2	0.2	9.7	1.7	3.4	0.5	0.82
B	25.6	58	13.3	2.9	31.9	4.2	9.8	1.8	0.86
C	14.2	103	7.9	1.4	30.7	3.0	8.2	1.2	0.70

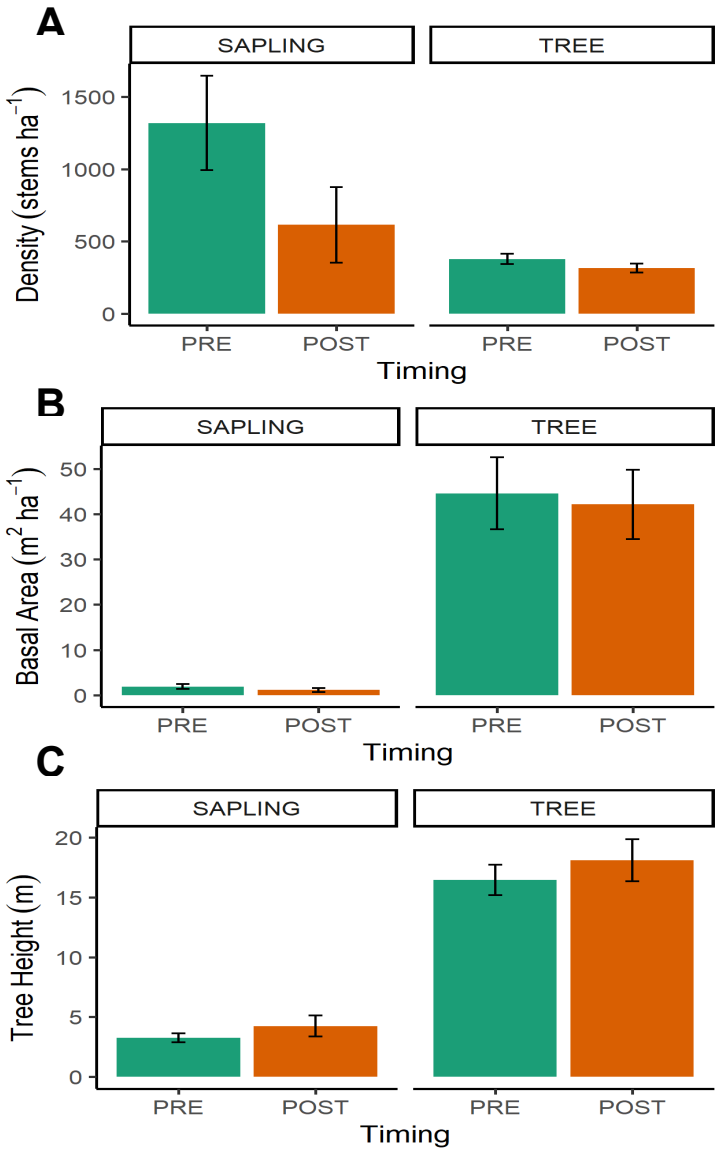

Despite the meaningful reductions in surface fuel loads, the prescribed fire had only modest effects on forest structure and minimal impacts of forest composition. Across the units, post-fire live tree density decreased by 17% (**Figure 2.2A**) and basal area by 5% **(Figure 2.2B**). Clearly, fire-related mortality was concentrated among the smaller diameter trees; more than half the saplings were killed in the fire (**Figure 2.2A**). This size-effect translated into taller average tree heights post-fire (**Figure 2.2C**). The pre-to-post fire differences in species dominance (**Figure 2.3**) were negligible indicating that there were no species-specific responses to the prescribed fire.

Figure 2.2 Changes in forest structure following 1st entry prescribed fire at Blodgett Forest Research Station. Values reported as the area-weighted mean and standard error from the three burn units. A. Stem density; B. Basal area; C. Tree height. Trees = live stems ≥ 11.4 cm DBH; saplings = live stems < 11.4 cm DBH and ≥ 1.37 m tall.

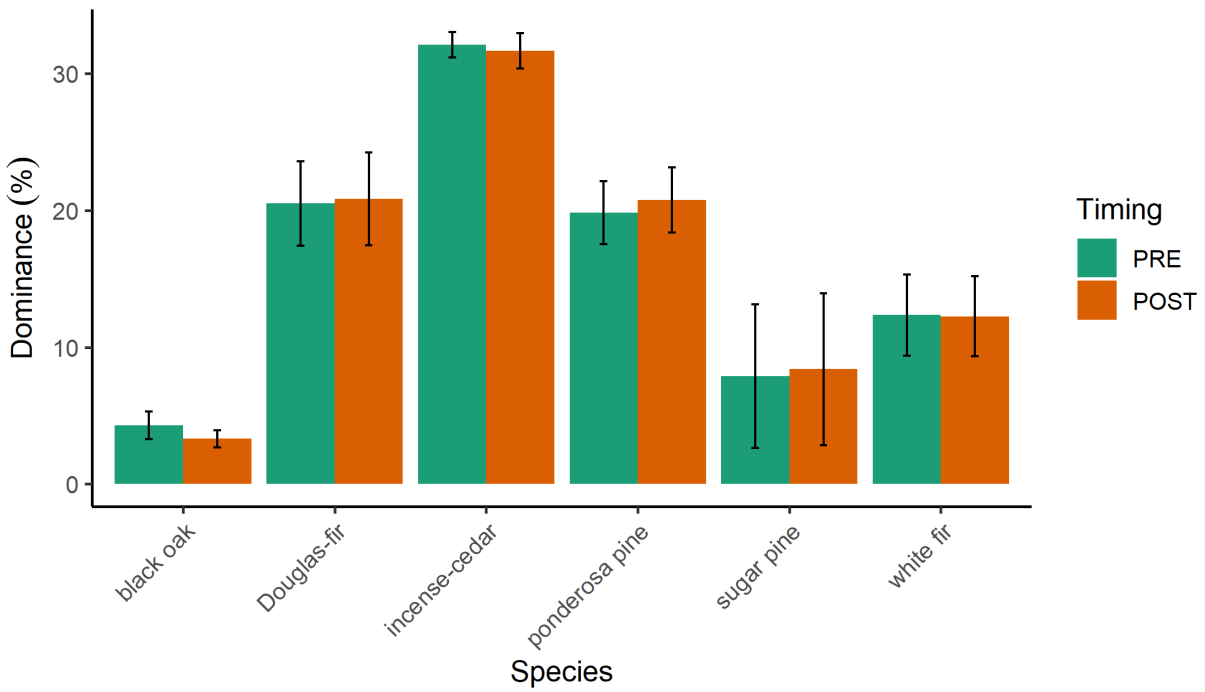

Figure 2.3 Changes in the species composition following 1st entry prescribed fire at Blodgett Forest Research Station. Dominance (i.e., relative basal area) reported as the area-weighted mean and standard error from the three burn units. Dominance includes live trees ≥ 11.4 cm DBH.

2.4. Carbon Storage

Immediately post-fire, aboveground carbon storage was reduced by 26.9 MgC ha^{-1} (**Table 2.5**). Most of this 13% reduction was due to losses in woody surface fuels (i.e., downed and dead wood) and duff. There were only minor losses (6%) in the largest aboveground carbon pool – live trees. However, elevated rates of tree mortality are expected to continue post-fire for several years (van Mantgem et al., 2011). While this 1st entry burn met prescription and meaningfully lowered surface fuel loads, it was a comparatively low-intensity fuel reduction treatment. The percentage of surface fuel carbon lost from 1st entry prescribed fires in comparable forest types ranged from 77% of pre-fire totals (Blodgett Forest, (Stephens and Moghaddas, 2005a)) to 71% (Sequoia Kings Canyon National Park, (Knapp et al., 2005)) to 22% (Teakettle Experimental Forest, (North et al., 2009)). In terms of the carbon pools included in California forest offsets (live plant biomass and standing dead trees, CARB 2015(California Air Resources Board, 2015)), the prescribed fire reduced carbon storage by only 1.2% of the pre-fire total (1.9 MgC ha^{-1}).

Table 2.5. Changes in the forest carbon pools following prescribed 1st entry prescribed fire at Blodgett Forest Research Station. Carbon density reported as the area-weighted mean (mean) and standard error (se) from the three burn units. Live and standing dead trees defined as stems ≥ 11.4 cm DBH. Understory pool includes live saplings (trees < 11.4 cm DBH and ≥ 1.37 m in height), shrubs, and herbs; Dead and downed wood includes fine and coarse woody debris.

Pool	**Pre-fire (MgC ha^{-1})**		**Post-fire (MgC ha^{-1})**		**Change**	
	mean	se	mean	se	%	MgC ha^{-1}
Live tree	150.9	35.2	142.2	32.2	-6%	-8.7
Standing dead tree	8.9	3.9	15.8	8.2	78%	6.9
Understory	0.6	0.2	0.5	0.1	-27%	-0.2
Dead and downed wood	16.6	3.1	8.1	1.8	-51%	-8.4
Litter	16.8	1.5	5.9	1.3	-65%	-10.9
Duff	13.8	2.4	8.2	2.1	-41%	-5.7
TOTAL	**207.6**		**180.7**		**-13%**	**-26.9**

2.5. Comparison of Fuels Consumed in 2017 vs 2021

Prior to treatment, the fuel load in the 1st entry burn was 60% higher than in the 3rd entry burn. Total pre-fire ground and surface fuel load for the 1st entry burn was 104 Mg ha^{-1}; for the 3rd entry burn, it was 65 Mg ha^{-1}. The percentage of fuel consumed by the prescribed burns was also greater at 1st entry: 53% vs 35% (**Table 2.6**). In addition, there was a distinct difference in the composition of the consumed fuels (Figure 2.4, Levine et al., 2020). As is typical for mixed conifer forests, duff and litter accounted for most of the fuels consumed (67% for 1st entry; 46% for 3rd entry). However coarse woody debris accounted for more than a 1/3 of the fuel consumed in the 3rd entry burn (**Figure 2.4**). In general, first entry burns are expected to have a greater absolute impact on fuel loads than subsequent entries (York et al., 2022). In the 1st entry burn, 3.3 Mg ha^{-1} of shrubs and tree crowns were combusted or about 6% of the total fuel lost. In the 3rd entry burn, a comparable total amount was combusted (4.4 Mg ha), but losses in tree crowns and shrubs represented 16% of the total.

Table 2.6. Changes in fuel loading following the 3rd entry prescribed fire at Blodgett Forest Research Station. Results summarized for burns across three "burn only" compartments. Means and standard errors (se) reported (n =3); coarse woody debris = 1000+hr fuels.

Fuel Class	**Pre-fire (Mg ha^{-1})**			**Post-fire (Mg ha^{-1})**			**Consumption**	
	mean	se		mean	se		(Mg ha^{-1})	% of Total
Duff	17.7	2.4		11.9	1.0		5.8	21.2
Litter	19.0	0.5		12.2	3.0		6.8	25.2
Fine woody debris	5.2	0.1		5.0	0.5		0.2	0.9
Coarse woody debris	23.2	6.7		13.3	2.9		9.9	36.5
Tree crown	74.8	3.8		72.2	3.9		2.6	9.6
Shrub	1.8	1.0		0.0	0.0		1.8	6.6

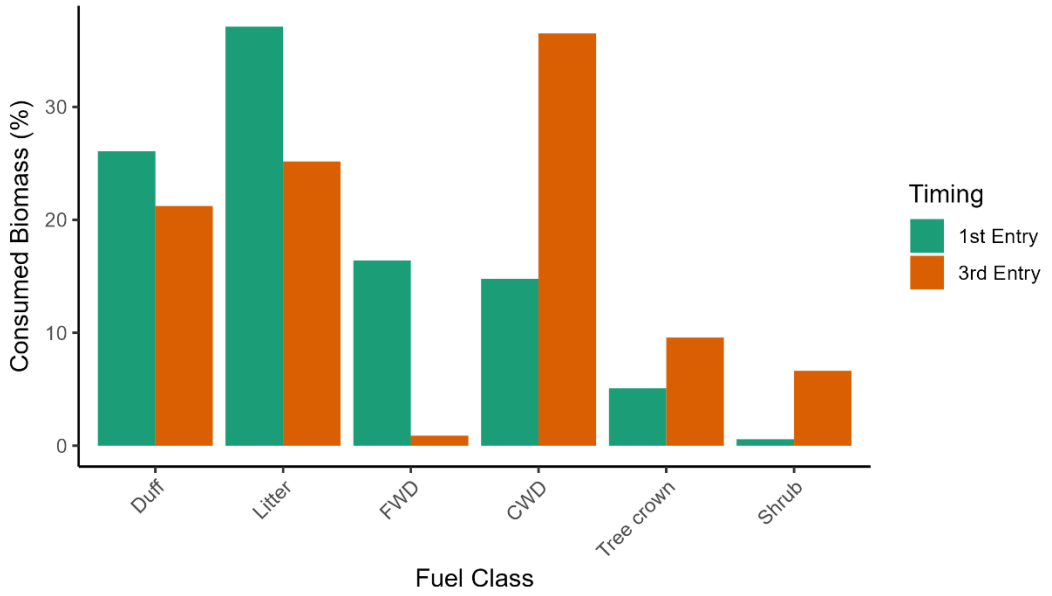

Figure 2.4 Composition of consumed fuels during 1st entry (2021) and 3rd entry (2017) studies.

3. Sampling Strategies and Particulate OC/EC/$PM_{2.5}$ Emission Factors

3.1. Methods

Gas and particle emissions were collected during two sets of prescribed burns. A pilot study was conducted during the fall of 2017 from 30 Nov-2 Dec as part of planned maintenance for 3rd entry burn compartments. A larger study was conducted in the spring of 2021from 20-23 April during the prescribed burning of a 1st entry compartment that was divided into three sub-units. **Figure 3.1** shows a satellite image of the 2021 prescribed burn stands with bounding unpaved roads and freshly cut fire breaks. The three units were burned over four days as labeled in **Figure 3.1**, along with the locations of the ground and aerial sampling indicated by symbols for universal terrain vehicle (UTV) and uncrewed aerial system (UAS), respectively.

Trace gas and black carbon (BC) emissions were collected continuously during the daytime on the ground, and periodically with aerial sampling, during the prescribed burns. Filter and sorbent tube samples were collected sequentially during the active burn phase and also during the smoldering phase, with each sampling period lasting ~3 hours. Sets of samples were collected similarly from the drone but for a shorter and variable duration (3-23 minutes per flight, 5-10 flights per burn day) to compensate for the higher concentration variations observed in smoke plumes using the real-time monitoring of excess CO_2. This sampling strategy resulted in an average of 9 sets from the ground and 8 sets from the air collected on each burn day.

Ground platform. On the ground, trace gases were collected using Horiba gas analyzers: carbon monoxide (CO) using an APMA370, carbon dioxide (CO_2) using an APCA370, and nitrogen oxides (NO_x) using an APNA370. Smoke was sampled at flow rates of 1.5 L/min, 0.7 L/min, and 0.8 L/min, respectively, through ¼" o.d. Teflon lines. Voltage data were recorded using a DATAQ

USB data acquisition system, DI-1100, with a frequency of 1 Hz (1 sample/sec). The Horiba gas monitors and a sequential sampler (further described below) were mounted on a UTV. The UTV was driven along the fire perimeter and was located at two locations on each day to best capture the visible smoke.

QA-QC procedures for the CO, CO_2, and NO_x data included checking for systematic offsets and drifts in the baseline. Post-campaign calibrations were performed on each of the Horiba analyzers after returning from the field; the calibration factors obtained were used to convert the raw CO, CO_2, and $NO+NO_2$ (NO_x) voltage data to mixing ratios. To calculate enhancements in CO, CO_2, NO, and NO_2 due to smoke (i.e., Δ_i, where *i* is the gas-phase compound of interest), background mixing ratios of each compound were determined and subtracted from the measured mixing ratios. For CO, NO, and NO_2 background mixing ratios were determined to be zero. The offset correction for the CO was -1.26 ppm. For CO_2, the minimum observed mixing ratios on each day were used

to define the following background mixing ratios: 409 ppm on 04/20/2021, 410 ppm on 04/21/2021, 404 ppm on 04/22/2021, and 402 ppm on 04/23/2021.

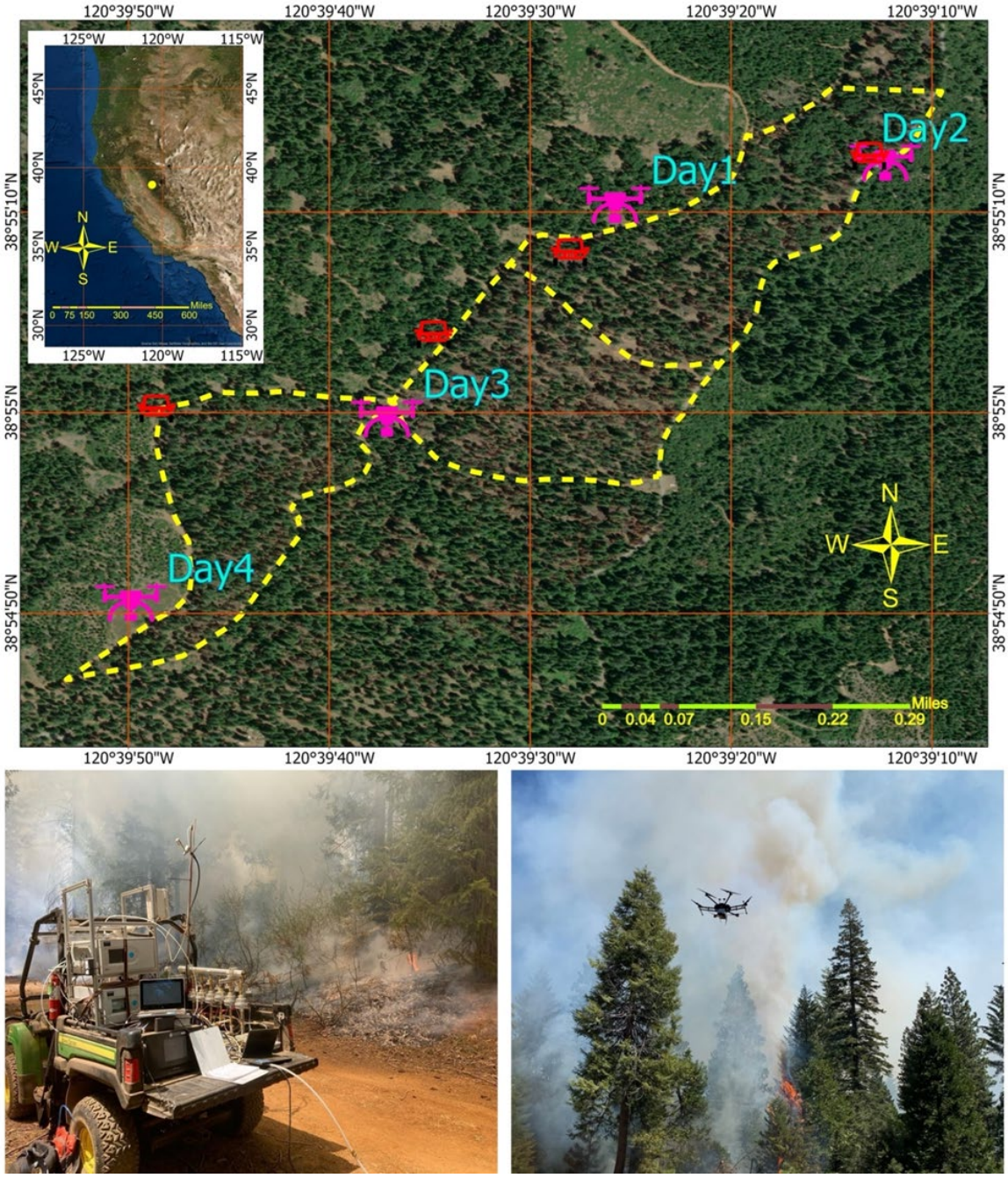

Figure 3.1 Satellite view of Blodgett Forest in the California Sierra-Nevada foothills (top and inset), showing the three units selected for prescribed burning in 2021. Bounded by roads and fire breaks (dashed lines), emissions were acquired using ground (UTV) and aerial (UAS) platforms from the positions indicated by symbols.

Particle and vapor samples were collected on a custom built sequential six-channel filter sampler (Yee et al., 2018) consisting of a common inlet manifold using an AIHL cyclone to provide a $PM_{2.5}$ cutpoint at 22 Lpm (John and Reischl, 1980). Particle samples were collected on pre-fired 100 mm quartz filters in parallel with TD cartridges for VOCs. Each channel was fitted with paired critical orifices such that the filter and sorbent tube could be operated by a single rotary vane pump. Sample flow through each of the 6 paired channels was controlled by solenoid valves using a programmable timer set to collect samples sequentially after a manual start. The total flow was continuously monitored by a mass flow meter (TSI model 4040) and the individual sample volumes for the particle and gas samples were apportioned based on the calibrated flow ratios for the paired critical orifices.

Aerial platform. The UAS used for aerial sampling was a DJI Matrice 600 Pro hexacopter with a 5 kg payload capacity sufficient for carrying the sampling instrument package with battery for operation during a 10-15 min flight (20 min max UAS flight capacity). Three sets of batteries for the UAS and instrument package, with ground recharging stations, allowed for continuous flying with down time limited by filter/tube/battery swapping. $PM_{2.5}$ filter samples were collected using a cyclone cassette (Mesa Labs p/n GK 2.05) operating at a nominal 4 Lpm. Miniature pumps were used to pull flow through the filter collectors (Particles Plus p/n UM27000 in 2021; KNF p/n KPDC-B in 2017). A parallel collection channel provided I/VOC collection on a sorbent cartridge using a dedicated miniature rotary vane pump (Schwarzer p/n 140FZ-LC). Flows were unregulated but continuously monitored using a pair of mass flow sensors (particle channel at 4 Lpm using Renesas p/n FS2012-1120-NG and the I/VOC channel at 200 ccm using Renesas p/n FS2012-1020-NG). Up to three flights per hour were made continuously over a period of 3-4 hours on each burn day.

A schematic of the sampling and sensor payload, Firehawk, in which the filter and sorbent tube samplers along with a gas filter are mounted to the outside, is shown in **Figure 3.2**. An additional gas sensor sampling line is protected at the entrance with a glass fiber filter to remove semi-volatiles that could potentially foul the gas sensors. On this gas line a pair of electrochemical cells (Alphasense CO-B4 and NO-B4) were employed to measure CO and NO followed by an NDIR CO_2 sensor (PP Systems SBA-5) that also provided the gas sample flow of approximately 200 ccm. The NO sensor was experimental and only provided reliable data on the first flight, after which the baseline became erratic. These data are not reported.

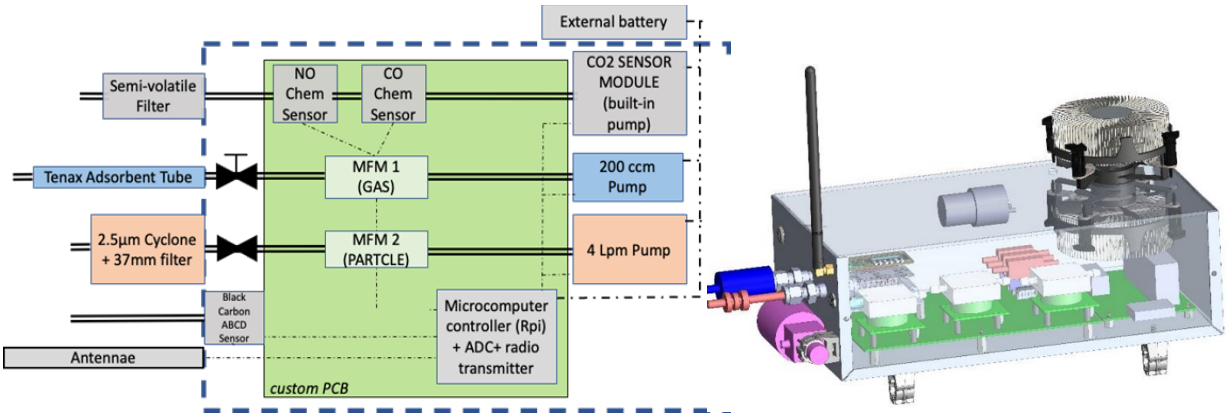

Figure 3.2 Schematic of Firehawk design (left) with components outside the dashed square indicating external mounting as illustrated in the CAD model (right).

The Firehawk was driven by a Raspberry PI Zero processor board running Raspbian Linux and programmed in Python. Three Texas Instruments ADS1115 analog-to-digital converter chips interface the processor to analog signals from the two electrochemical sensors, two mass flow sensors, an internal temperature sensor, and the CO_2 analyzer. The sampling pumps were controlled by power switches under digital line control from the processor board. During flight, sensor data, battery condition, pump status, and collection time were transmitted at 1 second intervals via a LoRa 915 MHz radio transmitter (Adafruit RFM9X) to a base station containing a Raspberry PI 3 and a matching LoRa receiver. A CRC check word and a message serial number was transmitted with the package data, and the data message was repeated three times for the sake of data fidelity. The base station drops any received message with a wrong CRC or a message whose serial number has already been received and verified. The operator controlled the sampling pumps via commands to the base station. Data were stored redundantly on the Firehawk file system as well as at the base station.

To complement the core sampling functions of the Firehawk and provide additional potential insight into the optical characteristics of the plume smoke, a miniature BC sensor (ABCD, (Caubel et al., 2018)) was added to the package for the 2021 study. This sensor is described more fully in Chapter 6 and is identical to one used on the ground platform alongside the research-grade BC analyzer. The core elements of the ABCD instrument were removed from the original packaging and mounted to the inside of the Firehawk housing cover with a dedicated sample line pulling directly from the outside. Data were integrated into the Firehawk data system using the ABCD serial output.

3.2. Results and Emission Factors

A typical example of data acquired during a single UAS flight is shown in **Figure 3.3** for the prescribed fire of April 22nd 2021. Once airborne and away from the launch site with potential CO_2/CO sources, the Firehawk sample pumps are turned on as indicated by the step-wise dashed

blue trace. The gas and BC sensors show both a range of combustion states (CO_2/CO ratio) along with large concentration variability as the UAS flies into and out of coherent smoke plumes. Particle concentrations are recorded as mass concentrations in units of mass/volume and gas concentrations are recorded as mixing ratios. The ability to sample a wider range of combustion states is an advantage of the aerial platform.

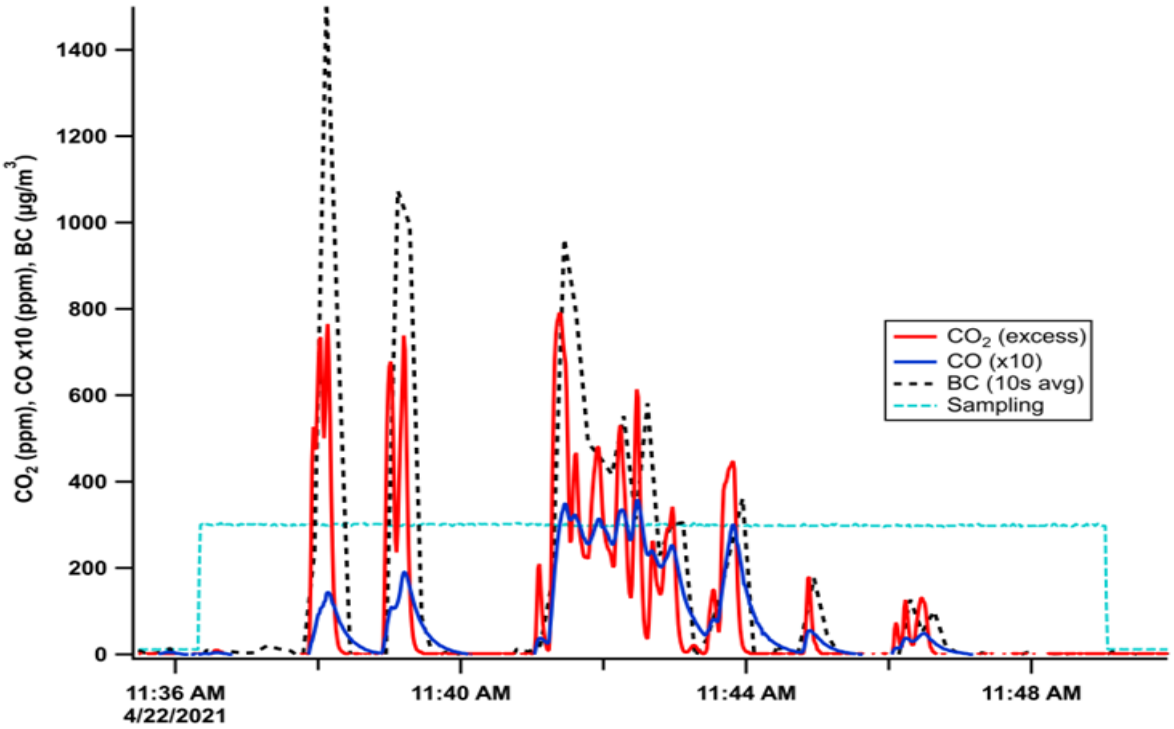

Figure 3.3 Example data acquired by the Firehawk during a single UAS flight with the CO and CO_2 gas sensors and black carbon (BC) sensor (10s average) showing clear transits of smoke plumes. Sample collection period is indicated by the pumps-on signal (dashed blue line).

Data from the drone were offset and background corrected similarly to the data from the ground. The offset correction for the CO data was 0 for 04/20/2021 and 04/21/2021, -1 ppm for 04/22/2021 and -1.7 ppm for 04/23/2021. The background CO_2 was determined to be the minimum observed mixing ratio: 420 ppm on 04/20/2021 and 04/21/2021, 402 ppm on 04/22/2021 and 397 ppm on 04/23/2021. The excess CO, CO_2 were calculated by subtracting the background CO, CO_2 from the observed CO, CO_2. MCE was calculated by:

$$\text{MCE} = \frac{\Delta CO_2}{\Delta CO + \Delta CO_2} \qquad [3.1]$$

where Δ indicates excess CO, CO_2. The MCE values are summarized in **Table 3.2**.

Comparing the measured MCE values from the ground and aerial platforms reveals differences in sampling conditions encountered by the two platforms. **Figure 3.4** shows MCE vs excess CO_2 for 2017, 2021 ground and 2021 aerial sampling. The UAS ('Aerial') relative to either ground data set sampled a greater range of MCE values and emission intensity consistent with the platform being able to selectively sample from more concentrated lofted smoke plumes derived from hotter, more intense combustion conditions. The average MCE values ± 1 standard deviation over the entire set of samples for each platform was 0.83 ± 0.03 for both ground sample sets (2017, 2021) and 0.87 ± 0.05 for the aerial sample set.

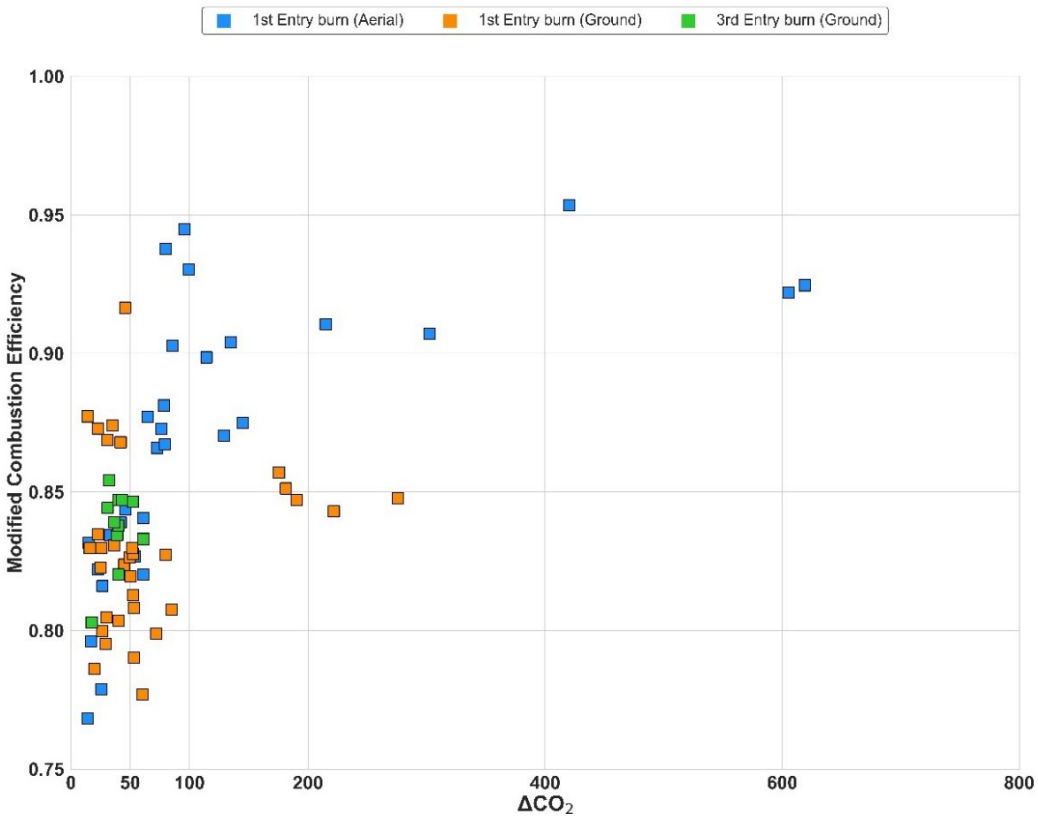

Figure 3.4 Intensity of smoke emissions during the 2017 and 2021 field campaigns as indicated by excess CO_2 ($\mu g/m^3$) and MCE during ground sampling on the 2017 field campaign (3rd entry) and ground plus airborne sampling on the 2021 field campaign (1st entry).

Organic and elemental carbon emission factors. Punches from the quartz filter samples collected from ground and aerial platforms were analyzed for organic and elemental carbon (OC and EC, respectively) using a Sunset Model 5 Lab OC/EC Aerosol Analyzer following the NIOSH870 protocol in the Air Quality Research Center at the University of California, Davis. Thermal pyrolysis (charring) was corrected using laser transmittance. Lab reported arial concentrations ($\mu g/cm^2$) were multiplied by the total filter area (8.6 cm^2) to give the absolute OC and EC masses collected on each filter. With a laboratory reported method detection limit of 0.2 $\mu g/cm^2$ carbon,

all reported organic carbon samples exceeded these limits by 1.1 to 286 times and on average was 40x MDL while elemental carbon was at or below the MDL for most of the samples owing to the reduced fire intensities for prescribed fires.

Along the lines outlined in EPA test method for characterizing open source emissions from a stationary sampling point (OTM-48,, EPA, 2022), the carbon mass balance method was used to calculated fuel based emission factors for carbonaceous species, OC and EC, determined from collected particulate matter on filters. In this method, all emissions are presumed well mixed such that gases and particles remain in fixed mixing ratios up to the point of sampling. This assumption is well accepted for combustion sources that involve intense heat and high levels of turbulent mixing at the point of emission. Continued atmospheric mixing during transport, over short distances to the point of sampling, supports the assumption that these initial mixing ratios are maintained. At some point, lower mixing ratios will be observed due to dilution; these typically can be corrected using emission ratios to CO. Lower mixing ratios also will be observed due to chemical loses, and these are harder to correct for. Nonetheless, the carbon mass balance method is widely used to derive emission factors.

The carbon balance method relies on the dominant combustion emission being represented by two primary gas species, carbon dioxide and carbon monoxide, with minor contributions from VOCs and negligible contributions from liquid and solid species (Nelson, 1982). Accordingly, we convert sampled OC and EC mass to an emission factor by dividing the sampled analyte mass by total carbon mass emitted by the prescribed fire corresponding to the filter sample volume V_s using the excess (background subtracted) ΔCO2 + ΔCO with each gas phase term derived from the respective gas sensor signal in ppm:

$$\Delta \mathrm{CO}_x = \left(\mathrm{CO}_{x,sample} - \mathrm{CO}_{x,background}\right) \times 12 \times V_s \times \left({}^{P}/_{RT}\right) \qquad [3.2]$$

With the last term a conversion of mass flow sensor measured sample volume to moles air under the assumption of an ideal gas with pressure P, temperature T and gas constant R. The emission factor EF_i for species i becomes:

$$EF_i = F_{\mathrm{C}} \times 1000(\mathrm{g\,kg^{-1}}) \times \frac{M_i}{\Delta CO_2 + \Delta CO} \qquad [3.3]$$

where i = OC, EC with M_i the corresponding collected mass in g, F_{C} is the dry mass fraction of carbon (assumed to be 0.5 for a mixed conifer fuel base), and ΔCO_2 and ΔCO in g are the background subtracted carbon mass corresponding to the filter sample volume and measured by the real-time sensors given by Eq. 3.2. The OC and EC EFs were calculated from the ground and aerial smoke samples taken during the 1st entry burn (2021) and from the ground samples taken during the 3rd entry burn (2017). To explore the impact of combustion state on the rate of carbon emissions, the OC EF and the ratio of EF_EC to EF_OC was plotted against the average MCE during each sample in **Figure 3.5**. The loosely defined transition between smoldering and flaming is taken to be an MCE value of 0.9 as indicated by the broken vertical line. As shown in **Figure**

3.4 and **3.5**, the aerial sampling experienced higher average MCE values relative to both sets of ground samples but the overall trend is similar and demonstrates a lack of clear dependence on MCE.

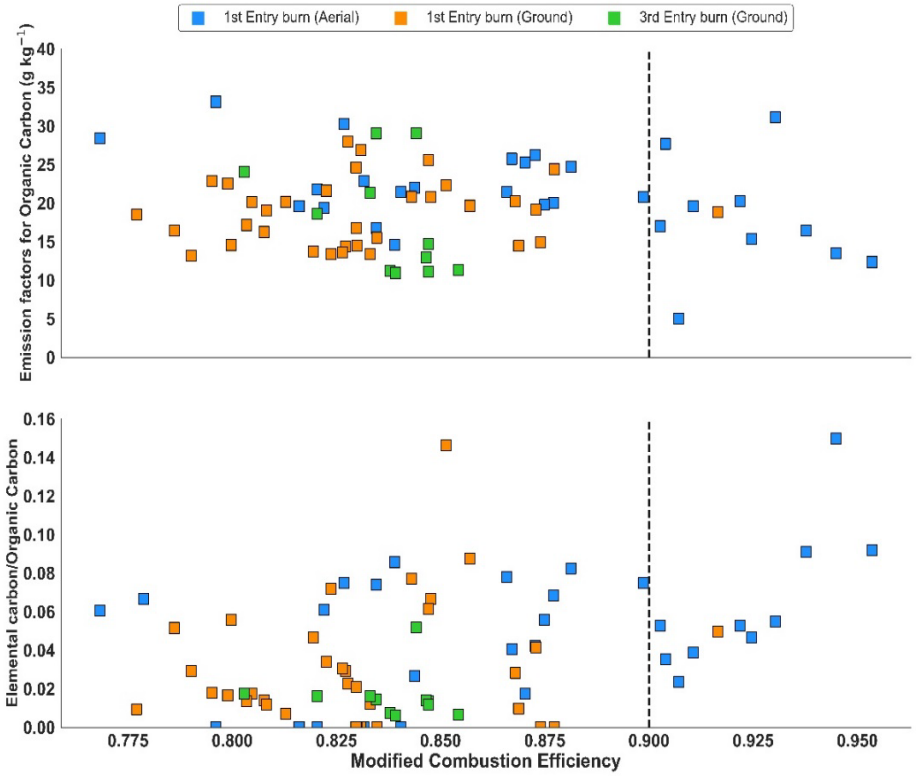

Figure 3.5 Organic carbon EF (top) and ratio of elemental carbon EF to organic carbon EF (bottom) versus the modified combustion efficiency for ground (2017, 2021) and aerial (2021) sampling.

3.3. Comparisons with Published Emission Factors

Figure 3.6 more clearly shows this absence of a strong dependence on MCE, in which individual EFs and the ratio of EC to OC EFs were binned into uniform MCE bins of 0.025 width. The horizontal and vertical placement of points were derived from the average EF or EF ratio and average MCE value for those data pairs falling within a given bin. Vertical error bars indicate ± 1 standard deviation of the mean. Unlike our previous laboratory studies using single or simple fuel mixtures, e.g. (Jen et al., 2019), there is no clear inverse relationship with organic carbon vs MCE. Grey symbols from laboratory emission factor experiments are shown for comparison taken from (Jen et al., 2019) for those fuels present in Blodgett Forest. Unlike the laboratory single fuels, the 1st and 3rd entry prescribed burns show a nearly MCE-independent emission factor for OC and only a suggested increase in EC emission factor for very high MCE values (~0.95 and above) where pure flaming state is known to favor elemental carbon emissions.

Study averaged OC, EC and PM emission factors and MCE. The absence of any strong dependence on MCE or burn history supports pooling the emissions data to form broader conclusions. **Table 3.1** lists the mean and standard errors (standard deviation) of EFs (MCE) by platform (aerial or ground) for the two studies (2017, 2021). The resulting mean MCE and organic EF are not statistically different between the two ground sets while the aerial mean MCE was slightly higher relative to the two ground MCE means at 0.87, 0.83 and 0.84, respectively. The mean aerial OC EF was 21.8 ± 6.0 g/kg as compared to the concurrent ground OC EF equal to 18.8 ± 4.2 g/kg and a similar value of 17.7 ± 8.8 g/kg for the mean ground OC EF for the 3rd entry burn. For biomass burning emissions that are dominated by carbon, the particulate mass can be approximated by scaling the OC mass by 1.8 to account for average oxygen and hydrogen content (taken as the fresh biomass burning dominated organic mass to organic carbon ratio measured by high-resolution aerosol mass spectrometry by Zhou et al. (Zhou et al., 2017)) plus the EC mass as follows:

$$\mathrm{PM}_{2.5} \sim 1.8 \times M_{\mathrm{OC}} + M_{\mathrm{EC}} \qquad [3.4]$$

Using this relation, the $PM_{2.5}$ EF can be approximated and is given in the final column of **Table 3.1** with the mean (standard deviation) of the aerial 2021, ground 2021 and ground 2017 values of

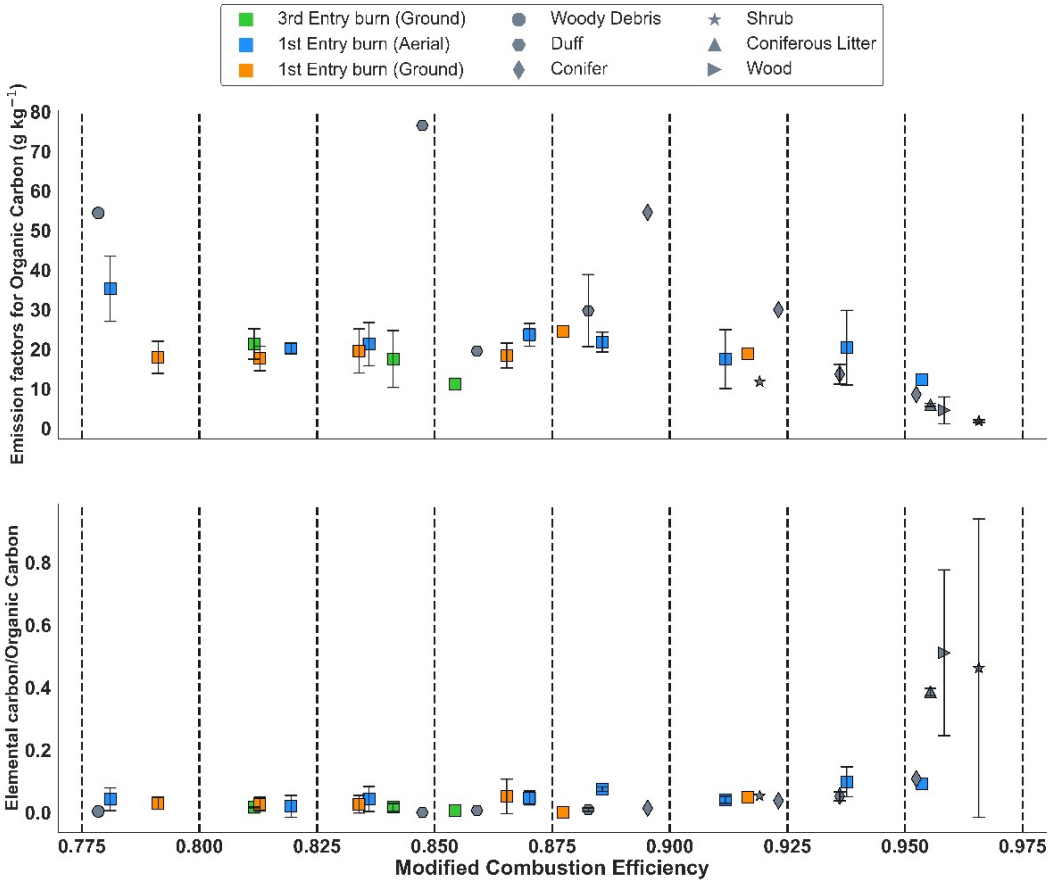

Figure 3.6 Same data as **Figure 3.5** collected into 0.025 wide MCE bins to illustrate the lack of a clear MCE dependence for most of the range of measured average MCE conditions.

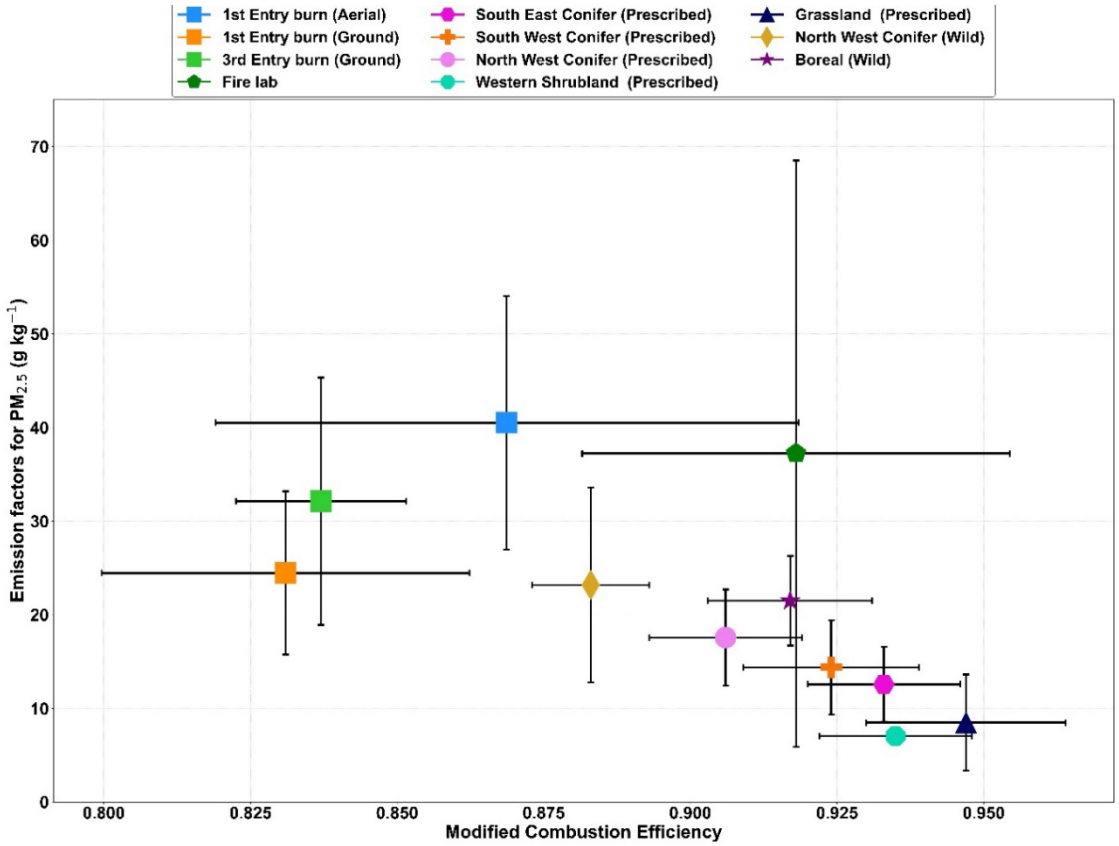

Figure 3.7 Study averaged PM emission factors vs. modified combustion efficiency are consistent with prior published emission factor trends for similar fuels (i.e. conifer).

40.4 (13.5) g/kg, 34.4 (7.8) g/kg and 32.1 (16.6) g/kg, respectively. Under the assumption of complete independence from MCE on emission factor, the three studies with a combined set of 75 total samples leads to a grand means shown in the last row of **Table 3.1**. Comparison of the mean value and standard deviation observed in the 1st entry and 3rd entry burns with available literature values is shown in **Figure 3.7**. These grand means are proposed for use in modeling the emissions from similar mixed conifer forest prescribed fires.

Table 3.1 Study averaged MCE, OC, EC and PM emission factors and ratio of EC/OC emission factors for first (’21) and third entry (’17) studies by sampling platform and pooled averages by platform (’21) and both studies (’17, ’21). Uncertainties are one standard deviation of the mean.

Study average emission factors and combustion efficiencies (+/- STDV)

Platform (yr)	N	MCE	OC (g/kg)	EC (g/kg)	EC/OC	PM (g/kg)
Aerial ('21)	30	0.87 ± 0.05	21.8 ± 6.0	0.88 ± 0.61	0.04 ± 0.028	40.4 ± 13.5
Ground ('21)	34	0.83 ± 0.03	18.8 ± 4.2	0.60 ± 0.67	0.03 ± 0.032	34.4 ± 7.8
Ground ('17)	11	0.84 ± 0.01	17.7 ± 8.8	0.34 ± 0.41	0.02 ± 0.028	32.1 ± 16.6
Ground ('17, '21)	45	0.83 ± 0.03	18.5 ± 5.0	0.54 ± 0.63	0.03 ± 0.029	33.9 ± 9.3
Pooled ('17, '21)	75	0.85 ± 0.04	19.8 ± 6.2	0.67 ± 0.64	0.03 ± 0.029	36.5 ± 11.5

4. Gas-Phase VOCs from Ground- and Drone-Based Measurements and Comparison with Wildfire Emissions

*A version of this chapter will be submitted to the International Journal of Wildland Fire under the title "Fuel Loadings Prove the Critical Constraint for Smoke Predictions using FOFEM as applied to a Mixed Conifer Forest in California", with the following authors: Tasnia, A. [1], Lara, G.[1], Foster, D.[2], Sengupta, D.[3], Butler, J.[4], Kirchstetter, T. [4], York, R.[5], Kreisberg, N.[6], Goldstein, A. G. [3], Battles, J. [2],*Barsanti, K. C. [1]*

4.1. Methods

Volatile organic compounds (VOCs) were collected from ground- and drone-based platforms during the 2021 BFRS prescribed burns using dual-bed sorption cartridges of 100 mg Tenax TA (35/60) and 200 mg Carbograph 1 TD (60/80) in series. The cartridges were preconditioned at 330 ºC for 3 hours prior to sampling during the field campaign. Samples were collected at a flow rate of ~170-190 ml/min for 30 minutes from the ground and 100 ml/min for 3-23 minutes from the drone. The ground samples were collected sequentially over an approximately 3 hour time period at each sampling location, shortly after ignition during the most active burn period and also during the most active smoldering period. The drone sequentially sampled flaming and smoldering burn periods, with the overall flight time determined by battery capability. This resulted in an average of 9 ground samples and 8 drone samples per day. Two background samples were collected the day before the first burn and field blanks were collected throughout the sampling period. This resulted in a total of 37 cartridges processed for the ground and 30 cartridges for the drone (excluding background and blank samples).

Following Hatch et al. (Hatch et al., 2015, 2019) the cartridges were analyzed using automated thermal desorption (ATD, Turbomatrix 650, PerkinElmer, Waltham, MA) coupled with a two-dimensional gas chromatograph with a time-of-flight mass spectrometer (GCxGC-ToFMS, Pegasus, 4D, Leco Corp., St. Joseph, MI). Prior to the analysis of each cartridge, an internal standard mixture (toluene-d8, 1-bromo-4-fluorobenzene, and 1,2-dichlorobenzene-d4) was injected using the ATD. Sorbent tubes were desorbed at 290 ºC with 11.5% of the sampled mass transferred via a 235 ºC fused-silica transfer line to the GC×GC-ToFMS. Samples were analyzed on the following column set: DB-VRX (30 m, 0.25 mm i.d., 1.4 µm film thickness) primary column (Agilent, Santa Clara, CA) and Stabilwax (1.5 m, 0.25 mm i.d., 0.5 µm film thickness) secondary column (Restek, Bellefonte, PA); and with the following temperature program: primary oven was held at 40 °C for 5 min, followed by a 3.8 °C/min ramp to 225 °C, with a final hold of 5 min. The secondary oven and modulator were held at +18 °C and + 28 °C relative to the primary oven.

Calibration curves were generated using sequential dilutions of standard solutions in methanol prepared using 72 compounds. A total of 67 compounds were identified and quantified across a

variety of compound classes including alkanes, aldehydes, ketones, terpenes, and furans. Background correction for each compound was performed by subtracting the maximum normalized peak area measured in either the background or blank samples. All mixing ratios (ppb) thus represent "excess emission ratios" or the amount of the compound above background and attributed to the prescribed burns. Mixing ratios were converted to emission factors (EFs, g/kg) using the carbon mass balance method described in Chapter 3.

4.2. Measured Mixing Ratios and Emission Factors

Comparisons between the mixing ratios and EFs measured in the ground and drone samples are summarized in **Figures 4.1-4.6**. The figures show the measured mixing ratios or EFs averaged across all samples and with individual compounds grouped by compound class. The drone sampled more concentrated smoke and thus the samples had generally higher mixing ratios (**Figures 4.1-4.3**). **Figs 4.1** and **4.2** show the mixing ratios for single compounds and groups of compounds, averaged across all sampling periods. It can be seen that of the compounds that were quantified, furfural had the highest mixing ratios in both ground and drone samples. Furfural is typically among the most abundantly emitted VOCs from wildland fires (e.g., (Hatch et al., 2017; Permar et al., 2021)). Taking a closer look at measured mixing ratios for each burn unit, the mixing ratios were highest in the ground samples from Unit A (**Figure 4.3**). Field notes support that the most concentrated smoke was sampled from the ground during the burning of Unit A on the first day, which is also consistent with better agreement between the ground and drone samples for Unit A (i.e., more concentrated smoke being sampled from both platforms). EFs can provide a better metric for comparison, since they account for the differences in dilution between ground and drone samples.

The EFs in the ground (**Figure 4.4**) and drone (**Figure 4.5**) samples were relatively consistent (**Figure 4.6**) and thus averaged together to provide final EFs. The averaged EFs are presented in **Figure 4.7** and **Table 4.1**; the table also indicates the number of compounds that were summed in each compound class, which influences that variability shown in the box and whisker plots.

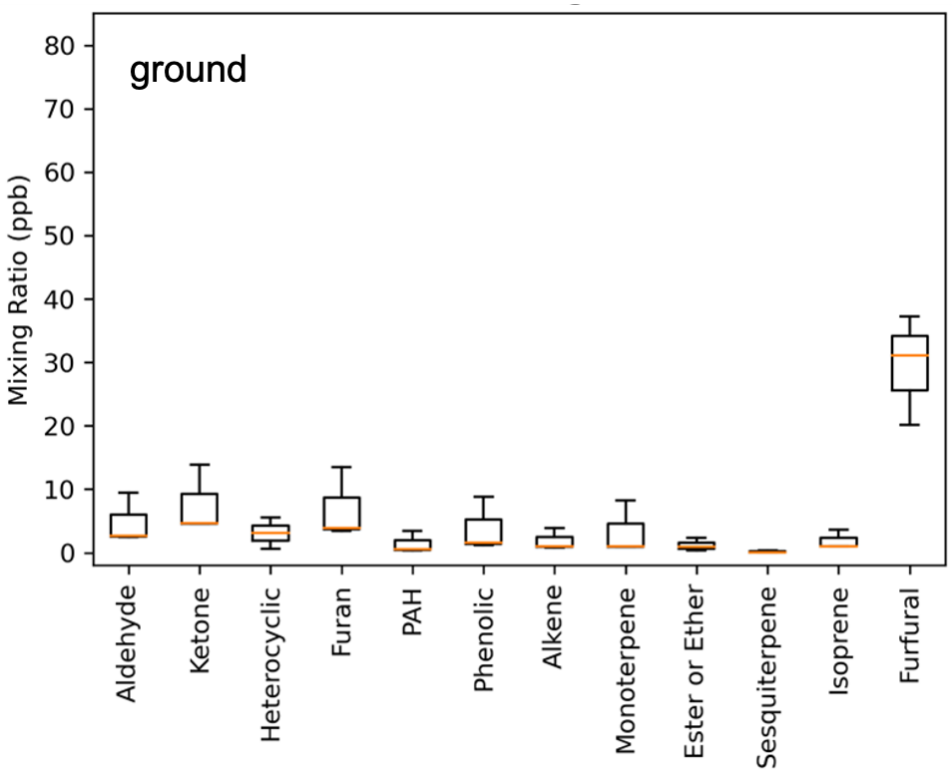

Figure 4.1 Averaged mixing ratios for individual compounds and summed compound classes as measured in samples collected from the ground-based platform.

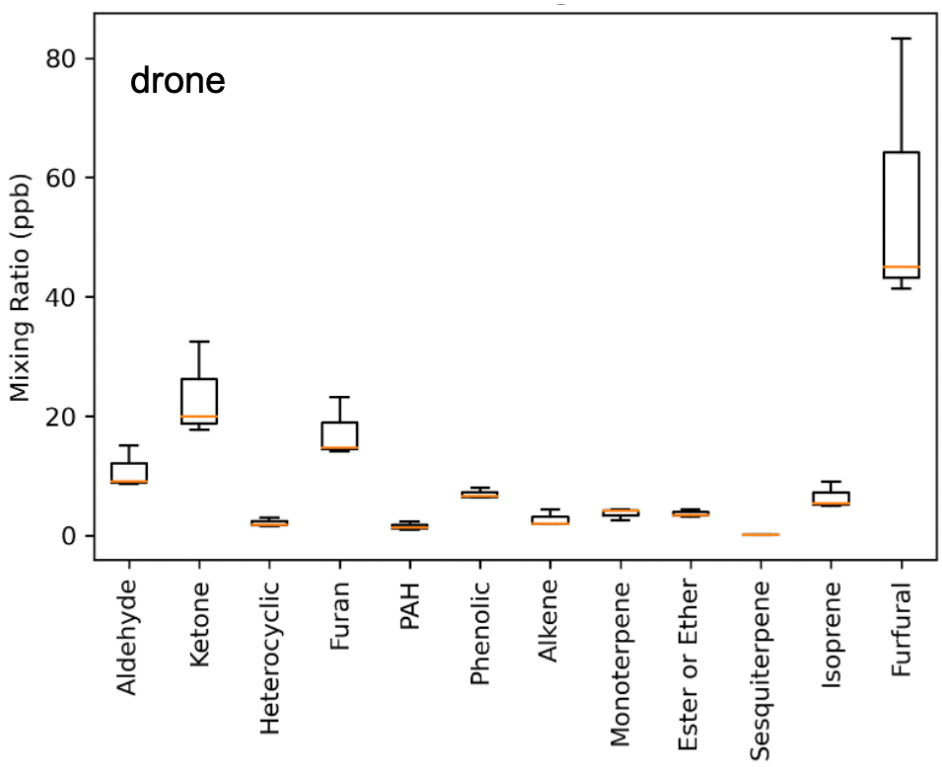

Figure 4.2 Averaged mixing ratios for individual compounds and summed compound classes as measured in samples collected from the drone-based platform.

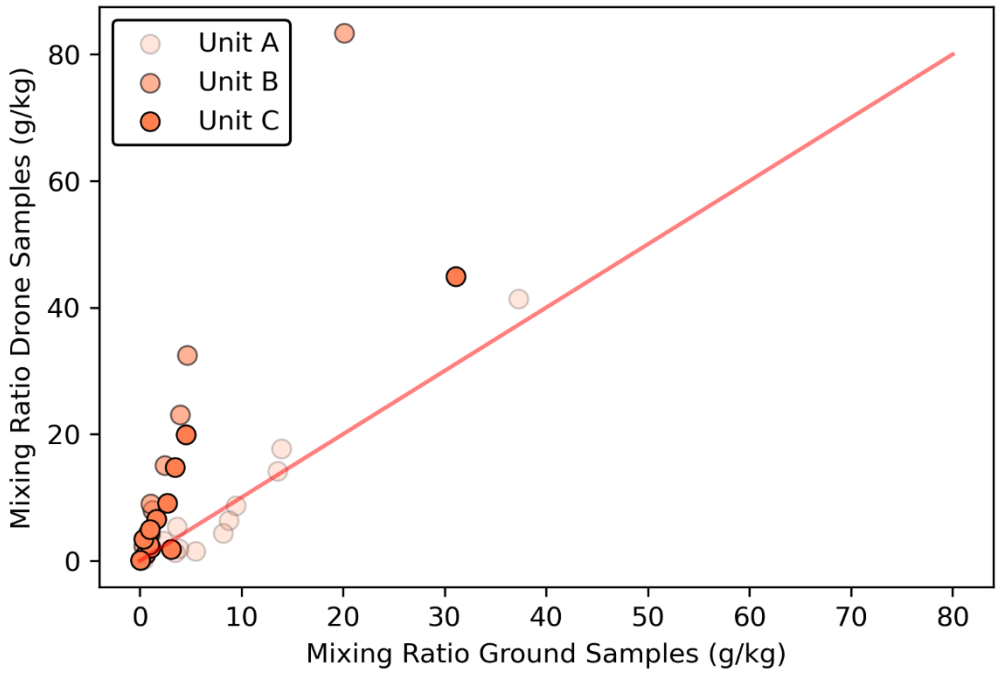

Figure 4.3 Comparison of averaged mixing ratios for summed compound classes as measured in drone-based vs. ground-based samples.

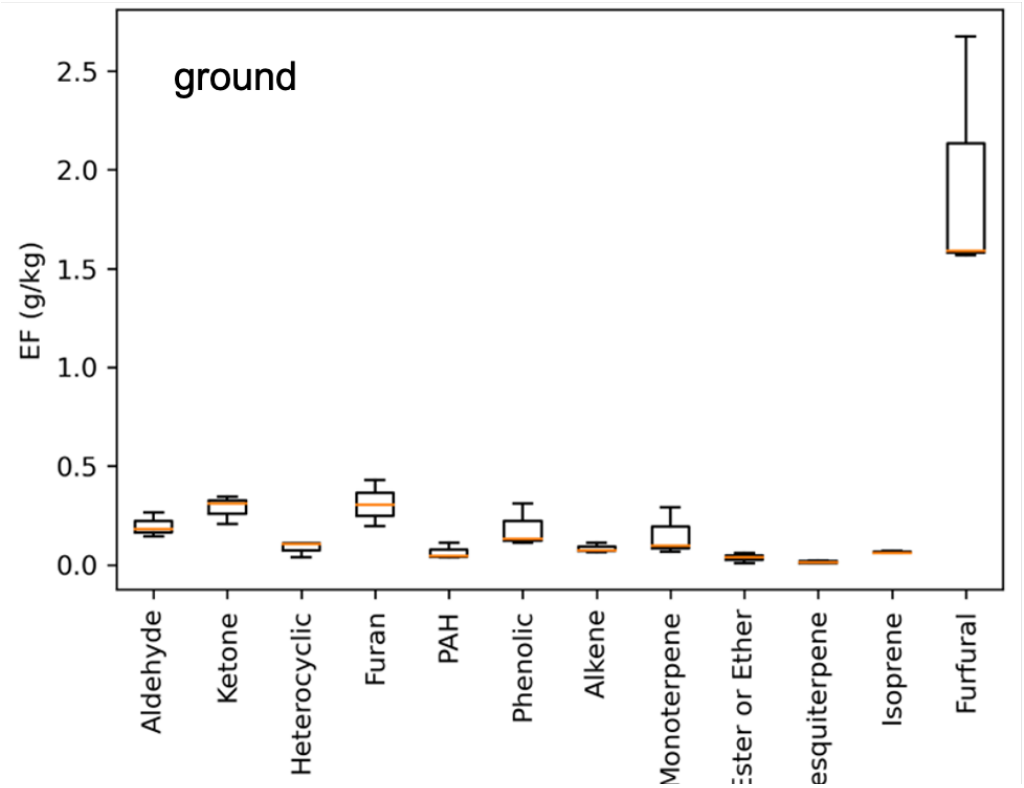

Figure 4.4 Averaged emission factors (EFs) for individual and summed compound classes as measured in ground-based samples.

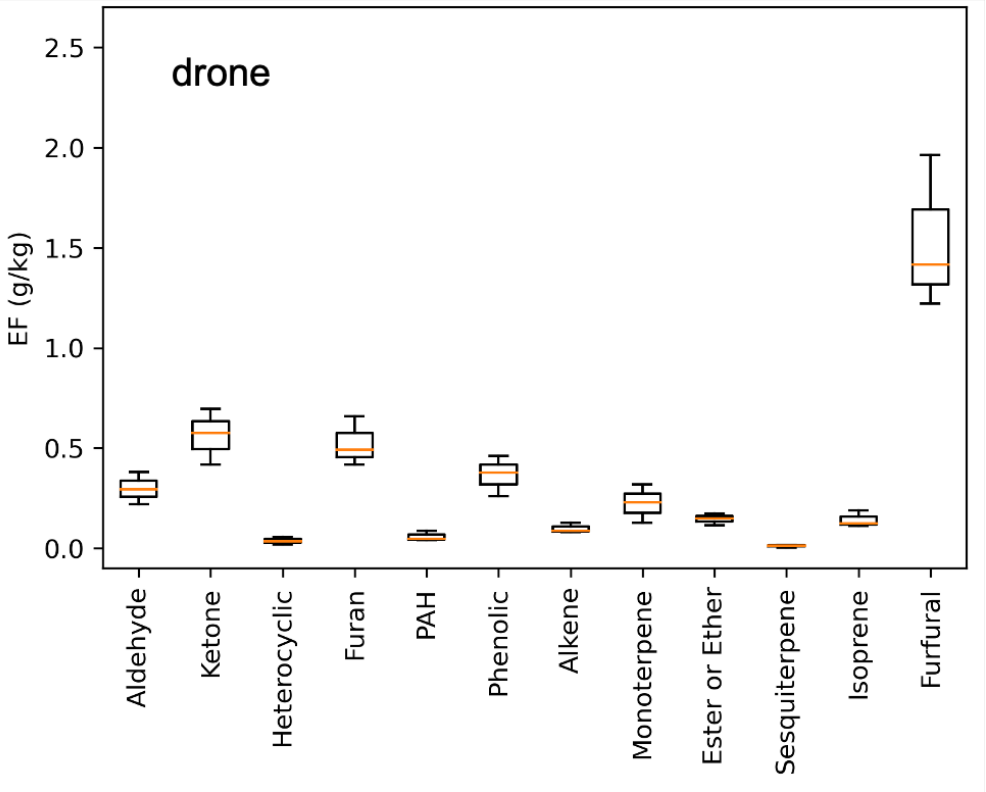

Figure 4.5 Averaged emission factors (EFs) for summed compound classes as measured in drone-based samples.

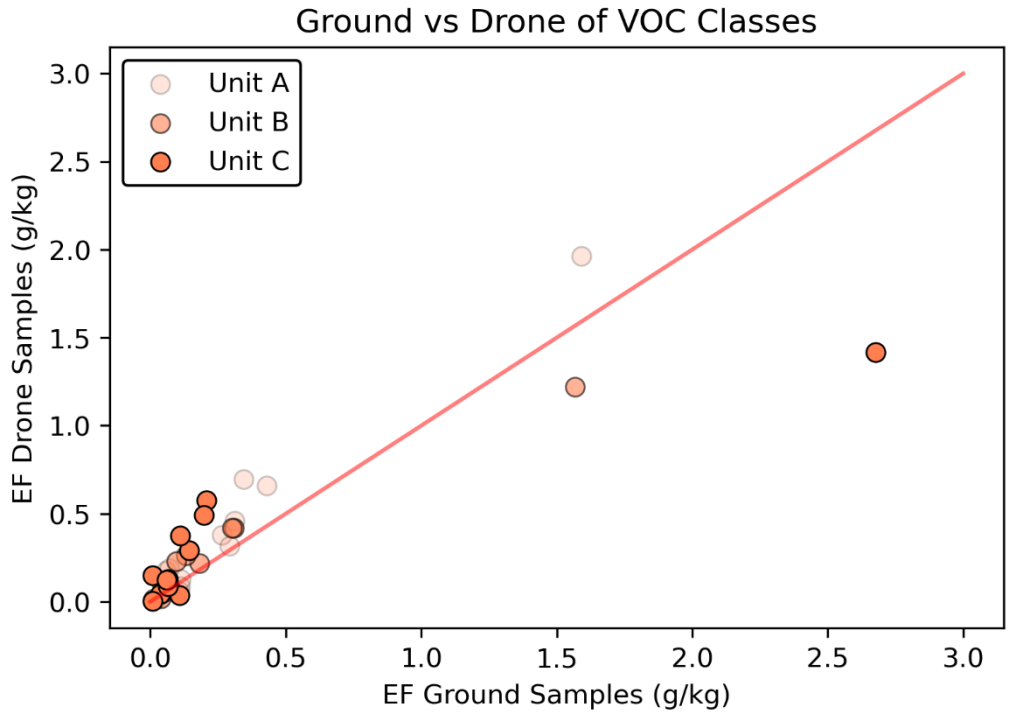

Figure 4.6 Comparison of averaged emission factors (EFs) for individual and summed compound classes as measured in drone vs. ground samples.

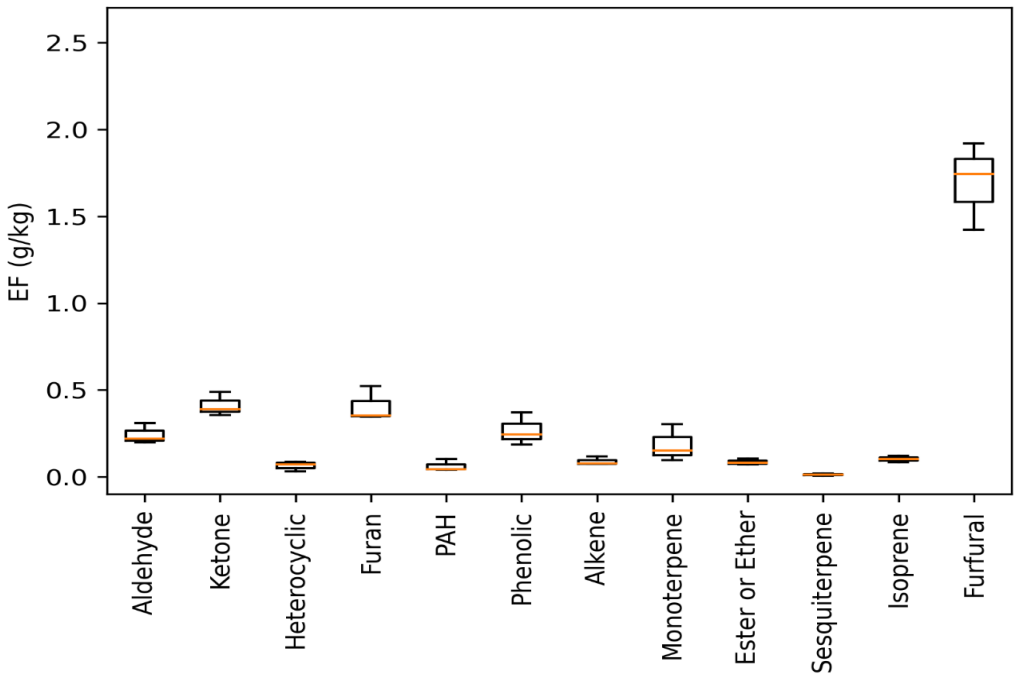

Figure 4.7 Emission factors (EFs) for individual compounds and summed compound classes averaged across drone- and ground-based samples.

Table 4.1 Average emission factors (EFs) for representative VOC compounds and compound classes. Standard deviation and number of individual compounds in each class are also reported.

	Average EF (g/kg)	**Standard Deviation (+/-)**	**Number of Individual Compounds**
Aldehydes	0.25	0.13	3
Ketones (w/acetone)	0.87	0.78	7
Ketones (w/o acetone)	0.42	0.24	6
Alkenes	0.10	0.05	8
Isoprene	0.10	0.07	1
Monoterpenes	0.20	0.19	13
Sesquiterpenes	0.01	0.01	1
Esters and Ethers	0.09	0.07	2
Heterocyclic compounds	0.06	0.08	4
Furans	0.42	0.21	5
Furfural	1.69	0.87	1
PAHs	0.07	0.06	9
Phenolic compounds	0.28	0.25	10

The cartridge sampling and GCxGC-ToFMS analysis methods are particularly well suited for detecting and quantifying terpenes, which are important ozone and SOA precursors. We have also demonstrated that specific monoterpenes can be used to differentiate fuel types, even with more complex fuel beds (Stamatis and Barsanti, 2022). In **Figure 4.8** (mixing ratios, left panel; EFs, right panel), we compare the distributions of monoterpenes measured during the 1st entry burns (2021, ground and drone) and 3rd entry burns (2017). Interestingly, the fractional distribution of compounds is more similar between the ground samples from the two different burns than between the ground and drone samples from the 2021 1st entry burns. Again, by accounting for dilution and comparing EFs, the differences in the distributions between the ground and drone are smaller; however there are clear differences in the composition. The reasons for these differences are currently unknown. One possibility is that upwind sources were more likely to influence the drone samples, and isoprene at BFRS has been previously attributed to oak forests nearby (Dreyfus, 2002; Holzinger et al., 2006). We note that this does not change our conclusions regarding the relative consistency between these samples or recommendations regarding the use of a single set of EFs.

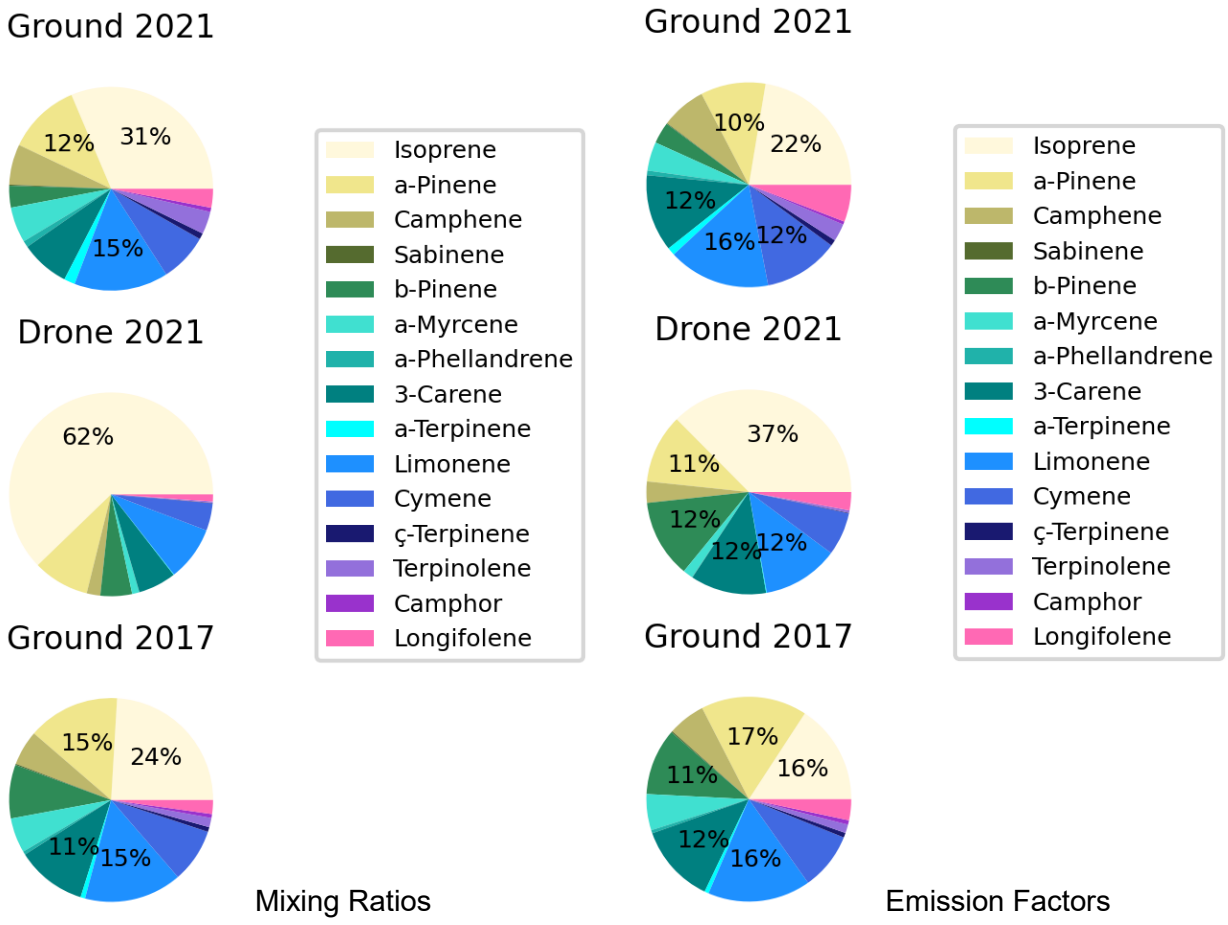

Figure 4.8 The fractional distribution of monoterpenes contributing to the average observed mixing ratios (left) and emission factors (right) measured in the 2021 1st entry burns (ground and drone) and the 2017 3rd entry burns.

In addition to the cartridge samples collected and analyzed from the prescribed fires at Blodgett field station, we also analyzed cartridge samples collected in California by CARB from wildfires, coordinated with the 2019 FIREX-AQ campaign. **Figure 4.9** shows representative chromatograms from the wildfires (top) and the 2021 prescribed burns (bottom). Compounds that are typically elevated in smoke samples are highlighted in the chromatograms. The larger/brighter peaks in the bottom figure illustrate more concentrated smoke sampling enabled by the prescribed burns. The samples were run using different programming for the GCxGC and ToFMS methods, thus some of the peaks are significantly shifted in the chromatogram. **Figure 4.10** shows normalized peak areas (proportional to mixing ratios) of representative compounds averaged across the 2019 "CARB" (left) and 2021 "Blodgett" (right) samples, respectively. For all identified compounds, the mixing ratios were higher in the prescribed burn samples than the wildfire samples. For directly emitted compounds, the higher mixing ratios in the prescribed burn samples are likely due to the fact that the prescribed burn samples were more concentrated (less dilution). In addition, reactive losses of compounds occurs during transport, and it is expected that such losses would be greater in the transported wildfire plumes. Likely of less importance for this particular comparison, there also may be some differences in the identities and quantities of compounds emitted because of differences in fuel consumption and/or burn conditions. This is suggested in **Figure 4.11**, which shows a comparison of the relative contribution of five major monoterpenes averaged across the CARB (left) and Blodgett (right) samples.

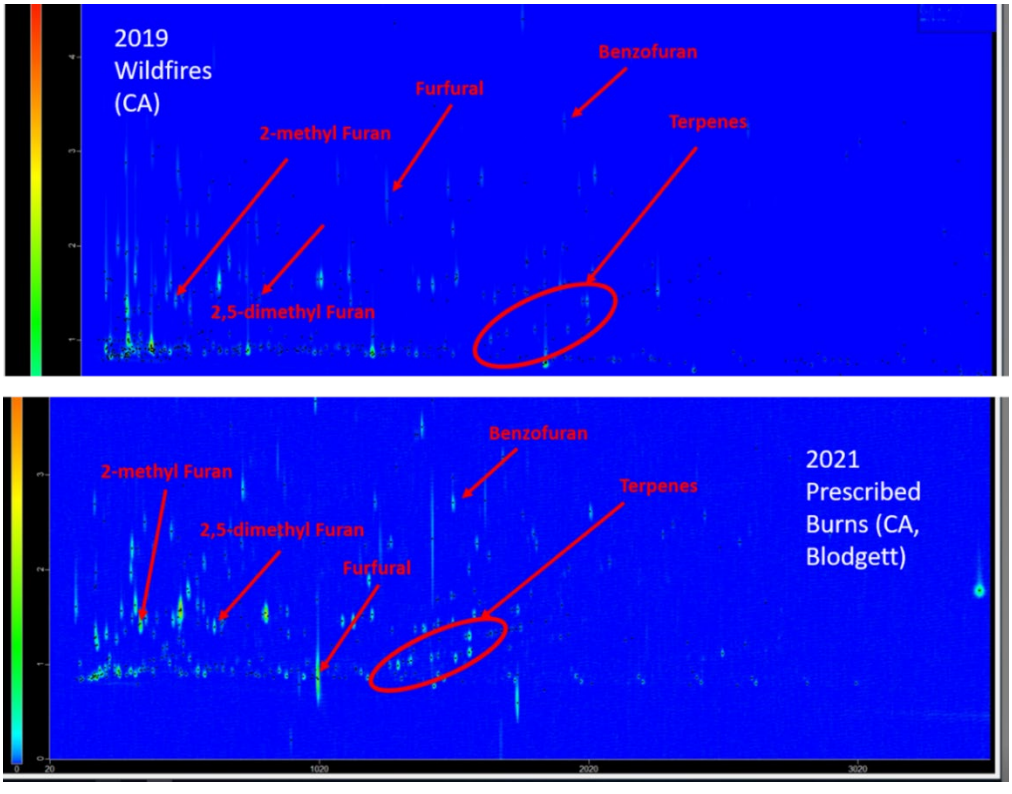

Figure 4.9 Representative chromatograms from the 2019 wildfire samples (top) and the 2021 prescribed burn samples (bottom); commonly identified compounds in smoke are labeled.

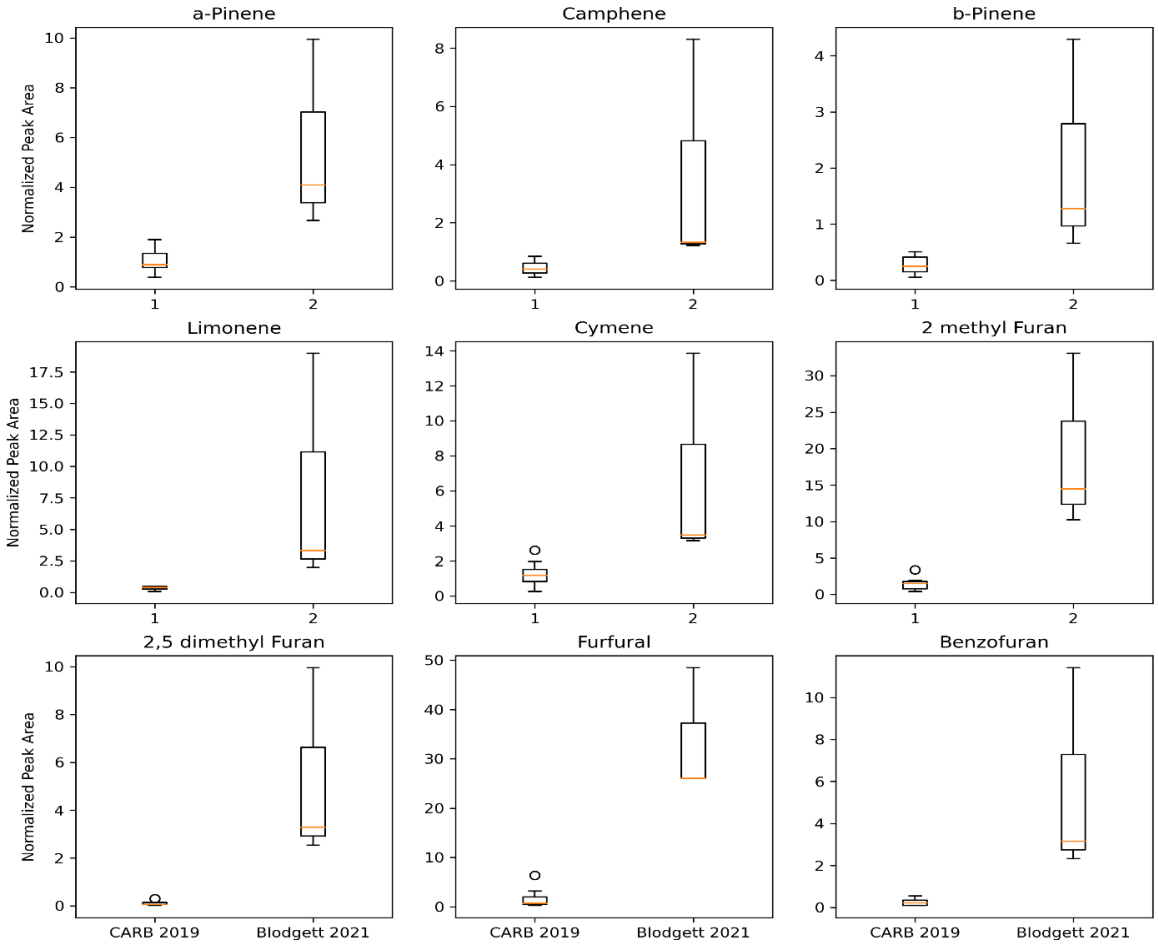

Figure 4.10 Normalized peak areas of representative compounds in 2019 wildfire samples (left) and 2021 prescribed burn samples (right).

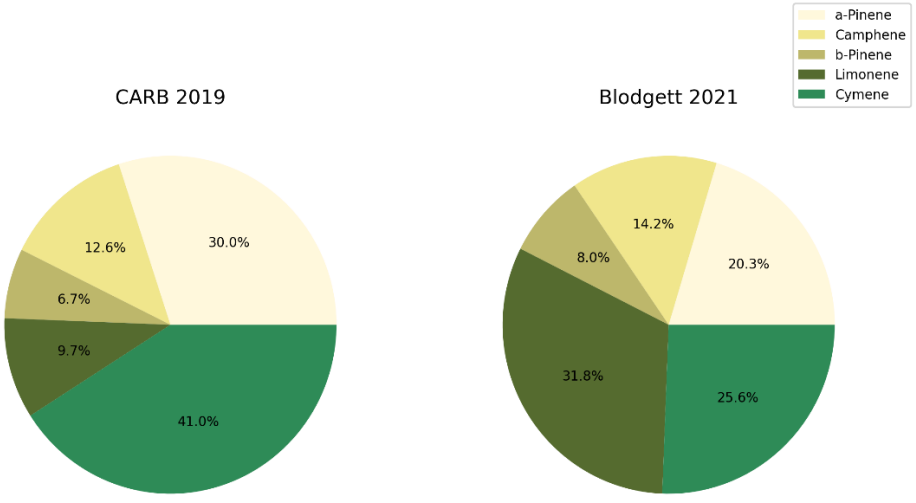

Figure 4.11 Fractional distributions of top five monoterpenes measured in wildfire samples (left) and prescribed burning samples (right).

4.3. Comparisons with Existing Emission Factors for Wildfires and Prescribed Burns

Figures 4.12-4.19 focus on measurements of individual compounds as a function of MCE and comparisons with existing EFs (wildfires and prescribed burns). The compounds in these figures were chosen because of their overlap with existing compounds in the SERA database (Prichard et al., 2020). In each of the figures, the ground sample markers are dark green while the drone sample markers are light green. The measured values represent the EF calculated for each sample, while the SERA value (tan plus marker) is an average of value(s) from the database (if more than one value is available). The SERA database query included all western coniferous forest field data for both wildfires and prescribed burns. As has been shown elsewhere, it can be seen that smoldering conditions were sampled using both drone and ground platforms, while flaming conditions were largely only sampled by the drone. For the individual compounds shown, there is no trend with MCE over the sampled MCE range, suggesting a single EF may be appropriate for modeling purposes given the variability across all MCE.

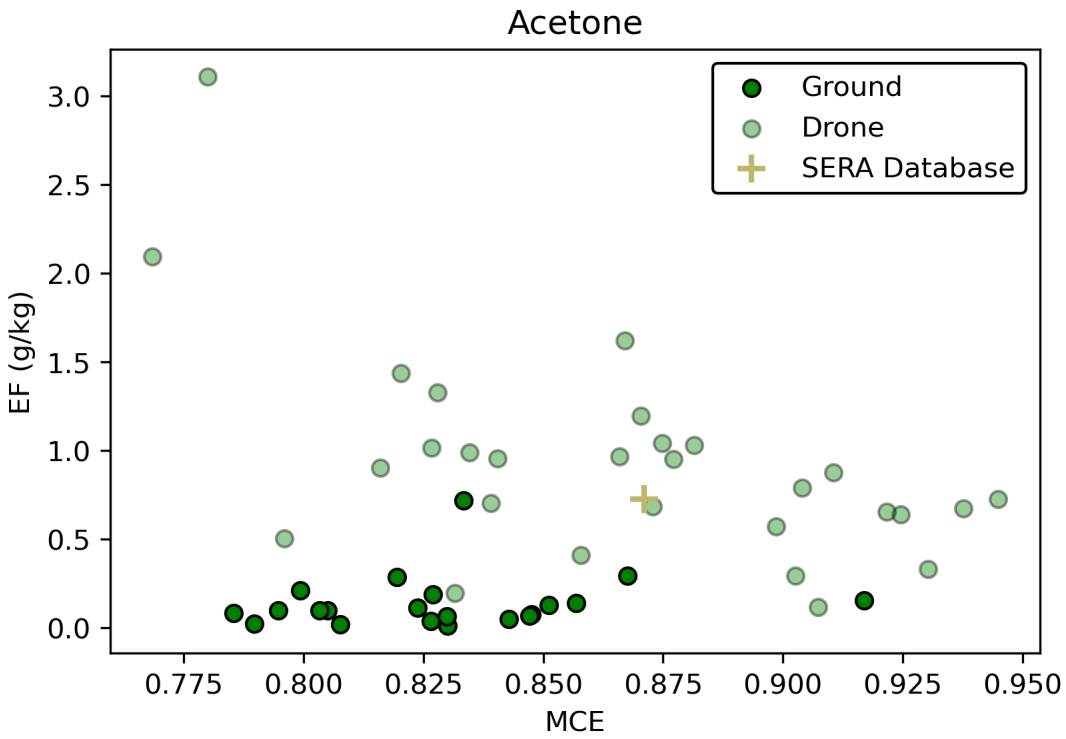

Figure 4.12 Emission factors (EFs) for acetone as measured in ground- and drone-based samples and reported for western coniferous forest in the SERA database.

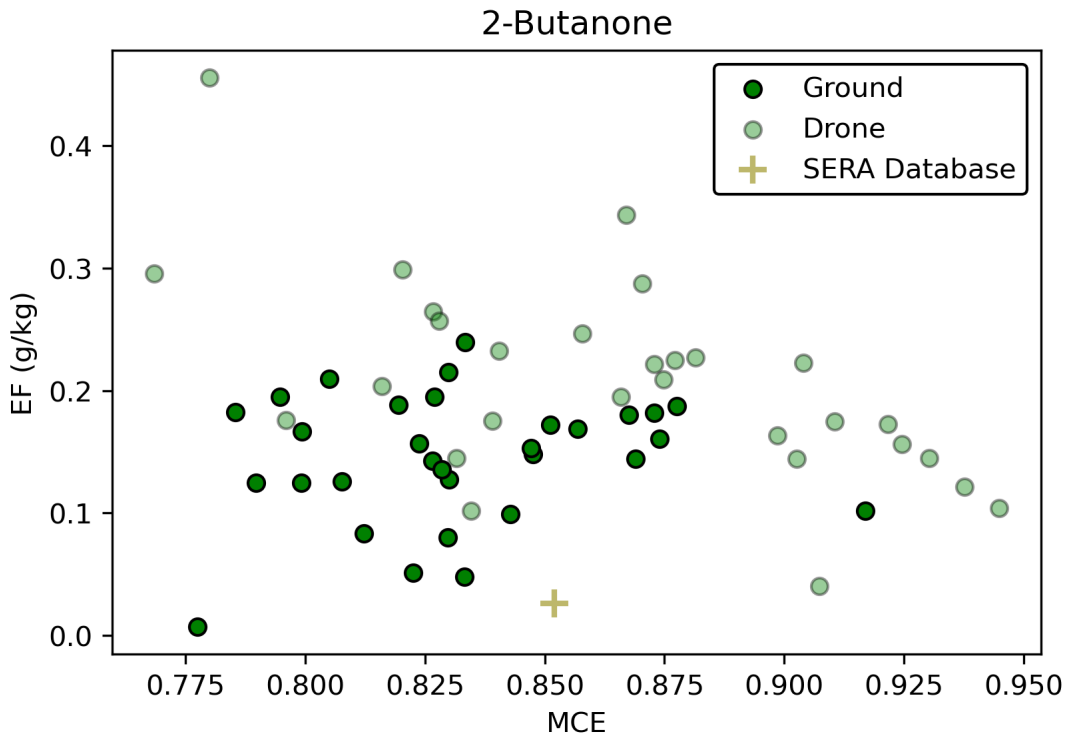

Figure 4.13 Emission factors (EFs) for 2-butanone as measured in ground- and drone-based samples and reported for western coniferous forest in the SERA database.

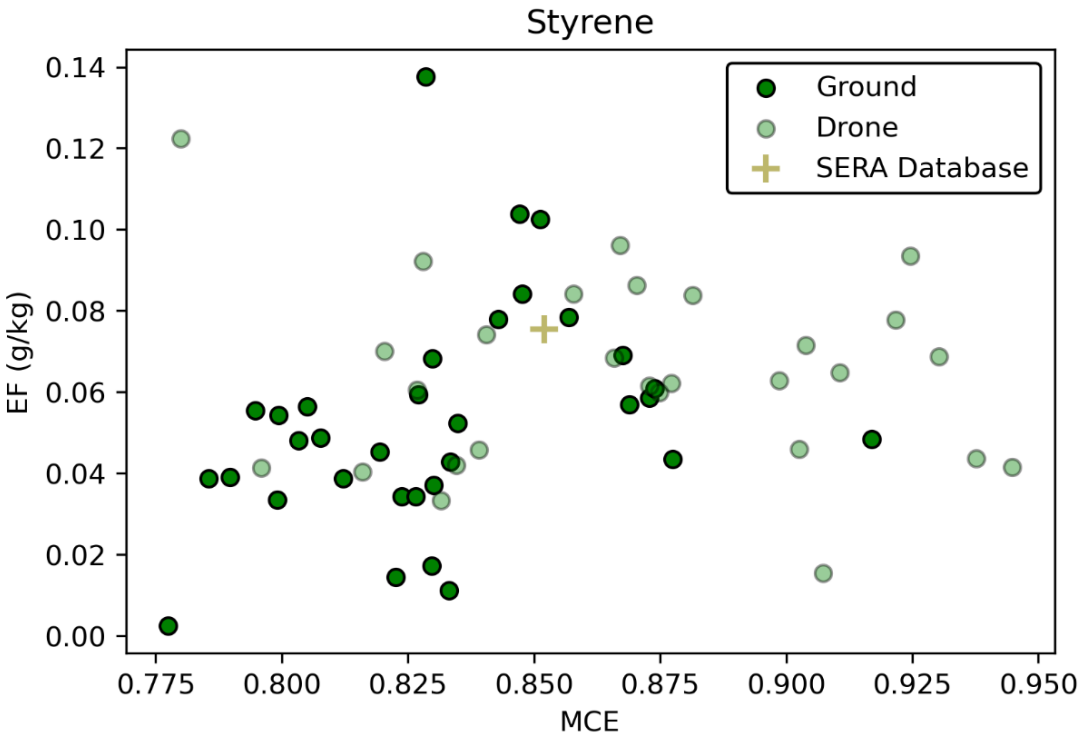

Figure 4.14 Emission factors (EFs) for styrene as measured in ground- and drone-based samples and reported for western coniferous forest in the SERA database.

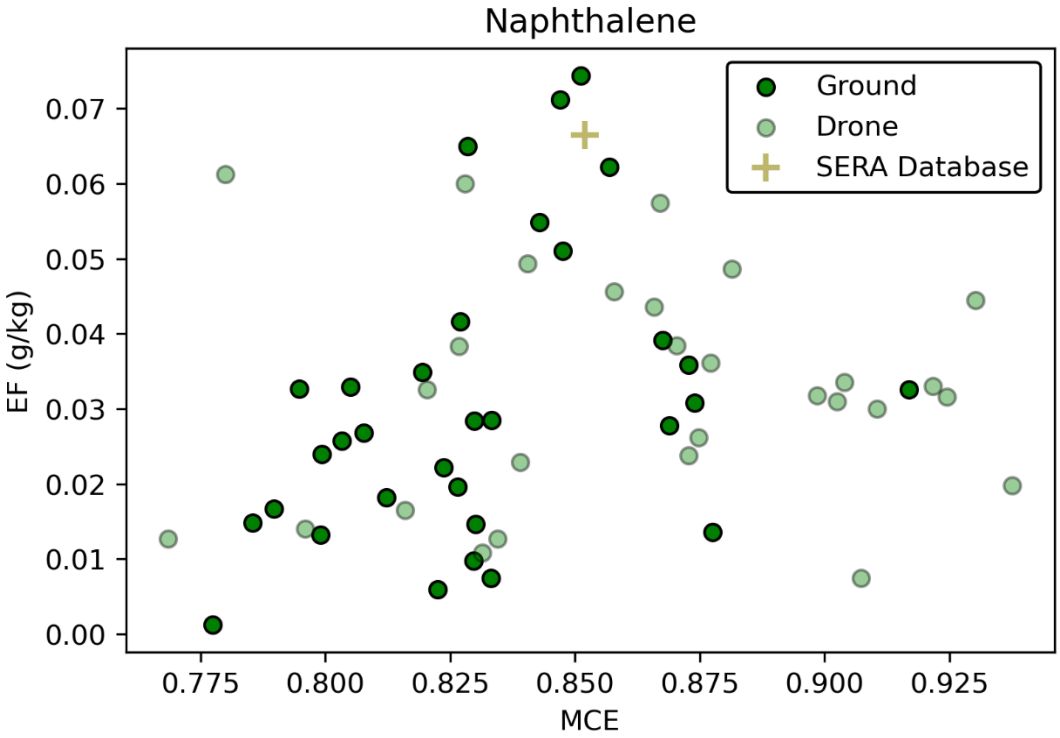

Figure 4.15 Emission factors (EFs) for naphthalene as measured in ground- and drone-based samples and reported for western coniferous forest in the SERA database.

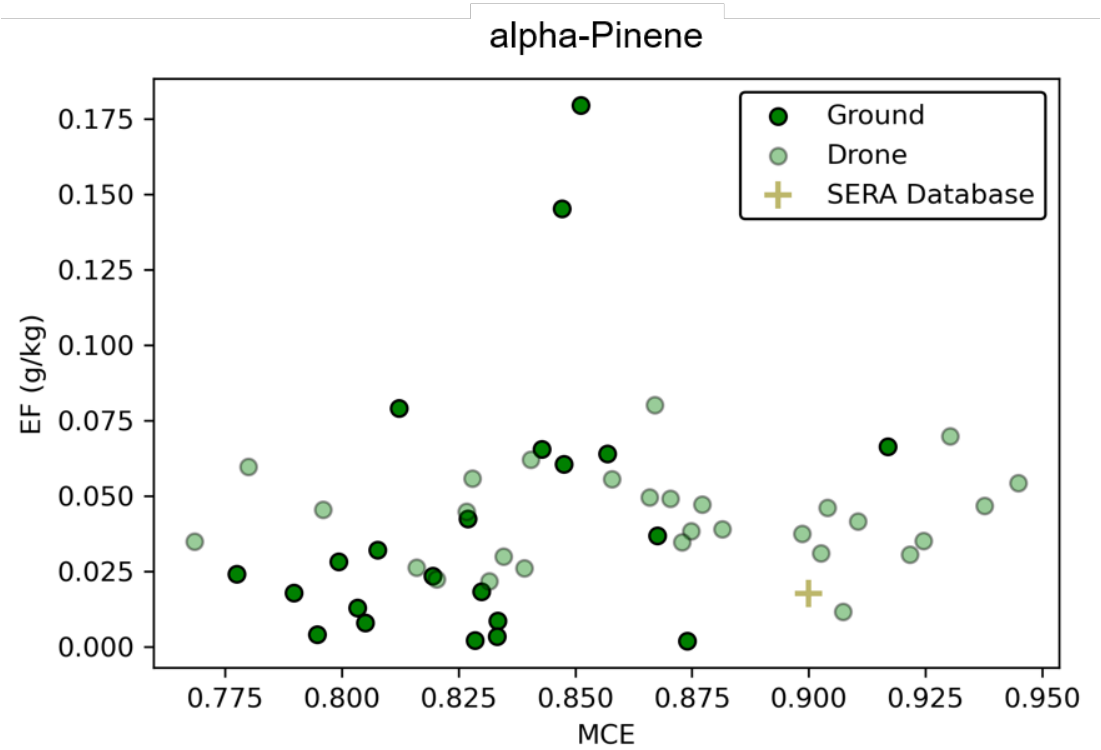

Figure 4.16 Emission factors (EFs) for alpha-pinene as measured in ground- and drone-based samples and reported for western coniferous forest in the SERA database.

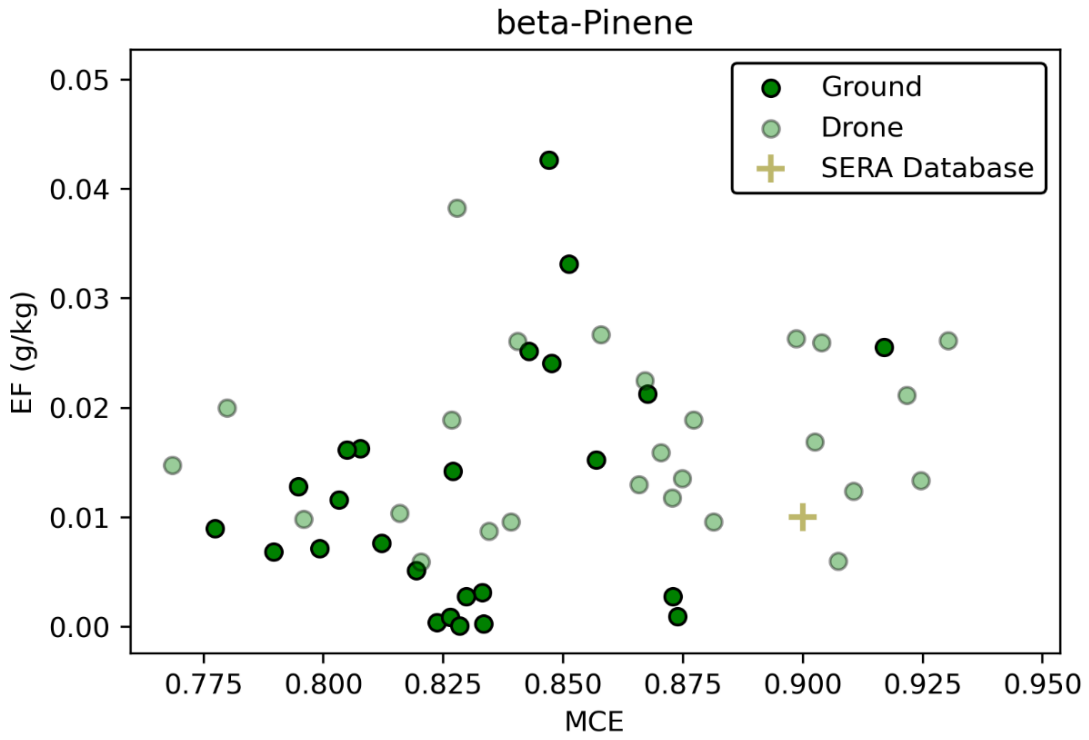

Figure 4.17 Emission factors (EFs) for beta-pinene as measured in ground- and drone-based samples and reported for western coniferous forest in the SERA database.

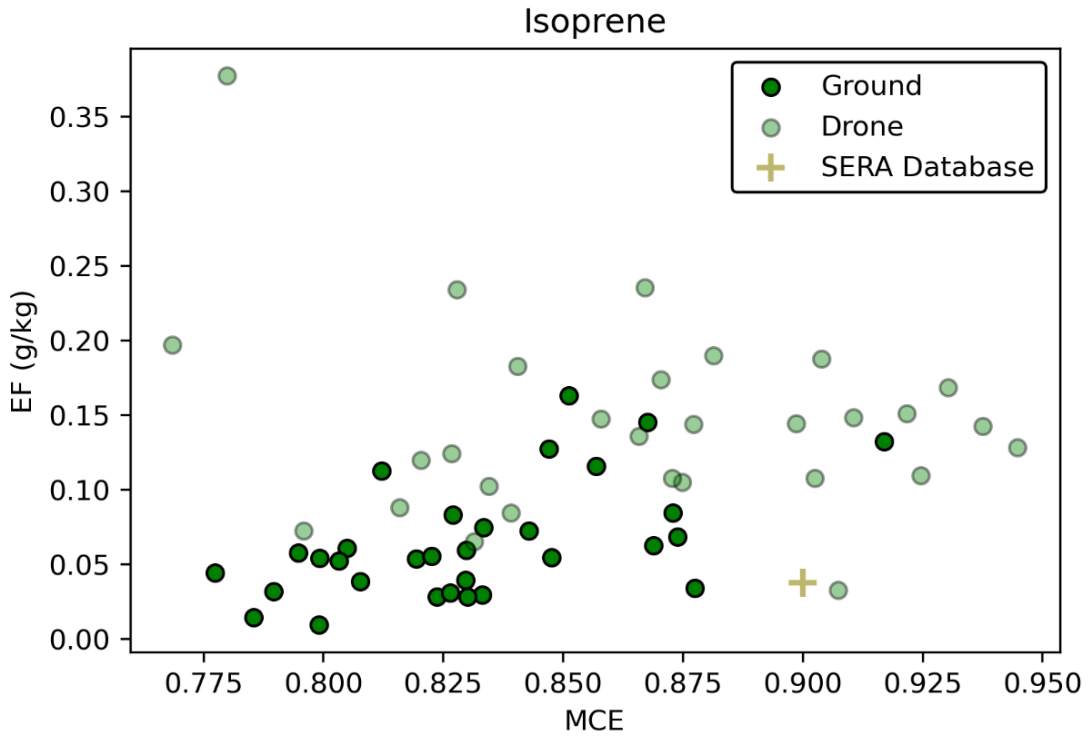

Figure 4.18 Emission factors (EFs) for isoprene as measured in ground- and drone-based samples and reported for western coniferous forest in the SERA database.

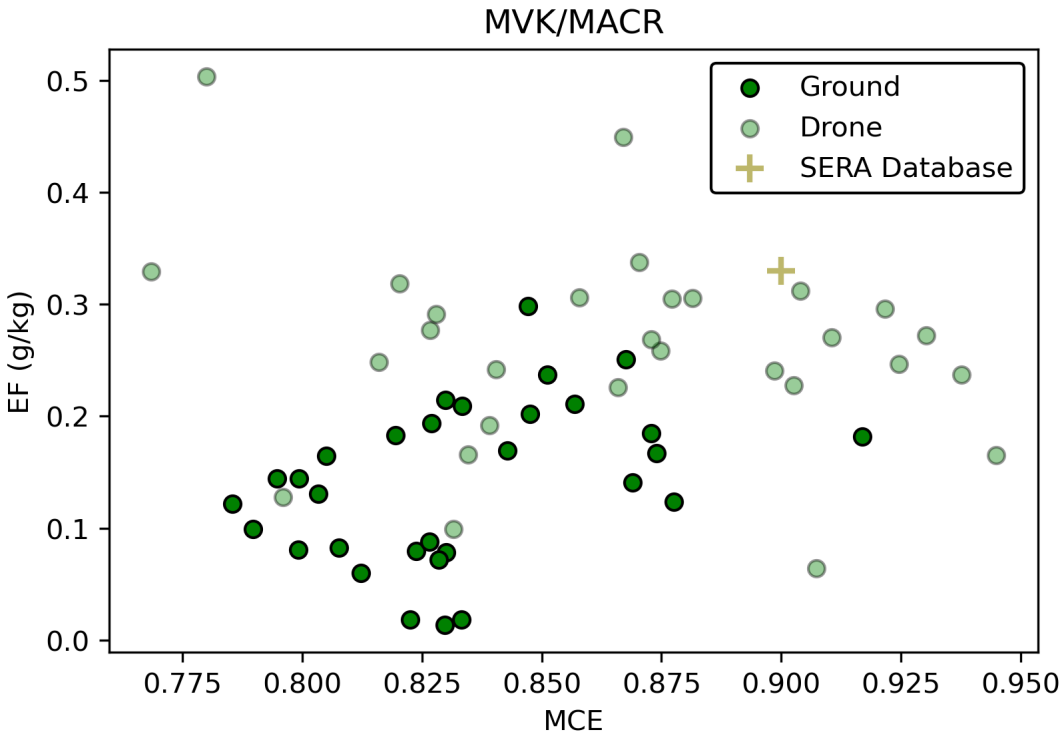

Figure 4.19 Emission factors (EFs) for methyl vinyl ketone/methacrolein (not differentiated in SERA database) as measured in ground- and drone-based samples and reported for western coniferous forest in the SERA database.

The agreement between the ground and drone samples was compound dependent, with significant differences in measured values for acetone and to a lesser extent 2-butanone and no significant differences in styrene, naphthalene, alpha- and beta-pinene. There are some differences in isoprene and methyl vinyl ketone/methacrolein, but these are not statistically significant. The EF values from the SERA database are within the ranges of values measured, with the exception of 2-butanone which is lower than the observed values.

We have recently developed an EF database (NEIVA Next-generation Emissions InVentory expansion of Akagi) that incorporates both laboratory and field data from over 35 publications, including comprehensive VOC measurements for coniferous fuels based on FLAME-IV, FIREX, and WE-CAN measurements (Shahid, S. B. et al., in prep.). Including the averaged EF values from the NEIVA database gives additional information on the representativeness of the measured values. **Figure 4.20** shows measured EFs based on ground and drone samples from BFRS, reported EFs from the SERA database, and averaged EFs from the NEIVA database. For compounds in which no differences were observed between the ground and drone samples, EFs represent the average of ground and drone samples (left panel). For compounds in which some differences were observed, the average EF from the ground samples is plotted separately from the average EF from the drone samples (right panel). EFs from the NEIVA database include a ponderosa pine average, which is the average of biomass burning laboratory studies using ponderosa pine as the fuel source;

and a temperate forest average, which is the average of biomass burning laboratory studies using any fuel found in temperate forests and wildland fire field studies in temperate forests.

Variability on the order of what is shown in **Figure 4.20** is not unexpected when considering experimental uncertainty as well as the large number of factors that control VOC levels in smoke plumes. The largest variability is seen in the acetone EFs, with database averages between the ground and drone based values. There is also large variability in the naphthalene EFs, though there was good agreement between the ground and drone values. For all compounds shown, the BFRS-based measurements were lower than the temperate forest average (with the exception of acetone and 2-butanone), which may be attributed to the dominant fuel components burned during the BFRS prescribed burns relative to the studies represented in the databases. Given that detailed VOC measurements are often not available, Figure 4.20 suggests that the VOCs measured at BFRS (and future coniferous forest sites) could be reasonably represented in smoke forecasting using the averages from either the SERA or NEIVA database (temperate forest) with no systematic biases. Additional field and laboratory measurements will, however, reduce the ranges and uncertainties presented.

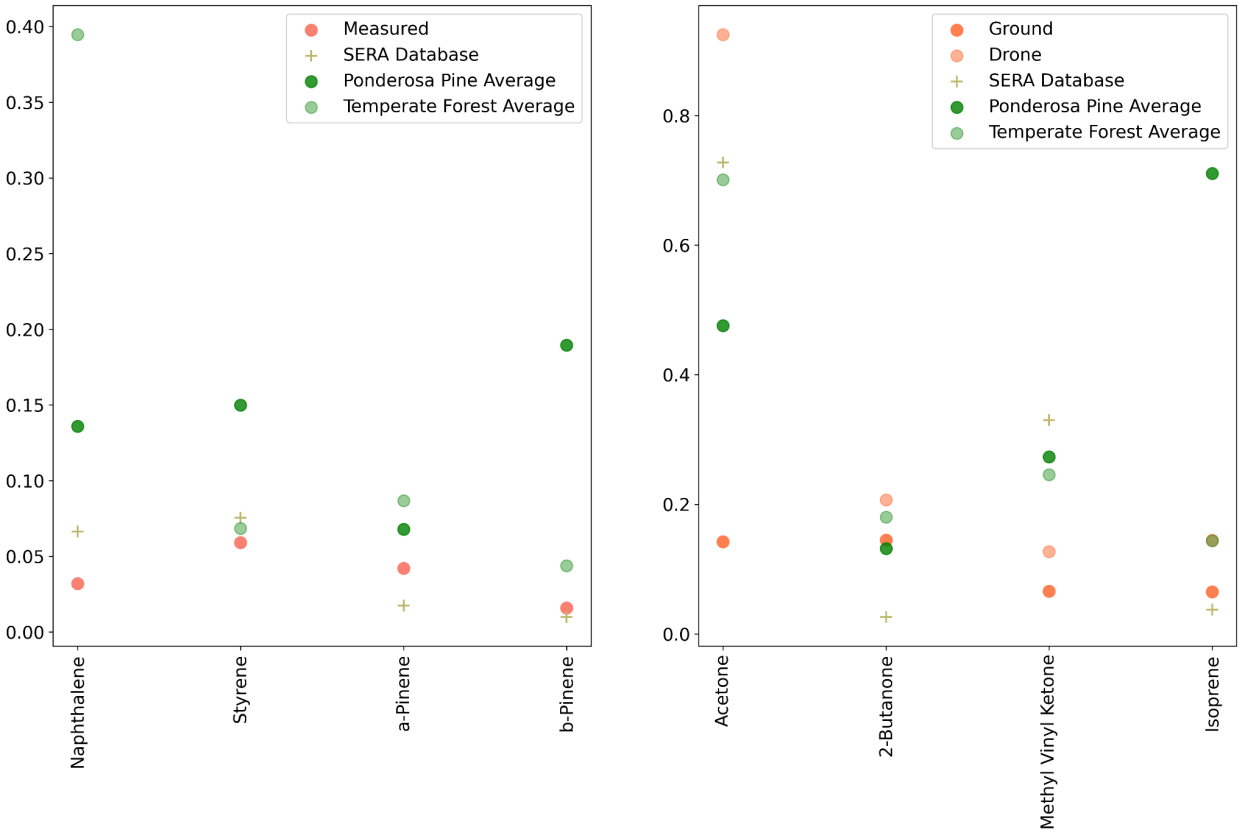

Figure 4.20 Emission factors (EFs) for individual compounds naphthalene, styrene, a-pinene, b-pinene, acetone, 2-butanone, methyl vinyl ketone and isoprene, averaged across ground-based samples, drone-based samples, and as found in the SERA and NEIVA (averages for Ponderosa pine and temperate forest) databases.

5. Particle-Phase SVOC from Ground- and Drone-Based Measurements and Comparison with Wildfire Emissions

5.1. Methods

Particulate matter (PM) samples collected on quartz filters by ground and aerial platforms for OC/EC analysis, as reported in Chapter 3, were also analyzed by multi-dimensional gas chromatography mass spectrometry for molecular level characterization. In addition to the prescribed fire samples collected and analyzed in 2021 (62, excluding blanks) and 2017 (11), we analyzed of a small set (3) of wildfire samples collected by CARB during the Springs Fire (August, 2019, https://www.fire.ca.gov/incidents/2019/9/6/springs-fire). The 2017 3rd entry prescribed burn pilot study samples were analyzed for 150 compounds using 99 calibration standards. The 2021 1st entry prescribed burn samples and the wildfire samples were analyzed for 114 compounds using 142 calibration standards (including all standards used for the 2017 sample analysis). The presentation of results focuses on the final data sets for the 2021 1st entry ground and aerial samples. Results are compared for specific compounds and compound classes measured in the 2019 wildfire samples, and specific compounds that were also measured in the 2017 third entry burns.

Quartz filters were analyzed using offline two-dimensional gas chromatography coupled to an electron impact ionization high-resolution time-of-flight mass spectrometer (GC×GC EI-HR-ToFMS), following the same protocol as documented in Jen et al. (Jen et al., 2019) and Liang et al. (YT Liang et al., 2021; Liang et al., 2022). Isotopically labeled internal standards (see list of compounds in (Jen et al., 2019)) were added to punched filter samples to account for any variability in instrument sensitivity. Then the punched samples were thermally desorbed in helium at 320 ºC in a Gerstel thermal desorption autosampler. Desorbed analytes were mixed with (N-methyl-N-(trimethylsilyl)- trifluoro-acetamide (MSTFA) added to the helium carrier gas, which converts hydroxyl groups in analyte molecules to trimethylsilyl esters (derivatization), making the analytes easier to elute from columns. The derivatized analytes were collected on a quartz wool liner at 30 ºC, before rapid injection into the GC system by heating at 320 ºC. The analytes were chromatographically separated by volatility using a Restek Rxi-5Sil-MS column (40 to 320˚C at 3.5℃ min^{-1}, hold for 5 min at 320℃), and then by polarity using a Restek Rtx-200MS column, and detected by the HR-ToFMS.

The GC chromatograms were analyzed using GC Image version 2020 (GC Image, LLC). Compounds were identified and classified by matching with authentic standards, custom mass spectral libraries from previous studies using the same instrument (Zhang et al., 2018; Jen et al., 2019), and commercial mass spectral libraries. Both retention index (chromatographic elution time relative to that of a series of deuterated alkanes) and mass spectrum are considered in this process. Details of compound identification and classification can be found in Liang et al. (YT Liang et al.,

2021). To convert signals of compounds into concentrations, we injected multiple levels of external standard mixture (following (Liang et al., 2022)) with known concentrations to determine their responses. We quantified sample compounds in this standard mix by using the response of the exact compound. This approach has around 10% uncertainty. Classified compounds not in the standard mix were quantified by the nearest standard in the same class (30% of uncertainty). Unclassified compounds or compounds without a nearby compound in the same class (less than 200 difference in retention index) were quantified by the nearest standard, which can have an uncertainty of around a factor of 2 (Jen et al., 2019).

The emission factor (EF) of each compound was calculated by:

$$EF_i = (C_i / C_{OC}) * EF_{OC} \qquad [5.1]$$

where EF_i is the emission factor of compound i in g kg^{-1}; C_i and C_{OC} are the concentrations of compound i and OC in µg m^{-3}, respectively; and EF_{OC} is the emission factor of OC in g kg^{-1} as presented in Chapter 3.

5.2. Emission Factors for Individual Compounds

Emission factors (EFs) for speciated organics from the PM samples collected during prescribed burn experiments are needed for emission modeling (e.g. FOFEM) to evaluate the potential impacts on climate and air quality from this important emission source. The EFs calculated from the 1st and 3rd entry burns are intended for use in estimating the prescribed burn emissions from mixed conifer forests in the western United States, and to understand whether there are significant relationships between EFs and modified combustion efficiency (MCE) for the individual compounds as well as for the compounds classified in different chemical functional groups for effective parameterization in emission models.

Over 100 individual compounds were analyzed in the two prescribed burns leading to 114 individual compound EFs reported from ground and aerial based samples collected in the 1st entry 2021 prescribed fire, and a smaller set of 28 compounds of these compounds that were also measured in ground-based samples in the 2017 3rd entry pilot study. **Figure 5.1** shows the results for the 10 largest single compound EFs drawn from each of these three sample sets showing the large overlap in dominant compounds (14 compounds total). Speciated EFs observed from the 2019 Springs Fire sample set are included for comparison. Bars indicate the mean EFs for each compound, with vertical lines indicating standard errors of the mean for each platform.

Levoglucosan has the highest measured single compound mean EF in the prescribed burns. Levoglucosan is an anhydrosugar pyrolysis product of cellulose (Simonelt et al., 1993; Nolte et al., 2001; Simoneit, 2002), with an EF that is 10 times larger than palmitic acid which has the next largest measured compound EF. Levoglucosan is typically the most abundant organic compound in aerosols emitted from biomass burning (Simoneit, 2002; Jen et al., 2019), is the dominant

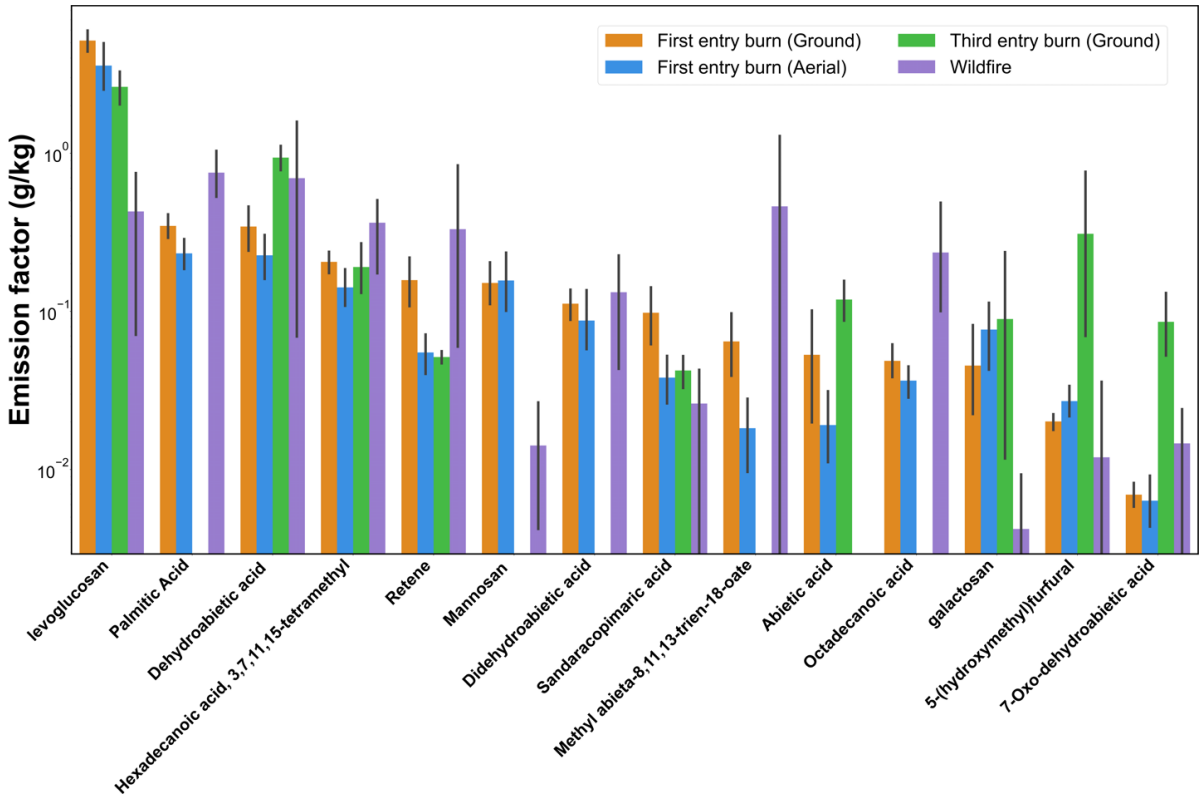

Figure 5.1 Individual compounds with the largest emission factors (EFs) observed from prescribed fire sampling platforms (1st entry burn ground and aerial, 3rd entry burn ground). Bars indicate the mean EFs for each compound, with vertical lines indicating standard errors of the mean for each platform. A comparison to the same compound EFs measured from a wildfire are presented.

contributor to the total sugars and anhydrosugars compound classes, and hence is used extensively as a BB tracer. Reported EFs for levoglucosan are mostly less than 1g kg^{-1} from chamber burning experiments of individual fuels (Jen et al., 2019). However, chamber-based burning experiments typically produce higher average MCEs potentially due to the inability to produce humid burning conditions akin to ambient burning, and thus the estimation of EFs from burning individual fuels in chambers may not be representative enough of prescribed burn conditions. Smoke samples collected during an aircraft-based campaign from a southeast United States prescribed fire was also less than 1g kg^{-1} (Sullivan et al., 2014; Jen et al., 2019). This may be because the fuels in this study were different, and that levoglucosan can undergo evaporation and photo-chemical oxidation (Hennigan et al., 2011), hence reported EFs may change as a function of 'time since emission' and distance from the fire location. To estimate the actual levoglucosan Efs from fires, more immediate sampling of smoke in the vicinity of the fire is required. In the FIREX-AQ field campaign, with the increased proximity to the fires using a mobile laboratory (rather than aircraft), Liang et al. (Liang et al., 2022) reported levoglucosan EFs ranging over an order of magnitude from 0.08-2 g kg^{-1}. However, during the FIREX-AQ campaign, the sampling was also done further downwind of the exact fire location and sampling included contributions from a wider range of smoke age. In the Blodgett Forest prescribed burn experiments (both 3rd and 1st entry burn) the average

levoglucosan EFs (mean = 4.4 g kg^{-1} for 1st entry burn and 2.6 g kg^{-1} for 3rd entry burn) are higher than these previously reported levoglucosan EF values and we infer that is at least partially due to our more immediate emission sampling. Sampling locations were chosen specifically to capture fresh emissions both on the ground near the fires and in rising plumes above the ecosystem using the aerial drone.

Other individual compounds, nannosan (mean EF= 154 mg kg^{-1} for 1st entry burn) and galactosan (mean EF= 60.8 mg kg^{-1} for 1st entry burn), which also belong to the class 'sugar' appeared as some of the highest individual compound emissions. Both EFs for mannosan and galactosan were an order of magnitude lower for the FIREX-AQ campaign (mean EF = 10.8 mg kg^{-1} and mean EF = 2.6 mg kg^{-1} respectively) (Liang et al., 2022). Diterpenoids were the 2nd most abundant chemical group found in the 1st entry burn. The average EFs from 1st entry burn for dehydroabietic acid, one of the most important diterpenoids in BB aerosol, was 286 mg kg^{-1} (**Table 5.1**). Resin acids, such as dehydroabietic acid, are most abundant in conifer stems ((Krokene, 2015; Ramage et al., 2017; Eksi et al., 2020). In the 3rd entry burns we measured 3x higher EFs for dehydroabietic acid (938 mg kg^{-1}) that is likely due to 3x greater levels of coarse woody debris with high coniferous signatures being consumed relative to the 1st entry burns (this fuel consumption composition was determined specifically for the stands where emissions were measured). Abietic acid and sandaracopimaric acid also were among the highest emission compounds with 1st entry burn EFs of 38.4 mg kg^{-1} and 68.6 mg kg^{-1}, respectively. The average EF of the most important biomass burning PAH compound, retene, from 1st entry burns was 107 mg kg^{-1}, which is comparable to the average EFs of retene reported from the FIREX-AQ campaign, 158 mg kg^{-1}. The difference in EFs for retene and overall, all EFs in **Figure 5.1** between aerial and ground sampling platform for 1st entry burns (ground being higher than aerial) is potentially due to differences in average MCE values for the samples collected on these two platforms, with the aerial samples covering a broader range including higher MCE (Chapter 3).

Figure 5.2 illustrates the dependence of individual compound EFs on the MCE. Of those compounds observed with high prevalence, defined as compounds detected in at least 50% of samples, the top 18 compounds with highest linear correlation of EF with MCE are shown. Compounds are ordered from top to bottom by high to low EF with the positive or negative correlation R for the two prescribed fires. The small set of three wildfire samples were excluded from the correlation analysis but included in the figure for comparison to show their general agreement with the prescribed fires. As with the OC/EC data presented in Chapter 3, individual compounds exhibit weak to zero correlations with MCE with consistent EFs measured across both prescribed burns and sampling platforms.

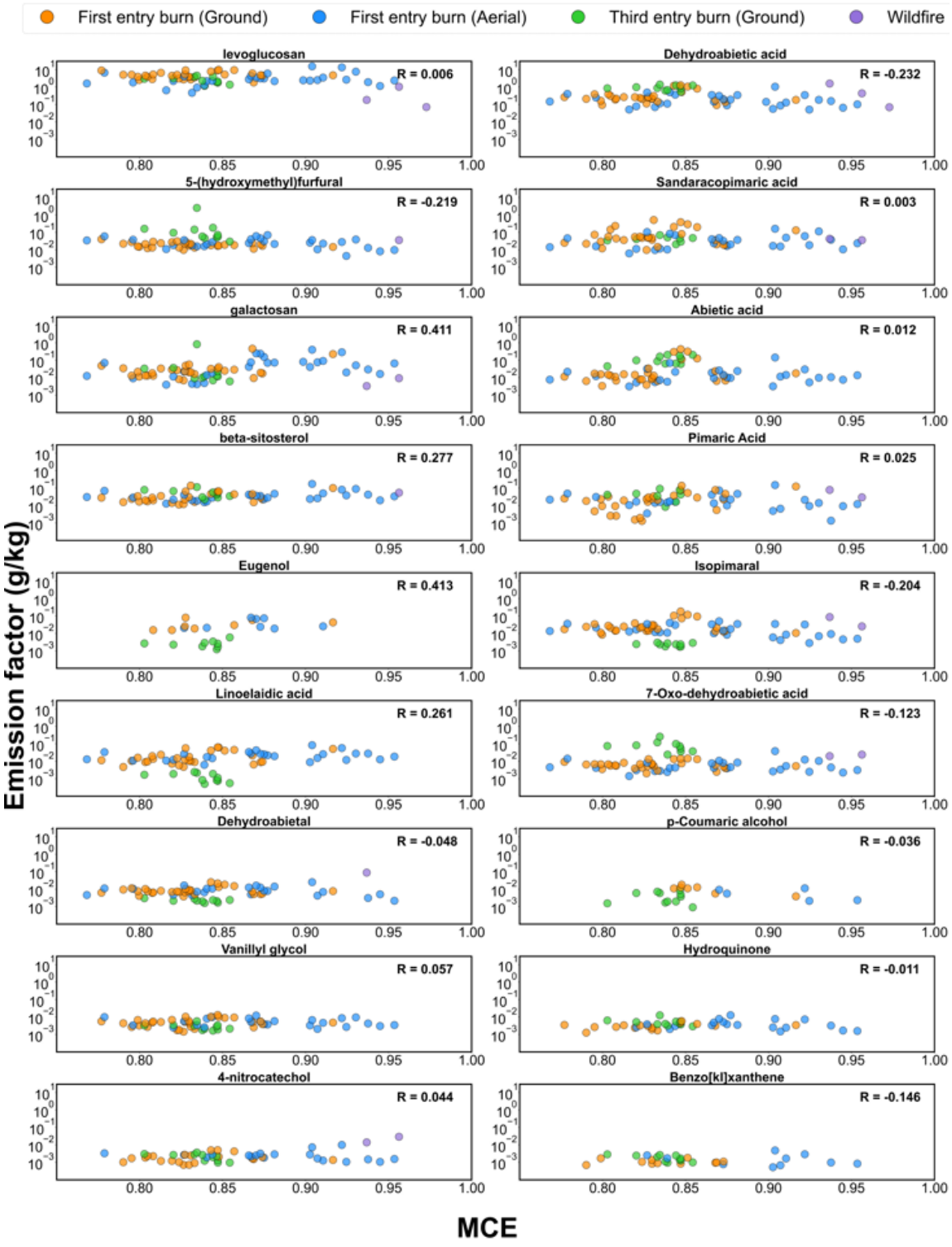

Figure 5.2 Individual organic compound emission factor (EF) versus modified combustion efficiency (MCE) for compounds with high prevalence (minimum 50% occurrence) across 1st entry burn (ground and aerial) and 3rd entry burn (ground) samples. The top 18 compounds were selected based on highest linear correlation R across 1st and 3rd entry burn samples, ordered from high (top) to low (bottom) EF.

Relationships between EF and MCE are sometimes used to provide simple but effective parameterizations for modeling biomass burning emissions by accounting for the spatio-temporal dependence of emission estimates on combustion state. Being commonly the single most abundant species detected in BB emissions, levoglucosan is often treated as a near universal BB tracer. Levoglucosan EF has been shown to have some linear MCE relationship in previous fire lab experiments (R=0.58) (Jen et al., 2019) and also in the FIREX-AQ field campaign (R=0.87) (Liang et al., 2022). However, from both 1st entry and 3rd entry burn prescribed fires we find little to no linear MCE relationship with levoglucosan EF (R=0.004). This lack of any strong linear dependence was also observed for OC versus MCE (Chapter 3), which likely follows from the dominance of the levoglucosan EF to the total OC EF. However, galactosan, belonging to the same compound group 'sugar', demonstrates a small positive linear correlation with MCE (R=0.411). This difference in MCE trend for specific compounds within the same functional class emphasizes the importance of speciated organic analysis for understanding the complexity of prescribed fire emissions. Dehydroabietic acid and isopimaral both demonstrate mild negative linear relationships with MCE (R= -0.232 & R= -0.204 respectively). Yet, this mild relationship diminishes to essentially zero for other compounds belonging to the diterpenoids group (e.g., R= 0.003 for sandaracopimaric acid). Aromatic compound vanillyl glycol and nitrogen-containing 4-nitrocatechol also displayed negligible dependence on MCE (R= -0.057 & R= -0.044 respectively, **Figure 5.2**)

The absence of strong correlations with MCE may be explained by two factors: 1) due to proximity of sampling, the extent of evaporative or oxidative loss in levoglucosan may be lower for the sampled location of prescribed fires than wildfires which were sampled further downwind; and 2) both fire lab and wildfire samples span a narrow but high range of MCE values with average MCE > 0.87. The prescribed fire sampling with ground and especially aerial observations have given us the opportunity to explore a wider range of burning conditions with an average MCE <0.87 and which shows no linear MCE relationship. Since our observations of prescribed fire generally tended to cover a wide range of MCE (see also Chapter 3), we recommend using the mean EFs from this field campaign representative of a broad range of MCE regimes emission modeling of mixed conifer forest prescription fires.

Table 5.1 Study averaged emission factors (EFs) for individual organic compounds. Mean, median, standard error of the mean (se) and percent occurrence are listed for 1st (ground and aerial samples) and 3rd (ground samples) entry burns. For 3rd entry burn the compounds included are those that are common to 1st entry burn and have at least 50% occurrence in 3rd entry burn samples.

	First entry burn EF (2021)				Third entry burn EF (2017)			
	mean	median	se	Occur	mean	median	se	Occur
Compound Name	mg/kg	mg/kg	mg/kg	%	mg/kg	mg/kg	mg/kg	%
levoglucosan	4380	3800	380	100	2630	2270	340	100
Palmitic Acid	290	250	20.0	100				
Dehydroabietic acid	286	207	34.9	100	938	875	84	100
UNK_sugar1	249	153	33.1	98				
Hexadecanoic acid, 3,7,11,15-	174	156	13.6	98	191	168	38	100
UNK_sugar2	169	126	18.7	100				
Mannosan	154	119	20.8	100				
Tetracosanoic acid	139	119	9.81	98				
UNK_aromatic1	113	105	9.03	98				
Retene	107	63.8	16.1	98	51.4	51.5	2.2	82
Didehydroabietic acid	99.9	76.6	11.6	98				
Vanillin	85.5	74.6	7.8	98				
Isopimaric acid	82.8	56.1	11.1	95				
Semperviro l	81.9	47.4	11.9	98				
Sandaracopimaric acid	68.6	37.3	12.1	98	42.3	43.6	4.5	73
Vanillic acid	66.8	51.9	6.98	100				
Acetovanillone	63.3	44.5	5.83	98				
UNK_alcohol1	62.7	24.9	14.0	66				
galactosan	60.8	27.2	11.9	100	89.5	12.0	73.4	100
Docosanoic acid	53.8	50.2	3.74	98				
Methyl isovanillate	50.7	34.9	6.45	97				
UNK_oxygenated1	47.2	34.5	5.05	97				
Octadecanoic acid	42.7	37.4	3.81	98				
Methyl abieta-8,11,13-trien-18-oate	41.8	15.8	8.72	73				
Myristic acid	39.7	28.0	4.50	98				
Abietic acid	36.4	12.2	10.2	98	118.8	98.2	18.4	100
beta-sitosterol	35.8	28.0	4.00	93	52.6	46.6	8.5	91
Palustric Acid	35.0	24.9	4.57	98				
UNK_PAH1	34.3	25.3	4.08	97				
UNK_sugar3	33.8	25.1	4.32	98				
Catechol	31.5	26.0	4.29	69				
UNK_acid1	30.8	25.2	2.43	98				
Isopimaral	26.9	17.7	3.95	98	2.33	2.37	0.14	91
Pimaric Acid	26.8	17.3	4.07	95	45.1	42.0	8.5	73
UNK_sugar4	26.0	19.8	2.60	98				
UNK_sugar5	24.0	21.0	2.11	97				

	First entry burn EF (2021)				Third entry burn EF (2017)			
Compound Name	mean mg/kg	median mg/kg	se mg/kg	Occur %	mean mg/kg	median mg/kg	se mg/kg	Occur %
1,7-dimethylphenanthrene	22.0	11.0	4.45	59				
UNK_sugar6	22.0	17.6	2.48	98				
5-(hydroxymethyl)furfural	23.6	21.4	1.71	98	309	72.4	220	100
4-methylcatechol	22.2	20.9	2.30	85				
UNK_sugar7	22.0	11.0	4.45	59				
UNK_sugar8	22.0	17.6	2.48	98				
Pinitol	21.9	0.0	6.95	22				
Linoelaidic acid	21.2	15.1	2.30	93	1.33	1.13	0.21	100
UNK_acid2	21.2	15.9	2.32	98				
16-Hydroxyhexadecanoic acid	19.7	16.1	1.90	90				
UNK_sugar9	19.5	16.4	2.30	97				
UNK_sugar10	18.8	11.4	2.97	98				
4-(3-hydroxypropyl)-2-methoxyphenol	18.3	14.1	1.58	100				
2- 4-Dihydroxy-acetophenone	17.8	15.5	1.54	95				
UNK_oxygenated2	17.4	12.2	2.90	69				
Divanillyl	17.2	15.2	1.44	97	7.69	7.23	0.79	55
UNK_diterpenoid1	16.8	10.8	2.27	98				
Pentadecanoic acid	16.8	15.9	1.07	98				
Totarol	16.4	8.79	2.57	97				
Methyl abietate	15.5	0.00	2.76	47				
2,3-Dehydroferruginol	15.3	3.83	4.80	56				
Sandaracopimarinal	14.4	7.77	2.71	86				
Deoxy-ribo-hexonic acid 1-4-lactone	13.8	5.84	2.49	98				
UNK_sugar11	12.9	9.48	1.65	98				
Dehydroabietinol	12.5	11.2	0.73	98				
UNK_diterpenoid2	12.4	10.9	1.22	98				
8-Isopropyl-1,3-dimethylphenanthrene	12.4	9.13	2.11	85				
Coniferyl aldehyde	10.5	8.93	0.98	97	83.5	75.47	9.72	55
Eugenol	10.4	0.00	2.75	27	2.72	2.61	0.41	82
1-monopalmitin	10.2	7.10	1.31	83				
UNK_nitrogen-containing1	10.2	4.76	2.26	95				
1-benzyl-3-methylnaphthalene	9.64	5.52	2.00	97				
Levopimaric acid	9.19	7.55	0.79	98				
3,4-Divanillyl-tetrahydrofuran	8.80	7.12	0.71	97				
UNK_triterpenoid1	8.28	5.36	1.09	81				
Dehydroabietal	8.16	7.17	0.72	90	2.23	2.17	0.13	91
E-9-Tetradecenoic acid	7.50	5.66	1.03	88				
UNK_triterpenoid2	6.97	2.24	1.19	61				
UNK_unknown1	6.97	2.24	1.19	61				
Syringol	8.16	7.17	0.72	90	2	2	0	91

	First entry burn EF(2021)				Third entry burn EF (2017)			
	mean	median	se	Occur	mean	median	se	Occur
Compound Name	mg/kg	mg/kg	mg/kg	%	mg/kg	mg/kg	mg/kg	%
7-Oxo-dehydroabietic acid	6.65	5.32	0.71	98	85.9	74.5	20.3	91
UNK_aromatic2	6.64	5.61	0.51	98				
UNK_sugar11	6.35	5.10	0.88	90				
Methylsyringol	5.44	5.86	0.77	56	667	540	127	100
Vanillyl glycol	5.09	4.64	0.40	93	2.85	2.83	0.35	100
Hexadecanamide	4.84	0.00	1.49	22				
Inositol	4.74	0.00	1.70	41				
Pyrogallol	4.45	4.25	0.45	81	1.64	1.67	0.25	64
stigmasta-3,5-diene	4.41	3.65	0.58	81				
9-Methylanthracene	3.83	1.92	0.79	83				
UNK_sugar12	3.54	3.25	0.34	90				
UNK_aromatic3	3.48	2.74	0.32	98				
Z-9-Octadecenamide	3.43	0.00	1.35	29				
Homovanillic Acid	3.30	2.59	0.31	98				
Fluoranthene	3.21	2.14	0.44	86	0.50	0.42	0.06	100
UNK_sugar13	3.14	1.42	0.79	58				
5-Podocarpa-8,11,13-trien-16-oic acid, methyl ester	2.86	0.00	0.97	20				
7-Oxodehydroabietic acid methyl ester	2.82	2.60	0.20	97	23.0	18.8	3.7	100
3-Deoxy-D-ribo-hexonic acid-lactone	2.69	0.00	1.39	31				
UNK_oxygenated3	2.41	1.51	0.47	66				
Coniferyl alcohol	2.27	1.59	0.33	73				
Hydroquinone	2.20	1.89	0.33	59	5.19	4.26	0.80	100
D-Arabino Hexonic acid 3-deoxy-lactone	2.04	0.48	0.41	64				
9-Ethyl-10-methylanthracene	1.82	1.23	0.25	80				
p-Coumaric alcohol	1.79	0.00	0.54	20	4.09	3.70	0.82	100
UNK_unknown2	1.75	0.72	0.32	69				
4-nitrocatechol	1.64	1.36	0.24	68	2.13	2.22	0.28	100
UNK_unknown3	1.50	0.90	0.26	92				
Azelaic acid	1.32	1.00	0.13	98				
Protocatechoic acid	1.29	0.00	0.28	34	2.51	2.44	0.43	55
1,5-Anhydroglucitol	1.26	0.00	0.70	10				
UNK_oxygenated4	1.16	0.84	0.18	95				
UNK_oxygenated5	0.99	0.00	0.39	17				
Terephtalic acid	0.82	0.29	0.24	93				
4-Coumaric acid	0.52	0.00	0.13	36				
Benzo[kl]xanthene	0.50	0.00	0.12	36	1.81	1.67	0.21	100
3-hydroxybenzoic acid	0.34	0.00	0.11	17				
3-methyl-5-nitrocatechol	0.13	0.00	0.06	8				

5.3. Emission Factors for Compound Classes

In the 2021 prescribed burn and 2019 wildfire sample sets, there are enough positively identified measured compounds with distinct moieties to allow classification of the EF data into distinct chemical classes. The 2017 pilot study data does not include an identical range of compounds, thus it is excluded from the summed compound class comparisons. The compound class names (# in class) are sugar (20), diterpenoid (22), (aliphatic) acid (12), aromatic (27), PAH (9), oxygenated (11), triterpenoid (4), and nitrogen-containing (5).

Figure 5.3 provides the mean class-summed EFs for 2021 1st entry burn ground and aerial samples with uncertainty bars equal to the standard errors of the mean. Comparable EFs are observed across platforms for most of the classes including the three most dominant: sugars, diterpenoids and acids. The three wildfire samples, even with much larger uncertainties, show noticeable differences in EFs for some classes but especially for sugars and aromatics.

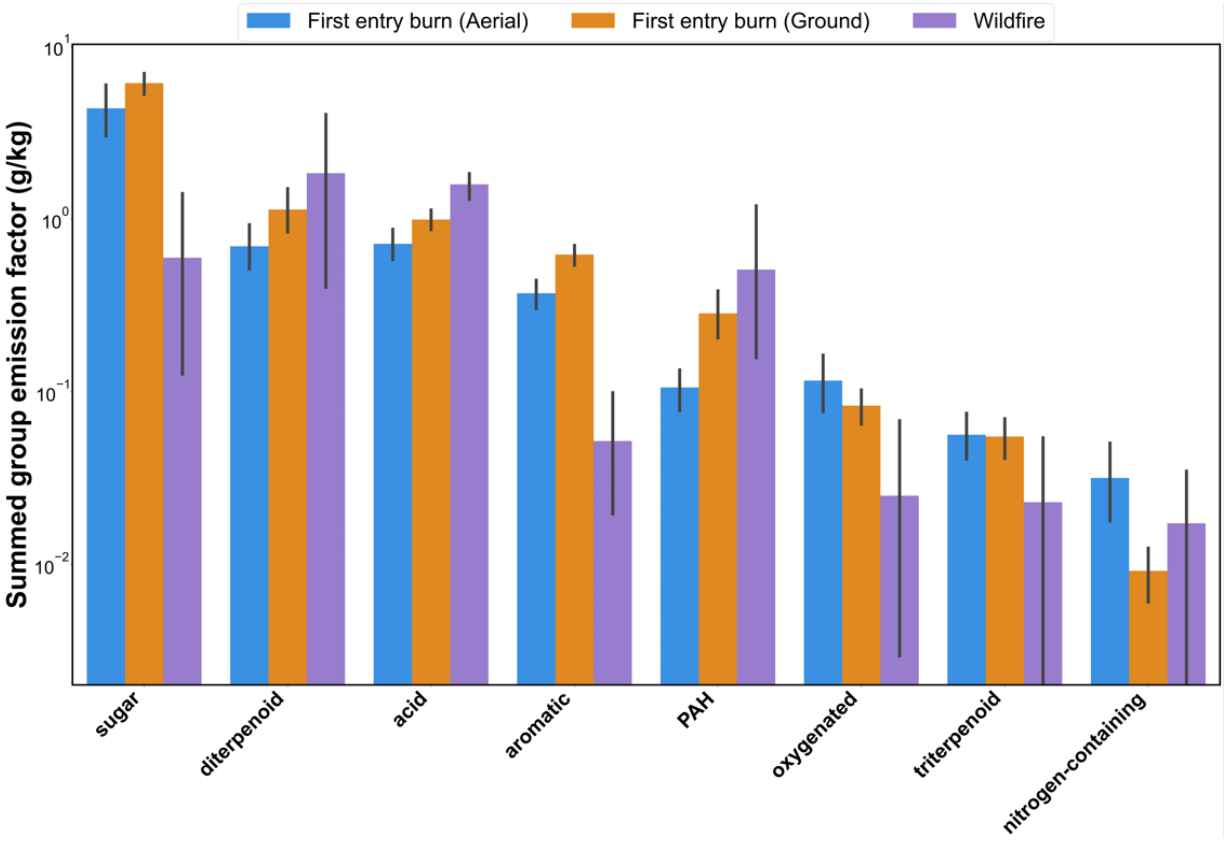

Figure 5.3 Emission factors summed by compound class from 1st entry prescribed fire samples (ground and aerial). Bars indicate the mean of summed group EFs for each compound by platform, with vertical lines indicating standard errors of the mean. The class sums of the same EFs measured from a wildfire are included for comparison.

Small differences in the mean values for summed EFs for the groups between two different platforms for 1st entry burn can be explained at least partially by the difference in average MCE. Grouping compounds into classes reveals some trends with MCE more clearly than is observed for many individual compound EFs. **Figure 5.4** shows the classified EFs versus MCE for the 8 dominant compound groups for 1st entry burn samples (ground and aerial) and the wildfire samples. The linear correlation (R) for each group is calculated for 1st entry ground and drone data excluding the wildfire samples.

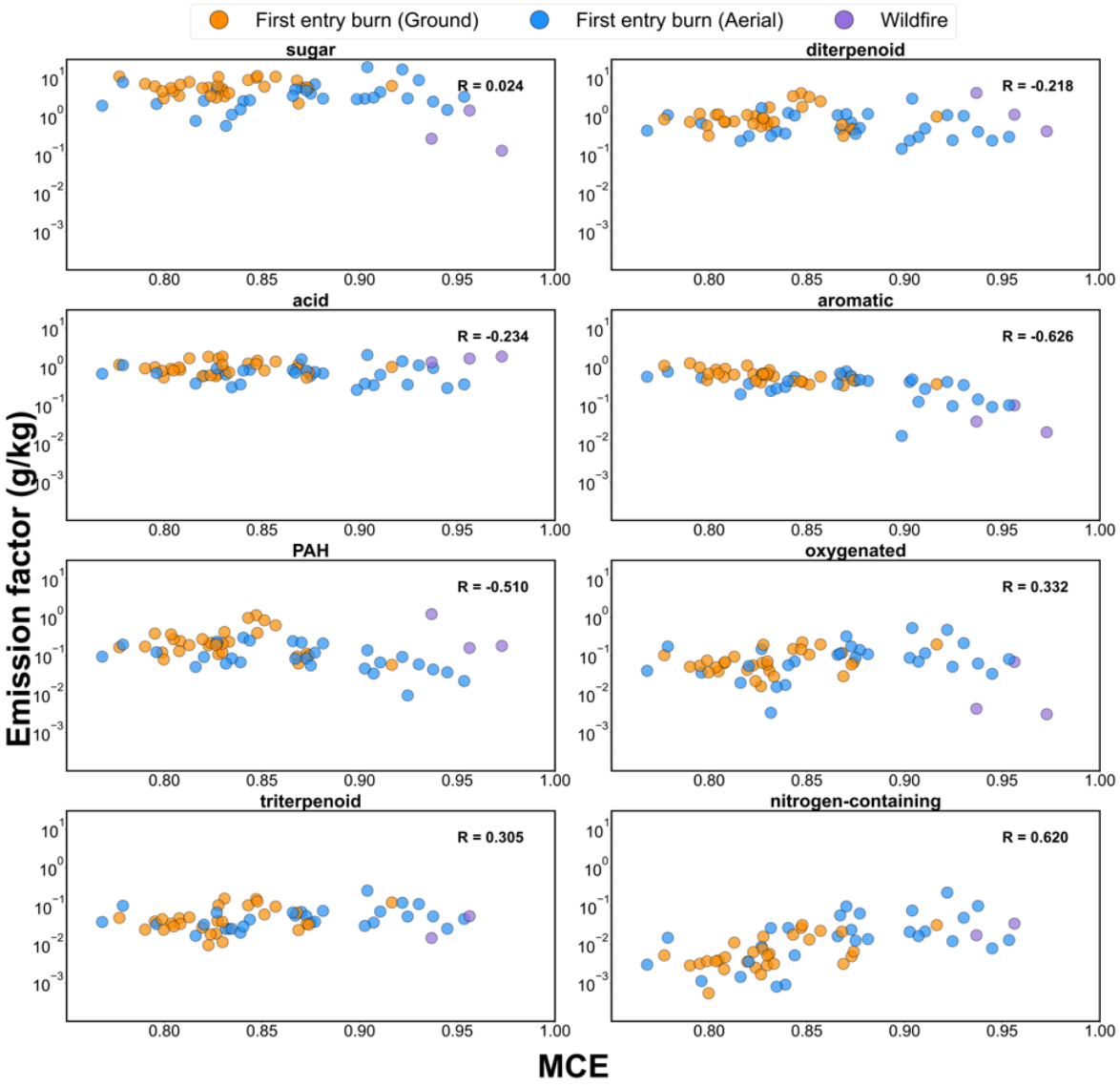

Figure 5.4 Emission factors in g/kg summed by compound class (sugar, diterpenoid, acid, aromatic, PAH, oxygenated, triterpenoid, nitrogen-containing) versus modified combustion efficiency (MCE) for 1st entry burn samples (ground and aerial). Linear correlation (R) is calculated for 1st entry ground and drone data (not including wildfire) with individual compounds ordered from high (top) to low (bottom) EF.

The aromatic group of compounds demonstrates light absorbing properties in the UV-VIS range due to the presence of an aromatic nucleus in the compound and hence important from a climate modeling perspective (Jacobson, 1999). When grouped, the aromatic compounds display relatively stronger negative correlation (R = -0.626) to MCE than the individual aromatic compounds, i.e., combustion with lower MCE produces more aromatic compounds. This inference is supported by summary statistics of individual aromatic compounds for 1st entry burns (**Figure 5.5**) in which 1st entry ground samples with lower average MCE values have either higher or almost comparable median EFs with 1st entry aerial samples. The median EFs for the aromatic compounds from wildfire samples with higher MCE values were always lower than the median EFs from both platforms of 1st entry burn. The one exception is terephthalic acid that has been associated with plastic burning (Simoneit et al., 2005), which may indicate the inclusion of some non-biomass fuels in the wildfire samples.

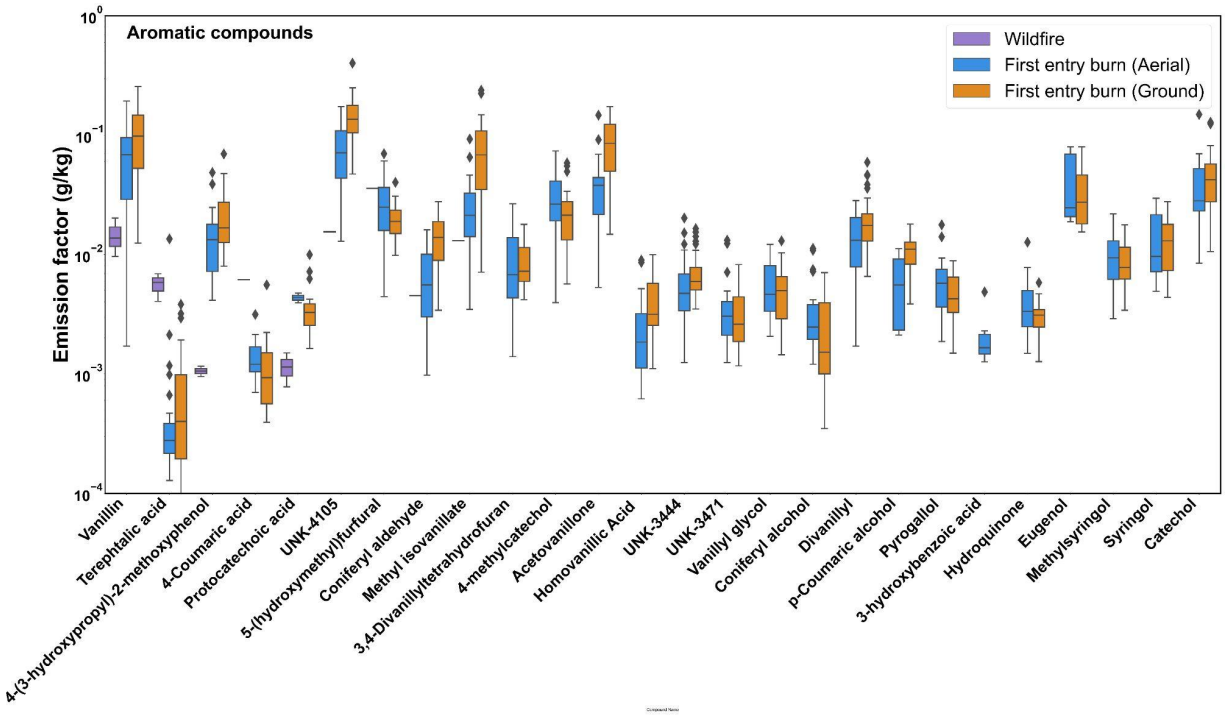

Figure 5.5 Emission factors (EFs) for aromatic compounds. Median values shown as horizontal lines within the colored boxes representing the 25th to 75th percentile (interquartile range, IQR). Whiskers stretch the IQR by 1.5 times. Data beyond 1.5*IQR is shown with diamonds.

Similarly, the summed group EFs for the 1st entry burn for both ground and aerial platforms was very similar with minor differences for some groups (e.g., PAHs). This is primarily due to the samples collected from the ground platform having overall lower average MCE= 0.84 +/- 0.05 as compared to the aerial platform with an average MCE=0.89 +/- 0.04 (Chapter 3). This bias is noticeable across the individual PAH EFs shown **Figure 5.6**.

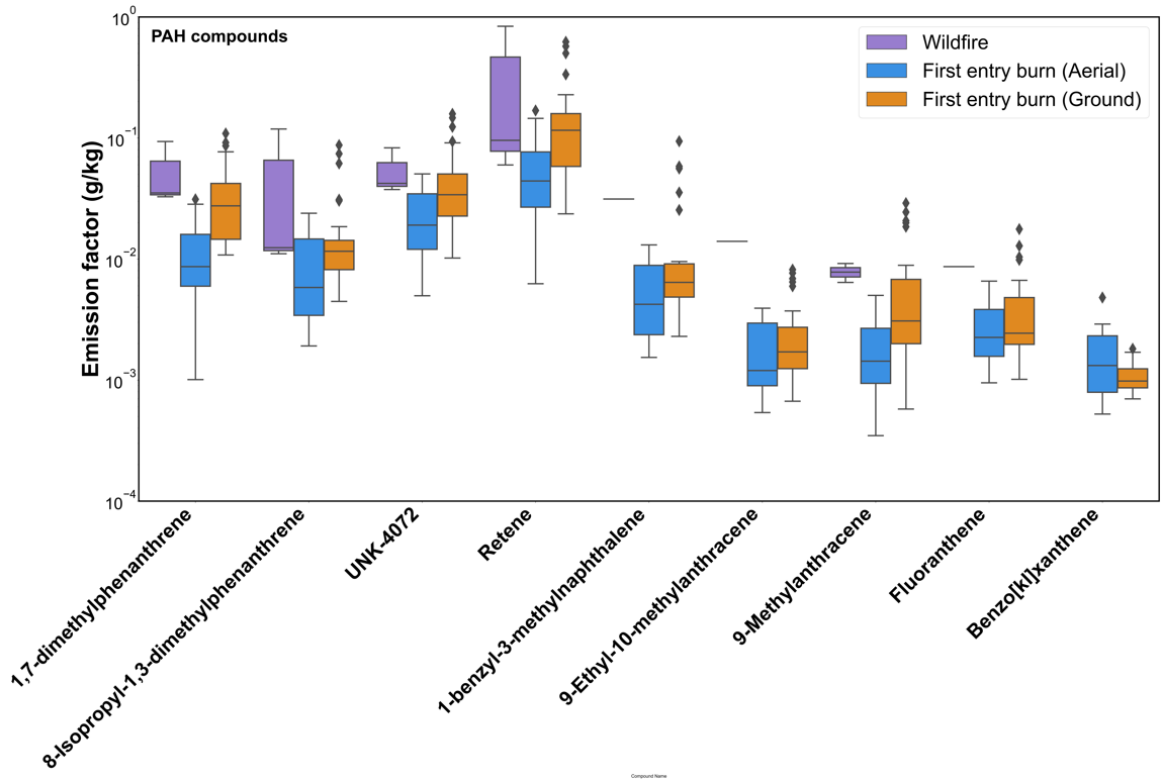

Figure 5.6 Emission factors (EFs) for polycyclic aromatic hydrocarbon (PAH) compounds. Median values shown as horizontal lines within the colored boxes representing the 25th to 75th percentile (interquartile range, IQR). Whiskers stretch the IQR by 1.5 times. Data beyond 1.5*IQR is shown with diamonds.

To provide average emission factors to the emission modeling community, group EFs from the 1st entry burn were separated into two combustion regimes (MCE < 0.88 & MCE > 0.88) with results summarized in **Table 5.2**. The summed PAH EFs (mean EF = 235 mg kg^{-1}) from samples with MCE < 0.88 are nearly 4 times more than summed PAH EFs (mean EF = 62.8 mg kg^{-1}) for samples MCE > 0.88. Higher summed PAH EFs at lower MCE indicate that PAHs are formed by the decomposition of di/tri-terpenoid during smoldering (Ramdahl, 1983; Simonelt et al., 1993; Standley and Simoneit, 1994; Liang et al., 2022). Prescribed fires have been reported in general to occur with lower combustion efficiencies than wildfires (Jaffe et al., 2020), as also shown in Chapter 3.

While we observed that summed EFs were higher in the low MCE regime for PAHs and aromatic compounds (~4x and ~2x, respectively, **Table 5.2**), there are chemical groups within the scope of our analysis that exhibit an increase in summed group EFs with increasing MCE (e.g., oxygenated: 2 times in high MCE range; nitrogen-containing: more than 3 times). The nitrogen-containing compound class demonstrates a stronger MCE relationship (R=0.62, **Figure 5.4**) with MCE relative to other groups. This could be explained by the aerial platform's ability to capture higher MCE plumes rising from the prescribed burn that exhibit higher EFs for the sum of nitrogen-

containing compounds **(Figure 5.3** and **Figure 5.4**). We infer that the increased summed EFs for the nitrogen-containing group in the high MCE regime are likely attributable to increased chemical production of those compounds under the more intense combustion conditions (e.g, hexadecanamide, **Table 5.1**). We observed a similar increase in summed EFs at high MCE for oxygenated compounds. However, unlike the nitrogen-containing group, we see no difference in EFs for the oxygenated from ground and aerial platforms (mean in **Figure 5.3** and whisker plot in **Figure 5.7**).

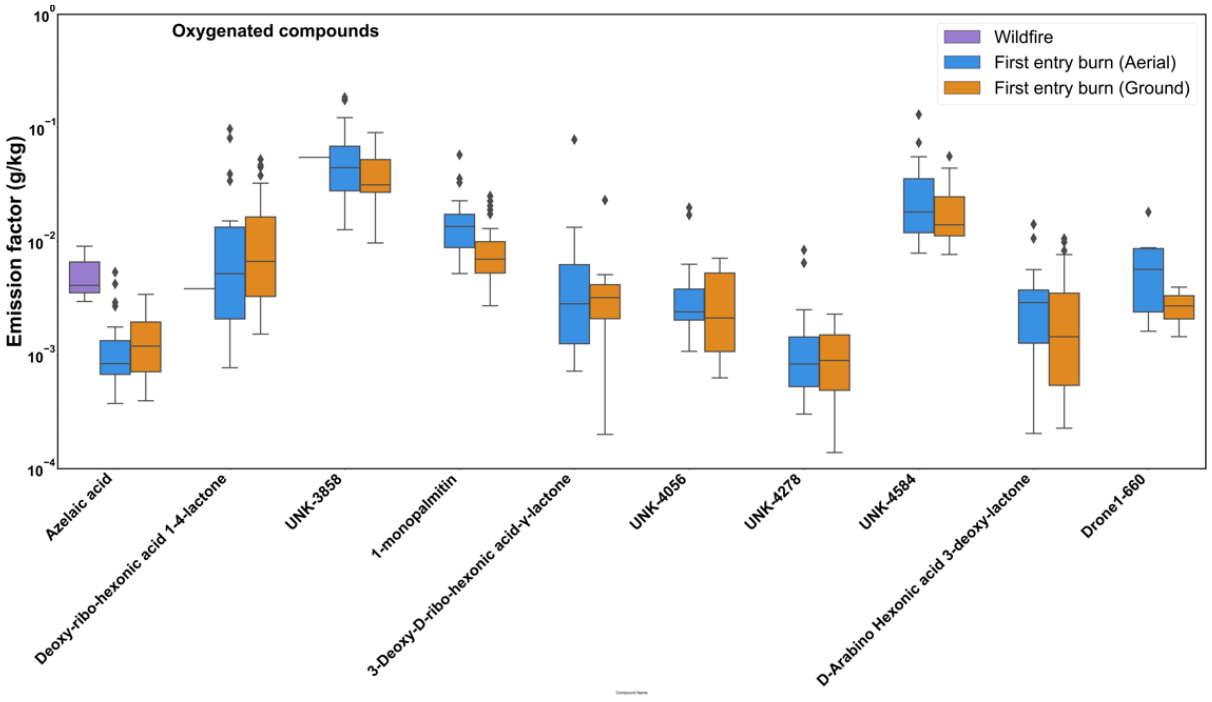

Figure 5.7 Emission factors (EFs) for oxygenated compounds. Median values shown as horizontal lines within the colored boxes representing the 25th to 75th percentile (interquartile range, IQR). Whiskers stretch the IQR by 1.5 times. Data beyond 1.5*IQR is shown with diamonds.

As mentioned earlier, in this prescribed fire campaign combining ground and aerial measurements led to a greater understanding of the prescribed burning emissions as governed by three factors: 1) combustion conditions indicated by MCE; 2) fuels consumed and 3) evaporation and oxidative aging (either homogenous or heterogeneous or both). The field experiments were designed to determine EFs and evaluate the impact of combustion conditions on the EFs. Combining ground and aerial measurements was complementary as we were able to explore a wide range of MCEs and it helped to understand the MCE relationships for both individual compounds and chemical groups.

The comparison of EFs from particulate matter samples collected in different platforms (including 3rd entry burn and 3 samples from wildfires) do not illustrate clear evidence of evaporation loss. However, due to the extensive list of compounds analyzed by GC×GC EI-HR-ToFMS (total

number of analyzed compounds =114), we can identify a few tracer compounds that are indicative of aging. For example, azelaic acid, a dicarboxylic acid, is generally formed by decomposition of long chain unsaturated fatty acids (e.g., oleic acid) (Sengupta et al., 2020). The comparison of EFs across multiple platforms demonstrates that wildfire samples have higher azelaic acid than 1st entry burn samples (**Figure 5.7**) supporting the interpretation of less aging of smoke sampled during the 1st entry burn. Nitrocatechols are formed from the oxidation of phenolic compounds by NO_3 or OH followed by NO_2 (Finewax et al., 2018; Fredrickson et al., 2022). The comparison of EFs for nitrocatechol and methyl nitrocatechol across platforms emphasizes a similar interpretation of these wildfire samples being more aged than the prescribed fire samples (**Figure 5.8**). While aging is reflected in the comparative EFs across the three sample sets, our results in current form cannot be utilized to understand the timescale and modes (homogeneous vs heterogeneous) of aging. Dehydroabietic acid EFs in 1st entry (0.283 g kg^{-1}) are comparable to wildfire FIREX_AQ (0.363 g kg^{-1}) (**Table 5.1**) while EFs for sugars like levoglucosan was lower at least by a factor of two or more indicating that they have lower propensity to decompose than sugars with distance and time of sampling.

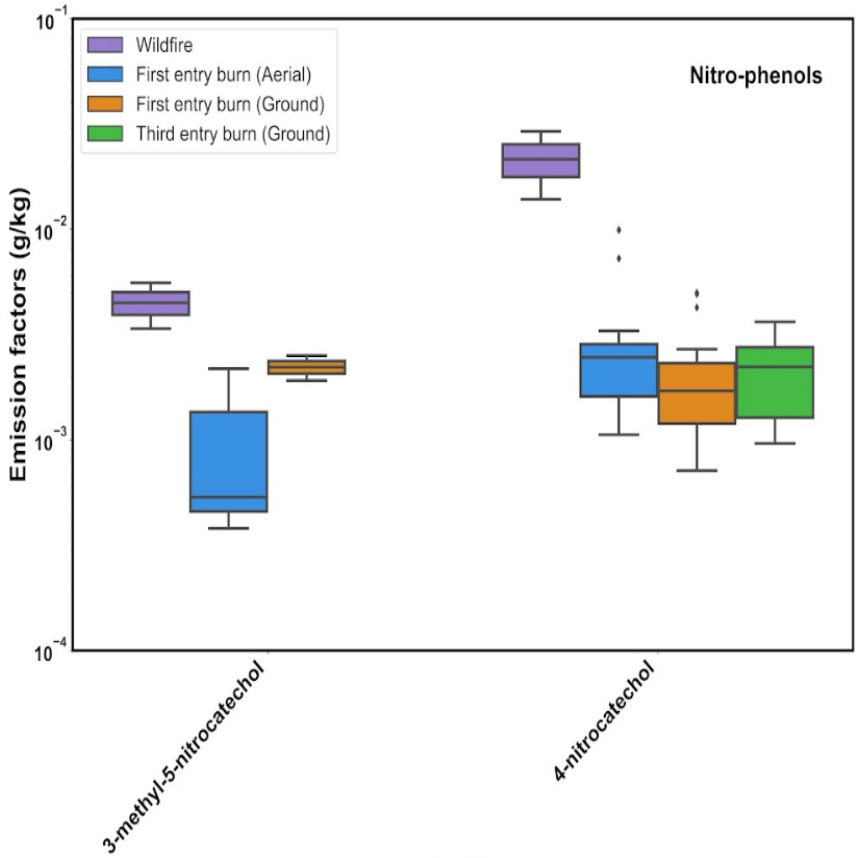

Figure 5.8 Emission factors (EFs) for nitro-phenol compounds. Median values shown as horizontal lines within the colored boxes representing the 25th to 75th percentile (interquartile range, IQR). Whiskers stretch the IQR by 1.5 times. Data beyond 1.5*IQR is shown with diamonds.

Table 5.2 Mean and standard error (se) of the mean for study averaged chemical group emission factors in mg kg^{-1} for the Blodgett Forest prescribed fires conducted in 2021. Values are shown grouped by low and high modified combustion efficiencies (below and above MCE of 0.88, respectively) with comparison to the 2019 "Springs Fire" wildfire samples collected by CARB at much higher mean MCE (0.96).

	Emission factors (mg/kg)					
	1st Entry Prescribed Fire				Springs Fire	
	MCE < 0.88		MCE > 0.88		MCE = 0.96	
Group	mean	se	mean	se	mean	se
sugar	5100	407	5830	113	597	410
diterpenoid	975	119	719	32.9	1840	1110
acid	893	55.3	735	15.3	1590	155
aromatic	571	32.9	246	9.14	51.9	24.0
PAH	235	33.5	62.1	9.29	510	342
oxygenated	83.9	9.46	154	2.62	25.0	21.5
triterpenoid	49.7	5.14	76.9	1.42	23.0	16.2
nitrogen-containing	13.2	2.74	45.2	0.76	17.3	10.0

5.4. Summary and Recommendations

Individual and chemically grouped emission factors were determined for two types of California prescribed fires (1st entry and 3rd entry) in the mixed conifer forests of Northern California and one California wildfire ("Springs Fire"). Emission factors for most individual compounds were found to be insensitive to the combustion phase as indicated by MCE much like the OC/EC results reported in Chapter 3. While individual compound emission factors were presented, the grouping by chemical class may provide a more useful approach for analyzing and modeling prescribed fire emissions. The 2021 1st entry burn study results, as presented in **Table 5.2**, are more representative of the current state of California mixed conifer forests. The four dominant chemical groups presented account for 95% of the speciated mass. Depending on fire intensity, two distinct combustion phase regimes were identified for use in modeling with an approximate threshold of MCE=0.9, the traditional definition of the onset of a flaming state (Akagi et al., 2011). While the total sugars emission factor shows little dependence on MCE, like the OC EFs, some chemical classes do show measurable differences between the low and high MCE regimes with a few groups exhibiting increases in EF with MCE (e.g. oxygenated and nitrogen-containing) that exemplify secondary formation while a few others show the typical decrease in EF with MCE under more flaming conditions (e.g. aromatics and PAHs).

6. Black Carbon Emission Factors and Light Absorbing Properties (AAE) from Aethalometer and ABCD Sensor Package

6.1. Introduction

Biomass burning is a major contributor to the atmospheric burden of carbonaceous particles in the atmosphere, including light absorbing black carbon (BC) and brown carbon (BrC), which adversely impacts human health and perturbs the Earth's radiation balance (Intergovernmental Panel On Climate Change, 2023). Whereas BC absorbs sunlight strongly over all visible and near-infrared wavelegnths, BrC light absorption is spectrally dependent and greatest in the near-UV range of visible light ($\lambda \simeq 370–500$ [nm]) ((Kirchstetter et al., 2004). The composition of carbonaceous aerosols (i.e., relative abundance of BrC and BC) may be quantified by the absorption Ångström exponent (AAE), which depends on the combustion source and is used for source characterization.

The California Air Resources Board (CARB) produced an inventory of BC emissions for California in 2013 as part of the Greenhouse Gas (GHG) Short-Lived Climate Pollutant Inventory (see **Figure 6.1**). The inventory in **Figure 6.1** does not include forestry sources of black carbon, namely non-agricultural prescribed burns, and wildfire BC emissions. CARB notes that these sources of BC are highly variable year-to-year and future projections are highly uncertain, due to the increased frequency, intensity, and nonlinear response of wildfire behavior to global climate change. CARB instead provides emissions estimates of BC from prescribed burns and wildfires on a ten-year averaged basis, as listed in **Table 6.1**. Both **Figure 6.1** and **Table 6.1** report BC in units of million metric tons of carbon dioxide equivalent 20-year global warming potential ($MMTCO_2e$ 20-year GWP).

Table 6.1 Ten-year average BC emissions inventory for forestry sources in California.

Source	MMTCO2e (20-year)
Prescribed burning	3.6
Wildfires	86.7

Source: https://ww2.arb.ca.gov/ghg-slcp-inventory

In the CARB forestry BC emissions inventory presented in **Table 6.1**, BC emissions from prescribed burns and wildland fires were quantified with the First-Order Fire Effects Model (FOFEM (Keane and Lutes, 2018)). This model takes inputs of geographic region, fuel types, soil texture and moisture, and other general burning conditions (i.e., flaming and smoldering combustion) and outputs fuel consumption and emissions of air pollutants: CO, CO_2, CH_4, SO_2, NO_x, $PM_{2.5}$, and PM_{10}. To estimate BC, a BC/$PM_{2.5}$ ratio was applied to the total $PM_{2.5}$ emitted, as calculated from fire activity and fuels data. BC emission factors from wildland fires remain

uncertain due to their dependence on fuel type, geographic region, combustion conditions and fuel moisture. The portion of BC in open burning emitted $PM_{2.5}$ varies by two orders of magnitude, with reported $BC/PM_{2.5}$ emission factor ratios between 0.8 - 80%. The CARB BC Emissions Inventory Technical Support Document notes that their methodology uses data and assumptions with high uncertainty due to large variability in $BC/PM_{2.5}$ ratios and a lack of sources tests and field measurements of wildfire smoke emitted from California-specific fuels. This methodology results in a forestry BC emissions inventory that may vary by an order of magnitude depending on what $BC/PM_{2.5}$ ratio was assumed.

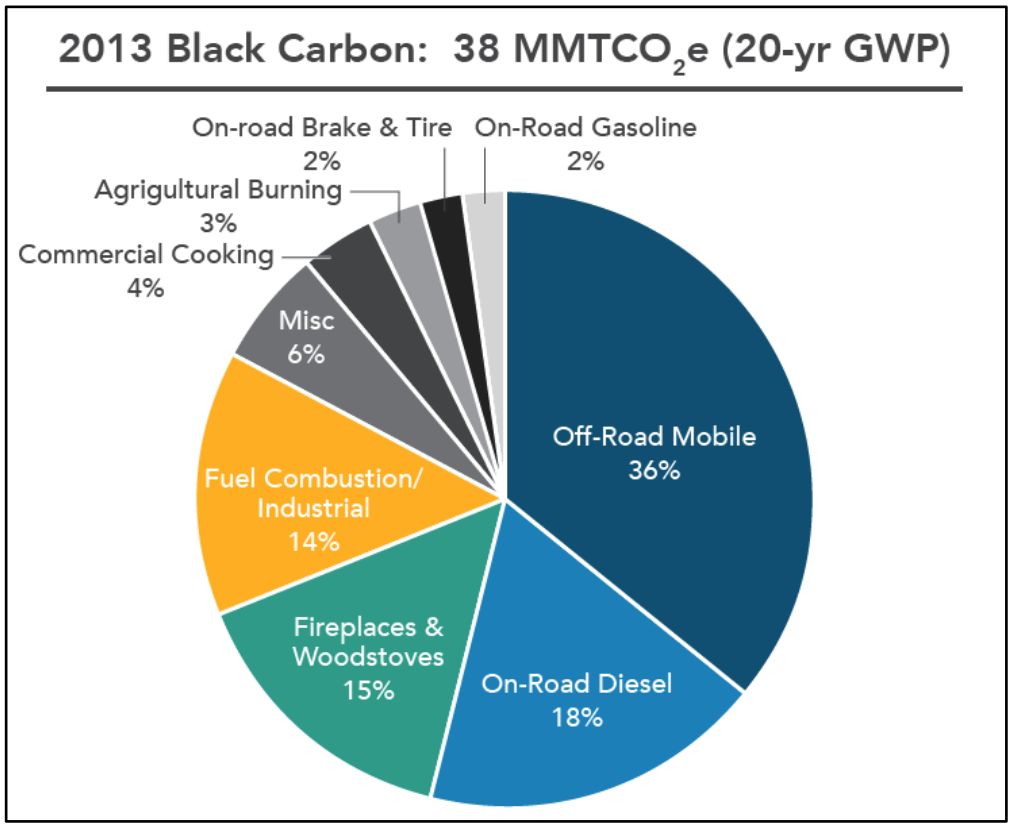

Figure 6.1 Pie chart of CARB 2013 Black Carbon emissions inventory excluding forestry sources. Source: https://ww2.arb.ca.gov/ghg-slcp-inventory

This work aims to constrain California's BC emissions inventory by measuring BC emission factors (EFs) at prescribed burns conducted in a typical California forest ecosystem and calculating BC EFs and $BC/PM_{2.5}$ emissions ratios from data obtained from regulatory stations and a low-cost BC sensor network during wildfire smoke events. These BC emission factors and $BC/PM_{2.5}$ emissions ratios improve the speciation profile for prescribed burn and wildfire smoke in California and may be employed in future FOFEM estimates of total BC emissions.

6.2. Methods

Data collection and sources

BC emission factors, pollutant ratios, and optical properties were determined by analysis of BC, CO, CO_2, and $PM_{2.5}$ data from two types of data sources: (1) field measurements made during this study to characterize smoke produced from the prescribed burning events, and (2) a combination of distributed sensor networks and publicly available local and federal air quality databases to characterize transported smoke during recent large wildfires in California.

Field measurements were conducted at the Blodgett Forest Research Station during four days of prescribed burns. BC was measured alongside CO and CO_2 on the ground and aerial platforms. BC was measured with a pre-commercial, custom-built Aerosol Black Carbon detector (ABCD, (Caubel et al., 2018)) and the Magee Scientific AE33 multi-wavelength dual-spot aethalometer (AE33). Both an AE33 and ABCD were deployed on the ground platform and a second ABCD was deployed on the aerial platform. CO was measured with a Horiba APMA370 and CO_2 with a Horiba APCA370 (see Chapter 3, *Ground Platform* for a detailed description of the gas analyzers). All analyzers measured their respective pollutants at a 1 Hz (secondly) time basis.

Distributed networks included the Richmond Air Monitoring Network (RAMN)—part of the CARB-funded Community Air Grants Program under Assembly Bill 617—and the Berkeley Environmental Air-Quality and CO_2 Network (BEACO2N, (Shusterman et al., 2018)), located in Richmond and Oakland, CA. BC and $PM_{2.5}$ were measured in Richmond at 22 locations with co-located ABCDs and Aeroqual AQY1 Micro Air Quality Monitoring System sensors for four weeks in 2020 (12 August–4 September). During this measurement window, a wildfire smoke plume was observed during the time windows listed in **Table 6.2**, with smoke originating primarily from the August Complex, CZU Lightning Complex, LNU Lightning Complex, and SCU Complex Fires that began on 16–17 August 2020. CO and CO_2 were separately measured at seven BEACO2N locations in Richmond and three sites in Oakland, and data were obtained from an API download script provided by the Cohen Research Group at UC Berkeley for the period of 2018–2020. CO_2 concentrations are not measured at government regulatory sites in California and the availability of CO_2 concentrations measured by the BEACO2N network offered an opportunity to estimate BC emission factors during extreme wildfire events that transported smoke to the Bay Area.

Table 6.2 Observed wildfire smoke events during Summer 2020 Richmond AB 617 Community Air Monitoring campaign

Wildfire Smoke Event	Start Time and Date	End Time and Date
1	00:00 19 August 2020	18:00 22 August 2020
2	06:00 23 August 2020	16:00 25 August 2020
3	19:00 27 August 2020	21:00 01 September 2020

BC, CO, and $PM_{2.5}$ data from regulatory sites were obtained through the US Environmental Protection Agency (US EPA) Air Quality System (AQS) API for all sites in California during 2018–2020. BC data reported to the AQS does not include multi-wavelength absorption data, like the raw data retrievable from the AE33 deployed at the prescribed burn, or any BC sites in the South Coast air basin. Raw multi-wavelength absorption data were acquired by collaboration with Bay Area Air Quality Management District (BAAQMD) staff and a public records request to the South Coast Air Management District (SCAQMD) for 2018–2020. Maps of the distributed networks sites and regulatory sites in the BAAQMD and SCAQMD jurisdictions are provided in **Figures 6.2** and **6.3**.

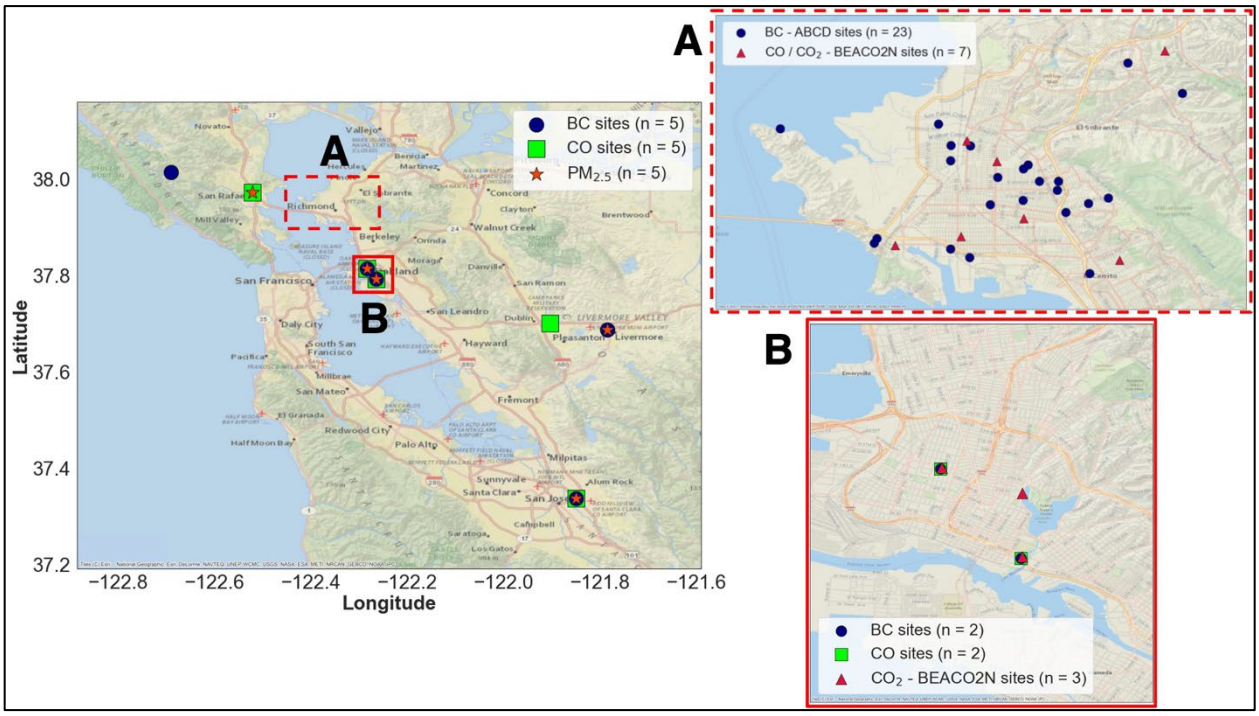

Figure 6.2 Locations of regulatory and distributed network BC, CO, CO_2, and $PM_{2.5}$ sites in the San Francisco Bay Area. Insets A and B depict the sites where BC emission factors were calculated. Inset A shows the Richmond Air Monitoring Network (RAMN; blue circles) and paired BEACO2N CO and CO_2 nodes (red triangles). Inset B plots the BAAQMD-operated West Oakland and Laney College BC and CO monitoring locations (blue circle and green rectangles, respectively) along with the BEACO2N CO_2 nodes (red triangles).

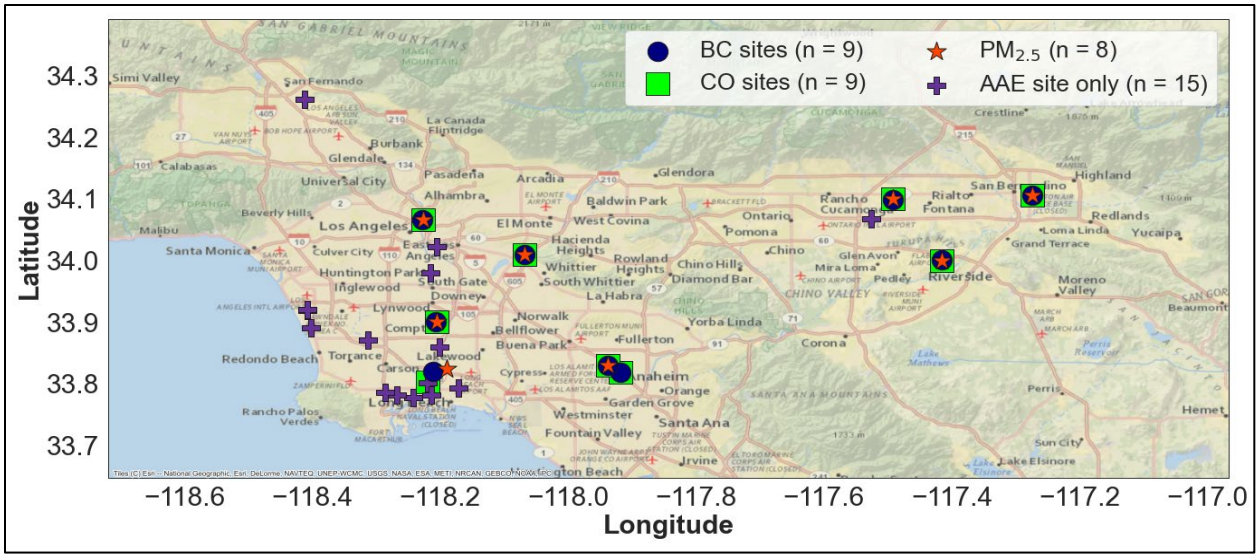

Figure 6.3 SCAQMD BC, CO, and $PM_{2.5}$ monitoring locations in the South Coast Air Basin and Greater Los Angeles Metropolitan Area. Data from BC, CO, and $PM_{2.5}$ sites denoted as blue circles, green triangles, and orange stars, respectively, were used to calculate BC/$PM_{2.5}$ ratios and ΔBC/ΔCO enhancement ratios. BC sites denoted by purple crosses were not within a distance threshold of a $PM_{2.5}$ and CO monitor and were only included in the AAE analysis (see text for explanation).

Pollutant peak matching

Rather than relying on instrument clocks on the ground platform BC and gas analyzers, which may drift at different rates, the 1-Hz datasets from each pollutant analyzer were time-aligned with a post-processing script that calculated the Pearson correlation, *r,* of the four days of measurement. CO_2 timestamps were chosen as the reference time basis, given its relative importance to calculate a fuel-based emission factor—CO_2 carbon typically accounts for 80% of the fuel carbon in the carbon balance. This peak matching analysis assumed when a puff of smoke passed the ground platform sampling inlets, all pollutant analyzers should record a peak at approximately the same time. For CO, AE33 BC, and ABCD BC, the script altered the datasets timestamp in one second increments between –120 seconds to +120 seconds and calculated the Pearson correlation *r* of the matched datasets with altered timestamps to the CO_2 with unaltered timestamps. The results of this analysis are presented in **Figure 6.4** below. Timestamp offset adjustments of –2, +51, and +54 seconds yielded the best correlations and were applied to the CO, BC AE33, and BC ABCD datasets, respectively, to best align each of them to the CO_2 timestamp and subsequently compute emission factors and other pollutant ratios.

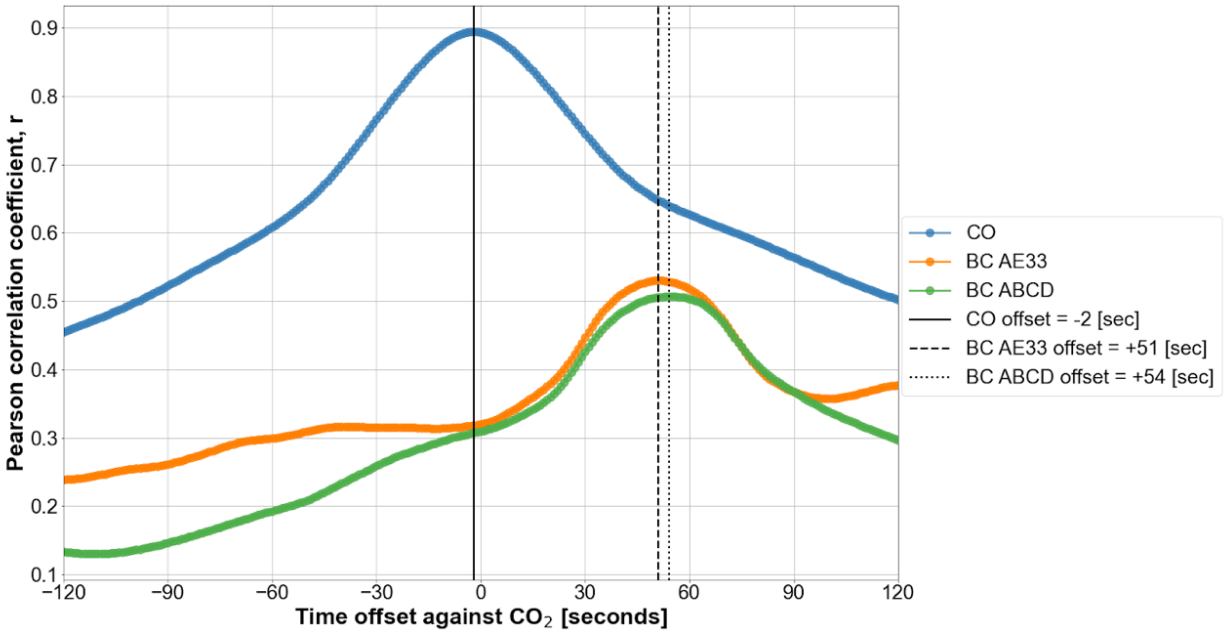

Figure 6.4 Pearson correlation coefficients of CO (blue), BC AE33 (orange), and BC ABCD (green) matched datasets to CO_2 dataset. Vertical lines mark the maximum Pearson correlation coefficient at –2, +51, and +54 seconds for CO, BC AE33, and BC ABCD, respectively.

Measurement principles and Artifact Adjustment Parameter (AAP) of BC data

Co-location of the AE33 and ABCD BC monitors on the ground platform allowed the research team to calculate the ABCD's loading artifact adjustment parameter for the biomass burning aerosols measured in this study. Aethalometers measure changes in light attenuation (ΔATN) of deposited carbonaceous aerosols and calculate the corresponding concentration of carbonaceous aerosol proportional to the ΔATN, given a wavelength-dependent mass absorption cross-section (**Table 6.3**). The AE33 multi-wavelength aethalometer measures ΔATN at seven wavelengths from the UV to near-infrared (IR) listed in **Table 6.3**, which allows the instrument to characterize the spectral dependence of light absorption by the aerosols and may be employed for source apportionment.

The aethalometer response to each marginal carbonaceous aerosol deposited on its filter becomes less sensitive and decreases because of a loading (or sampling) artifact of previously deposited aerosols (Kirchstetter and Novakov, 2007). As the ATN increases, the loading artifact causes the ΔATN associated with each equal marginal deposition of aerosols to decrease and results in an underestimation of the carbonaceous aerosol concentration. A loading artifact correction algorithm must be applied to BC concentration data, either in real-time or in post-processing. Different carbonaceous aerosols, like from fossil fuel combustion or biomass burning, result in different loading artifacts and require compensation schemes to be source or airshed specific.

Table 6.3 Measured wavelengths of light attenuation (ATN) and mass absorption cross-sections for the Magee Scientific AE33.

Channel	Measurement wavelength [nm]	Mass absorption cross-section, σ_{air} [m^2/g]
1 - Ultraviolet particulate matter (UVPM)	370	18.47
2	470	14.54
3	520	13.14
4	590	11.58
5	660	10.35
6 - Black carbon	880	7.77
7	950	7.19

The AE33 employs a real-time DualSpot™ method, which deposits sampled aerosols on two spots at different flow rates, whereby the spot with the higher flow rate loads and the ATN increases more quickly than on lower flow rate spot. In this study, the AE33 was operated at Q_{high}= 3.5 L min^{-1} and Q_{low} = 1.5 L min^{-1}. Since both spots sample the same concentration and composition of aerosols, the reported BC concentration calculated for both the high-flow and low-flow spots should be equal (i.e., $BC_{high} = BC_{low}$). Instead, as the filter loads, high-flow spot attenuation signal response (ATN_{high}) becomes less sensitive than the low-flow spot attenuation signal response (ATN_{low}) such that $BC_{high} < BC_{low}$ and $BC_{high} \neq BC_{low}$. The AE33 compensates for the loading artifact by calculating a compensation parameter k_λ at each wavelength:

$$BC_{high} = BC_{comp}\left(1 - k_\lambda \cdot ATN_{high}\right) \quad [6.1]$$

$$BC_{low} = BC_{comp}(1 - k_\lambda \cdot ATN_{low}) \quad [6.2]$$

where BC_{high}, BC_{low}, ATN_{high}, ATN_{low} are known and reported by the instrument and k_λ is the wavelength-specific compensation parameter. To find k_λ, equations [6.1] and [6.2] are rearranged to equal the compensated BC concentration BC_{comp}, set equal and k_λ is isolated, resulting in equation [6.3]:

$$k_\lambda = \frac{BC_{low} - BC_{high}}{ATN_{high} \cdot BC_{low} - ATN_{low} \cdot BC_{high}} \quad [6.3]$$

The compensation parameter k_λ is reported at the same time basis as the instrument operation.

The ABCD does not employ a real-time correction scheme and BC data must be corrected in post-processing data quality assurance/quality control (QA/QC). Previous studies have used the Kirchstetter loading artifact correction (Jimenez et al., 2007), presented as equation [6.4]:

$$BC_{comp} = \frac{BC_{raw}}{a * \exp\left(-\frac{ATN}{100}\right) + (1 - a)} \quad [6.4]$$

where BC_{raw} is the raw BC concentration reported by the ABCD, ATN is instantaneous light attenuation, and a is the artifact adjustment parameter (AAP) applied to calculate the compensated BC concentration BC_{comp}. Previous studies determined an appropriate AAP by operating two ABCDs at different flow rates, like the AE33 compensation scheme. However, in this work, only one ABCD was deployed on each sampling platform. Co-location of the AE33 and ABCD BC monitors on the ground platform allowed the research team to calculate the ABCD's loading artifact adjustment parameter for the biomass burning aerosols measured in this study.

The AAP was determined by applying an ordinary least squares (OLS) linear regression of compensated AE33 BC data against uncompensated ABCD BC concentration data. ABCD BC data was averaged from secondly to minute-averaged data to reduce instrument noise but maintain temporal resolution of the smoke emissions profile. Both ABCD and AE33 BC data were filtered to exclude BC measurements above 100 µg m^{-3} and below the minute-averaged mean absolute error (MAE) during background measurements, when the BC concentration should have been near-zero. The background BC concentration was likely non-zero, with possible sources of BC including a gasoline generator located ~25 ft from the ground platform, residual smoke from previous days burning, and passing vehicles. Background measurements were collected before the start of the third and fourth days of the prescribed burn for around 45 minutes total. The linear regression upper threshold of 100 µg m^{-3} excluded 5% and 6% of ABCD and AE33 BC minute-averaged measurements for all four days of sampling. The MAE of the ABCD and AE33 on a minute-averaged basis were 0.4 and 0.1 µg m^{-3}, with mean minute-averaged concentrations of 0.3 and 0.08 µg m^{-3}, respectively.

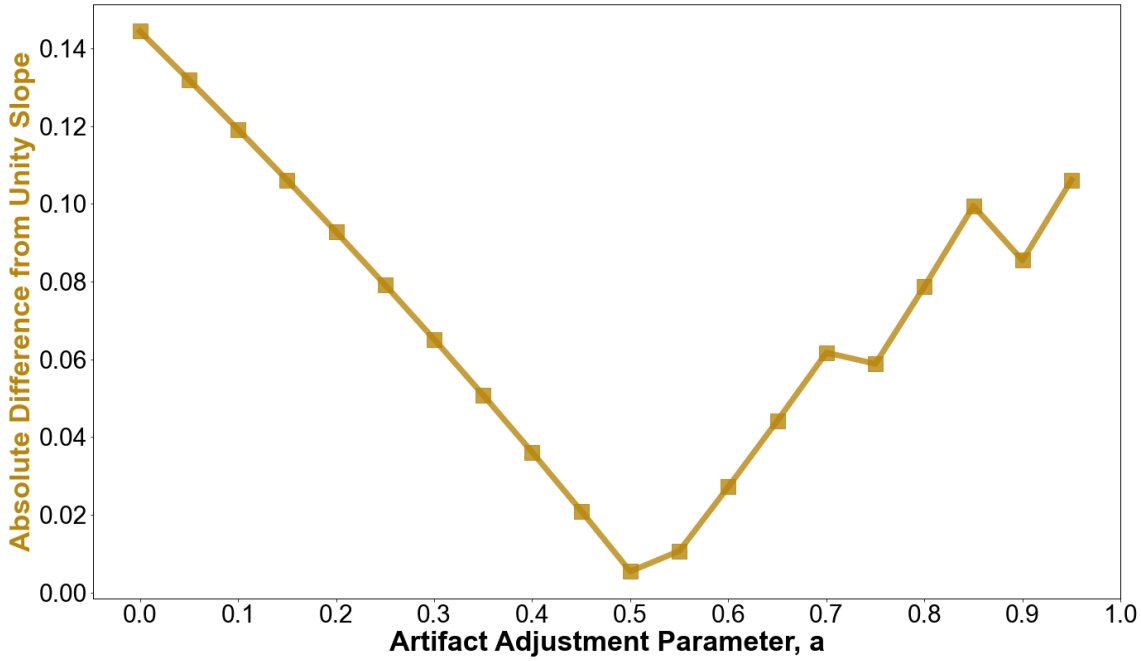

Figure 6.5 Absolute difference of ordinary least squares (OLS) linear regression of minute-averaged AE33 and ABCD BC measurements from unity slope for artifact adjustment parameters (AAP).

To determine the appropriate AAP, we compensated the ABCD BC data with a range of AAPs between 0 (uncompensated) to 1 in 0.05 increments with Equation 6.4 and identified the AAP where the slope of the OLS linear regression matched a one-to-one line. For each AAP, the absolute difference of the linear regression slope and unity slope are plotted in **Figure 6.5** above. For all AAPs, the coefficient of determination was $0.82 < r^2 < 0.85$. The slope of the OLS linear regression with $a = 0.5$ was $m_{comp} = 0.99$, near unity. This value of a was applied to the BC data from the ground and aerial platforms and compared to the un, as shown in **Figure 6.6**. The uncompensated slope with a = 0 was $m_{uncomp} = 0.87$. A slope less than unity indicated that the ABCD generally underestimated the BC concentration measured by the AE33. This result was consistent with the measurement principle of filter-based photometers, with the uncompensated instrument underestimating the aerosol concentration due to a measurement artifact.

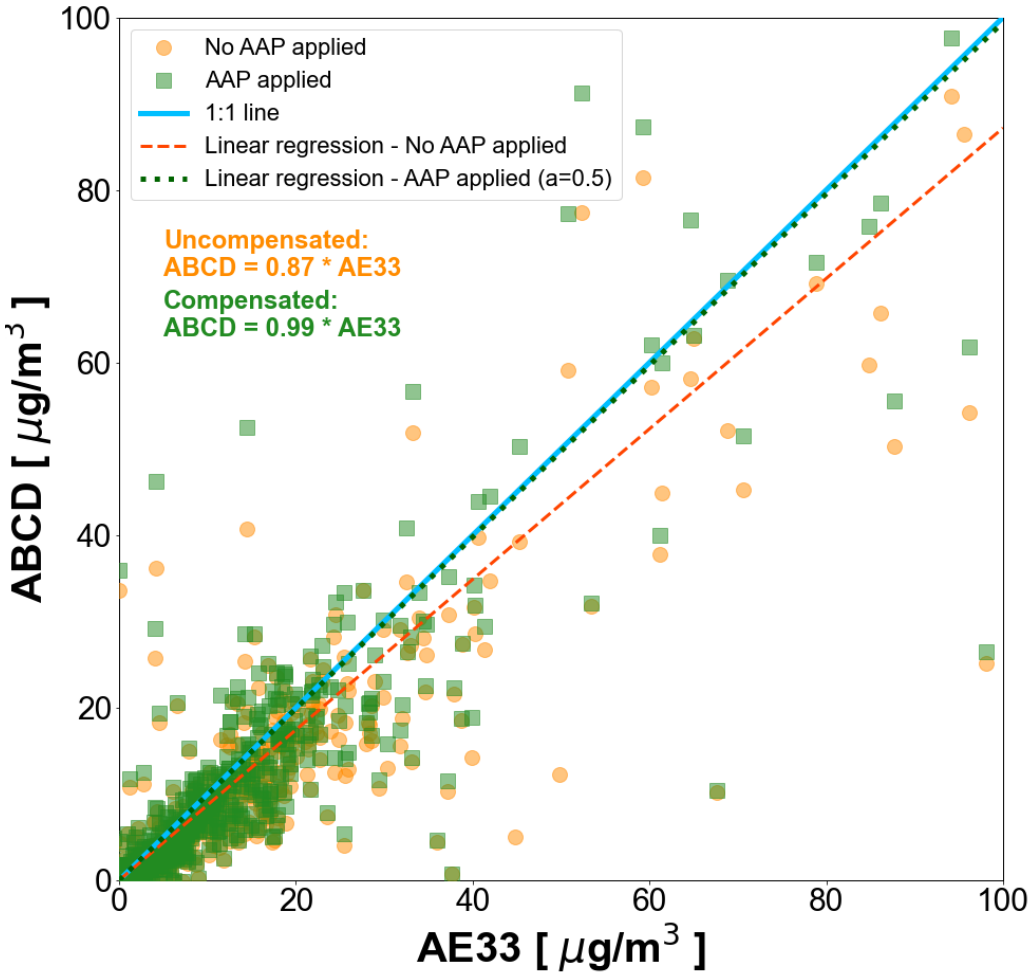

Figure 6.6 Ordinary least squares (OLS) linear regression of minute-averaged AE33 and compensated minute-averaged ABCD BC data with an artifact adjustment parameter (AAP) of a = 0.5.

Brown Carbon (BrC) concentration calculation

The concentration of BrC, or the light absorbing portion of organic aerosol, was calculated for the ground platform AE33 by equation [6.5] below:

$$BrC = UVPM - BC \qquad [6.5]$$

where BC was the reported BC concentration and UVPM was the reported BC concentration at = 370 [nm] (**Table 6.3**). We assumed a wavelength dependence characterized by AAE = 1 for BC and attributed absorption at λ = 370 nm above the BC concentration at λ = 880 nm to be BrC.

BC emission factor, BC/CO enhancement ratio and BC/$PM_{2.5}$ ratio calculation

At the prescribed burn, ground BC and BrC EFs were calculated by integrations of 1 Hz pollutant traces for the 30-minute sampling periods that align with the VOC samples presented in Chapter 4 (n = 34). Three 30-minute sampling periods were dropped due to a lack of observed capture at the ground station when smoke was transported vertically and/or away from the sampling inlet. Aerial BC EFs were calculated for each drone flight that lasted between 4–15 minutes (n = 30). Fuel-based emission factors were calculated by carbon balance:

$$EF_{BC} = \frac{\Delta BC * w_c}{(\Delta CO + \Delta CO_2) * MW_C} \qquad [6.6]$$

where ΔBC is the excess BC above background concentration, w_c = 0.5 is the weight-fraction of carbon in the biomass fuel (ref), ΔCO is the excess CO above background concentration, ΔCO_2 is the excess CO_2 above background concentration, and MW_C = 12 g mol^{-1} is the molar mass of carbon. For the prescribed burn emission factors, the background BC concentration was assumed to be 0 μg m^{-3}. For BC EFs calculated from ambient data from the distributed network and regulatory sites, excess BC above an ambient background concentration was calculated on an hourly, hour-of-day (HoD) basis. The background BC for wildfire smoke emission factors determined from RAMN and regulatory sites are discussed in subsequent sections.

CO_2 concentrations are not reported in the AQS database in California. BEACO2N CO_2 nodes deployed in the SF Bay Area air basin during 2018–2020, therefore, present a unique opportunity to calculate fuel-based BC emission factors when wildfire smoke was transported to the region. Unfortunately, BC emission factors could not be calculated for wildfire smoke events in the South Coast Air Basin because of the unavailability of CO_2 data.

BC/CO enhancement ratios (ΔBC/ΔCO) were calculated and compared for the prescribed burn events and during periods when wildfire smoke was very present in the SF Bay Area and South Coast air basins to provide a comparison of the relative emission rates of BC and CO in prescribed burns and wildfires. The BC/CO enhancement ratio is defined by Equation 6.7:

$$r_{BC/CO} = \frac{\Delta BC}{\Delta CO} = \frac{BC_{wf} - BC_{bkg2019}}{CO_{wf} - CO_{bkg2019}} \qquad [6.7]$$

where BC_{wf} was the hourly BC measured at a regulatory site during a wildfire smoke event, $BC_{bkg2019}$ was the background HoD BC concentration during calendar year (CY) 2019, CO_{wf} was the hourly CO measured at a regulatory site during a wildfire smoke event, and $CO_{bkg2019}$ was the background HoD CO concentration during CY2019 when, absent of wildfires, the background BC and CO concentrations were assumed to be zero.

$BC/PM_{2.5}$ ratios were determined where BC and $PM_{2.5}$ measurements were co-located in both the SF Bay Area and South Coast Air Basins. As noted above, this ratio has implications for use in a FOFEM to better estimate statewide BC emissions. The $BC/PM_{2.5}$ ratio was computed as:

$$r_{BC/PM_{2.5}} = \frac{BC}{PM_{2.5}} \qquad [6.8]$$

where BC was the hourly BC measurement from a regulatory site or RAMN ABCD node and $PM_{2.5}$ was the hourly fine particulate matter measurement from a co-located $PM_{2.5}$ regulatory site or RAMN Aeroqual node, respectively. It is worth noting that BC and $PM_{2.5}$ are not conserved during transport, and secondary formation may increase levels of $PM_{2.5}$ as plumes are transported to the regulatory sites. While quantitative adjustment of this ratio to account for dilution and formation of secondary $PM_{2.5}$ would require further investigation and modeling, directionally the adjustment would further support the use of these $BC/PM_{2.5}$ ratios over default FOFEM values.

Absorption Ångström Exponent calculation

Measurement of carbonaceous aerosols with a multi-wavelength aethalometer provides the spectrally dependent absorption of light for an aerosol sample, or a spectral absorption curve. A log transformation of the spectral absorption curve may be linearly regressed against the measured wavelengths to calculate the absorption Ångström exponent (AAE), or the slope of the log-transformed OLS linear fit. The AAE is commonly reported in literature to provide source characterization of carbonaceous aerosols, usually between fossil fuel where BC is the dominant light absorbing species (AAE ~1) and biomass burning combustion that includes a significant amount of BrC in addition to BC (AAE > 2). The AAE as defined by Liu et al. (Liu et al., 2018) is:

$$b_{abs}(\lambda) = \lambda^{-AAE} \qquad [6.9]$$

where the AAE is a power-law fit of the aerosol absorption $b_{abs}(\lambda)$ against the measured wavelength λ. If equation [6.9] above is log-transformed the AAE may be determined by a linear regression:

$$\ln\left(b_{abs}(\lambda)\right) = -AAE \ln(\lambda) \quad [6.10]$$

where the AAE is the slope of the linear regression. In Equation 10, the spectral absorption $b_{abs}(\lambda)$ is approximated by the spectral attenuation, $ATN(\lambda)$, measured by the AE33. In this work, the aerosol spectral attenuation and measured wavelength of the AE33 (refer to **Table 6.3**) were log-transformed and regressed against each other with an ordinary least squares (OLS) linear

regression function in the *scipy* library in Python. For the prescribed burn data, the OLS linear regression was applied on a 1 Hz basis and for the regulatory data at highest temporal resolution present in the dataset. AAEs were then averaged to minutely and hourly for the prescribed burn and regulatory sites, respectively.

Wildfire smoke hours identification for regulatory site analyses

During periods of extreme wildfires when smoke was transported around much of the state, measured $PM_{2.5}$, BC, and CO concentrations at regulatory sites were generally well above the typical concentration of these pollutants. To determine the hours when a regulatory site was wildfire-smoke impacted, a 50 μg m^{-3} threshold was applied to all the $PM_{2.5}$ data in 2018, 2019, and 2020. This technique is based the work presented in Chapter 8 in which a daily 35 μg m^{-3} was applied to low-cost $PM_{2.5}$ sensors to identify wildfire smoke impacted time periods. The hourly threshold was applied to SF Bay Area and South Coast datasets separately to produce two lists of smoke impacted hours (e.g., 13:00:00 10 September 2020) for each region.

While high hourly $PM_{2.5}$ tends to be associated with wildfire smoke events, some hours above the threshold were likely due episodic high-PM emission events (e.g., fireworks), inversions in coastal air basins, high formation of secondary $PM_{2.5}$, etc. To ensure the hours identified were during wildfire smoke events, any day with the hour above the hourly threshold was verified with NOAA Satellite Smoke Product (SSP), a satellite product in which NOAA scientists note any smoke or dust visible from geostationary satellites (i.e., GOES-WEST) over the continental US. For each day with a possible smoke hour, the NOAA SSP was checked to see if it included any mention of wildfire smoke over California or the Western United States. If the text narrative included such a description, the smoke hour was included in the analysis; otherwise, the possible smoke hour was dropped from the list.

For the South Coast Air Basin AQS data, wildfire smoke data qualifiers were also used to identify the hours when sites were impacted by wildfire smoke. When AQMDs report pollutant concentrations to the AQS, air quality regulators sometimes include a data flag of *IT – Wildfire US* or *RT – Wildfire US.* The first qualifier, *IT – Wildfire US,* is for informational purposes only. The second qualifier, *RT – Wildfire US,* indicates that for a criteria air pollutant like $PM_{2.5}$ or CO, the AQMD would like to request an exclusion of this hourly measurement from NAAQS attainment calculations. These wildfire qualifiers were not provided for all 24 BC sites used in the $BC/PM_{2.5}$ ratio, $\Delta BC/\Delta CO$ ratio, and AAE analyses, but for any datetime when a site contained a wildfire qualifier it was assumed that all sites were wildfire smoke impacted. This second wildfire smoke identification method provided a useful comparison to the 50 μg m^{-3} threshold discussed above.

Background concentration for regulatory BC EFs and BC/CO enhancement ratios

For each regulatory and distributed network site, a background concentration of BC, CO, and CO_2 was determined for each wildfire smoke hour. The background pollutant concentrations could not be assumed to be zero like at the prescribed burn since the pollutant monitors shown in **Figures 6.3** and **6.4** were deployed to measure regional sources of pollution in the SF Bay Area and South Coast Air Basins. For example, many of the BC monitors shown in **Figure 6.4** are located near the Ports of Los Angeles and Long Beach to measure port and diesel truck emissions. The concentration of these air pollutants also varies by season and due to varying meteorology.

Concentration data from CY2019 was used to calculate site-specific BC, CO, and CO_2 background concentrations since no wildfire hours were identified in CY2019 by the 50 $\mu g\ m^{-3}$ criteria defined in the previous section. For the regulatory BC EFs determined at the West Oakland and Laney College sites (**Figure 6.2B**), the three BEACO2N CO_2 nodes were averaged to provide better temporal coverage during the 2019 background and 2018/2020 wildfire smoke years. The BC HoD background concentrations were derived from a window of 31 days of observations in 2019 and the BC/CO enhancement ratios from a window 9 days of observations in 2019, both centered on the day of the year in the 2018/2020 wildfire years. For example, for the wildfire hour *13:00 10 September 2020*, the BC EF HoD background concentration was calculated as the mean concentration at 13:00 for the 15 days before and after 10 September 2019. Similarly, the BC/CO enhancement ratio background concentration for this wildfire hour would be the mean concentration at 13:00 for the 4 days before and after 10 September 2019.

This method accounts for the diurnal and season variation in pollutant concentrations due to activity patterns and meteorology by calculating the background at the same HoD and during the same time of year during the 2019 background year. For the BC EFs, most of the 2019 background year a full 31 days of HoD measurements were not available as presented in **Figure 6.7**. For most wildfire smoke hour background concentrations at least 5 days of HoD observations were available and the pollutant enhancement was not biased by the number of available observations. Enhancements less than zero were dropped from the EF and BC/CO enhancement analyses.

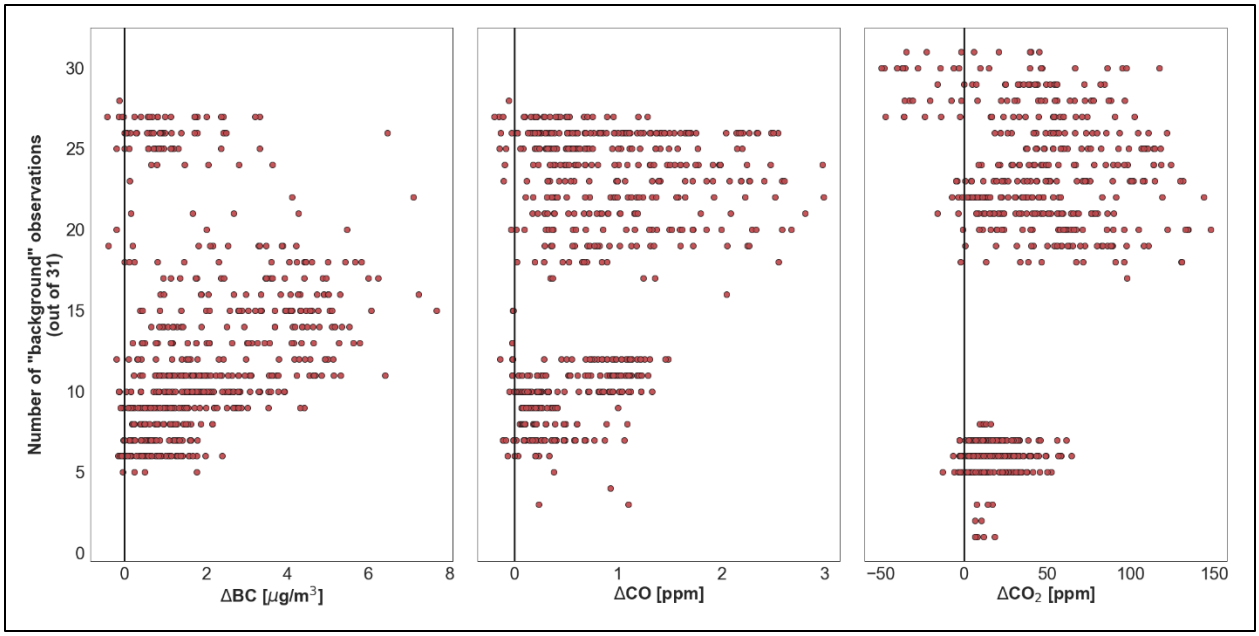

Figure 6.7 Number of HoD observations used to calculate the wildfire hour background concentration against the enhancement of BC, CO and CO_2.

For the RAMN BC EFs, each ABCD was paired with the nearest BEACO2N CO/CO_2 node (**Figure 6.2A**). The ABCDs in the RAMN were deployed only in 2020 (12 August–4 September). As such, a 2019 HoD background concentration could not be established. Instead, the background BC concentration was calculated as the average of all hourly BC measurements before the first wildfire smoke event (see **Table 6.1**) from 00:00 12 August 2020 to 00:00 19 August 2020, highlighted in blue in the top panel of **Figure 6.8**. For CO and CO_2, the background concentration was calculated from 29 July–12 August 2020, also highlighted in blue in middle and bottom panels of **Figure 6.8**. The CO and CO_2 background periods were set before the BC background period due to the drift of these signals, as seen in the CO_2 timeseries in the bottom panel of **Figure 6.8**. This time offset ensures a steady baseline concentration was established before pollutant concentration was elevated by the wildfire smoke events. To calculate pollutant enhancements and a BC EF with Equation 6, the background concentrations were subtracted from the 24-hour BC rolling average and 2-week rolling average of CO and CO_2 for each hour during the wildfire smoke periods.

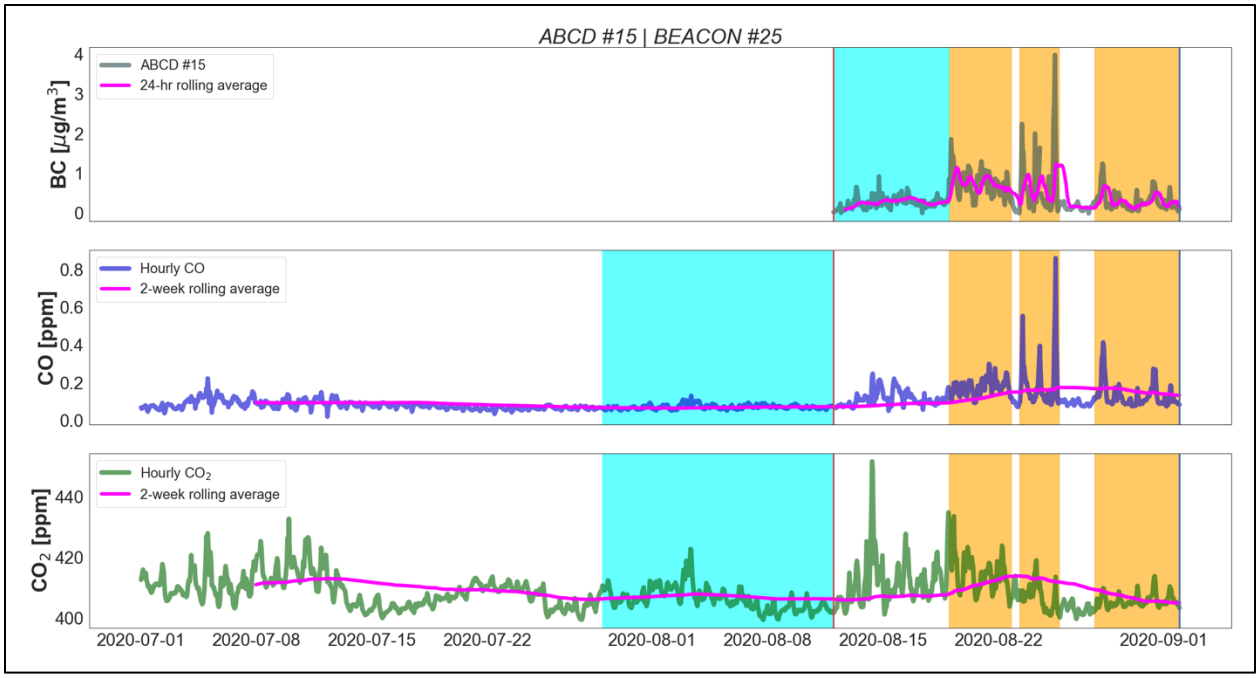

Figure 6.8 Example pairing of ABCD to the nearest BEACO2N node with the hourly concentration of BC, CO and CO_2 plotted from top to bottom, overlayed with the 24-hour rolling average for BC and the 2-week rolling average for CO and CO_2. Background concentration periods for each pollutant highlighted in blue; wildfire smoke hours highlighted in yellow (see **Table 6.1**).

6.3. Results and Discussion

Prescribed burn ground- and aerial-based black carbon (BC) emission factors

Figure 6.9 shows the linear regressions of BC EFs determined at the prescribed burns against calculated MCE. The BC EFs generally increased as the MCE approached unity and the combustion conditions transition from smoldering regime (MCE < 0.9) to flaming regime (MCE > 0.9) with coefficient of determination $r^2 = 0.48$. The modest r^2 value indicates that MCE is a good but not great predictor of the BC EF, as a wide range of BC EFs were measured for a given MCE value. BC EFs averaged ~0.2 g kg^{-1} when MCE was approximately 0.80 and 1.0–1.5 g kg^{-1} when MCE was 0.90 or larger. The ground-based BC EFs were all within the smoldering combustion regime, except for one AE33 ground BC EF, whereas the aerial-based BC EFs spanned both the flaming and smoldering regimes. In general, the aerial-based BC EFs agreed with the ground-based BC EFs within the smoldering regime. Ground-based BC EFs may have been biased towards the smoldering regime due to the sampling platform placement on the edge (i.e., the adjacent roadway) of the prescribed burn unit. While the aerial-based sampling platform could be flown to sample above the flame front moving through the burn unit and continually sample emissions in the flaming regime, the ground platform was relatively stationary. Once the initial flame front burned past the ground platform, most sampled emissions were likely dominated by smoldering combustion.

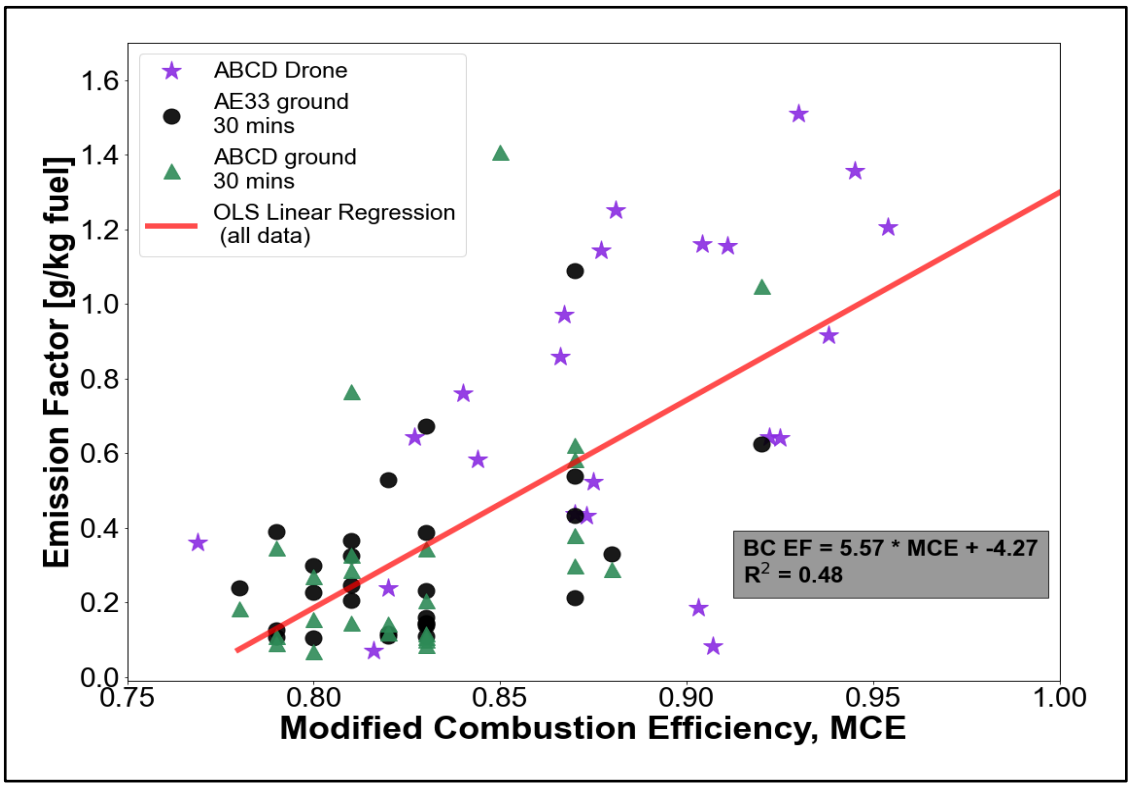

Figure 6.9 Ordinary least squares (OLS) linear regression of prescribed burn BC emission factors against modified combustion efficiency (MCE) for AE33 ground (black circles), ABCD ground (green triangles) and ABCD aerial (purple stars) sampling platforms.

Figure 6.10 compares prescribed burn BC EFs from this study those in another study by Aurell and Gullet (Aurell and Gullett, 2013) that took place in the southeastern US and employed similar sampling techniques. In the Aurell and Gullet study, BC EFs were measured on the ground with an all-terrain vehicle (ATV) platform and on an aerial platform held aloft by an aerostat. The BC EFs for both the ground- and aerial-platforms exceeded 0.8 g kg^{-1} in that study and tended to be in the near-flaming (MCE = 0.9) or flaming combustion regime (MCE > 0.9). By contrast, only 4 of 62 (6%) of the combined AE33 and ABCD ground BC EFs in our study exceeded 0.8 g kg^{-1} or an MCE > 0.9. The aerial EFs corresponding to the highest MCE values during the prescribed burns in the current study were in general agreement with the EFs measured during the southeastern US prescribed burns, which ranged from 0.9–1.4 g kg^{-1}. The absence of low MCEs in the southeastern U.S. study may be due to differences in fuel type and fuel moisture that skew the combustion conditions towards the flaming regime more than the CA prescribed burn.

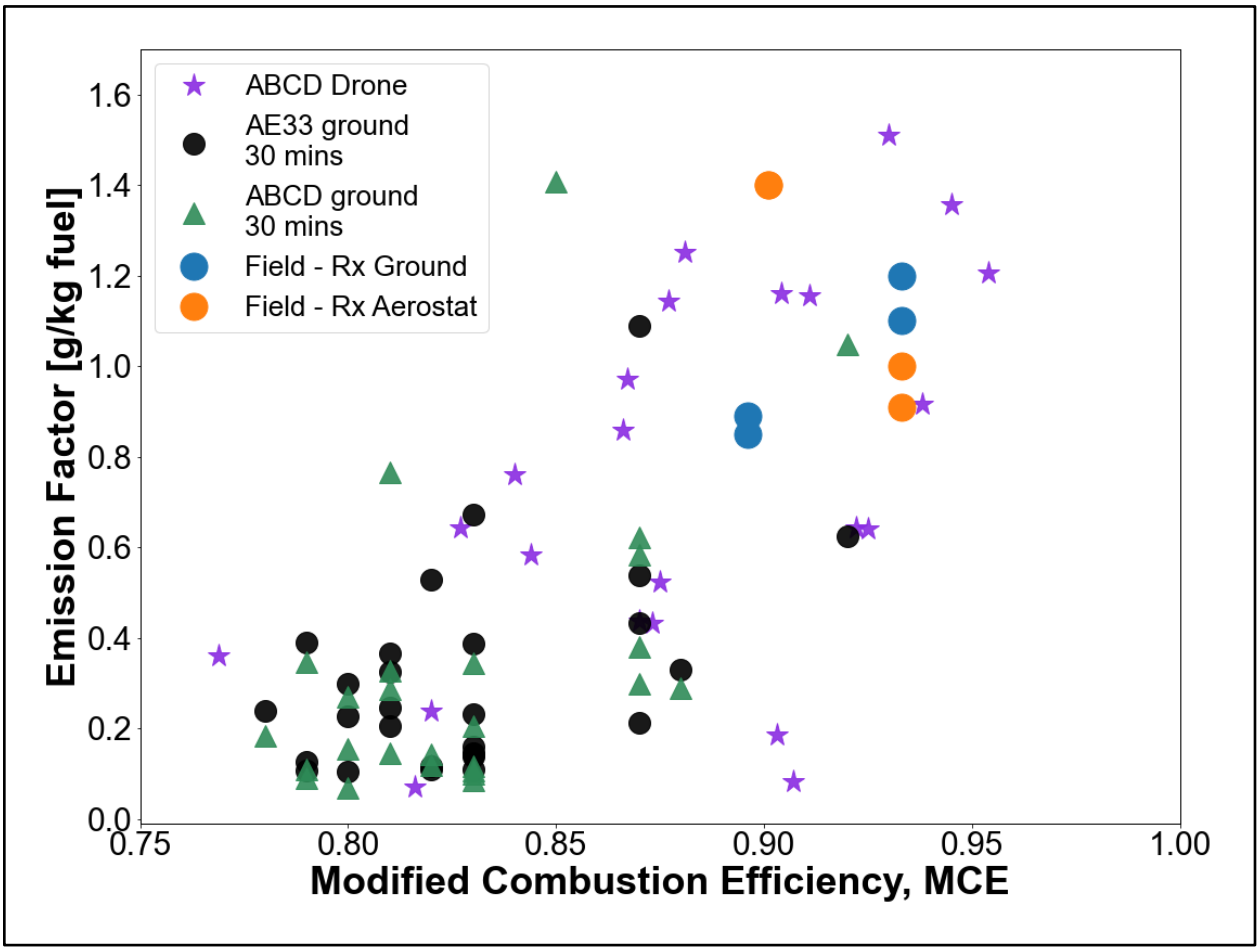

Figure 6.10 Comparison of prescribed burn ground and aerial BC EFs from this study to southeastern US prescribed (Rx) burn BC EFs found by (Aurell and Gullett, 2013), with their ground measurements shown as blue circles and aerial samples as orange circles. BC EFs from this study are the same as **Figure 6.9**, with the AE33 ground sampling platform indicated by black circles, ABCD ground as green triangles, and ABCD aerial as purple stars.

Figure 6.11 compares the prescribed burn BC EFs from this study to those measured during laboratory burning of three western US fuel types: conifer, duff, and shrub. These laboratory EFs were obtained from the Smoke Emissions Reference Application (SERA) database (Prichard et al., 2020). The range of MCEs (~0.80 to 0.95) and BC EFs (0.2–1.5 g kg^{-1}) measured during the laboratory burning of western US fuels were similar to those measured in the current study of prescribed burning in Blodgett Forest. Like the southeast US field study, nearly all the western conifer and shrub fuel types burned in the laboratory were marked by high MCE values that are characteristic of flaming combustion. The lab results for western duff generally agree with both field studies, with comparable MCEs that indicate burning in the smoldering regime and ground-based BC EFs less than ~0.8 g kg^{-1}. This result is consistent with the fuel types and smoke emissions observed during ground platform sampling, with most of the emissions after the initial flame front burned through the unit coming from duff smoldering in the forest understory.

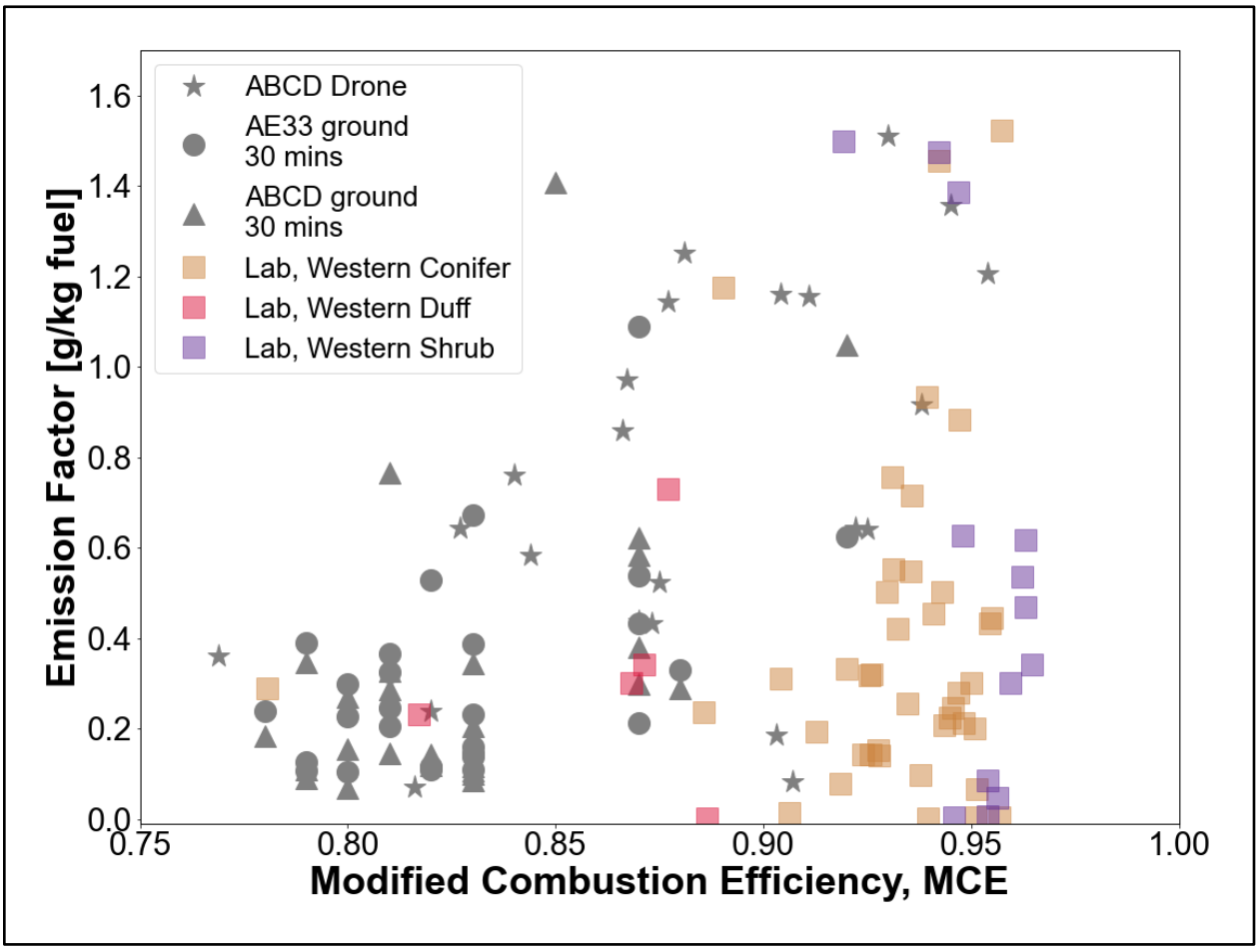

Figure 6.11 Comparison of prescribed burn ground and aerial BC EFs from this study to lab BC EFs of typical western US fuels from the Smoke Emissions Reference Application (SERA) (Prichard et al., 2020). BC EFs from this study are shown in grey with the same symbology from **Figure 6.9**: AE33 ground (circles), ABCD ground (triangles), and ABCD aerial (stars) sampling platforms.

BC emission factors from regulatory sites and distributed networks

BC EFs were calculated at two Oakland regulatory sites (BAAQMD's West Oakland and Laney College) and from the Richmond Air Monitoring Network during the periods identified as being heavily impacted by smoke from a remote extreme wildfire (see **Table 6.1**). Summary statistics are provided in **Table 6.4**. The distributions of BC EFs calculated by measuring the composition of the transported wildfire smoke are shown along with the BC EF distributions measured at the site of the prescribed burns in Blodgett Forest in **Figure 6.12**. Mean wildfire smoke BC EFs at the Oakland regulatory sites and RAMN sites were 0.10 and 0.17 g kg^{-1}, respectively. By contrast, mean prescribed burn EFs were all greater than 0.35 g kg^{-1}. BC emission factors for open burning of savanna and forests were also much higher (~0.5 g kg^{-1}) than those calculated for the transported smoke (Bond et al., 2004).

Table 6.4 Summary statistics of BC EFs calculated from the prescribed burn, Oakland regulatory sites and Richmond Air Monitoring Network (RAMN).

Source	Aethalometer	Time Basis [minutes]	Count	Mean ± Standard Error [g/kg-fuel]	Standard Deviation [g/kg-fuel]
Prescribed burn ground	AE33	30	34	0.46 ± 0.08	0.44
Prescribed burn ground	ABCD	30	28	0.37 ± 0.08	0.40
Prescribed burn aerial	ABCD	4-15 (variable)	23	0.75 ± 0.09	0.41
Oakland regulatory site wildfire smoke	AE33	60	1162	0.10 ± 0.01	0.24
RAMN wildfire smoke	ABCD	60	2392	0.17 ± 0.02	0.98

The lower BC EFs measured during the wildfire event are likely due to: (i) a greater degree of smoldering combustion during the wildfire event, (ii) unequal dilution of BC and CO_2, for example, due to loss of BC during the transport of the smoke to the Bay Area, or (iii) error in calculating BC or CO_2 enhancements. Prescribed burn sampling took place within a few hundred meters of smoke emission with no other significant pollutant sources, whereas transported wildfire smoke sampling occurred many kilometers and days after smoke emission. An order of magnitude estimate of the loss of BC due to dry deposition during transport requires knowing the BC dry deposition velocity, the effective atmospheric mixing height, and the transport time. Prior studies of give an estimate of the BC dry deposition velocity (v_d = 26 m day^{-1} (Emerson et al., 2018)). The transport time and especially the trajectory of the smoke to the Bay Area and the South Coast air basins have not been characterized. Especially uncertain is the effective mixing height of the atmosphere as smoke from the wildfire may have been injected into the stratosphere, where dry deposition losses to the earth's surface would be negligible. Despite major uncertainties, it is illustrative to consider that fractional loss of BC due to a first-order dry deposition process (1-exp(-vdt/H)) is 0.23 for assumed values of transport time (t = 3 days) and atmospheric mixing

height (H = 300 m). Although uncertain, this calculation illustrates that BC deposition may result in an underestimated BC EF and likely needs to be taken into consideration.

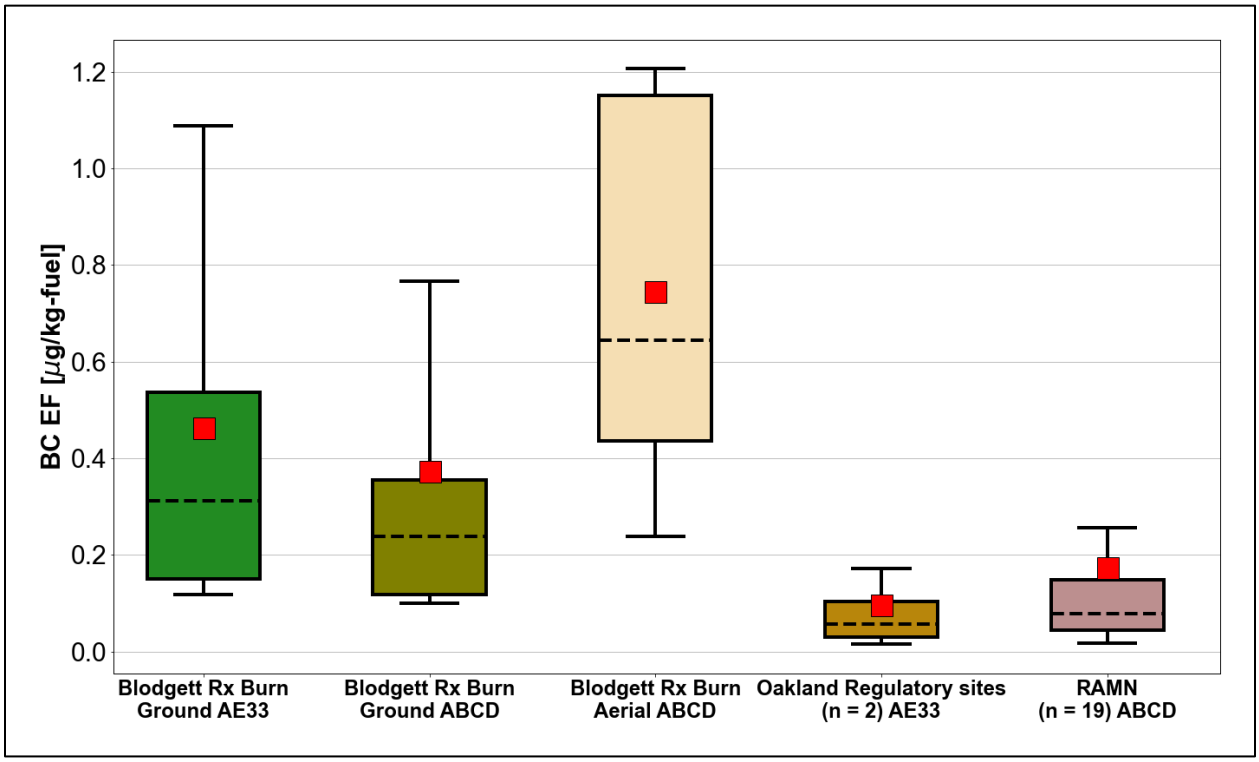

Figure 6.12 Box and whisker plot of BC EFs calculated from the Blodgett prescribed burn, Oakland regulatory sites and Richmond Air Monitoring Network (RAMN). Means presented as red squares, medians as horizontal dashed lines, boxes as the interquartile range and whiskers as 10th and 90th percentiles.

Wildfire smoke sampling also included measurement of other urban sources of BC like industrial and mobile sources. While care was taken to ensure the background concentration from urban sources was subtracted from the wildfire smoke BC, CO, and CO_2 concentrations to calculate an enhancement, this method of exploiting regulatory and distributed networks to derive BC EFs was challenging. The lack of available statewide CO_2 data made it impossible to determine a BC EF for 60% of the SF Bay Area regulatory sites (n = 5) and 100% of the South Coast regulatory sites (n = 24). CO_2 data for RAMN and the Oakland regulatory sites were collected by low-cost sensors which had gaps in temporal coverage from 2018–2020 and required averaging of three CO_2 nodes for the Oakland regulatory BC EFs. Low-cost CO and CO_2 sensors, like those at BEACO2N nodes, also have greater uncertainty than the high-cost CO and CO_2 analyzers on the ground and aerial platforms at the prescribed burn. Uncertainty in the CO_2 enhancement, which accounts for a supermajority of the carbon in the carbon balance in Equation 6.6, may have led to artificially low BC EFs if the wildfire smoke enhancement was artificially high. The co-location of regulatory, high-cost CO and CO_2 instruments with aethalometers would decrease the uncertainty associated with calculating a BC EF by the methods presented in this study by establishing a more temporally

complete CO and CO_2 background concentration and thereby more accurate CO and CO_2 enhancement.

Regulatory network BC/$PM_{2.5}$ ratios during wildfire smoke events and ambient conditions

BC/$PM_{2.5}$ ratios from wildfire smoke were determined for four datasets of co-located sites. For this analysis, sampling sites were considered co-located if they were within 2 km of each other. Box and whisker plots of BC/$PM_{2.5}$ ratios for both wildfire smoke events and ambient conditions are presented in **Figure 6.13** below. The primary objective of establishing a typical wildfire BC/$PM_{2.5}$ ratio was to apply this ratio to an output $PM_{2.5}$ mass emissions estimate of a FOFEM. By applying this ratio, CARB could better estimate a BC mass emissions estimate for wildfires in California (see Introduction).

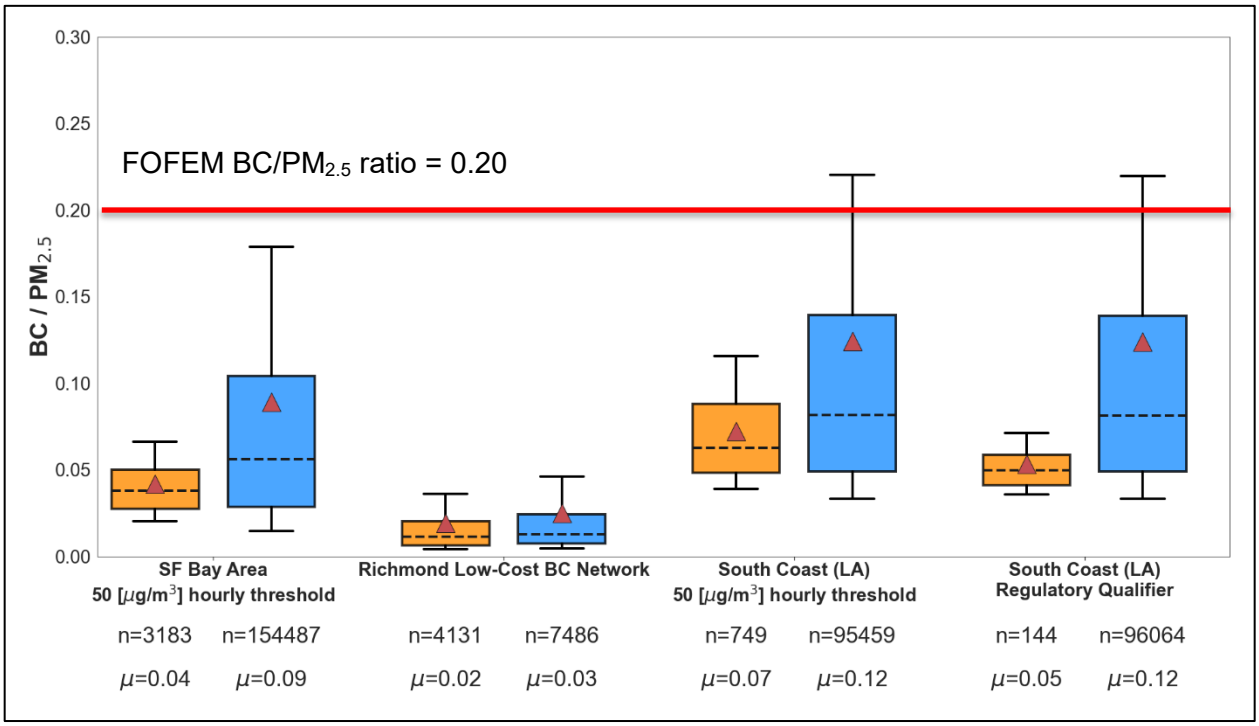

Figure 6.13 BC/$PM_{2.5}$ ratios for the SF Bay Area regulatory sites, RAMN, and South Coast regulatory sites for both wildfire (left, orange) and non-wildfire (right, blue) hours identified by the $PM_{2.5} > 50$ µg m^{-3} and regulatory qualifier methods. The number of paired hourly observations (n) and mean ratios (µ) are reported below each box and whisker plot. Means are shown as red triangles and medians as horizontal dashed lines, and the box and whiskers represent the interquartile range and 10^{th} and 90^{th} percentiles of each distribution.

In all four datasets, the mean BC/$PM_{2.5}$ ratio decreased during wildfire smoke events. For the South Coast air basin, the ambient non-wildfire BC/$PM_{2.5}$ ratio was 0.12 by both smoke identification methods. The $PM_{2.5}$ threshold method identified ~5 times more wildfire hours than were reported by regulatory qualifiers in the South Coast BC and $PM_{2.5}$ data and had a slightly higher wildfire BC/$PM_{2.5}$ ratio of 0.07 compared to 0.05. In general, mean wildfire BC/$PM_{2.5}$ ratios in both air

basins (excluding RAMN) were 0.04–0.07 whereas ambient non-wildfire BC/$PM_{2.5}$ ratios averaged 0.09–0.12. It should be noted that RAMN was deployed for three weeks in August 2020 and the ambient non-wildfire distribution may not represent the seasonal variation in BC/$PM_{2.5}$ ratios in Richmond, CA.

The depression of BC/$PM_{2.5}$ ratios during wildfire smoke events is due to much greater emissions of $PM_{2.5}$ from wildfires compared to BC. In the 2013 CARB forestry BC emissions inventory (**Table 6.1**), a BC/$PM_{2.5}$ ratio of 0.2 (20%) was assumed for brush and timber fire. Box and whisker plots of wildfire smoke BC/$PM_{2.5}$ ratios presented in **Figure 6.13** indicate that this value overestimates the fraction of BC in wildfire $PM_{2.5}$ by a factor of 3–4 for hours identified by this study as extreme smoke events. The formation of secondary $PM_{2.5}$ would further lower the BC/$PM_{2.5}$ ratios compared to fresh emissions, implying that the assumed 20% BC composition of wildfire $PM_{2.5}$ leads to a significant overestimate of BC from wildfires in California. If the wildfire BC/$PM_{2.5}$ ratios in this study were employed in the FOFEM methodology used in the CARB forestry BC emissions inventory, the total BC forestry emissions would decrease by the same factor.

The effect of which BC and $PM_{2.5}$ data are identified as wildfire-smoke impacted was evident in the two South Coast datasets. In general, the regulatory qualifier approach was more conservative and depended upon an air quality regulator flagging data as wildfire smoke impacted from observation or weather reports. It is unknown if this data flagging is a standard operating procedure at AQMDs or if, for example, only $PM_{2.5}$ used for attainment receive wildfire smoke flags. The $PM_{2.5}$ threshold approach may filter out some wildfire smoke events were the $PM_{2.5}$ concentration was less than 50 μg m^{-3} and limit the analysis to high $PM_{2.5}$ smoke events.

Regulatory network BC/CO enhancement ratios during wildfire smoke events and ambient conditions

In addition to the $PM_{2.5}$ threshold, the BC/CO enhancement may be useful as a means of identifying periods when wildfire smoke is present in AQMD air basins. BC and CO are both products of incomplete combustion and are emitted from biomass burning, however BC is preferentially produced during flaming while CO is preferentially produced during smoldering combustion conditions. The BC/CO enhancement ratios (ΔBC/ΔCO) were calculated on a minutely-basis at the prescribed burn and an hourly basis for both air basins for both wildfire and non-wildfire hours by the two methods of wildfire hour identification. Summary statistics for these ratios are reported in **Table 6.5** and box and whisker plots of BC/CO enhancement distributions are presented in **Figure 6.14**.

Table 6.5 Summary statistics of BC/CO enhancement ratios from the prescribed burn and regulatory sites				
Source and Wildfire Identification Method	**Wildfire Hours?**	**Count**	**Mean ± Standard Error [µg/m³/ppm]**	**Standard Deviation [µg/m³/ppm]**
Prescribed Burn – Ground AE33*	N/A	1081	3.8 ± 0.9	28
SF Bay Area $PM_{2.5}$ threshold	Yes	2650	4.0 ± 0.06	3
	No	151646	1.3 ± 0.005	2
South Coast $PM_{2.5}$ threshold	Yes	957	5.7 ± 0.3	9
	No	154289	2.8 ± 0.005	2
South Coast Regulatory Qualifier	Yes	795	3.3 ± 0.1	3
	No	154554	2.8 ± 0.01	2

* Prescribed burn BC/CO enhancement ratios averaged on a minutely time basis

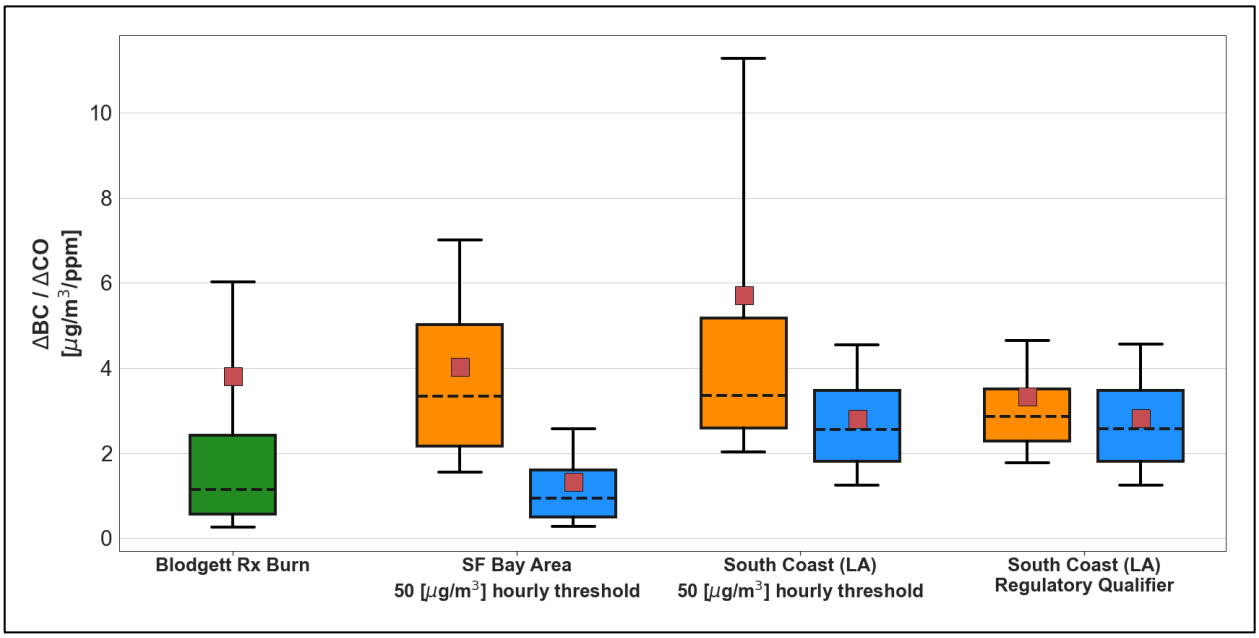

Figure 6.14 BC/CO enhancement ratios for the prescribed burn ground platform (AE33) (green), SF Bay Area and South Coast air basins for both wildfire (left, orange) and non-wildfire (right, blue) hours identified by the $PM_{2.5} > 50$ [µg/m³] and regulatory qualifier methods. Means presented as red squares, medians as horizontal dashed lines, boxes as the interquartile range and whiskers as 10th and 90th percentiles.

In both air basins, the ΔBC/ΔCO attributable to wildfire smoke, especially using the hours of data where $PM_{2.5}$ concentrations exceeded the 50 µg m^{-3} threshold, had higher mean and medians than ΔBC/ΔCO from ambient pollution conditions. In the SF Bay Area air basin, wildfire smoke elevated the ΔBC/ΔCO from 1.3 to 4.0 µg m^{-3} ppm^{-1}. In the South Coast air basin, wildfire smoke elevated the BC/CO enhancement from 2.8 to 5.7 µg m^{-3} ppm^{-1} when the wildfire smoke hours were based on the $PM_{2.5}$ threshold. Interestingly, the ΔBC/ΔCO ratio was approximately the same for ambient pollution conditions and wildfire smoke hours when the latter was based on the regulatory qualifier method. A possible explanation for this is that the $PM_{2.5}$ threshold is a better discriminator for wildfire smoke than is the regulatory qualifier. The interquartile ranges of

ΔBC/ΔCO ratios measured in the Bay Area and South Coast air basins when they were heavily impacted by transported wildfire smoke were greater than the interquartile range of ΔBC/ΔCO measured on the ground at the prescribed burn. As discussed, the ground AE33 BC and CO measurements mostly captured smoldering emissions, when CO emissions were higher (by definition), and BC emissions were lower (see **Figure 6.9**). Wildfires ΔBC/ΔCO were likely higher due to the capture of flaming emissions, where BC emissions would be higher and CO emissions lower.

Absorption Ångström Exponent (AAE) for prescribed burn and transported wildfire smoke

The AAE, like the $BC/PM_{2.5}$ ratio, provided another measure of the effect transported wildfire smoke has on the composition and optical properties of carbonaceous aerosols in an urban airshed. This analysis would not have been possible without direct sharing of multi-wavelength absorption data between BAAQMD and SCAQMD staff and the research team, as these data are notpublicly available. Distributions of AAEs for the prescribed burn (from the ground AE33), SF Bay Area air basin and South Coast Air basin are presented in **Figure 6.15** below. Descriptions of the enveloped box and whisker plots provided in the **Figure 6.15** caption.

The mean AAE was highest at the prescribed burn with a value of 2.6 and measured by the ground AE33. Biomass burning smoke containing light absorbing organic carbon (i.e., BrC) typically has an AAE > 2 whereas the aerosols in urban areas dominated by fossil fuel combustion (e.g., from diesel engines) typically have an AAE ≅ 1. When impacted by transported wildfire smoke, the SF Bay Area AAE increased from an urban background of 1.3 to 1.7 and South Coast from 1.2 to 1.6 or 1.4, depending on which smoke identification method was used. **These results indicated that while wildfire smoke did increase the AAE distribution above an ambient value of 1.2–1.3, carbonaceous aerosols during smoke events were not overwhelmingly dominated by biomass burning BrC but were a mix of biomass burning and fossil fuel combustion BC and BrC.** The distributions of AAE between smoke and ambient conditions overlapped considerably (**Figure 6.15**). As a result, the prescribed-burn-measured AAE alone is unable to identify periods when regulatory sites are heavily influenced by wildfire smoke.

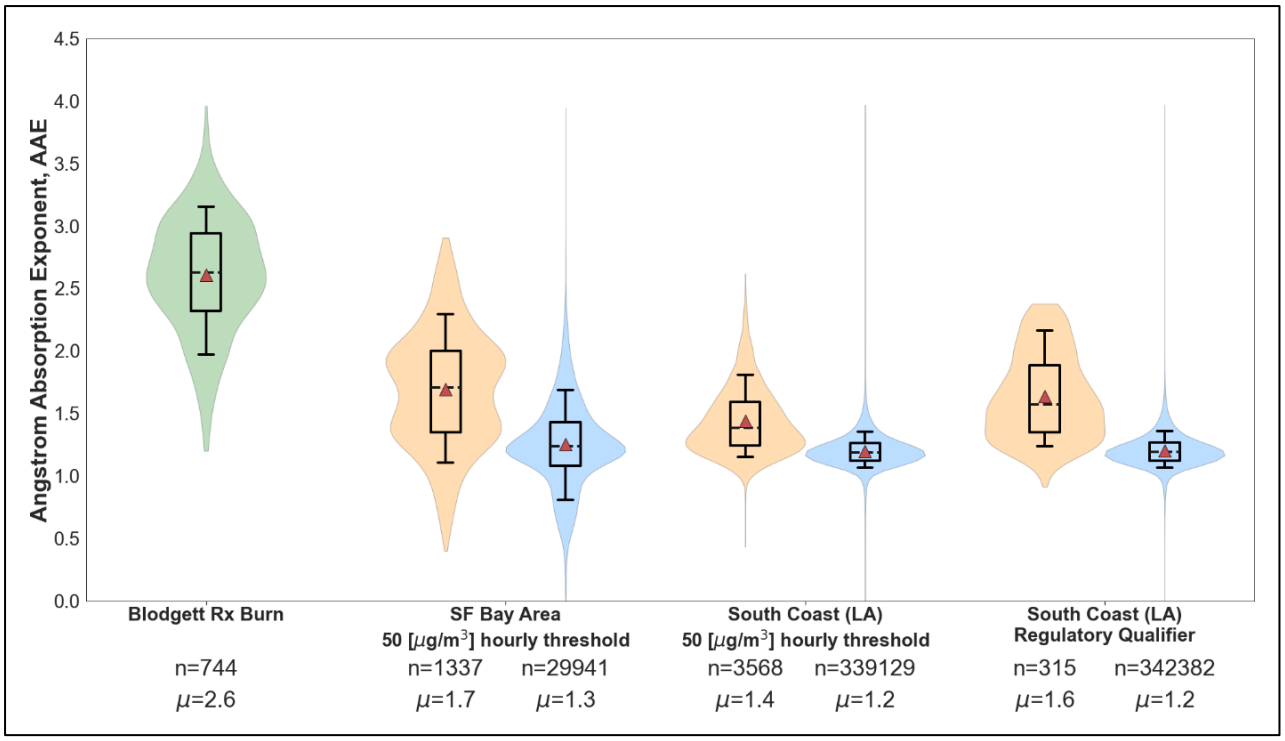

Figure 6.15 Violin plots of Absorption Ångström Exponent (AAE) distributions, calculated from multi-wavelength absorption data for prescribed burn (green), wildfire smoke (left, yellow), and non-wildfire ambient periods (right, blue) in the SF Bay Area and South Coast air basins. Means are shown as red triangles and medians as horizontal dashed lines; the boxes and whiskers represent the interquartile range and the 10th and 90th percentiles. The shaded areas indicate the density distribution of the data, with wider sections indicating a higher probability that members of the population take on the given value and skinnier sections representing a lower probability. The number of hourly (minutely for the prescribed burn) observations (n) and mean value (μ) are reported below each distribution.

7. First Order Fire Effects Model (FOFEM) validation

*A version of this chapter will be submitted to the International Journal of Wildland Fire under the title "Fuel Loadings Prove the Critical Constraint for Smoke Predictions using FOFEM as applied to a Mixed Conifer Forest in California", with the following authors: Tasnia, A.[1], Lara, G.[1], Foster, D.[2], Sengupta, D.[3], Butler, J.[4], Kirchstetter, T.[4], York, R.[5], Kreisberg, N.[6], Goldstein, A. G.[3], Battles, J.[2],*Barsanti, K. C.[1]*

7.1. Introduction

As the number of catastrophic wildfires increases across the western United States (US), land management practices such as prescribed burning become increasingly important to minimize the risks and occurrences of these fires. Although prescribed burns are performed under specific conditions favorable for dispersion of smoke, the air quality effects of prescribed burning events are not negligible and must be considered (Hardy et al., 2001), particularly with calls to significantly increase the amount of prescribed burning in the western US. Air quality and smoke management teams have programs in place that establish procedures and requirements for monitoring the impacts of smoke on air quality. These programs depend on reliable and connected landcover databases, meteorological monitoring tools, and various fire behavior and emission models. A comprehensive smoke management plan therefore considers the perspectives and needs of both land and air quality management teams (Riebau and Fox, 2001).

Fire behavior models provide information on the spread rate and heat intensity of a fire (Scott and Burgan, 2005), while smoke models provide information on the spatial and temporal distributions of smoke plumes, sometimes including smoke composition (Liu et al., 2019). Fire and smoke models are integrated in the widely-used First Order Fire Effects Model (FOFEM, (Keane and Lutes, 2018)). FOFEM assists resource managers in predicting the first order effects, or immediate consequences, of a fire including tree mortality, soil heating, mineral soil exposure, fuel consumption, and smoke emissions. FOFEM generates quantitative reports for fuel consumption and smoke emissions of a prescribed burn or wildfire using flexible inputs that allow representation of a diverse range of regions, seasons, and ecosystems to inform fuel loading inputs, fuel consumption algorithms, and applied emission factors (Reinhardt and Dickinson, 2010).

FOFEM inputs and algorithms are described in Keane and Lutes (Keane and Lutes, 2018). Briefly, as relevant for this work, fuel loading can be based on default fuelbed assumptions for user-defined landcover classifications or can be entirely user-defined. Fuel consumption is calculated in FOFEM using the Burnup model, and is sensitive to vegetation cover group, fuel category, and moisture of the region being modeled. Canopy fuel consumption is user-defined as a percentage of crown and foliage canopy consumed. FOFEM has two options for emission factors (EFs): Default EF and Expanded EF. The Expanded EF setting selects EFs for over two hundred smoke components informed by Urbanski (Urbanski, 2014). Short-term flaming (STFS) EFs are applied to litter, herbaceous, shrubs, and canopy fuel components, or fuels that are consumed early in the

fire. Duff residual smoldering combustion (DuffRSC) EFs are applied to all duff consumed. Woody fuels can have STFS EFs, or coarse wood residual smoldering combustion (CWDRS) EFs, depending on the combustion intensity as calculated by the Burnup model. There are six different STFS EFs, each representing a different forest cover type including: Southeastern Forest, Boreal Forest, Western Forest-Rx (prescribed), Western Forest-WF (wildfire), Shrubland, and Grassland STFS EFs.

The ability to predict smoke-derived pollutant concentrations using smoke models is important for regulatory communities, particularly for mitigating risk to the most vulnerable communities and for managing prescribed burns as we move towards fire being necessary to restore landscapes. Smoke models are a key decision support tool in smoke mitigation and evaluation of the performance of these models is useful for building their efficacy. In this work detailed fuel loading, fuel consumption, and emissions measurements from prescribed fires at the Blodgett Forest Research Station in northern California were leveraged to evaluate the sensitivity of FOFEM smoke predictions to fuel loading, fuel consumption, and EFs; and the ability of FOFEM to represent measured emissions including fine particulate matter ($PM_{2.5}$), carbon monoxide (CO), and carbon dioxide (CO_2). Simulation results were compared with data to understand the limits of application, data needs, and performance of FOFEM for this forest type.

7.2. Methods

FOFEM Model Inputs

FOFEM 6.7 was used to predict fuel consumption and smoke emissions during the BFRS prescribed burns. Model inputs can generally be separated into two categories: those that were selected from a range of options and those that were measured and entered as discrete values. The values that were used in this work are summarized in **Table 7.1** (range inputs) and **Table 7.2** (measured/discrete inputs). The sensitivity studies were performed by changing the input values in **Table 7.2** as further described below. The input values in **Table 7.1** were held constant for all simulations, with the exception of the F-BFRS simulation in which fuel moisture was based on measured values. With the range value of 'moderate' selected, 10-hr fuel moisture was 10% and 100-hr fuel moisture was 18%; measured values were 10% and 30%, respectively.

Table 7.1 Range inputs for FOFEM simulations

Field Name	Description	Selected Range
10 Hour Moisture	Moisture of the 10 Hour fuels	Moderate
1000 Hour Moisture	Moisture of the 1000 Hour fuels	Moderate
1000 Hour Weight Distribution	How 1000 hour fuel is distributed into size classes	Even
Duff Moisture	Duff moisture range (%)	75%
Duff Moisture Method	Method used to measure duff moisture	Entire
Region	Select which region of 4 available fire is located in	Pacific West
Season	Season in which fire event took place	Spring
Fuel Category	How fuel is present. 'Natural', 'Piles', 'Slash'	Natural
Soil Family	Type of soil in environment. 5 soil type options	Coarse-Loamy
Soil Moisture	Soil moisture range (%)	15%

Table 7.2 Discrete value inputs for FOFEM (F) simulations.

Field	F-BFRS (measured)			F-FCCS-M (CARB)			F-FCCS-053 (default)	F-FCCS-024 (LANDFIRE)
	Plot A	**Plot B**	**Plot C**	**Plot A**	**Plot B**	**Plot C**		
Cover Group (as input in FOFEM)	FCCS - 999: No Data	FCCS - 999: No Data	FCCS - 999: No Data	Multi-FCCS (4, **16**, 601, 602, 601, 633)	Multi-FCCS (4, 7, 16, 610, **633**, 635)	Multi-FCCS (4, **610**, 611, 627, 633, 635)	FCCS 053: Pacific ponderosa pine forest	FCCS 024: Pacific ponderosa pine – Douglas-fir forest
Litter (kg/m^2)	3.49	2.76	3.87	2.54	3.08	2.96	0.34	0.40
1 Hour (kg/m^2)	0.13	0.13	0.10	0.28	0.56	0.41	0.02	0.02
10 Hour (kg/m^2)	0.43	0.43	0.35	0.60	1.47	0.82	0.34	0.04
100 Hour (kg/m^2)	1.01	0.81	1.61	1.55	2.17	1.91	0.34	0.17
1000 Hour (kg/m^2)	1.72	2.19	1.65	7.90	15.53	12.72	3.47	1.19
1000 Hour Percent Rotten	25.9%	53.1%	49.7%	79.9%	81.9%	68.0%	29.0%	47.2%
Duff (kg/m^2)	3.52	3.09	5.06	4.68	8.07	7.91	2.29	0.86
Duff Depth (in)	0.89	0.81	1.29	0.61	0.95	0.9	1.50	0.60
Herbaceous (kg/m^2)	0.00	0.00	0.00	1.02	0.36	0.42	0.01	0.11
Shrub (kg/m^2)	0.13	0.13	0.08	2.51	3.19	3.38	0.00	0.00
Crown Foliage (kg/m^2)	1.52	1.50	1.91	3.80	8.53	6.07	1.73	1.03
Crown Branch (kg/m^2)	4.93	4.68	6.16	0.95	2.14	1.52	0.43	0.26

The sensitivity of FOFEM predictions, specifically fuel consumption and smoke emissions, to fuel composition and loading was evaluated by conducting simulations using three different inputs for cover type: measured fuel loadings from the BFRS study and two FCCS inputs. The simulation using measured fuel loadings is hereafter referred to as F-BFRS. For the first simulation using FCCS inputs it was assumed that FCCS fuelbed ID 053, Pacific ponderosa pine forest, best represented the BFRS plots based on vegetation composition and is hereafter referred to as F-FCCS-053. For the second simulation using FCCS inputs, burned areas were plotted in ArcGIS Living Atlas and matched with Landscape Fire and Resource Management Planning Tools Program (LANDFIRE) raster layers (2016 Remap, ("LANDFIRE Program," 2016)). Using this approach it was assumed FCCS fuelbed ID 024, Pacific ponderosa pine–Douglas-fir forest, best represented the BFRS plots and is hereafter referred to as F-FCCS-024.

The expanded EF option was used in all simulations. EFs for the components of interest in this work ($PM_{2.5}$, CO, and CO_2) under short-term flaming (STFS) and/or residual smoldering combustion (RSC) conditions are listed in **Table 7.3**.

Table 7.3 Expanded emission factors (g/kg) for Western Forest-Rx, Western Forest-WF, Woody RSC, and Duff RSC.

Cover Type	Description	Fuel Applied To	Type	CO (g/kg)	CO_2 (g/kg)	$PM_{2.5}$ (g/kg)
Western Forest-Rx	Prescribed fire – Montane conifer forest of Idaho, Montana, eastern Oregon, southern British Columbia	Litter, fine woody (1-hr, 10-hr, 100-hr), herb, shrub, foliage and branch	STFS	17.57	1598	105
Western Forest-WF	Wildfire - Montane conifer forest of Idaho, Montana, eastern Oregon, southern British Columbia	Litter, fine woody (1-hr, 10-hr, 100-hr), herb, shrub, foliage and branch	STFS	23.2	1600	135
Woody RSC*	Residual smoldering of coarse woody debris	Woody fuels when fire intensity is <15 kW	CWDRSC	33	1408	229
Duff RSC	Average of residual smoldering of duff / organic soils mostly based on measurements from the southeast and residual smoldering of duff from Alaska (mostly laboratory based)	Duff	DuffRSC	35.3	1371	257

*When fire intensity is less than 15 kW/m^2, representative of smoldering conditions, CWDRSC EFs are applied to coarse woody fuels, otherwise STFS EFs are applied.

FOFEM Model Simulations

The modeling simulations were designed to evaluate the sensitivity of FOFEM smoke predictions to fuel loading, fuel consumption, and EFs; and the ability of FOFEM to represent measured $PM_{2.5}$, CO, and CO_2 emissions. A total of five model simulations were run with inputs summarized in **Table 7.4**. To evaluate fuel loadings, outputs from the FOFEM simulations F-FCCS-053 and F-FCCS-024 were compared with measured fuel loadings. To evaluate consumption, outputs from

FOFEM simulations F-BFRS, F-FCCS-053, and F-FCCS-024 were compared with measured consumption (BFRS-M). To evaluate sensitivity to uncertainty in EFs, two additional simulations (-WF) were run using Western-Forest WF EFs in place of Western-Forest Rx EFs. Canopy consumption was set to 0% when using the Rx EFs and 75% when using the WF EFs. Predicted emissions were compared between F-BFRS and F-BFRS-WF and between F-FCCS-024 and F-FCCS-024-WF.

The ability of FOFEM to represent measured emissions was evaluated by comparing the output of simulations F-BFRS and F-FCCS-024 with measurements. Predicted $PM_{2.5}$, CO, and CO_2 emissions were converted from units of kg/m^2 to total emissions in units of kg using the measured area of each of the plots.

We also compared our measurements and FOFEM modeling inputs and predictions with FOFEM inputs and predictions produced by CARB staff in May 2022. The CARB FOFEM simulations utilize default FOFEM EFs and rely on a more sophisticated assignment of fuel classifications in which multiple FCCS classes are used to represent the fractional distribution of fuels within each burn unit. Those simulations are hereafter referred to as "F-FCCS-M". The 10-hr fuel moisture value was 10% and the 100-hr fuel moisture was 10.6% based on gridMET raster averaged over the burn period.

Table 7.4 Summary of FOFEM simulations.

Name	Fuel Cover and Loading	Western Forest EFs	% Canopy Burned
F-BFRS	Measured	Rx	0%
F-BFRS-WF	Measured	WF	75%
F-FCCS-053	FCCS Default	Rx	0%
F-FCCS-024	FCCS LANDFIRE	Rx	0%
F-FCCS-024-WF	FCCS LANDFIRE	WF	75%

7.3. Results

Fuel Composition

The measured and predicted (F-FCCS-053 and F-FCCS-024) fuel compositions are shown in **Figure 7.1**. For the observations and the F-FCCS-CARB simulations, area weighted averages were calculated for subsequent measurement-model comparisons. The FCCS 024 classification generally represented the measurements well with a maximum difference of 16% (woody fuels) between measurements and model. The differences between the measured and predicted distributions were greater for the FCCS 053 classification with a maximum difference of 27% (woody fuels). Both FCCS classifications resulted in underprediction of the fractional distribution of litter and crown fuels: FCCS 024 by 10% and 8%, respectively, and FCCS 053 by 16% and 15%, respectively. Both FCCS classifications resulted in overprediction of the fractional distribution of woody fuels, by 16% for FCCS 024 and 27% for FCCS 053. The duff fuel

distribution was underpredicted by 0.5% using FCCS 024 (within sampling error between units) and overpredicted by 3.9% using FCCS 053. In all cases the shrub fraction was negligible (< 1%); in all but the FCCS 024 case the herbaceous fraction also was negligible. The F-FCCS-M results are not shown in **Figure 7.1**, but the predicted distributions were similar to the other FOFEM simulations, with the largest overestimation for woody fuels (23%), the largest underestimation

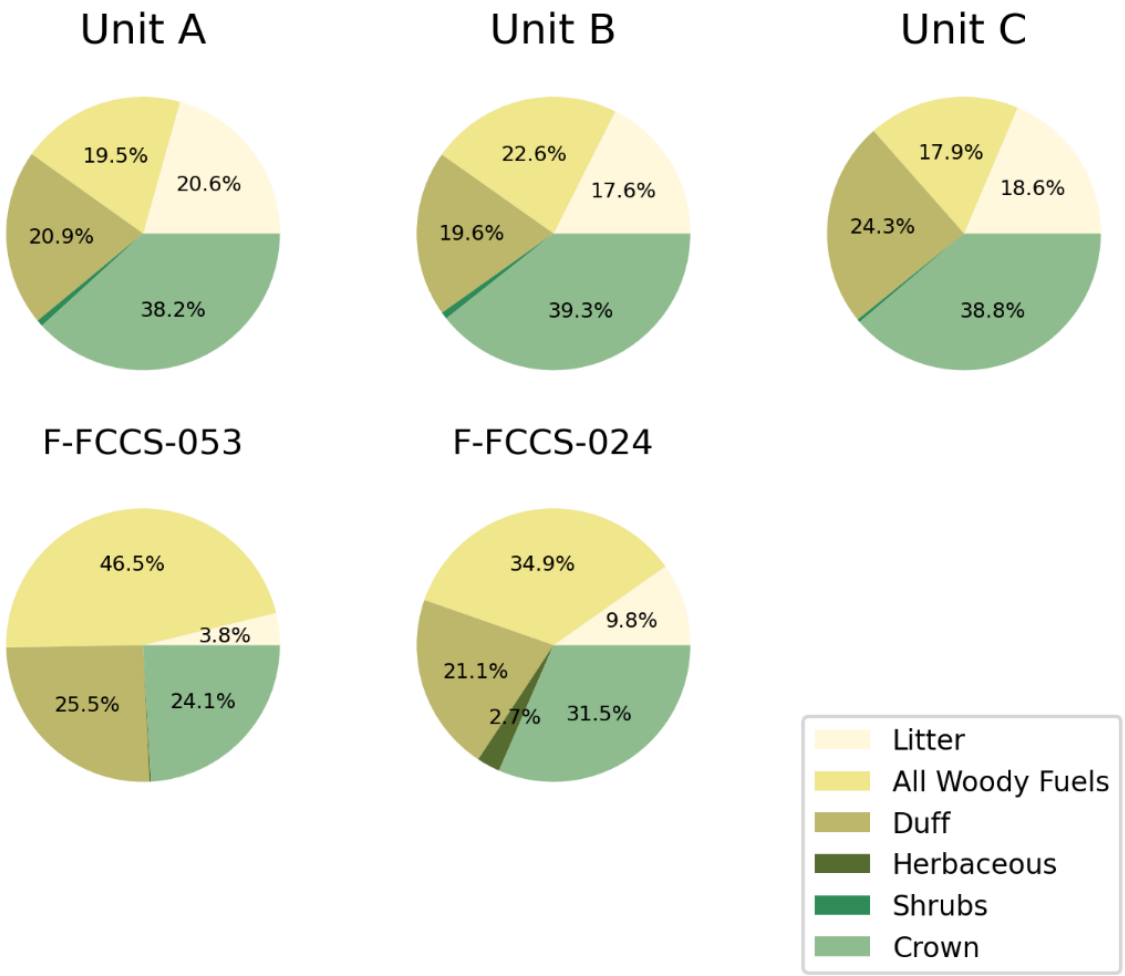

Figure 7.1 Fractional distribution of fuel type measured at Blodgett Forest Research Station in units A, B, and C, and as estimated using FCCS fuelbed ID 053 (default) and FCCS fuelbed ID 024 (LANDFIRE) in FOFEM.

for crown fuels (18%), and the best agreement for the herbaceous fraction (+2%) and duff (-3%).

Fuel Loading

Though the measured fuel distributions were better represented by the F-FCCS-024 simulations, both the F-FCCS-024 and F-FCCS-053 simulations severely underpredicted, by up to 90%, measured fuel loads (**Figure 7.2**, **Table 7.5**). The most severe underpredictions were in the litter, duff, and crown fuel components, where FCCS 024 underpredicted loadings by 3.0 kg/m^2, 2.9

kg/m^2, and 5.5 kg/m^2, respectively, and FCCS 053 by 3.0 kg/m^2, 1.5 kg/m^2, and 4.7 kg/m^2, respectively. The agreement was better for woody fuels, but underpredicted using FCCS 024 (57%, 1.9 kg/m^2) and overpredicted using FCCS 053 (26%, 0.9 kg/m^2). In contrast, the fuel loads were generally overpredicted in the F-FCCS-M simulations, particularly the woody fuels, duff, and shrub (**Table 7.5**).

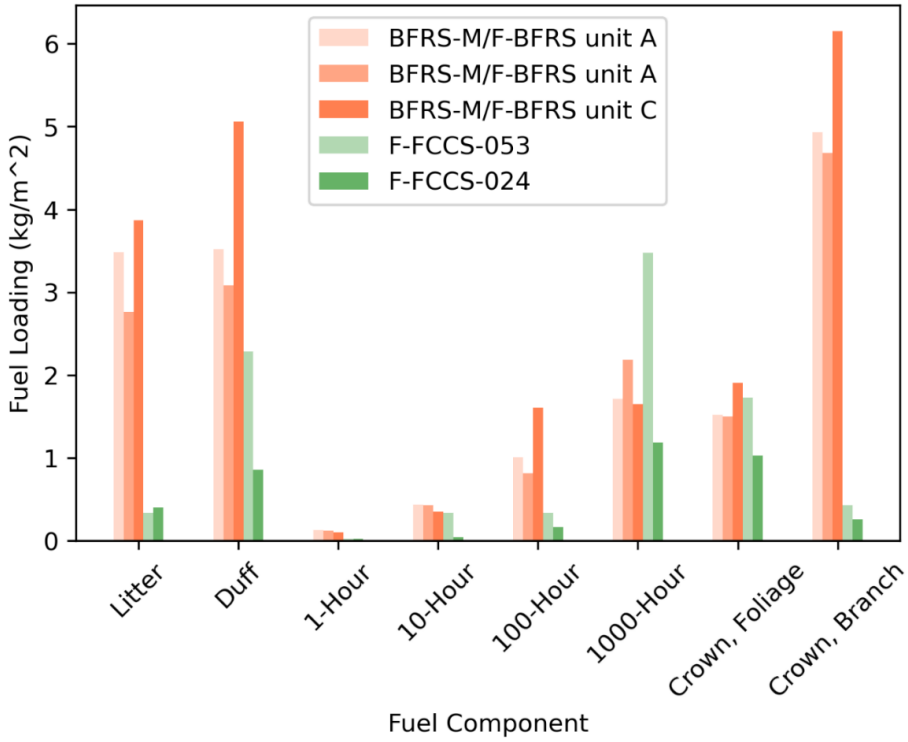

Figure 7.2 Fuel loading (kg/m^2) measured at Blodgett Forest Research Station in units A, B, and C, and estimated using FCCS fuelbed ID 053 (default) and FCCS fuelbed ID 024 (LANDFIRE).

Table 7.5 Fuel loadings (kg/m^2) for each fuel component. Measured values (BFRS) and FOFEM model runs by CARB (F-FCCS-M) represent the area-weighted average of units A, B, and C.

Fuel Component (kg/m^2)	BFRS Data	F-FCCS-M (CARB)	% Error	F-FCCS-053 (default)	% Error	F-FCCS-024 (LANDFIRE)	% Error
Litter	3.35	2.83	-16%	0.34	-90%	0.40	-88%
All Woody Fuels	3.31	14.81	347%	4.17	26%	1.42	-57%
Duff	3.74	6.64	77%	2.29	-39%	0.86	-77%
Herbaceous	0	0.65	-	0.01	--	0.11	--
Shrubs	0.12	2.96	2298%	0	-	0	--
Crown (branch+foliage)	6.81	7.39	8%	2.16	-68%	1.29	-81%

Fuel Consumption

When measured fuel loadings were used as inputs for the FOFEM simulations, FOFEM predicted fuel consumption reasonably well (**Figure 7.3**, **Tables 7.5 and 7.6**). The measured area-weighted average consumption was 5.9 kg/m^2, while the predicted consumption in F-FCCS-M was 7.7 kg/m^2. The default assumption in FOFEM is that 100% of litter is consumed, which results in an overestimation of litter consumption relative to measurements. The underestimates in the modeled fuel loadings were reflected in the predicted fuel consumption (**Figure 7.3**, **Tables 7.5 and 7.6**). Total fuel consumption in F-FCCS-024 was 1.0 kg/m^2, resulting in an 83% underprediction of total fuel consumption compared to the measurements. Total fuel consumption in F-FCCS-053 was 3.1 kg/m^2, resulting in a 47% underprediction compared to the measurements.

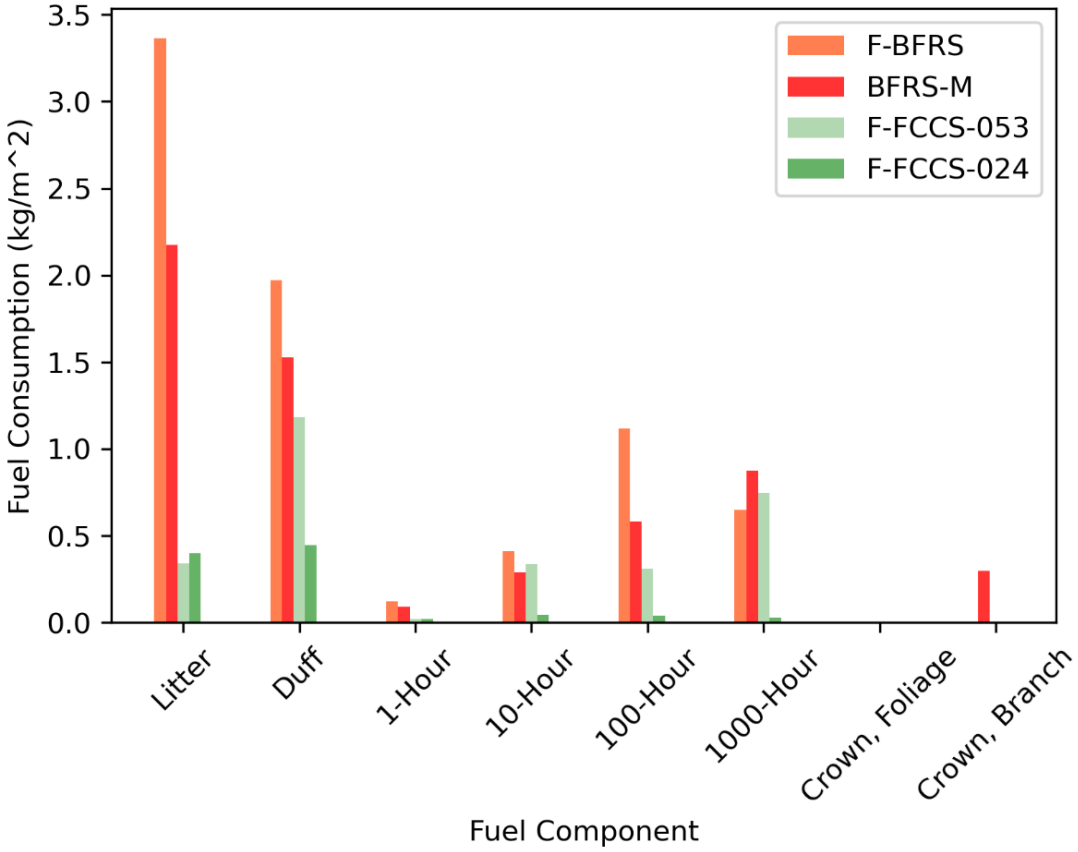

Figure 7.3 Fuel consumption (kg/m^2) measured at Blodgett Forest Research Station (BFRS-M) and predicted using measured fuel loadings (F-BFRS), FCCS fuelbed ID 053 (default) and FCCS fuelbed ID 024 (LANDFIRE).

Table 7.5 Measured and modeled fuel consumption (kg/m^2) for each fuel component. "F-" denotes a FOFEM model run and the information in the () describes the source of inputs.

	BFRS-M	F-BFRS (measured)	F-FCCS-M (CARB)	F-FCCS-053 (default)	F-FCCS-024 (LANDFIRE)
Litter (kg/m^2)	2.2	3.4	2.8	0.3	0.4
1 Hour (kg/m^2)	0.1	0.1	0.4	0.0	0.0
10 Hour (kg/m^2)	0.3	0.4	0.9	0.3	0.0
100 Hour (kg/m^2)	0.6	1.1	1.7	0.3	0.0
1000 Hour (kg/m^2)	0.9	0.6	5.2	0.9	0.0
Duff (kg/m^2)	1.5	2.0	4.4	1.2	0.4
Herbaceous (kg/m^2)			0.6	0.01	0.1
Shrub (kg/m^2)	0.0	0.1	1.8	0.0	0.0
Crown Foliage (kg/m^2)					
Crown Branch (kg/m^2)	0.3	0.01	0.0	0.0	0.0

Table 7.6 Measured and modeled total fuel consumption (kg) for each fuel component. "F-" denotes a FOFEM model run and the information in the () describes the source of inputs.

Fuel Component (kg)	BFRS Data	F-BFRS (measured) (% Error)	F-FCCS-M (CARB) (% Error)	F-FCCS-053 (default) (% Error)	F-FCCS-024 (LANDFIRE) (% Error)
Litter	5.2×10^5	8.0×10^5 (55%)	6.7×10^5 (30%)	8.1×10^4 (-84%)	9.5×10^4 (-82%)
All Woody Fuels	4.4×10^5	5.5×10^5 (25%)	2.0×10^6 (348%)	3.7×10^5 (-15%)	3.3×10^4 (-93%)
Duff	3.6×10^5	4.7×10^5 (29%)	1.1×10^6 (190%)	2.8×10^5 (-23%)	1.1×10^5 (-71%)
Herbaceous	-	-	1.5×10^5	3.2×10^3	2.7×10^4
Shrubs	5.4×10^3	1.7×10^4 (209%)	4.4×10^5 (8152%)	-	-
Crown* (branch+ foliage)	7.1×10^4	-	1.6×10^4	-	-

*Canopy consumption was set to 0% in the three FOFEM model runs F-BFRS, F-FCCS-053, and F-FCCS-024.

Emissions

Total emissions (kg) for CO, CO_2, CH_4 and $PM_{2.5}$, from the F-BFRS, F-FCCS-M, F-FCCS-053, and F-FCCS-024 simulations are shown in **Table 7.7**, along with the calculated modified combustion efficiency (MCE). The differences between the FOFEM simulations largely reflect the differences in the fuel loadings, with lower emissions in the F-FCCS-053 and F-FCCS-024 simulations relative to F-BFRS, and higher emissions in the F-FCCS-M simulation. The MCE values were lower in the F-FCCS-053 simulations, reflecting more smoldering combustion than in the other simulations. In the F-FCCS-053 simulation, total fuel consumption was dominated by duff and woody fuels, which are consumed during smoldering combustion. Additionally F-FCCS-053 had the lowest litter consumption, which is consumed during flaming combustion. While the magnitude of emissions was different between F-BFRS, F-FCCS-M, and F-FCCS-024, the relative abundances were similar, reflecting similarities in distribution of fuel components. The relative $PM_{2.5}$ emissions were higher in F-FCCS-024, reflecting higher consumption of duff than in the F-BFRS and F-FCCS-M simulations.

Table 7.7 Measured and modeled emissions (kg) for air quality and climate pollutants.

Pollutant (kg)	BFRS	F-BFRS (measured) (% error)	F-FCCS-M (CARB) (% error)	F-FCCS-053 (default) (% error)	F-FCCS-024 (LANDFIRE) (% error)
CO	2.5×10^5	3.6×10^5 (46%)	2.7×10^6 (982%)	1.6×10^5 (-35%)	4.8×10^4 (-81%)
CO_2	2.2×10^6	3.2×10^6 (48%)	2.1×10^7 (859%)	1.0×10^6 (-54%)	3.9×10^5 (-82%)
$PM_{2.5}$	5.2×10^4	5.4×10^4 (3%)	2.1×10^5 (300%)	2.3×10^4 (-57%)	7.0×10^3 (-87%)
MCE	0.90	0.90	0.89	0.86	0.89

Measured vs. Modeled Emissions

Total $PM_{2.5}$, CO, and CO_2 emissions measured at BFRS and modeled using F-BFRS and F-FCCS-024 are shown in **Table 7.7**. The differences between the measured emissions ("BFRS") and the predicted emissions using measured inputs ("F-BFRS") are largely due to the errors in predicted consumption and to a lesser extent, the uncertainty in the EFs. The overprediction of emissions in the F-FCCS-M simulation reflects the overestimation of fuel loading, and particularly loading and consumption of woody fuels and duff. The underprediction of emissions in the F-FCCS-053 and F-FCCS-024 simulations reflects the underestimation of fuel loading.

The FOFEM modeling simulations demonstrated the high sensitivity of modeled emissions to fuel loading, and highlighted the critical need for better constraints on fuel loading. Consumption estimates and uncertainty in EFs (at least for these major pollutants) resulted in differences

between measured and modeled emissions, but to a lesser extent than fuel loading. This supports findings in the emissions literature that total emissions are most sensitive to fuel characteristics, including fuel type/component and fuel loading, as noted by Larkin et al. (2012). They also noted that a potential caveat to this observation is for the VOCs, which were not fully evaluated in this work (primarily due to the limited overlap in measured and modeled VOCs).

8. Wildfire Smoke Impacts on Indoor Air Quality Assessed using Crowdsourced Data in California

A version of this chapter was published in the Proceedings of the National Academy of Sciences (118 (36) e2106478118, 2021) under the title "Wildfire smoke impacts on indoor air quality assessed using crowdsourced data in California", with the following authors: Liang, Y., D. Sengupta, M.J. Campmier, D.M. Lunderberg, J.S. Apte, A.H. Goldstein.

Significance

Wildfires are an increasingly large source of particulate matter ($PM_{2.5}$) in the western US. Previous characterizations of exposure to wildfire smoke particles were based mainly on outdoor concentrations of $PM_{2.5}$. Since people mainly shelter indoors during smoke events, the infiltration of wildfire $PM_{2.5}$ into buildings determines exposure. We present analysis of infiltration of wildfire $PM_{2.5}$ into more than 1,400 buildings in California using more than 2.4 million sensor hours of data from the PurpleAir sensor network. Our study reveals that infiltration of $PM_{2.5}$ during wildfire days was substantially reduced compared with non-fire days, due to people's behavioral changes. These results improve understanding of exposure to wildfire particles and facilitate informing the public about effective ways to reduce their exposure.

Abstract

Wildfires have become an important source of particulate matter ($PM_{2.5}$, < 2.5 μm diameter) leading to unhealthy air quality index occurrences in the western United States. Since people mainly shelter indoors during wildfire smoke events, the infiltration of wildfire $PM_{2.5}$ into buildings is a key determinant of human exposure, and is potentially controllable with appropriate awareness, infrastructure investment, and public education. Using time-resolved observations outside and inside over 1400 buildings from the crowdsourced PurpleAir sensor network in California, we found that the geometric mean infiltration ratios (indoor PM-$_{2.5}$ of outdoor origin/outdoor $PM_{2.5}$) reduced from 0.4 during non-fire days to 0.2 during wildfire days. Even with reduced infiltration, mean indoor concentration of $PM_{2.5}$ nearly tripled during wildfire events, with lower infiltration in newer buildings and those utilizing air conditioning or filtration.

8.1. Introduction

Fine particulate matter ($PM_{2.5}$) air pollution is the single-largest environmental risk factor for human health and death in the United States (US) (CDC). Wildfires are a major source of $PM_{2.5}$, and are documented to cause adverse respiratory health effects and increased mortality ((Reid C. E. et al., 2016). Toxicological and epidemiological studies suggest that PM-$_{2.5}$ from wildfires is more harmful to the respiratory system than equal doses of non-wildfire $PM_{2.5}$ (Wegesser T. C. et al., 2009; Aguilera et al., 2021). The number and magnitude of wildfires in the western US has increased in recent decades due to climate change and land management (Westerling et al., 2006;

Dennison et al., 2014; Abatzoglou and Williams, 2016). Although the annual mean level of $PM_{2.5}$ has substantially declined over this period following the implementation of extensive air quality policies to reduce emissions from controllable sources, the frequency and severity of smoke episodes with $PM_{2.5}$ exceedances has increased sharply due to wildfires in the Pacific Northwest and California ((McClure and Jaffe, 2018; O'Dell et al., 2019)). The annual mean $PM_{2.5}$ in Northern California has increased since 2015 (*SI Appendix*, Figure S8.1) due to massive seasonal fire events, and these events have become the dominant cause of $PM_{2.5}$ exceedances.

People in the United States spend 87% of their time indoors (Klepeis et al., 2001). However, the protection against air pollutants of outdoor origin provided by buildings is commonly overlooked in air quality, epidemiologic, and risk assessment studies (Goldstein et al., 2021). To accurately characterize and reduce population exposures to wildfire $PM_{2.5}$, it is necessary to understand then optimize how buildings are used by their occupants to mitigate exposure. Previous estimations of indoor particles of outdoor origin typically relied on measurements from a limited number of buildings, and extrapolation of these measurements to other buildings based on the empirical infiltration and removal parameters (Diapouli et al., 2013; Barkjohn et al., 2021a). However, such extrapolation is not applicable to wildfire events because it does not take into account the distribution of protection provided by buildings (including natural and mechanical ventilation) due to lack of data measuring infiltration under representative conditions. The infiltration of outdoor particles is dependent on people's behavior (Chen and Zhao, 2011; Baxter et al., 2017; Goldstein et al., 2021)), which changes during wildfires (and in 2020 during the COVID-19 pandemic). Pollution levels during wildfire events, and knowledge of those pollution levels through available air quality data, directly impact human responses aimed at controlling the infiltration of outdoor $PM_{2.5}$ including reducing ventilation, using air conditioning, and using active filtration. Statistically robust observations of the variability of $PM_{2.5}$ infiltration during actual wildfire events across a broad cross-section of normally occupied residences provides the opportunity to understand the distribution of real infiltration rates affecting human exposure, and the factors controlling them, potentially informing guidance towards improvement.

Here, we exploit a recent trend in air quality sensing – public data from a network of ubiquitous crowdsourced low-cost $PM_{2.5}$ sensors – to characterize how indoor air quality during wildfire episodes is affected by buildings and their occupants. We demonstrate that buildings provide substantial protection against wildfire $PM_{2.5}$, and that behavioral responses of building occupants contribute to effective mitigation of wildfire smoke. Real-time $PM_{2.5}$ sensors based on aerosol light scattering have proliferated as easy-to-use and low-cost consumer devices in recent years, providing a novel opportunity to explore the indoor intrusion of wildfire $PM_{2.5}$. Among various devices available, the crowdsourced PurpleAir network has developed the most extensive public-facing network currently available. As of June 2, 2021, there are 15,885 publicly accessible active PurpleAir sensors reporting data from across the earth, 76% are outdoor (12,088), and 24% are indoor (3,797). Of these PurpleAir sensors, 57% are installed in California (9,072), split into 69%

outdoor (6,273) and 31% indoor (2,799). As shown in Figure 8.1, California accounts for 74% of all indoor PurpleAir sensors worldwide, with adoption increasing most rapidly following individual wildfire episodes, as noted by prior work (Krebs et al., 2021). We focus here on analyzing the data from these sensors deployed across the metropolitan regions of San Francisco and Los Angeles, California, where the public adoption of indoor and outdoor PurpleAir sensors is especially high, at least partially in response to the high frequency of recent wildfire events. Analyses are presented for the wildfire season in the San Francisco Bay Area of Northern California (NC) during August-September 2020 (denoted NC 2020) and November 2018 (NC 2018), and for the Los Angeles area of Southern California (SC) in August-September 2020 (SC 2020). Maps of the measurement regions are provided in *SI Appendix,* Figures S8.2 and S5.3. We analyzed the data from over 1,400 indoor sensors and their outdoor counterparts to characterize levels of and dynamics of indoor $PM_{2.5}$ and the fraction of outdoor $PM_{2.5}$ that entered buildings, comparing wildfire and non-fire periods. The vast majority (> 87%) of sensors in our dataset are in buildings that are unambiguously identified as residential. We mainly focus on residential buildings, which is facilitated by linking individual PurpleAir sensor locations with a dataset of detailed home property characteristics (Zillow).

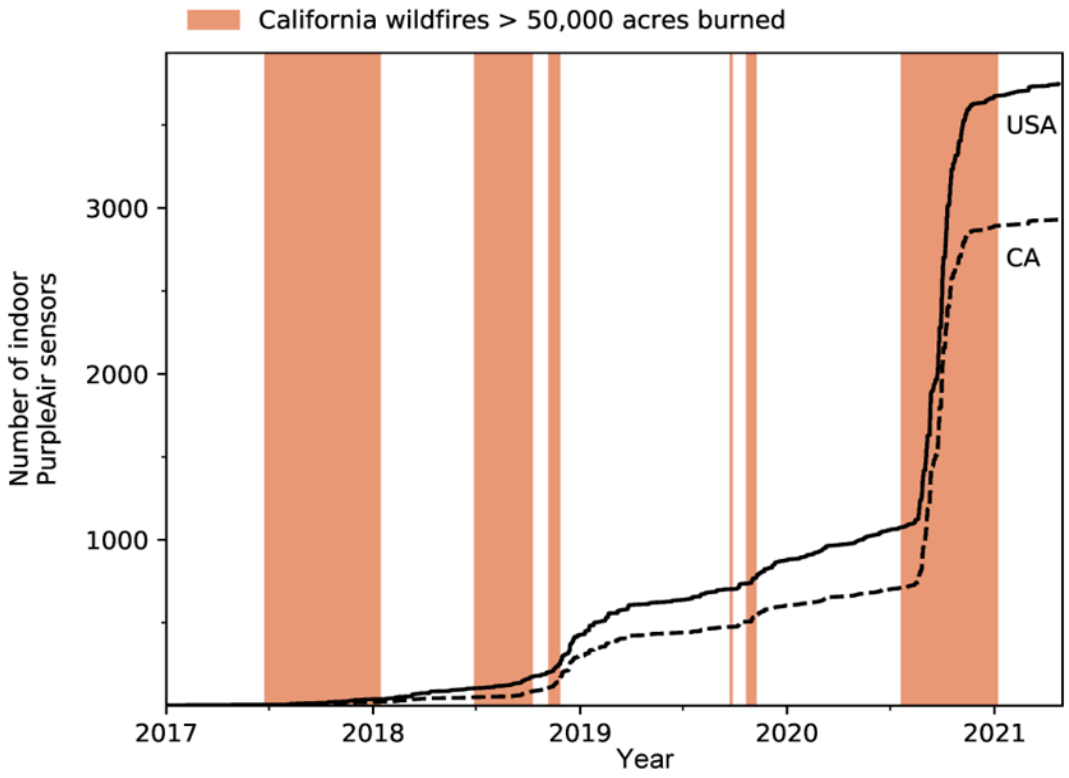

Figure 8.1 Number of publicly accessible indoor PurpleAir sensors in the United States and California. Shadings show major wildfire periods (start date to containment date of fires with > 50,000 total acres burned) in California. Wildfire periods are from CAL FIRE website (https://www.fire.ca.gov/incidents/).

8.2. Materials and Methods

Selection of Sensor Correction Models. The performance of low-cost $PM_{2.5}$ sensors is dependent on humidity, temperature, particle size distribution and level of particulate matters (Zheng et al., 2018, 2019; Ardon-Dryer et al., 2020; Bi et al., 2020; Delp and Singer, 2020; Holder et al., 2020; Kuula et al., 2020; Barkjohn et al., 2021a, 2021b). To evaluate the performance of the PurpleAir sensors against reference US EPA $PM_{2.5}$, we linked hourly average measurements from all 16 reference monitors in the study domain (for the entire study period) with surrounding (within 5 km) outdoor PurpleAir sensors, as detailed in the *SI Appendix* (section "Selection of Sensor Correction Models", Figures S8.6-S8.9, Tables S8.1 and S8.2). We then evaluated the relationship between $PM_{2.5}$ data from PurpleAir sensors and US EPA monitors for multiple calibration schemes in three categories: (i) previously reported calibration factors for wildfire smoke from the literature (Barkjohn et al., 2020b; Holder et al., 2020), (ii) parsimonious empirical calibration relationships based on linear regression using this dataset, and (iii) a machine learning (random forest) based calibration scheme using this dataset. Our parsimonious ordinary least-square fit (correction factor = 0.53, intercept = 0) provided good agreement with the EPA measurements for this dataset, with R^2 = 0.87 and normalized root mean square error = 0.50. For the range of increasingly complex calibration models considering extra parameters for the PurpleAir vs. reference monitor that we developed, we found moderate further improvement to sensor precision and accuracy, but with qualitatively unchanged results (see *SI Appendix*). Accordingly, we rely on our no-intercept linear calibration equation for its more straightforward interpretability in our core analyses.

Decomposition of Indoor $PM_{2.5}$ In addition to infiltration of $PM_{2.5}$ from outdoors, cooking, cleaning and resuspension are the main sources of indoor $PM_{2.5}$ (Ferro et al., 2004; Patel et al., 2020; Tian et al., 2021). Prior to assessing the amount of indoor $PM_{2.5}$ resulting from infiltration of wildfire smoke, we first identified and removed the events (peaks) caused by indoor sources based on the magnitude and duration of indoor $PM_{2.5}$ peaks. Details of the algorithm can be found in the *SI Appendix.*

Other QA and QC

As described in detailed QA/QC procedures in the *SI Appendix,* we sought to ensure appropriate sensor selection, and to exclude sensors that were likely mislabeled.

Mass Balance Model. We explored the dynamics of indoor $PM_{2.5}$ with a well-mixed box model. When the indoor and outdoor particles are in steady state, and the indoor source is small, we have:

$$\frac{dC_{in}}{dt} = 0 = aPC_{out} - (a + k_{loss})C_{in} \Rightarrow F_{in} = \frac{C_{in}}{C_{out}} = \frac{aP}{a + k_{loss}} \quad \textbf{[8.1]}$$

where a is the air exchange rate, P is the penetration factor of particles, k_{loss} is the loss rate constant including deposition and indoor filtration. C_{in} and C_{out} are the indoor and outdoor concentrations,

respectively (Wallace and Williams, 2005; Chen and Zhao, 2011). F_{in} is the infiltration factor (which is close to the infiltration ratio).

Particle Loss Rate Constant Calculation. After major indoor emission events, the indoor concentration of $PM_{2.5}$ will decay following:

$$\frac{dC_{in}}{dt} = -(a + k_{loss})C_{in} \quad \textbf{[8.2]}$$

Therefore, $(a+k_{loss})$ can be estimated by fitting the curve of $C_{in}(t)$ (Stephens and Siegel, 2012). We define the total indoor particle loss rate constant (λ_t) as:

$$\lambda_t = a + k_{loss} \quad \textbf{[8.3]}$$

Details of the derivation of these equations and the algorithms are provided in the *SI Appendix*.

Building information. Property data were obtained by matching coordinates associated with the PurpleAir sensors to addresses. The list of addresses was then inputted to Zillow, a publicly accessible website to find the publicly available building information such as building age and livable area. Zillow uses existing building information and a proprietary algorithm to derive an estimate of the current (as of December 2020) price of the home or apartment. More details are provided in the *SI Appendix*.

Data availability Data used in this work can be freely downloaded from the PurpleAir and EPA websites (links are provided in the *SI Appendix*).

8.3. Results and Discussion

$PM_{2.5}$ inside and outside an example house. Figure 8.2 displays the $PM_{2.5}$ concentrations measured by an indoor sensor and its nearest outdoor counterpart on wildfire days and non-wildfire days (classified by whether the daily average $PM_{2.5}$ level measured by the nearest EPA Air Quality Measurement Station was above or below 35 $\mu g\ m^{-3}$). The outdoor $PM_{2.5}$ concentration was clearly affected by wildfire plumes for August 14-28, September 6-15, and September 28-30. On fire days, the 10-min average outdoor $PM_{2.5}$ exceeded 250 $\mu g\ m^{-3}$ several times. The indoor concentration was more than doubled in these periods due to the infiltration of wildfire particles. We also observed peaks of indoor $PM_{2.5}$ exceeding the outdoor $PM_{2.5}$ even on the most polluted days. These peaks typically lasted between 1 hour and 4 hours, which match well with the characteristics of cooking/cleaning peaks, reported in studies such as Patel *et al*. and Tian *et al.* (Patel et al., 2020; Tian et al., 2021). **Figure 8.2C** shows the concentration profiles of indoor and outdoor $PM_{2.5}$, and 2D shows the outdoor $PM_{2.5}$ and indoor $PM_{2.5}$ with outdoor origins (after removal of identified indoor emission events). The infiltration of outdoor wildfire smoke caused the concentration of indoor $PM_{2.5}$ to exceed 75 $\mu g\ m^{-3}$ in this building occasionally (**Figure 8.2D**).

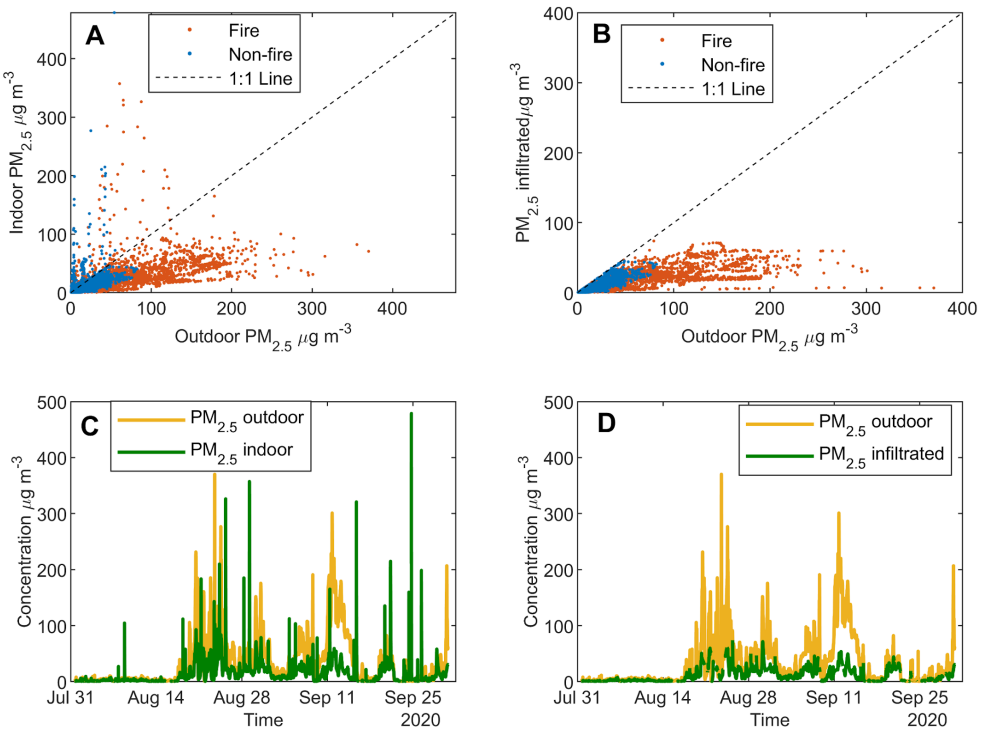

Figure 8.2 Relationship of indoor and outdoor $PM_{2.5}$ for an example house **(A)** Scatterplots of calibrated $PM_{2.5}$ measured at 10-min resolution by an indoor PurpleAir sensor against the nearest outdoor PurpleAir measurement, differentiating fire days (red) and non-fire days (blue), illustrative of the levels of $PM_{2.5}$ pollution of buildings in the NC 2020 case. (**B)** Scatterplots of calibrated indoor $PM_{2.5}$ of outdoor origin against outdoor $PM_{2.5}$. **(C)** Concentration time profile of calibrated indoor and outdoor $PM_{2.5}$ measured by the two sensors. **(D)** Concentration time profile of calibrated infiltrated $PM_{2.5}$ and outdoor $PM_{2.5}$. The figures demonstrate the indoor $PM_{2.5}$ were clearly affected by the outdoor smoke, and our algorithm can effectively remove the indoor peaks due to indoor emissions.

Table 8.1 Statistics of the concentration indoor/outdoor ratios for buildings with PurpleAir sensors in August-September 2020 in the San Francisco Bay Area (35 μg m^{-3} daily average $PM_{2.5}$ concentration measured at the nearest EPA measurement site was used as the threshold for fire days and non-fire days). N = 1274. Unhealthy days are defined as days with daily average EPA $PM_{2.5}$ concentration above 55.4 μg/m^3. GM = Geometric Mean, GSD = Geometric Standard Deviation.

	Mean outdoor conc μg m^{-3}	**Mean indoor conc μg m^{-3}**		**Indoor/outdoor ratio**		**Infiltration ratios**	
	Mean ± s.d.	Mean ± s.d.	GM, GSD	Mean ± s.d.	GM, GSD	Mean ± s.d.	GM, GSD
Non-fire days	9.1±4.0	4.1±2.5	3.7, 1.6	0.90±0.88	0.73, 1.8	0.45±0.15	0.42, 1.5
Fire days	45.4±17.0	11.1±8.3	8.9, 2.0	0.41±0.44	0.31, 2.1	0.27±0.14	0.23, 1.8
Unhealthy days	61.2±20.5	13.5±10.6	10.3, 2.1	0.31±0.42	0.23, 2.1	0.23±0.14	0.19, 1.9

Quantile-quantile plots (*SI Appendix,* Figure S8.4) show the mean concentration of indoor $PM_{2.5}$ in all the buildings can be satisfactorily described by the Weibull distribution. Parameters of the Weibull fit are shown in Table S8.5 in the *SI Appendix*. Parameters of the SC 2020 and NC 2018 cases are not shown here due to the small sample sizes, which are less representative of all the buildings in these areas at that time.

Differences of infiltration on fire days and non-fire days. Taking all the buildings in the NC 2020 case into consideration, we found that the mean concentration of indoor $PM_{2.5}$ nearly tripled on the fire days compared to the non-fire days due to the infiltration of outdoor smoke (**Table 8.1**, *SI Appendix,* Figure S8.4). On the fire days, the average outdoor concentration of $PM_{2.5}$ was more than 4 times the mean indoor $PM_{2.5}$. **Figure 8.3A** displays the distribution of the mean indoor/outdoor $PM_{2.5}$ ratio of each building on the fire days and the non-fire days. The average indoor/outdoor $PM_{2.5}$ ratios for many buildings exceeded 1 due to indoor emission events, particularly on non-fire days. On fire days, the majority of indoor $PM_{2.5}$ infiltrated from outdoors, but the indoor/outdoor $PM_{2.5}$ ratios were much lower because people closed their buildings and many also filtered their indoor air for protection from the smoke. **Figure 8.3B** shows the ratio of indoor $PM_{2.5}$ of outdoor origin to outdoor $PM_{2.5}$ (defined as the infiltration ratio). The infiltration factor (F_{in}) is the steady-state fraction of outdoor $PM_{2.5}$ that enters the indoor environment and remains suspended there (Chen and Zhao, 2011). It quantifies the extent that the building provides protection against outdoor particles (Goldstein et al., 2021). For particulate matter, F_{in} can be obtained from the ratio of indoor/outdoor concentration when there are not additional indoor sources or loss processes (Wallace and Williams, 2005; Bhangar et al., 2011). On fire days ($PM_{2.5}$ > 35 μg m^{-3}), due to the predominance of $PM_{2.5}$ of outdoor origin, the infiltration ratio approaches the infiltration factor. The infiltration factors of $PM_{2.5}$ for different buildings in NC 2020 have a geometric mean (GM) of 0.23 (0.16, 0.36 for 25th and 75th percentiles, same below). On non-fire days ($PM_{2.5}$ < 35 μg m^{-3}), the GM infiltration ratio increases to 0.42 (0.35, 0.56), while on days

with unhealthy air quality ($PM_{2.5}$ > 55.4 μg m^{-3}), the GM infiltration ratio reduces to 0.19 (0.13, 0.31) (Table 5.1). However, around 18% of buildings had $PM_{2.5}$ infiltration factors above 0.4 on the fire days (Figure 8.3B). Occupants of these exposure hotspot buildings could have experienced much higher levels of wildfire smoke. For context, infiltration factors of homes and commercial buildings measured in the US are usually above 0.5 (Chen and Zhao, 2011; Wu et al., 2012), and the infiltration factor of office buildings with 85% ASHRAE filters were predicted to be around 0.18 (Riley et al., 2002). The difference in mean infiltration ratio between fire days and non-fire days are most apparent in the daytime (*SI Appendix,* Figure S8.5), consistent with more ventilation typically occurring during daytime (Erhorn, 1988). The lower infiltration factors for the buildings on fire days indicates the efficacy of reduced ventilation and enhanced removal of particles as people took measures to protect themselves from smoke exposure, and that more behavioral changes happened in daytime. Infiltration ratios of $PM_{2.5}$ were not significantly different between fire days and non-fire days in the SC 2020 case (**Figure 8.4**), in contrast to the 2020 NC observations. This difference is probably because the hotter weather in Southern California caused more frequent use of air conditioning systems (and shutting windows), which is implied by a higher 2 pm mean indoor-outdoor temperature difference (~4ºC) than buildings in the San Francisco Bay Area (~2ºC). Another possibility is that the $PM_{2.5}$ pollution levels in the Greater Los Angeles area were not high enough to induce people to change their behaviors (*SI Appendix,* Figures S8.6-S8.9).

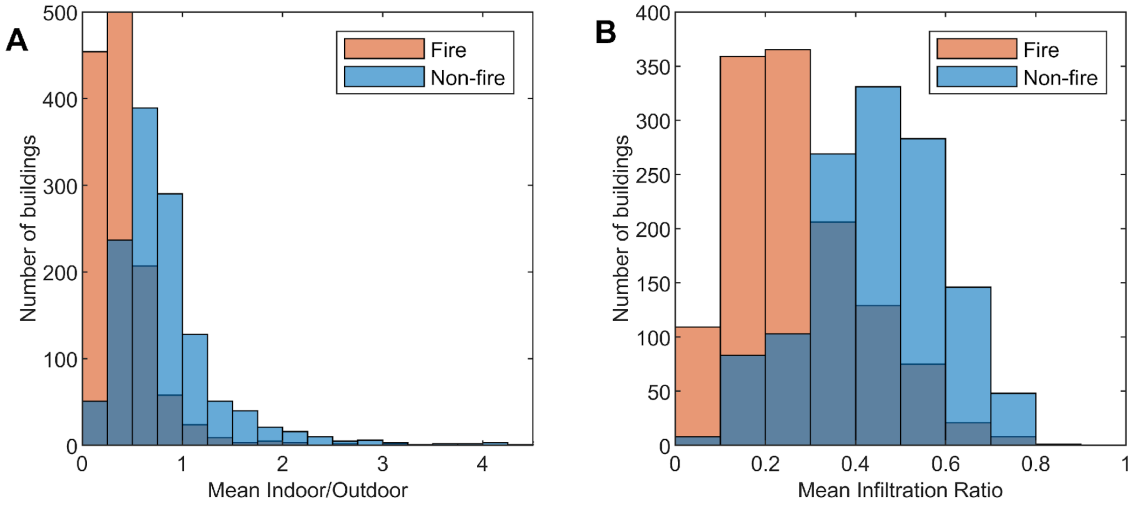

Figure 8.3 Distribution of the indoor/outdoor ratio and the infiltration ratio in the San Francisco Bay Area in August and September 2020. **(A)** Mean Indoor/Outdoor $PM_{2.5}$ ratio of buildings during fire days and non-fire days and **(B)** mean infiltrated $PM_{2.5}$/Outdoor $PM_{2.5}$ ratio of buildings during fire days and non-fire days. Buildings have lower indoor/outdoor $PM_{2.5}$ ratio and infiltration ratio on fire-days.

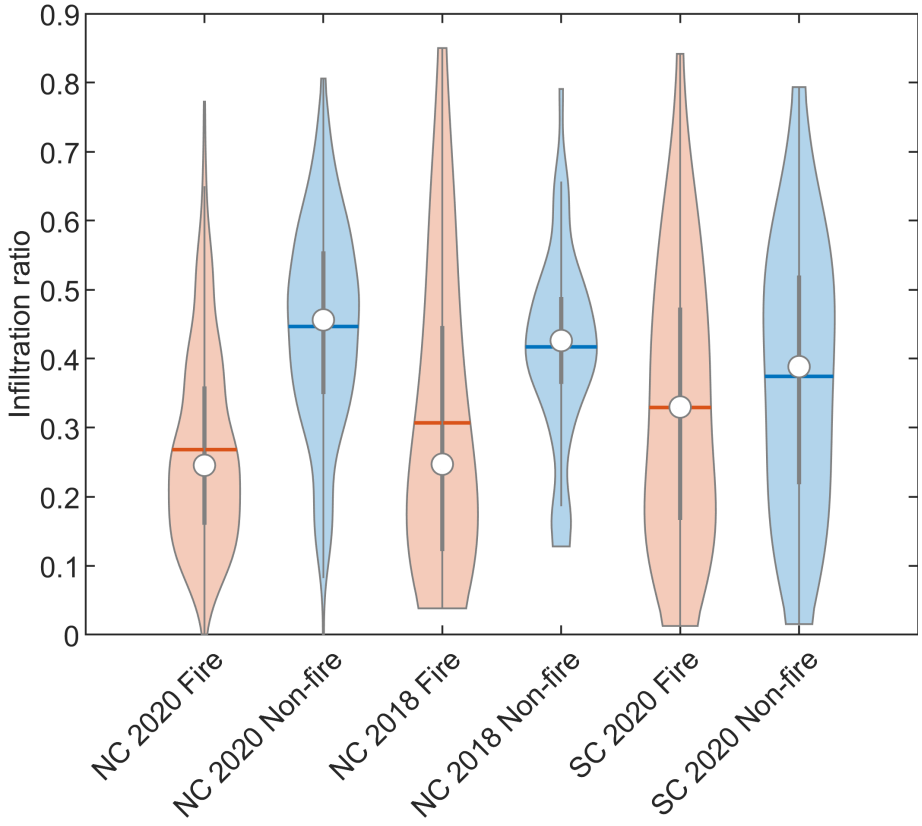

Figure 8.4 Violin plots of particle infiltration ratios during fire and non-fire periods. N = 1274 buildings, 2.1×10^6 sensor-hours for NC 2020, N = 115 buildings, 2.8×10^5 sensor-hours for SC 2020 and N = 52 buildings, 4.4×10^4 sensor-hours for NC 2018. Each violin plot shows the probability density of the infiltration ratio and a boxplot of interquartile range with whiskers extended to 1.5 times the interquartile range. Circles indicate the median, and horizontal lines indicate the mean.

Infiltration and building characteristics. Differences in fire-day infiltration ratios may also stem from differences in building characteristics. As shown in Table S8.4 in *SI Appendix*, buildings with fire-day infiltration ratio < 0.14 were widely distributed in the study area. However, buildings with fire-day infiltration ratio > 0.4 were mostly located in San Francisco where the climate is cooler and air conditioning is much less common. Buildings in California Climate Zone 12 (Northern California Central Valley) had lower infiltration ratios than any other climate zones in the San Francisco Bay Area (*SI Appendix,* Figure S8.10). Due to the summer hot weather, substantial cooling is required for buildings in this zone (Pacific Energy Center, 2006). Air conditioning and associated filtration systems apparently decrease the indoor $PM_{2.5}$ in those buildings. In addition, since the mid-late 1990s, most new residential buildings in the US are equipped with air conditioning systems (US Census Bureau, 2019). Since 2008, new buildings in California are mandated to have mechanical ventilation systems (California Energy Commission, 2008). Many of the newer buildings also have filtration systems (Singer et al., 2020). The changes in the building stock are apparent in the resulting data, as residences built after 2000 had significantly lower

infiltration ratios on both fire days and non-fire days compared with older buildings (*SI Appendix,* Figure S8.10), which is consistent with the findings of a recent wildfire smoke infiltration study in Seattle (Xiang et al., 2021). We further classified the buildings in the NC 2020 case into cool buildings and hot buildings based on whether the 95th percentile indoor temperature reached 30ºC. These cool buildings were more likely to have air conditioning systems on. As shown in *SI Appendix,* Figure S8.11, the cool buildings have significantly lower fire-day infiltration ratios than the hot ones ($p < 0.01$), and around 17% of cool buildings had extremely low infiltration ratios (< 0.1). In sum, these results demonstrate that (i) this sensing and analysis approach yields findings in line with mechanistic plausibility (ii) and that the diversity of building characteristics within a region leads to substantial heterogeneity in the degree to which populations are protected indoors from wildfire $PM_{2.5}$.

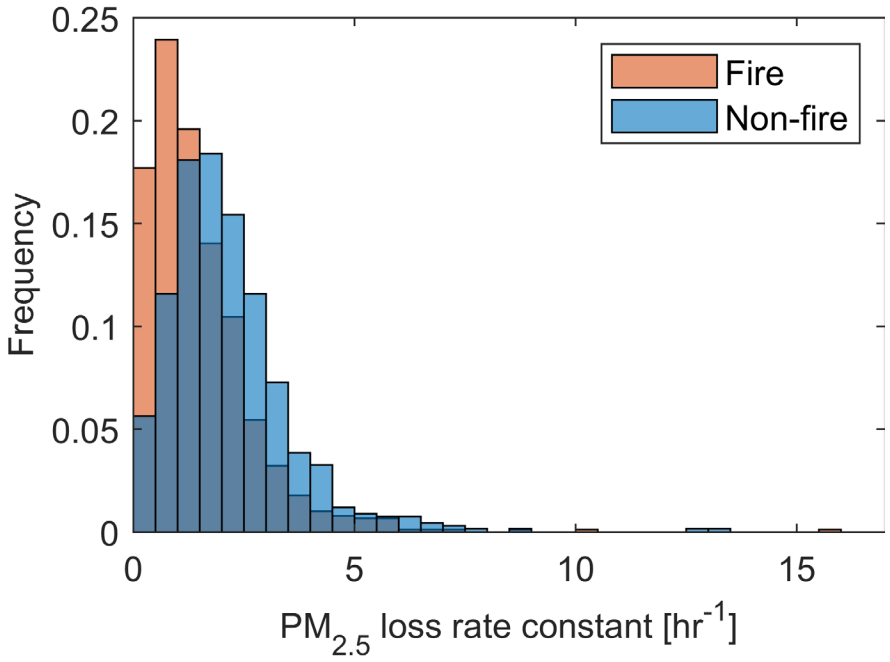

Figure 8.5 Frequency distribution of indoor $PM_{2.5}$ total loss rate constants (λ_t) in buildings in the San Francisco Bay Area on the fire days and non-fire days in August-September 2020 (decay peaks were found in N = 1000 buildings). A reduced total $PM_{2.5}$ loss rate constant on the fire days indicates a reduction in ventilation.

Decay rate constants for $PM_{2.5}$ were determined for all indoor observations using a box model (Equation 2). The difference in the decay rate constants of $PM_{2.5}$ indoors further reveals why the infiltration ratio was lower on fire days. **Figure 8.5** shows the distribution of mean total loss rate constant of $PM_{2.5}$ on fire days and non-fire days in the buildings. The mean and median total loss rate constants (λ_t) are 1.5 h^{-1} and 1.2 h^{-1} on fire days, and 2.2 h^{-1} and 1.9 h^{-1} on non-fire days, respectively. Comparing individual buildings on fire days and non-fire days, 67% of them have lower particle loss rate constants on fire days, indicating a high percentage of buildings whose occupants took effective action to reduce $PM_{2.5}$ infiltration. During the fire days, the decrease in air exchange rate exceeded the enhanced indoor filtration, making the loss rate smaller. Since the infiltration ratio (infiltration rate/total loss rate, $aP/(a+k_{loss})$) was also lower on fire days, it can

be inferred that the infiltration rate (air exchange rate × penetration factor, aP) was lower on fire days (Equations 8.1 and 8.3). We expect both air exchange rate and penetration factor to drop on fire days. Closure of windows and doors will lead to a lower air exchange rate. The usage of filtration systems on incoming air and closure of openings will lead to a lower penetration factor (Diapouli et al., 2013). For the SC 2020 case, the mean estimated particle loss rate constants (1.3 h^{-1} on fire days and 1.4 h^{-1} on non-fire days) are lower than in the San Francisco Bay Area (*SI Appendix,* Figure S8.12), which further implies that a larger fraction of PurpleAir sensor owners in the Los Angeles area kept their windows/doors closed.

People are more likely to open the windows when the indoor temperature is higher than the outdoor temperature in summer (Andersen et al., 2013; Yan et al., 2015). In the NC 2020 and SC 2020 cases, the difference in daytime indoor/outdoor temperature alternated between positive and negative values (*SI Appendix,* Figure S8.13). However, in the NC 2018 case, due to the colder outdoor temperatures in November, we infer that people probably closed their windows for a longer time, explaining the lower loss rate constants observed. This was expected to reduce the difference between the infiltration ratio on fire days and non-fire days. However, this ratio is still statistically significantly higher ($p < 0.05$) on fire days, which suggests the widespread application of filtration systems.

Our conclusions come with caveats. First, we treated each building as a well-mixed box, which assumes the indoor sensor measurement can represent the $PM_{2.5}$ levels of the entire building. Second, our algorithm to remove the indoor-source peaks could miss lower indoor emission events. In addition, we assumed a universal quasi-linear response for all the PurpleAir sensors throughout the analysis period. Such treatment could lead to biases, but our results should still reflect the average trend. Indoor environments with PurpleAir sensors may not be representative of the entire distribution of buildings (details are provided in the *SI Appendix*). Adoption of PurpleAir sensors (at least ~200 US dollars per sensor) is higher among affluent people concerned about exposure to $PM_{2.5}$. Consistent with the expectation of an affluent "early-adopter" effect, PurpleAir owners live in homes with estimated average property values 21% greater than the median property value for their cities (*SI Appendix,* Table S8.3 and Figure S8.14). The 2015 U.S. Residential Energy Consumption Survey shows that households with less than $40,000 annual income are less likely to use air-conditioning equipment than other households (Residential Energy Consumption Survey (RECS), 2015). Low-income houses tend to be older, and they are shown to have larger leakage than other houses (Chan et al., 2005; Adamkiewicz et al., 2011). Lower-income households can therefore have disproportionately higher exposure to wildfire smoke. Finally, although we were not able to disentangle the influence of multiple regionally varying parameters (such as building type, floor area, property values) on penetration of wildfire smoke with the current distribution of indoor sensors, more extensive sensor adoption in coming years may allow future work to address this limitation.

This work demonstrates that crowdsourced environmental sensing can provide valuable information about how people are protecting themselves from the increasingly severe environmental hazard of wildfire smoke. We find that common adaptation measures, including reducing ventilation and active air filtration, effectively mitigate the average indoor exposures of all the buildings by 18% and 73% relative to indoor baseline and outdoor conditions, respectively.

This work further suggests that such protective measures could be enhanced through public education to substantially mitigate indoor exposures at the population scale in the future. Given anticipated increases in wildfire smoke in coming decades, it is critical to evaluate these findings in other settings, including in lower-income communities and in other climate regions affected by wildfires. While our data imply that early adoption of crowdsourced indoor PurpleAir sensors seems to be propelled by wildfire events (Figure 8.1), gaining more broadly representative insight into the distribution of indoor PM conditions might benefit from complementary approaches to disseminating these sensors, such as targeted deployments in lower-income communities. Overall, our results suggest the increasing ubiquity of indoor and outdoor air pollution sensors can aid in understanding exposures to episodic pollution sources such as wildfires.

Acknowledgments

The authors acknowledge Tongshu Zheng at Duke University for his advice on processing the data from the PurpleAir sensors. We thank the owners of PurpleAir sensors who generously shared the measurement data online.

9. Summary and Conclusions

Through this contract, we were uniquely able to: 1) combine detailed pre- and post-fire fuel measurements with comprehensive ground and aerial measurements, and 2) compare measured fuel consumption and emissions with model predictions using the First-Order Fire Effects Model (FOFEM). Fuel and emissions measurements were obtained from 1st and 3rd entry prescribed burns at the Blodgett Forest Research Station (BFRS), representing differences in land management practices. The burns were in a mixed conifer forest, where the third-entry burns were burned twice previously for management purposes. These two extremes capture what will in the future become a gradient in management status. This allowed us to characterize smoke emissions, measured and modeled, as a function of fuel consumption and land management practices, and to develop datasets for use by air quality management and scientific communities.

The main focus of this contract was the 1st entry prescribed burns that were conducted over four consecutive days in April 2021. These burns occurred during spring conditions that allowed for high fuel consumption without excessive risk of escape and with minimal smoke impacts on downwind communities. Pre- and post-fire fuel measurements were conducted to assess distributions of plant species and fuel components (i.e., litter, duff, fine woody debris, etc.) and carbon losses. The spring burns met or exceeded the management goals to: 1) consume at least 50% of surface fuels, primarily litter and fine woody debris (FWD, includes 1-, 10-, and 100-hour fuel categories); and 2) manage the burn intensity to avoid either low or high intensity scenarios that would typically be undesirable for most management contexts (i.e., limit the crown scorch of canopy trees to less than 50% on average and limit post-burn mortality to no more than 10% of trees greater than 50 cm diameter at breast height).

Prior to treatment, the fuel load in the 1st entry burn was nearly double that of the 3rd entry burn. Total pre-fire ground and surface fuel load for the 1st entry burn was 104 Mg ha^{-1}; for the 3rd entry burn it was 55 Mg ha^{-1}. The percent of fuel consumed by the prescribed burns was also greater at 1st entry: 53% vs 35%. However the composition of the consumed fuels was similar between the two studies. The similarity in consumed fuels between the 1st and 3rd entry burns was reflected in the overlap in modified combustion efficiency (MCE) values observed during these burns and consistencies between measured emission factors (EFs). The 1st entry burn consisted of three separate units burned over four days, in which unit A was burned over two days and units B and C were burned over the third and fourth day respectively. The composition and combustion of fuels across the units was very similar and also reflected in consistencies between measured EFs. The similarities between the 1st entry units and between the 1st and 3rd entry burns led to our first recommendation of pooling data from these studies to obtain a single set of EFs.

Smoke was sampled using ground and aerial (drone) platforms. From these samples, we characterized gas- and particle-phase constituents including organic compounds, carbon monoxide and dioxide (CO, CO_2), black carbon (BC), brown carbon (BrC), and total fine particulate matter

($PM_{2.5}$). Smoldering conditions were sampled using both ground and aerial platforms, while flaming conditions were largely only sampled by the drone. The average MCE values ± 1 standard deviation was 0.83 ± 0.03 for ground sample sets in 2017 (3rd entry) and 2021 (1st entry) and 0.87 ± 0.05 for the aerial sample set. The drone also sampled more concentrated smoke and thus the samples had generally higher mixing ratios for measured volatile organic compounds (VOCs). When we compared EFs, which take into account dilution, there was generally good consistency between measured EFs from the ground and the drone, with some exceptions for individual gas and particle phase compounds. This led to our second recommendation of pooling ground and drone data for EF calculations.

Many constituents in smoke have been shown to exhibit clear trends with MCE. Flaming-dominant compounds tend to be higher and higher MCE values and smoldering-dominant compounds tend to be higher at lower MCE values. BC showed the strongest correlation with MCE across all sampled ranges and EC increased at the highest MCE values. There was little to no correlation between OC, $PM_{2.5}$, and individual VOCs across the range of MCE values sampled. For some particulate-phase constituents, we presented EFs separated into two combustion regimes (MCE < 0.88 & MCE > 0.88) to show where differences were observed. Our third recommendation is thus that for most compounds reported here and across the range of sampled MCE values, EFs are independent of MCE.

Relationships between BC and $PM_{2.5}$ and BC and CO were explored in the data from BFRS, as well as data obtained from local air quality stations. In all datasets, the mean $BC/PM_{2.5}$ ratio decreased during smoke events. This is due to the much greater emissions of $PM_{2.5}$ from wildfires compared to BC. In general, mean wildfire $BC/PM_{2.5}$ ratios in studied air basins were 0.04–0.07 whereas ambient non-wildfire $BC/PM_{2.5}$ ratios averaged 0.09–0.12. For regulatory modeling, a $BC/PM_{2.5}$ ratio of 0.2 (20%) was assumed for brush and timber fire. The analysis of $BC/PM_{2.5}$ ratios presented here indicate that this value overestimates the fraction of BC in wildfire $PM_{2.5}$ by a factor of 3–4. Our fourth recommendation is thus to revise the assumed $BC/PM_{2.5}$ ratios for wildfires in emissions modeling.

Measured concentrations and EFs from samples collected during the 2021 1st entry prescribed burns were compared with data from samples of California wildfires collected by CARB staff using their mobile platform in coordination with the FIREX-AQ aircraft campaign. Lower VOC mixing ratios were measured in the wildfire samples than in the prescribed burns, which was likely due to enhanced evaporation and aging in the wildfire samples given that they were collected much farther from the fires than the BFRS samples. Wildfire samples also had higher azelaic acid than 1st entry burn samples, supporting the interpretation of less dilution and aging of smoke sampled during the 1st entry burn. The agreement between the 2021 1st entry burn ground and drone samples with published values was compound dependent. Generally there was a range of values for all

compounds considered and there were no systematic biases in BFRS ground/drone measurements vs. literature.

For the FOFEM modeling simulations, model performance was improved with the use of measured fuel loadings as inputs. In the context of fuel composition, the FCCS 024 classification generally represented the measurements well with a maximum difference of 16% (woody fuels) between measurements and model. The differences between the measured and predicted distributions were greater for the FCCS 053 classification with a maximum difference of 27% (woody fuels). Both the F-FCCS-024 and F-FCCS-053 simulations severely underpredicted fuel loadings, by up to 90%, which translated into severe underpredictions of consumption and emissions. The FOFEM modeling simulations demonstrated high sensitivity of modeled emissions to fuel loading, and highlighted the need for better constraints on fuel loading. Consumption estimates and uncertainty in EFs (at least for these major pollutants) resulted in differences between measured and modeled emissions, but to a lesser extent than fuel loading. This led to our fifth recommendation, that better characterization of fuel loading in the western US may be the highest priority for improved smoke modeling.

10.Recommendations

Based on our measurements of prescribed burn emissions from 1st and 3rd entry mixed conifer forest, and comparison to the literature and the FOFEM model, we recommend the following:

1) Pool data from the 2017 and 2021 studies to obtain a single set of EFs, representing the combined 1st and 3rd entry burns, for use in modeling emissions from prescribed burns of managed and previously unmanaged mixed conifer forests.

2) Pool ground and drone data for mean EF recommendations to represent the full range of burning conditions observed.

3) For most compounds reported here and across the range of sampled MCE values, EFs from controlled burns should be assumed as independent of MCE for the purposes of emissions modeling.

4) Revise the assumed BC/$PM_{2.5}$ ratios for wildfires in emissions modeling.

5) Prioritize improving characterization of fuel loading to increase accuracy of smoke emission modeling.

References

Abatzoglou, J.T., Williams, A.P., 2016. Impact of anthropogenic climate change on wildfire across western US forests. Proceedings of the National Academy of Sciences 113, 11770–11775. https://doi.org/10.1073/pnas.1607171113

Adamkiewicz, G., Zota, A.R., Fabian, M.P., Chahine, T., Julien, R., Spengler, J.D., Levy, J.I., 2011. Moving Environmental Justice Indoors: Understanding Structural Influences on Residential Exposure Patterns in Low-Income Communities. Am J Public Health 101, S238–S245. https://doi.org/10.2105/AJPH.2011.300119

Aguilera, R., Corringham, T., Gershunov, A., Benmarhnia, T., 2021. Wildfire smoke impacts respiratory health more than fine particles from other sources: observational evidence from Southern California. Nat Commun 12, 1493. https://doi.org/10.1038/s41467-021-21708-0

Akagi, S.K., Yokelson, R.J., Wiedinmyer, C., Alvarado, M.J., Reid, J.S., Karl, T., Crounse, J.D., Wennberg, P.O., 2011. Emission factors for open and domestic biomass burning for use in atmospheric models. Atmospheric Chemistry and Physics 11, 4039–4072. https://doi.org/10.5194/acp-11-4039-2011

Allen, R., Larson, T., Sheppard, L., Wallace, L., Liu, L.-J.S., 2003. Use of Real-Time Light Scattering Data To Estimate the Contribution of Infiltrated and Indoor-Generated Particles to Indoor Air. Environ. Sci. Technol. 37, 3484–3492. https://doi.org/10.1021/es021007e

Allen, R., Wallace, L., Larson, T., Sheppard, L., Liu, L.-J.S., 2004. Estimated Hourly Personal Exposures to Ambient and Nonambient Particulate Matter Among Sensitive Populations in Seattle, Washington. Journal of the Air & Waste Management Association 54, 1197–1211. https://doi.org/10.1080/10473289.2004.10470988

Andersen, R., Fabi, V., Toftum, J., Corgnati, S.P., Olesen, B.W., 2013. Window opening behaviour modelled from measurements in Danish dwellings. Building and Environment 69, 101–113. https://doi.org/10.1016/j.buildenv.2013.07.005

Apte, J.S., Messier, K.P., Gani, S., Brauer, M., Kirchstetter, T.W., Lunden, M.M., Marshall, J.D., Portier, C.J., Vermeulen, R.C.H., Hamburg, S.P., 2017. High-Resolution Air Pollution Mapping with Google Street View Cars: Exploiting Big Data. Environ. Sci. Technol. 51, 6999–7008. https://doi.org/10.1021/acs.est.7b00891

Ardon-Dryer, K., Dryer, Y., Williams, J.N., Moghimi, N., 2020. Measurements of $PM_{2.5}$ with PurpleAir under atmospheric conditions. Atmospheric Measurement Techniques 13, 5441–5458. https://doi.org/10.5194/amt-13-5441-2020

Aurell, J., Gullett, B.K., 2013. Emission Factors from Aerial and Ground Measurements of Field and Laboratory Forest Burns in the Southeastern U.S.: PM2.5, Black and Brown Carbon, VOC, and PCDD/PCDF. Environ. Sci. Technol. 47, 8443–8452. https://doi.org/10.1021/es402101k

Barkjohn, K.K., Gantt, B., Clements, A.L., 2021a. Development and application of a United States-wide correction for $PM_{2.5}$ data collected with the PurpleAir sensor. Atmospheric Measurement Techniques 14, 4617–4637. https://doi.org/10.5194/amt-14-4617-2021

Barkjohn, K.K., Norris, C., Cui, X., Fang, L., Zheng, T., Schauer, J.J., Li, Z., Zhang, Y., Black, M., Zhang, J. (Jim), Bergin, M.H., 2021b. Real-time measurements of PM2.5 and ozone to assess the effectiveness of residential indoor air filtration in Shanghai homes. Indoor Air 31, 74–87. https://doi.org/10.1111/ina.12716

Battles, J.J., Dushoff, J.G., Fahey, T.J., 1996. Line intersect sampling of forest canopy gaps. Forest Science 42, 131–138.
Baxter, L.K., Stallings, C., Smith, L., Burke, J., 2017. Probabilistic estimation of residential air exchange rates for population-based human exposure modeling. J Expo Sci Environ Epidemiol 27, 227–234. https://doi.org/10.1038/jes.2016.49
Bhangar, S., Mullen, N.A., Hering, S.V., Kreisberg, N.M., Nazaroff, W.W., 2011. Ultrafine particle concentrations and exposures in seven residences in northern California. Indoor Air 21, 132–144. https://doi.org/10.1111/j.1600-0668.2010.00689.x
Bi, J., Wallace, L.A., Sarnat, J.A., Liu, Y., 2021. Characterizing outdoor infiltration and indoor contribution of PM2.5 with citizen-based low-cost monitoring data. Environmental Pollution 276, 116763. https://doi.org/10.1016/j.envpol.2021.116763
Bi, J., Wildani, A., Chang, H.H., Liu, Y., 2020. Incorporating Low-Cost Sensor Measurements into High-Resolution PM2.5 Modeling at a Large Spatial Scale. Environ. Sci. Technol. 54, 2152–2162. https://doi.org/10.1021/acs.est.9b06046
Bond, T.C., Streets, D.G., Yarber, K.F., Nelson, S.M., Woo, J.-H., Klimont, Z., 2004. A technology-based global inventory of black and organic carbon emissions from combustion. Journal of Geophysical Research: Atmospheres 109. https://doi.org/10.1029/2003JD003697
Brown, J.K., 1974. Handbook for Inventorying Downed Woody Material. USDA Forest Service: General Technical Report INT-16.
Bustic, V., McCann, H., Axelson, J., Gray, B., Mount, J., Stephens, S., Stewart, W., 2017. Improving the Health of California's Headwater Forests, Public Policy Institute of California.
California Air Resources Board, 2015. Compliance Offset Protocol U.S. Forest Projects.
California Energy Commission, 2008. Building Energy Efficiency Standards [WWW Document]. California Energy Commission. URL https://www.energy.ca.gov/programs-and-topics/programs/building-energy-efficiency-standards (accessed 8.31.23).
Campbell, J., Alberti, G., Martin, J., Law, B.E., 2009. Carbon dynamics of a ponderosa pine plantation following a thinning treatment in the northern Sierra Nevada. Forest Ecology and Management 257, 453–463. https://doi.org/10.1016/j.foreco.2008.09.021
Caubel, J.J., Cados, T.E., Kirchstetter, T.W., 2018. A New Black Carbon Sensor for Dense Air Quality Monitoring Networks. Sensors 18, 738. https://doi.org/10.3390/s18030738
Chan, W.R., Nazaroff, W.W., Price, P.N., Sohn, M.D., Gadgil, A.J., 2005. Analyzing a database of residential air leakage in the United States. Atmospheric Environment 39, 3445–3455. https://doi.org/10.1016/j.atmosenv.2005.01.062
Chen, C., Zhao, B., 2011. Review of relationship between indoor and outdoor particles: I/O ratio, infiltration factor and penetration factor. Atmospheric Environment 45, 275–288. https://doi.org/10.1016/j.atmosenv.2010.09.048
Collins, B.M., Everett, R.G., Stephens, S.L., 2011. Impacts of fire exclusion and recent managed fire on forest structure in old growth Sierra Nevada mixed-conifer forests. Ecosphere 2, 1–14.
Delp, W.W., Singer, B.C., 2020. Wildfire Smoke Adjustment Factors for Low-Cost and Professional PM2.5 Monitors with Optical Sensors. Sensors 20, 3683. https://doi.org/10.3390/s20133683

Dennison, P.E., Brewer, S.C., Arnold, J.D., Moritz, M.A., 2014. Large wildfire trends in the western United States, 1984–2011. Geophysical Research Letters 41, 2928–2933. https://doi.org/10.1002/2014GL059576

Dettinger, M.D., Alpert, H., Battles, J.J., Kusel, J., Safford, H.D., Fougeres, D., Knight, C., Miller, L., Sawyer, S., 2018. Sierra Nevada Region Report: California's Fourth Climate Change Assessment.

Diapouli, E., Chaloulakou, A., Koutrakis, P., 2013. Estimating the concentration of indoor particles of outdoor origin: A review. Journal of the Air & Waste Management Association 63, 1113–1129. https://doi.org/10.1080/10962247.2013.791649

Dreyfus, G.B., 2002. Observational constraints on the contribution of isoprene oxidation to ozone production on the western slope of the Sierra Nevada, California. J. Geophys. Res. 107, 4365. https://doi.org/10.1029/2001JD001490

Eksi, G., Kurbanoglu, S., Erdem, S.A., 2020. Analysis of diterpenes and diterpenoids. Recent Advances in Natural Products Analysis 313–345, 313–345. https://doi.org/10.1016/B978-0-12-816455-6.00009-3

Emerson, E.W., Katich, J.M., Schwarz, J.P., McMeeking, G.R., Farmer, D.K., 2018. Direct Measurements of Dry and Wet Deposition of Black Carbon Over a Grassland. Journal of Geophysical Research: Atmospheres 123, 12,277-12,290. https://doi.org/10.1029/2018JD028954

EPA, 2022. Emission Factor Determination by the Carbon Balance Method (No. OTM-48).

Erhorn, H., 1988. Influence of meteorological conditions on inhabitants' behaviour in dwellings with mechanical ventilation. Energy and Buildings 11, 267–275. https://doi.org/10.1016/0378-7788(88)90042-4

Ferro, A.R., Kopperud, R.J., Hildemann, L.M., 2004. Source Strengths for Indoor Human Activities that Resuspend Particulate Matter. Environ. Sci. Technol. 38, 1759–1764. https://doi.org/10.1021/es0263893

Finewax, Z., De Gouw, J.A., Ziemann, P.J., 2018. Identification and Quantification of 4-Nitrocatechol Formed from OH and NO3 Radical-Initiated Reactions of Catechol in Air in the Presence of NOx: Implications for Secondary Organic Aerosol Formation from Biomass Burning. Environmental Science and Technology 52, 1981–1989. https://doi.org/10.1021/acs.est.7b05864

Fredrickson, C.D., Palm, B.B., Lee, B.H., Zhang, X., Orlando, J.J., Tyndall, G.S., Garofalo, L.A., Pothier, M.A., Farmer, D.K., Decker, Z.C.J., Robinson, M.A., Brown, S.S., Murphy, S.M., Shen, Y., Sullivan, A.P., Schobesberger, S., Thornton, J.A., 2022. Formation and Evolution of Catechol-Derived SOA Mass, Composition, Volatility, and Light Absorption. ACS Earth and Space Chemistry. https://doi.org/10.1021/acsearthspacechem.2c00007

Fulé, P.Z., Crouse, J.E., Roccaforte, J.P., Kalies, E.L., 2012. Do thinning and/or burning treatments in western USA ponderosa or Jeffrey pine-dominated forests help restore natural fire behavior? For.Ecol.Manage. 269, 68–81.

Goldstein, A.H., Nazaroff, W.W., Weschler, C.J., Williams, J., 2021. How Do Indoor Environments Affect Air Pollution Exposure? Environ. Sci. Technol. 55, 100–108. https://doi.org/10.1021/acs.est.0c05727

Hardy, C.C., Ottmar, R.D., Peterson, J.L., Core, J.E., Seamon, Paula, 2001. Smoke Management Guide for Prescrbied and Wildland Fire. National Widlfire Coordinating Group.

Hatch, L.E., Jen, C.N., Kreisberg, N.M., Selimovic, V., Yokelson, R.J., Stamatis, C., York, R.A., Foster, D., Stephens, S.L., Goldstein, A.H., Barsanti, K.C., 2019. Highly Speciated Measurements of Terpenoids Emitted from Laboratory and Mixed-Conifer Forest Prescribed Fires. ENVIRONMENTAL SCIENCE & TECHNOLOGY 53, 9418–9428. https://doi.org/10.1021/acs.est.9b02612

Hatch, L.E., Luo, W., Pankow, J.F., Yokelson, R.J., Stockwell, C.E., Barsanti, K.C., 2015. Identification and quantification of gaseous organic compounds emitted from biomass burning using two-dimensional gas chromatography-time-of-flight mass spectrometry. ATMOSPHERIC CHEMISTRY AND PHYSICS 15, 1865–1899. https://doi.org/10.5194/acp-15-1865-2015

Hatch, L.E., Yokelson, R.J., Stockwell, C.E., Veres, P.R., Simpson, I.J., Blake, D.R., Orlando, J.J., Barsanti, K.C., 2017. Multi-instrument comparison and compilation of non-methane organic gas emissions from biomass burning and implications for smoke-derived secondary organic aerosol precursors. ATMOSPHERIC CHEMISTRY AND PHYSICS 17, 1471–1489. https://doi.org/10.5194/acp-17-1471-2017

Hennigan, C.J., Miracolo, M.A., Engelhart, G.J., May, A.A., Presto, A.A., Lee, T., Sullivan, A.P., McMeeking, G.R., Coe, H., Wold, C.E., Hao, W.M., Gilman, J.B., Kuster, W.C., de Gouw, J., Schichtel, B.A., Collett, J.L., Kreidenweis, S.M., Robinson, A.L., 2011. Chemical and physical transformations of organic aerosol from the photo-oxidation of open biomass burning emissions in an environmental chamber. Atmospheric Chemistry and Physics 11, 7669–7686. https://doi.org/10.5194/acp-11-7669-2011

Hiers, J.K., O'Brien, J.J., Varner, J.M., Butler, B.W., Dickinson, M., Furman, J., Gallagher, M., Godwin, D., Goodrick, S.L., Hood, S.M., Hudak, A., Kobziar, L.N., Linn, R., Loudermilk, E.L., McCaffrey, S., Robertson, K., Rowell, E.M., Skowronski, N., Watts, A.C., Yedinak, K.M., 2020. Prescribed fire science: the case for a refined research agenda. Fire Ecology 16, 11. https://doi.org/10.1186/s42408-020-0070-8

Holder, A.L., Mebust, A.K., Maghran, L.A., McGown, M.R., Stewart, K.E., Vallano, D.M., Elleman, R.A., Baker, K.R., 2020. Field Evaluation of Low-Cost Particulate Matter Sensors for Measuring Wildfire Smoke. Sensors 20, 4796. https://doi.org/10.3390/s20174796

Holzinger, R., Lee, A., McKay, M., Goldstein, A.H., 2006. Seasonal variability of monoterpene emission factors for a Ponderosa pine plantation in California. Atmos. Chem. Phys.

Intergovernmental Panel On Climate Change, 2023. Climate Change 2021 – The Physical Science Basis: Working Group I Contribution to the Sixth Assessment Report of the Intergovernmental Panel on Climate Change, 1st ed. Cambridge University Press. https://doi.org/10.1017/9781009157896

Jacobson, M.Z., 1999. Isolating nitrated and aromatic aerosols and nitrated aromatic gases as sources of ultraviolet light absorption. Journal of Geophysical Research Atmospheres 104, 3527–3542. https://doi.org/10.1029/1998JD100054

Jaffe, D.A., O'Neill, S.M., Larkin, N.K., Holder, A.L., Peterson, D.L., Halofsky, J.E., Rappold, A.G., 2020. Wildfire and prescribed burning impacts on air quality in the United States. Journal of the Air and Waste Management Association 70, 583–615. https://doi.org/10.1080/10962247.2020.1749731

Jen, C.N., Hatch, L.E., Selimovic, V., Yokelson, R.J., Weber, R., Fernandez, A.E., Kreisberg, N.M., Barsanti, K.C., Goldstein, A.H., 2019. Speciated and total emission factors of particulate organics from burning western US wildland fuels and their dependence on

combustion efficiency. ATMOSPHERIC CHEMISTRY AND PHYSICS 19, 1013–1026. https://doi.org/10.5194/acp-19-1013-2019

Jen, C.N., Liang, Y., Hatch, L.E., Kreisberg, N.M., Stamatis, C., Kristensen, K., Battles, J.J., Stephens, S.L., York, R.A., Barsanti, K.C., Goldstein, A.H., 2018. High Hydroquinone Emissions from Burning Manzanita. ENVIRONMENTAL SCIENCE & TECHNOLOGY LETTERS 5, 309–314. https://doi.org/10.1021/acs.estlett.8b00222

Jenkins, J.C., Chojnacky, D.C., Heath, L.S., Birdsey, R.A., 2003. National-Scale Biomass Estimators for United States Tree Species.

Jimenez, J., Claiborn, C., Larson, T., Gould, T., Kirchstetter, T.W., Gundel, L., 2007. Loading Effect Correction for Real-Time Aethalometer Measurements of Fresh Diesel Soot. Journal of the Air & Waste Management Association 57, 868–873. https://doi.org/10.3155/1047-3289.57.7.868

John, W., Reischl, G., 1980. A Cyclone for Size-Selective Sampling of Ambient Air. Journal of the Air Pollution Control Association 30, 872–876. https://doi.org/10.1080/00022470.1980.10465122

Jolleys, M.D., Coe, H., McFiggans, G., Capes, G., Allan, J.D., Crosier, J., Williams, P.I., Allen, G., Bower, K.N., Jimenez, J.L., Russell, L.M., Grutter, M., Baumgardner, D., 2012. Characterizing the Aging of Biomass Burning Organic Aerosol by Use of Mixing Ratios: A Meta-analysis of Four Regions. Environmental Science & Technology 46, 13093–13102. https://doi.org/10.1021/es302386v

Karner, A.A., Eisinger, D.S., Niemeier, D.A., 2010. Near-Roadway Air Quality: Synthesizing the Findings from Real-World Data. Environ. Sci. Technol. 44, 5334–5344. https://doi.org/10.1021/es100008x

Keane, R.E., Lutes, D., 2018. First-Order Fire Effects Model (FOFEM), in: Manzello, S.L. (Ed.), Encyclopedia of Wildfires and Wildland-Urban Interface (WUI) Fires. Springer International Publishing, Cham, pp. 1–5. https://doi.org/10.1007/978-3-319-51727-8_74-1

Kirchstetter, T.W., Novakov, T., 2007. Controlled generation of black carbon particles from a diffusion flame and applications in evaluating black carbon measurement methods. Atmospheric Environment 41, 1874–1888. https://doi.org/10.1016/j.atmosenv.2006.10.067

Kirchstetter, T.W., Novakov, T., Hobbs, P.V., 2004. Evidence that the spectral dependence of light absorption by aerosols is affected by organic carbon. Journal of Geophysical Research: Atmospheres 109. https://doi.org/10.1029/2004JD004999

Klepeis, N.E., Nelson, W.C., Ott, W.R., Robinson, J.P., Tsang, A.M., Switzer, P., Behar, J.V., Hern, S.C., Engelmann, W.H., 2001. The National Human Activity Pattern Survey (NHAPS): a resource for assessing exposure to environmental pollutants. J Expo Sci Environ Epidemiol 11, 231–252. https://doi.org/10.1038/sj.jea.7500165

Knapp, E.E., Keeley, J.E., Ballenger, E.A., Brennan, T.J., 2005. Fuel reduction and coarse woody debris dynamics with early season and late season prescribed fire in a Sierra Nevada mixed conifer forest. Forest Ecology and Management 208, 383–397. https://doi.org/10.1016/j.foreco.2005.01.016

Krokene, P., 2015. Conifer Defense and Resistance to Bark Beetles. Bark Beetles: Biology and Ecology of Native and Invasive Species 177–207. https://doi.org/10.1016/B978-0-12-417156-5.00005-8

Kuula, J., Mäkelä, T., Aurela, M., Teinilä, K., Varjonen, S., González, Ó., Timonen, H., 2020. Laboratory evaluation of particle-size selectivity of optical low-cost particulate matter sensors. Atmospheric Measurement Techniques 13, 2413–2423. https://doi.org/10.5194/amt-13-2413-2020

LANDFIRE Program [WWW Document], 2016. . LANDFIRE Program: Data Products - Fuel - Fuel Characteristic Classification System Fuelbeds. URL https://landfire.gov/fccs.php (accessed 8.31.23).

Larkin, N.K., Strand, T., Drury, S.A., Raffuse, S., Solomon, R., O'Neill, S.M., Wheeler, N., Huang, S., Rorig, M., Hafner, H.R., 2012. Phase 1 of the Smoke and Emissions Model Intercomparison Project (semip): Creation of Semip and Evaluation of Current Models (No. PROJECT #08-1-6-10).

Lena, T.S., Ochieng, V., Carter, M., Holgu, ín-V.J., Kinney, P.L., 2002. Elemental carbon and PM(2.5)levels in an urban community heavily impacted by truck traffic. Environmental Health Perspectives 110, 1009–1015. https://doi.org/10.1289/ehp.021101009

Levine, J.I., Collins, B.M., York, R.A., Foster, D.E., Fry, D.L., Stephens, S.L., Levine, J.I., Collins, B.M., York, R.A., Foster, D.E., Fry, D.L., Stephens, S.L., 2020. Forest stand and site characteristics influence fuel consumption in repeat prescribed burns. Int. J. Wildland Fire 29, 148–159. https://doi.org/10.1071/WF19043

Liang, YT, Jen, C., Weber, R., Misztal, P., Goldstein, A., 2021. Chemical composition of PM2.5 in October 2017 Northern California wildfire plumes. ATMOSPHERIC CHEMISTRY AND PHYSICS 21, 5719–5737. https://doi.org/10.5194/acp-21-5719-2021

Liang, Yutong, Sengupta, D., Campmier, M.J., Lunderberg, D.M., Apte, J.S., Goldstein, A.H., 2021. Wildfire smoke impacts on indoor air quality assessed using crowdsourced data in California. Proceedings of the National Academy of Sciences 118, e2106478118. https://doi.org/10.1073/pnas.2106478118

Liang, Y., Stamatis, C., Fortner, E.C., Wernis, R.A., Van Rooy, P., Majluf, F., Yacovitch, T., I., Daube, C., Herndon, S.C., Kreisberg, N.M., Barsanti, K.C., Goldstein, A.H., 2022. Emissions of organic compounds from western US wildfires and their near-fire transformations. ATMOSPHERIC CHEMISTRY AND PHYSICS 22, 9877–9893. https://doi.org/10.5194/acp-22-9877-2022

Liu, C., Chung, C.E., Yin, Y., Schnaiter, M., 2018. The absorption Ångström exponent of black carbon: from numerical aspects. Atmospheric Chemistry and Physics 18, 6259–6273. https://doi.org/10.5194/acp-18-6259-2018

Liu, Y., Kochanski, A., Baker, K.R., Mell, W., Linn, R., Paugam, R., Mandel, J., Fournier, A., Jenkins, M.A., Goodrick, S., Achtemeier, G., Zhao, F., Ottmar, R., French, N.H.F., Larkin, N., Brown, T., Hudak, A., Dickinson, M., Potter, B., Clements, C., Urbanski, S., Prichard, S., Watts, A., McNamara, D., Liu, Y., Kochanski, A., Baker, K.R., Mell, W., Linn, R., Paugam, R., Mandel, J., Fournier, A., Jenkins, M.A., Goodrick, S., Achtemeier, G., Zhao, F., Ottmar, R., French, N.H.F., Larkin, N., Brown, T., Hudak, A., Dickinson, M., Potter, B., Clements, C., Urbanski, S., Prichard, S., Watts, A., McNamara, D., 2019. Fire behaviour and smoke modelling: model improvement and measurement needs for next-generation smoke research and forecasting systems. Int. J. Wildland Fire 28, 570–588. https://doi.org/10.1071/WF18204

Lydersen, J.M., Collins, B.M., Ewell, C.M., Reiner, A.L., Fites, J.A., Dow, C.B., Gonzalez, P., Saah, D.S., Battles, J.J., 2014. Using field data to assess model predictions of surface and

ground fuel consumption by wildfire in coniferous forests of California. Journal of Geophysical Research: Biogeosciences 119, 223–235.
McClure, C., Jaffe, D., 2018. Investigation of high ozone events due to wildfire smoke in an urban area. ATMOSPHERIC ENVIRONMENT 194, 146–157. https://doi.org/10.1016/j.atmosenv.2018.09.021
McGinnis, T., Shook, C., Keeley, J., 2010. Estimating aboveground biomass for broadleaf woody plants and young conifers in Sierra Nevada, California, forests. Western Journal of Applied Forestry 25, 203–209.
McMeeking, G.R., Kreidenweis, S.M., Baker, S., Carrico, C.M., Chow, J.C., Collett, J.L., Hao, W.M., Holden, A.S., Kirchstetter, T.W., Malm, W.C., Moosmuller, H., Sullivan, A.P., Wold, C.E., 2009. Emissions of trace gases and aerosols during the open combustion of biomass in the laboratory. Journal of Geophysical Research: Atmospheres 114, n/a-n/a. https://doi.org/10.1029/2009JD011836
Nelson, R.M., 1982. An evaluation of the carbon balance technique for estimating emission factors and fuel consumption in forest fires (No. SE-RP-231). U.S. Department of Agriculture, Forest Service, Southeastern Forest Experiment Station, Asheville, NC. https://doi.org/10.2737/SE-RP-231
Nolte, C.G., Schauer, J.J., Cass, G.R., Simoneit, B.R.T., 2001. Highly polar organic compounds present in wood smoke and in the ambient atmosphere. Environmental Science and Technology 35, 1912–1919. https://doi.org/10.1021/es001420r
North, M., Hurteau, M., Innes, J., 2009. Fire suppression and fuels treatment effects on mixed-conifer carbon stocks and emissions. Ecological Applications 19, 1385–1396. https://doi.org/10.1890/08-1173.1
North, M.P., Hurteau, M.D., 2011. High-severity wildfire effects on carbon stocks and emissions in fuels treated and untreated forest. Forest Ecology and Management 261, 1115–1120. https://doi.org/10.1016/j.foreco.2010.12.039
O'Dell, K., Ford, B., Fischer, E.V., Pierce, J.R., 2019. Contribution of Wildland-Fire Smoke to US PM2.5 and Its Influence on Recent Trends. Environ. Sci. Technol. 53, 1797–1804. https://doi.org/10.1021/acs.est.8b05430
Ott, W., Wallace, L., Mage, D., 2000. Predicting Particulate (PM10) Personal Exposure Distributions Using a Random Component Superposition Statistical Model. Journal of the Air & Waste Management Association 50, 1390–1406. https://doi.org/10.1080/10473289.2000.10464169
Patel, S., Sankhyan, S., Boedicker, E.K., DeCarlo, P.F., Farmer, D.K., Goldstein, A.H., Katz, E.F., Nazaroff, W.W., Tian, Y., Vanhanen, J., Vance, M.E., 2020. Indoor Particulate Matter during HOMEChem: Concentrations, Size Distributions, and Exposures. Environ. Sci. Technol. 54, 7107–7116. https://doi.org/10.1021/acs.est.0c00740
Penman, J., Gytarsky, M., Hiraishi, T., Krug, T., Kruger, D., Pipatti, R., Buendia, L., Miwa, K., Ngara, T., Tanabe, K., 2003. Good Practice Guidance for Land Use, Land-Use Change and Forestry. Institute for Global Environmental Strategies IGES, Japan.
Permar, W., Wang, Q., Selimovic, V., Wielgasz, C., Yokelson, R., Hornbrook, R., Hills, A., Apel, E., Ku, T., Zhou, Y., Sive, B., Sullivan, A., Collett, J., Campos, T., Palm, B., Peng, Q., Thornton, J., Garofalo, L., Farmer, D., Kreidenweis, S., Levin, E., DeMott, P., Flocke, F., Fischer, E., Hu, L., 2021. Emissions of Trace Organic Gases From Western US Wildfires Based on WE-CAN Aircraft Measurements. JOURNAL OF

GEOPHYSICAL RESEARCH-ATMOSPHERES 126. https://doi.org/10.1029/2020JD033838
Prichard, S., O'Neill, S., Eagle, P., Andreu, A., Drye, B., Dubowy, J., Urbanski, S., Strand, T., 2020. Wildland fire emission factors in North America: synthesis of existing data, measurement needs and management applications. INTERNATIONAL JOURNAL OF WILDLAND FIRE 29, 132–147. https://doi.org/10.1071/WF19066
Ramage, M.H., Burridge, H., Busse-Wicher, M., Fereday, G., Reynolds, T., Shah, D.U., Wu, G., Yu, L., Fleming, P., Densley-Tingley, D., Allwood, J., Dupree, P., Linden, P.F., Scherman, O., 2017. The wood from the trees: The use of timber in construction. Renewable and Sustainable Energy Reviews 68, 333–359. https://doi.org/10.1016/J.RSER.2016.09.107
Ramdahl, T., 1983. Retene - a molecular marker of wood combustion in ambient air. Nature 306, 580–582. https://doi.org/10.1038/306580a0
Reid C. E., Brauer Michael, Johnston Fay H., Jerrett Michael, Balmes John R., Elliott Catherine T., 2016. Critical Review of Health Impacts of Wildfire Smoke Exposure. Environmental Health Perspectives 124, 1334–1343. https://doi.org/10.1289/ehp.1409277
Reinhardt, E.D., Dickinson, M.B., 2010. First-Order Fire Effects Models for Land Management: Overview and Issues. fire ecol 6, 131–142. https://doi.org/10.4996/fireecology.0601131
Residential Energy Consumption Survey (RECS), 2015.
Riebau, A.R., Fox, D., 2001. The new smoke management. Int. J. Wildland Fire 10, 415–427. https://doi.org/10.1071/wf01039
Riley, W.J., McKone, T.E., Lai, A.C.K., Nazaroff, W.W., 2002. Indoor Particulate Matter of Outdoor Origin: Importance of Size-Dependent Removal Mechanisms. Environ. Sci. Technol. 36, 200–207. https://doi.org/10.1021/es010723y
Roos, M., Pope, K., Stevenson, R., 2018. Climate Justice Summary Report. California's Fourth Climate Change Assessment:SUM-CCCA4-2018-012.
Safford, H.D., Paulson, A.K., Steel, Z.L., Young, D.J.N., Wayman, R.B., 2022. The 2020 California fire season: A year like no other, a return to the past or a harbinger of the future? Global Ecology and Biogeography 31, 2005–2025. https://doi.org/10.1111/geb.13498
Safford, H.D., Stevens, J.T., 2017. Natural range of variation for yellow pine and mixed-conifer forests in the Sierra Nevada, southern Cascades, and Modoc and Inyo National Forests, California, USA (No. PSW-GTR-256). U.S. Department of Agriculture, Forest Service, Pacific Southwest Research Station, Albany, CA. https://doi.org/10.2737/PSW-GTR-256
Scott, J.H., Burgan, R.E., 2005. Standard fire behavior fuel models: a comprehensive set for use with Rothermel's surface fire spread model (No. RMRS-GTR-153). U.S. Department of Agriculture, Forest Service, Rocky Mountain Research Station, Ft. Collins, CO. https://doi.org/10.2737/RMRS-GTR-153
Sengupta, D., Samburova, V., Bhattarai, C., Watts, A.C., Moosmüller, H., Khlystov, A.Y., 2020. Polar semivolatile organic compounds in biomass-burning emissions and their chemical transformations during aging in an oxidation flow reactor. Atmospheric Chemistry and Physics 20, 8227–8250. https://doi.org/10.5194/acp-20-8227-2020
Shahid, S. B., Yokelson, R. Y., Weidinmyer, C. W., Barsanti, K. C., in prep. Next-generation Emissions Inventory Expansion of Akagi: NEIVAv1. GEOSCIENTIFIC MODEL DEVELOPMENT.

Shusterman, A.A., Kim, J., Lieschke, K.J., Newman, C., Wooldridge, P.J., Cohen, R.C., 2018. Observing local CO_2 sources using low-cost, near-surface urban monitors. Atmospheric Chemistry and Physics 18, 13773–13785. https://doi.org/10.5194/acp-18-13773-2018

Simoneit, B.R.T., 2002. Biomass burning - A review of organic tracers for smoke from incomplete combustion. Applied Geochemistry. https://doi.org/10.1016/S0883-2927(01)00061-0

Simoneit, B.R.T., Medeiros, P.M., Didyk, B.M., 2005. Combustion products of plastics as indicators for refuse burning in the atmosphere. Environmental Science and Technology 39, 6961–6970. https://doi.org/10.1021/es050767x

Simonelt, B.R.T., Rogge, W.F., Mazurek, M.A., Standley, L.J., Hildemann, L.M., Cass, G.R., 1993. Lignin Pyrolysis Products, Lignans, and Resin Acids as Specific Tracers of Plant Classes in Emissions from Biomass Combustion. Environmental Science and Technology 27, 2533–2541. https://doi.org/10.1021/es00048a034

Singer, B.C., Chan, W.R., Kim, Y.-S., Offermann, F.J., Walker, I.S., 2020. Indoor air quality in California homes with code-required mechanical ventilation. Indoor Air 30, 885–899. https://doi.org/10.1111/ina.12676

Stamatis, C., Barsanti, K.C., 2022. Development and application of a supervised pattern recognition algorithm for identification of fuel-specific emissions profiles. ATMOSPHERIC MEASUREMENT TECHNIQUES 15, 2591–2606. https://doi.org/10.5194/amt-15-2591-2022

Standley, L.J., Simoneit, B.R.T., 1994. Resin diterpenoids as tracers for biomass combustion aerosols. Journal of Atmospheric Chemistry 18, 1–15. https://doi.org/10.1007/BF00694371

Stephens, B., Siegel, J.A., 2012. Penetration of ambient submicron particles into single-family residences and associations with building characteristics. Indoor Air 22, 501–513. https://doi.org/10.1111/j.1600-0668.2012.00779.x

Stephens, S.L., 2001. Fire history differences in adjacent Jeffrey pine and upper montane forests in the eastern Sierra Nevada. Int.J.Wildland Fire 10, 161–167.

Stephens, S.L., Burrows, N., Buyantuyev, A., Gray, R.W., Keane, R.E., Kubian, R., Liu, S., Seijo, F., Shu, L., Tolhurst, K.G., 2014. Temperate and boreal forest mega-fires: characteristics and challenges. Frontiers in Ecology and the Environment 12, 115–122.

Stephens, S.L., Collins, B.M., Roller, G., 2012. Fuel treatment longevity in a Sierra Nevada mixed conifer forest. Forest Ecology and Management 285, 204–212. https://doi.org/10.1016/j.foreco.2012.08.030

Stephens, S.L., Moghaddas, J.J., 2005a. Experimental fuel treatment impacts on forest structure, potential fire behavior, and predicted tree mortality in a California mixed conifer forest. For.Ecol.Manage. 215, 21–36.

Stephens, S.L., Moghaddas, J.J., 2005b. Silvicultural and reserve impacts on potential fire behavior and forest conservation: Twenty-five years of experience from Sierra Nevada mixed conifer forests. Biological Conservation 125, 369–379. https://doi.org/10.1016/j.biocon.2005.04.007

Stephens, S.L., Moghaddas, J.J., Edminster, C., Fiedler, C.E., Haase, S., Harrington, M., Keeley, J.E., Knapp, E.E., McIver, J.D., Metlen, K., Skinner, C.N., Youngblood, A., 2009. Fire treatment effects on vegetation structure, fuels, and potential fire severity in western U.S. forests. Ecological Applications 19, 305–320. https://doi.org/10.1890/07-1755.1

Sullivan, A.P., May, A.A., Lee, T., McMeeking, G.R., Kreidenweis, S.M., Akagi, S.K., Yokelson, R.J., Urbanski, S.P., Collett Jr., J.L., 2014. Airborne characterization of smoke marker ratios from prescribed burning. Atmospheric Chemistry and Physics 14, 10535–10545. https://doi.org/10.5194/acp-14-10535-2014

Tian, Y., Arata, C., Boedicker, E., Lunderberg, D.M., Patel, S., Sankhyan, S., Kristensen, K., Misztal, P.K., Farmer, D.K., Vance, M., Novoselac, A., Nazaroff, W.W., Goldstein, A.H., 2021. Indoor emissions of total and fluorescent supermicron particles during HOMEChem. Indoor Air 31, 88–98. https://doi.org/10.1111/ina.12731

Tiitta, P., Raunemaa, T., Tissari, J., Yli-Tuomi, T., Leskinen, A., Kukkonen, J., Härkönen, J., Karppinen, A., 2002. Measurements and modelling of PM2.5 concentrations near a major road in Kuopio, Finland. Atmospheric Environment 36, 4057–4068. https://doi.org/10.1016/S1352-2310(02)00309-6

Urbanski, S., 2014. Wildland fire emissions, carbon, and climate: Emission factors. FOREST ECOLOGY AND MANAGEMENT 317, 51–60. https://doi.org/10.1016/j.foreco.2013.05.045

US Census Bureau, 2019. 2019 Characteristics of New Housing [WWW Document]. Census.gov. URL https://www.census.gov/newsroom/press-releases/2020/new-housing.html (accessed 8.31.23).

USDA, 2023. Tools and Data - Forest Inventory and Analysis National Program [WWW Document]. URL https://www.fia.fs.usda.gov/tools-data/index.php (accessed 8.4.23).

Vaillant, N.M., Fites-Kaufman, J., Reiner, A.L., Noonan-Wright, E.K., Dailey, S.N., 2009. Effect of Fuel Treatments on Fuels and Potential Fire Behavior in California, USA, National Forests. fire ecol 5, 14–29. https://doi.org/10.4996/fireecology.0502014

van Mantgem, P.J., Stephenson, N.L., Knapp, E., Battles, J., Keeley, J.E., 2011. Long-term effects of prescribed fire on mixed conifer forest structure in the Sierra Nevada, California. Forest Ecology and Management 261, 989–994. https://doi.org/10.1016/j.foreco.2010.12.013

Van Wagdendonk, J.W., Benedict, J.M., Sydoriak, W.M., 1998. Fuel bed characteristics of Sierra Nevada conifers. Western Journal of Applied Forestry 13, 73–84.

Van Wagdendonk, J.W., Benedict, J.M., Sydoriak, W.M., 1996. Physical properties of woody fuel particles of Sierra Nevada conifers. Int.J.Wildland Fire 6, 117–123.

Van Wagner, C.E., 1982. PRACTICAL ASPECTS OF THE LINE INTERSECT METHOD.

Vilanova, E., Mortenson, L.A., Cox, L.E., Bulaon, B.M., Lydersen, J.M., Fettig, C.J., Battles, J.J., Axelson, J.N., 2023. Characterizing ground and surface fuels across Sierra Nevada forests shortly after the 2012–2016 drought. Forest Ecology and Management 537, 120945. https://doi.org/10.1016/j.foreco.2023.120945

Wallace, L., Williams, R., 2005. Use of Personal-Indoor-Outdoor Sulfur Concentrations to Estimate the Infiltration Factor and Outdoor Exposure Factor for Individual Homes and Persons. Environ. Sci. Technol. 39, 1707–1714. https://doi.org/10.1021/es049547u

Wegesser T. C., Pinkerton K. E., Last Jerold A., 2009. California Wildfires of 2008: Coarse and Fine Particulate Matter Toxicity. Environmental Health Perspectives 117, 893–897. https://doi.org/10.1289/ehp.0800166

Weise, D.R., Wright, C.S., 2014. Wildland fire emissions, carbon and climate: Characterizing wildland fuels. Forest Ecology and Management, Wildland fire emissions, carbon, and climate: Science overview and knowledge needs 317, 26–40. https://doi.org/10.1016/j.foreco.2013.02.037

Westerling, A.L., Hidalgo, H.G., Cayan, D.R., Swetnam, T.W., 2006. Warming and Earlier Spring Increase Western U.S. Forest Wildfire Activity. Science 313, 940–943. https://doi.org/10.1126/science.1128834

Wu, C., Yu, J.Z., 2018. Evaluation of linear regression techniques for atmospheric applications: the importance of appropriate weighting. Atmospheric Measurement Techniques 11, 1233–1250. https://doi.org/10.5194/amt-11-1233-2018

Wu, X. (May), Apte, M.G., Bennett, D.H., 2012. Indoor Particle Levels in Small- and Medium-Sized Commercial Buildings in California. Environ. Sci. Technol. 46, 12355–12363. https://doi.org/10.1021/es302140h

Xiang, J., Huang, C.-H., Shirai, J., Liu, Y., Carmona, N., Zuidema, C., Austin, E., Gould, T., Larson, T., Seto, E., 2021. Field measurements of PM2.5 infiltration factor and portable air cleaner effectiveness during wildfire episodes in US residences. Science of The Total Environment 773, 145642. https://doi.org/10.1016/j.scitotenv.2021.145642

Yan, D., O'Brien, W., Hong, T., Feng, X., Burak Gunay, H., Tahmasebi, F., Mahdavi, A., 2015. Occupant behavior modeling for building performance simulation: Current state and future challenges. Energy and Buildings 107, 264–278. https://doi.org/10.1016/j.enbuild.2015.08.032

Yee, L.D., Isaacman-VanWertz, G., Wernis, R.A., Meng, M., Rivera, V., Kreisberg, N.M., Hering, S.V., Bering, M.S., Glasius, M., Upshur, M.A., Gray Bé, A., Thomson, R.J., Geiger, F.M., Offenberg, J.H., Lewandowski, M., Kourtchev, I., Kalberer, M., de Sá, S., Martin, S.T., Alexander, M.L., Palm, B.B., Hu, W., Campuzano-Jost, P., Day, D.A., Jimenez, J.L., Liu, Y., McKinney, K.A., Artaxo, P., Viegas, J., Manzi, A., Oliveira, M.B., de Souza, R., Machado, L.A.T., Longo, K., Goldstein, A.H., 2018. Observations of sesquiterpenes and their oxidation products in central Amazonia during the wet and dry seasons. Atmospheric Chemistry and Physics 18, 10433–10457. https://doi.org/10.5194/acp-18-10433-2018

Yokelson, R.J., Burling, I.R., Gilman, J.B., Warneke, C., Stockwell, C.E., de Gouw, J., Akagi, S.K., Urbanski, S.P., Veres, P., Roberts, J.M., Kuster, W.C., Reardon, J., Griffith, D.W.T., Johnson, T.J., Hosseini, S., Miller, J.W., Cocker, D.R., Jung, H., Weise, D.R., 2013. Coupling field and laboratory measurements to estimate the emission factors of identified and unidentified trace gases for prescribed fires. Atmospheric Chemistry and Physics 13, 89–116. https://doi.org/10.5194/acp-13-89-2013

York, R.A., Battles, J.J., Wenk, R.C., Saah, D., 2012. A gap-based approach for regenerating pine species and reducing surface fuels in multi-aged mixed conifer stands in the Sierra Nevada, California. Forestry: An International Journal of Forest Research 85, 203–213. https://doi.org/10.1093/forestry/cpr058

York, R.A., Levine, J., Foster, D., Stephens, S., Collins, B., 2022. Silviculture can facilitate repeat prescribed burn programs with long-term strategies. Calif Agr 104–111. https://doi.org/10.3733/ca.2021a0016

Zhang, H., Yee, L.D., Lee, B.H., Curtis, M.P., Worton, D.R., Isaacman-VanWertz, G., Offenberg, J.H., Lewandowski, M., Kleindienst, T.E., Beaver, M.R., Holder, A.L., Lonneman, W.A., Docherty, K.S., Jaoui, M., Pye, H.O.T., Hu, W., Day, D.A., Campuzano-Jost, P., Jimenez, J.L., Guo, H., Weber, R.J., de Gouw, J., Koss, A.R., Edgerton, E.S., Brune, W., Mohr, C., Lopez-Hilfiker, F.D., Lutz, A., Kreisberg, N.M., Spielman, S.R., Hering, S.V., Wilson, K.R., Thornton, J.A., Goldstein, A.H., 2018. Monoterpenes are the largest source of summertime organic aerosol in the southeastern

United States. Proceedings of the National Academy of Sciences 115, 2038–2043. https://doi.org/10.1073/pnas.1717513115

Zheng, T., Bergin, M.H., Johnson, K.K., Tripathi, S.N., Shirodkar, S., Landis, M.S., Sutaria, R., Carlson, D.E., 2018. Field evaluation of low-cost particulate matter sensors in high- and low-concentration environments. Atmospheric Measurement Techniques 11, 4823–4846. https://doi.org/10.5194/amt-11-4823-2018

Zheng, T., Bergin, M.H., Sutaria, R., Tripathi, S.N., Caldow, R., Carlson, D.E., 2019. Gaussian process regression model for dynamically calibrating and surveilling a wireless low-cost particulate matter sensor network in Delhi. Atmospheric Measurement Techniques 12, 5161–5181. https://doi.org/10.5194/amt-12-5161-2019

Zhou, S., Collier, S., Jaffe, D.A., Briggs, N.L., Hee, J., Sedlacek III, A.J., Kleinman, L., Onasch, T.B., Zhang, Q., 2017. Regional influence of wildfires on aerosol chemistry in the western US and insights into atmospheric aging of biomass burning organic aerosol. Atmospheric Chemistry and Physics 17, 2477–2493. https://doi.org/10.5194/acp-17-2477-2017

Appendices

Chapter 8 Supplementary Information

8.4.1 Extended Materials and Methods

Data Sources and Study Regions. The PurpleAir sensors report the mass of size-resolved particulate matter, as well as environmental parameters such as temperature and relative humidity (RH). Data from many of these sensors are voluntarily shared online by the owners (including the citizens, and government agencies like the California Air Resources Board, Bay Area Air Quality Management District and Southern California Air Resource Board). For this study we downloaded the 10-min average $PM_{2.5}$ concentration data from the PurpleAir website (https://www2.purpleair.com/). For the NC 2020 case, we used data from the areas boxed by latitudes [38.77º N, 38.04º N] and longitudes [123.19º W, 121.15º W]; [38.04º N, 37.98º N] and [123.19º W, 121.60º W]; [37.98º N, 37.67º N] and [122.69º W, 121.90º W]; [37.67º N, 37.21º N] and [122.47º W, 121.36ºW] for August and September 2020 (Figure S8.2). These boxes cover most of the San Francisco Bay Area and part of the Sacramento County. In this period, residents in this area experienced smoky days caused by the LNU Lightning Complex Fire, the August Complex Fire, the SCU Lightning Complex Fires, the CZU Lightning Complex Fires, and at the end of September the Glass Fire, as well as the massive fires in Oregon (https://www.fire.ca.gov/incidents/2020/). The same study area was used in the NC 2018 case, although fewer sensors were operating at that time. The study area for the SC 2020 case is boxed by [33.47º N, 34.50º N] and [116.85º W, 119.40º W], as shown in Figure S8.3.

Selection of Sensor Correction Models. Plantower sensors (Plantower Technology) used by PurpleAir measure the mass of particulate matter by measuring light scattering at 680±10 nm (Sayahi et al., 2019). The manufacturer has a proprietary algorithm to convert the light scattering signal to the mass concentration of particulate matter. The effective measurement range of $PM_{2.5}$ according to the manufacturer's product manual is 0-500 µg m^{-3}, with resolution of 1 µg m^{-3} (https://www.aqmd.gov/docs/default-source/aq-spec/resources-page/plantower-pmS8003-manual_v2-3.pdf). The response time of the sensors is less than or equal to 10 s. Each sensor is also embedded with a BME 280 sensor (Bosch Sensortec) to measure the temperature, pressure, and relative humidity in real time. The working temperature and relative humidity ranges are -10 to 60ºC and 0-99%, respectively. The performance of low-cost $PM_{2.5}$ sensors is dependent on humidity, temperature and level of particulate matters (Ardon-Dryer et al., 2020; Barkjohn et al., 2020a; Bi et al., 2020; Delp and Singer, 2020; Holder et al., 2020; Zheng et al., 2018). Many corrections have been proposed to convert the raw $PM_{2.5}$ data ($PM_{2.5}$ CF=1) measured by Plantower sensors to values consistent with research grade instruments. In our analysis, hourly average primary $PM_{2.5}$ data measured by 16 EPA Air Quality Measurement Stations (AQMSs) in August and September 2020 in the study area was downloaded from the EPA AirNow's API website (https://docs.airnowapi.org/). According to the California Air Resource Board (https://ww2.arb.ca.gov/our-work/programs/ambient-air-monitoring-regulatory/annual-monitoring-network-report), the primary $PM_{2.5}$ monitors in these sites are MetOne BAM (beta-ray attenuation) continuous monitors. For each EPA measurement site, we compared the data measured by outdoor PurpleAir sensors within 5 km (using at most 50 sensors near each EPA site to avoid data being skewed towards a small number of sites). We excluded outdoor sensors that (a) reporting less than 4 weeks of data. (b) had weak correlation with the EPA station's

measurement ($r < 0.8$) because it might be affected by other local pollution sources or it could be listed as an outdoor sensor by mistake, (c) reported $PM_{2.5}$ larger than 800 μg m^{-3} and sensors always reporting data lower than 10 μg m^{-3} as they were either malfunctioning or were operating outside of the recommended limits of detection. In total, data from 446 outdoor sensors surrounding the 16 EPA sites were included in the correction factor evaluation.

To get correction factors for converting PurpleAir sensor measurements to federal reference/equivalent method measurements, some studies performed a linear regression of $PM_{2.5}$ measured by the PurpleAir sensors with data from nearby EPA regulatory instruments ((Delp and Singer, 2020), while others also considered the effect of temperature and relative humidity on the sensor's performance ((Zheng et al., 2018; Barkjohn et al., 2021a, 2021b). There are two main types of PurpleAir sensors available for purchase on the PurpleAir website (https://www2.purpleair.com/collections/air-quality-sensors). The PA-I sensors only have one channel (Plantower PMS 1003) for PM measurement. Each PA-II PurpleAir sensor has two Plantower PMS 5003 sensors inside (Channel A and Channel B). Ideally, it is good to average the values reported by the two sensors and to remove some abnormal data because of sensor failures that can be captured by the difference of PM reported for the two channels. However, many sensors did not report $PM_{2.5}$ data from Channel B, presumably because they were the indoor PA-I sensor model. To incorporate as many sensors (buildings) as possible in the analysis, we only used Channel A data if data from both channels are available. According to the evaluation by Barkjohn et al. (8), the $PM_{2.5}$ concentrations reported by Channels A and B agree well. In line with this prior result, we compared 42 sensors with fully available Channel A and B data and found excellent agreement [slopes of linear fit between two channels' $PM_{2.5}$ data have IQR of (0.97, 1.06) with median at 1.01; R^2 of fit between two channels' $PM_{2.5}$ are all above 0.95]. More broadly, we believe that many instances of abnormal data are reliably excluded by our other QA/QC procedures (described in "Other QA and QC" section below). The sensors report both $PM_{2.5}$ CF = 1 data and $PM_{2.5}$ CF = ATM (atmospheric) data. It is not known how the CF = 1 data are converted to CF = ATM data in the proprietary algorithm from the manufacturer. However, it is known that the ATM data can result in a nonlinearity for concentrations below and above around 20-40 μg m^{-3} (Kelly et al., 2017; Malings et al., 2020), while CF = 1 data do not have this problem. The $PM_{2.5}$ CF = 1 data have also been shown to correlate better with the EPA federal reference methods or federal equivalent methods. The $PM_{2.5}$ CF = 1 data were therefore chosen as the raw input data in our calibration.

Seven correction methods were compared in our analysis, with their performance summarized in Table S8.1. Method 1 and 2 are based on linear regressions (ordinary least square method) of the EPA $PM_{2.5}$ data with the PurpleAir $PM_{2.5}$ CF = 1 data (of individual sensors, not the average of all sensors within 5 km of each AQMS). Method 3 uses an orthogonal distance regression (ODR) with zero intercept. The Barkjohn et al. (Barkjohn et al., 2021b) US fire correction was based on comparison of PurpleAir measurement data with collocated federal equivalent methods in 7 sites across the United States affected by prescribed fires, ambient aged fires, woodstove fires and wildfires. It considers the effect of relative humidity on the measurement. A similar field comparison was performed by Holder et al. (Holder et al., 2020). The correction factors from these two studies were also evaluated here for our dataset. We also constructed a "New fit incorporating RH" correction by a multivariate regression of EPA $PM_{2.5}$ against $PM_{2.5}$ and RH measured by nearby outdoor PurpleAir sensors using data in August and September 2020 from the San

Francisco Bay Area. In some studies, a nonlinear RH term $RH^2/(1-RH)$ was used (Zheng et al., 2018; Barkjohn et al., 2021b). However, recently it has been demonstrated that a linear term of RH can perform even better than the non-linear term (Barkjohn et al., 2021a). Therefore, the linear RH function is used in our "New fit incorporating RH" correction. Finally, using EPA $PM_{2.5}$ as the response, and $PM_{2.5}$ and RH reported by the nearby PurpleAir sensors as input, we trained a binary decision tree for regression model using the Statistics and Machine Learning Toolbox in MATLAB. The temperature term was not included in our correction models because it has been shown that including the temperature term can only negligibly improve the performance of such correction models ((Zheng et al., 2018; Barkjohn et al., 2021a). The commonly used Lane Regional Air Protection Agency (LRAPA) correction, which uses the CF = ATM data in the correction equation (Barkjohn et al., 2021a), was not compared here.

Adding a non-zero intercept to the model did not substantially improve the R^2 or reduce the root mean square error (RMSE). A major disadvantage of adding such an intercept is it can lead to an overestimation when the $PM_{2.5}$ concentration is very low. We also evaluated whether the linear regression of the EPA $PM_{2.5}$ data with the PurpleAir $PM_{2.5}$ (CF = 1) data are sensitive to the distance threshold. Table S8.2 shows that the regression coefficients are not very sensitive to the distance threshold from 2 km to 20 km.

In ordinary least square regression, it is assumed that the independent variable is free from errors (Wu and Yu, 2018). However, this assumption may not be true for PurpleAir sensor measurements. We therefore also calculated the slope using orthogonal distance regression (ODR). The ODR minimizes the sum of orthogonal distances of the data points from the regression line (Wu and Yu, 2018). Using the ODR method changed the correction factor by only 0.01 and increased the RMSE (Table S8.1). Adding RH in the linear regression also only made an almost negligible improvement. We therefore chose the linear regression without intercept correction. In this case, the fitted correction factor is 0.53. Figure S8.6 displays the hourly concentration time profiles of $PM_{2.5}$ measured by each EPA monitor in the San Francisco Bay Area, and the average concentrations of PurpleAir sensors (after correction with CF = 0.53) within 5 km in August and September 2020. They agree reasonably well with each other.

It is important to note that the correction equations evaluated here are only applicable for this analysis, and they should not be generalized to other places and/or at other times. As shown in Holder et al. (Holder et al., 2020), even the correction factors for wildfire smoke from different fires in the US can differ by a factor of more than 2. It is also worth noting that our analysis is not heavily dependent on the exact correction factor because the concentration ratios are the targets. The correction factors only affected which peaks were defined as indoor source peaks. When wildfire smoke affected a region, the composition of indoor and outdoor $PM_{2.5}$ were expected to be similar because wildfire particles dominated even in the indoor environments (Table 5.1). Therefore, it is reasonable to use the same correction for both indoor and outdoor $PM_{2.5}$, especially we focus on the indoor/outdoor ratios, as suggested by Bi et al. (Bi et al., 2021).

As shown in Table S8.1 and Figure S8.15, the binary decision tree method can improve the correlation of PurpleAir data with EPA measurements. Results from the same analysis with this correction are shown in Figure S8.16. The trend of the result is the same as the no-correction case,

but the difference between the fire days and non-fire days are larger, which is probably due to a non-zero intercept in the correction.

We also performed regression for the correction of Greater Los Angeles Area sensors (SC 2020 case). Based on linear regression of EPA monitor data with the nearby PurpleAir sensor using the same approach as in the NC 2020 case, a correction factor of $\beta_1 = 0.58$ was adopted (NRMSE = 0.42, see Figures S8.8-S8.9). Similar analysis has been performed by Delp and Singer (Delp and Singer, 2020) for San Francisco Bay Area sensors in November 2018. A correction factor of $\beta_1 = 0.48$ was adopted in our analysis.

Other QA and QC. We selected indoor sensors that had measurement value for at least 1/6 of the time (~10 days) in the two-month period considered in our study. We found 1459 indoor monitors in this region meeting this criterion. For each indoor sensor selected, we used its longitude and latitude to locate the nearest outdoor sensor. More than 2000 outdoor sensors in this region reported at least 10 days data during the period considered, compared with only 16 EPA Air Quality Monitoring Stations (AQMS) in this region. The geometric mean (GM) distance from an indoor sensor to the nearest AQMS is 6.7 km, but it is only 0.21 km to the nearest outdoor sensor (Figure S8.17). The substantially reduced distance allows much more accurate evaluation of indoor/outdoor concentration relationships. To prevent the possibility that the nearest outdoor sensor was located near major pollution sources, when the nearest outdoor sensor is more than 500 m away from the indoor sensor, we required the 50th percentile concentration at this outdoor node when it was not affected by wildfires to be below 25 μg m^{-3}, according to the levels and spatial decay rate of $PM_{2.5}$ measured near roads (Lena et al., 2002; Tiitta et al., 2002; Karner et al., 2010; Apte et al., 2017). We further required the outdoor sensor to cover at least 85% of the time when the indoor sensor reported data. If the $PM_{2.5}$ concentration measured by an "indoor" sensor is correlating too well with a nearby outdoor sensor ($r^2 > 0.8$), it is likely that this sensor was placed outdoors. This mislabeled or dislocated sensor is therefore not used in the analysis. Figure S8.18 shows an example of an indoor node discarded for this reason. We removed 165 "indoor" sensors from the analysis because of this problem. Another 20 indoor sensors were not considered because we could not find a nearby outdoor sensor that reported data for more than 85% of the time when the indoor sensor reported data. With all these criteria in place, data from $N = 1274$ indoor sensors in this region could be used. The same procedure was applied to data in the NC 2018 and SC 2020 cases. Negative values of $PM_{2.5}$ concentration were also discarded.

Decomposition of Indoor $PM_{2.5}$ We separated the indoor $PM_{2.5}$ from indoor and outdoor origins by removing short-term indoor $PM_{2.5}$ peaks that were unlikely due to penetration. A very similar approach has been demonstrated in previous studies by Allen et al. (Allen et al., 2004, 2003). According to high time-resolution measurements of particulate matter in previous indoor studies, the major indoor emission processes (mainly cooking and cleaning) typically last for half an hour to an hour, and after that a longer period is needed for the $PM_{2.5}$ perturbation to decay to less than half of its peak value (Patel et al., 2020). When these processes happen, the indoor level of $PM_{2.5}$ was at least 30 μg m^{-3}. We therefore selected all the peaks with half-prominence width (w) between 1 hour and 4 hour and prominence level above 30 μg m^{-3} as indoor-source peaks. It is possible that in some buildings the windows were opened for around an hour during the fires and created peaks that meet this criterion. Out of the 1274 buildings considered, we identified these large indoor source peaks in 834 buildings. Buildings without such peaks might be commercial buildings

without large indoor $PM_{2.5}$ sources, or the sensor in that building was placed in a location free from large indoor emissions. We assumed the indoor $PM_{2.5}$ other than that caused by these large peaks to be infiltrated $PM_{2.5}$. We reconstructed the infiltrated $PM_{2.5}$ by linearly interpolating indoor $PM_{2.5}$ concentration 3*w* before and after these large peaks with respect to time. The long 3*w* window was chosen to ensure that the indoor source peaks can be more thoroughly removed. For data outside of this window, the indoor concentration was assumed to be equal to the infiltrated $PM_{2.5}$. As a QA/QC step, if the calculated non-cooking indoor concentration was higher than outdoor concentration, that data point was removed from the analysis.

Mass Balance Model and Total Indoor Particle Loss Rate Constant Calculation. The indoor concentration of $PM_{2.5}$ depends on infiltration, indoor emission, and loss. We explored the dynamics of indoor $PM_{2.5}$ with a box model. If we assume the $PM_{2.5}$ is well-mixed indoors, the mass balance of $PM_{2.5}$ in a building can be written as:

$$V\frac{dC_{in}}{dt} = aPVC_{out} - aVC_{in} - k_{loss}VC_{in} + S \quad \text{(S8.1)}$$

where V is the volume of the room, a is the air exchange rate, P is the penetration factor of particles, k_{loss} is the loss rate constant including deposition and indoor filtration, and S is the indoor emission rate. C_{in} and C_{out} are the indoor and outdoor concentrations, respectively (Wallace and Williams, 2005; Chen and Zhao, 2011). Dividing by V on both sides, we can simplify the equation to:

$$\frac{dC_{in}}{dt} = aPC_{out} - (a + k_{loss})C_{in} + \frac{S}{V} \quad \text{(S8.2)}$$

When the indoor and outdoor particles are in steady state, and S is small, we have:

$$\frac{dC_{in}}{dt} = 0 = aPC_{out} - (a + k_{loss})C_{in} \Rightarrow F_{in} = \frac{C_{in}}{C_{out}} = \frac{aP}{a + k_{loss}} \quad \text{(S8.3)}$$

where F_{in} is the infiltration factor. For particulate matter, F_{in} can be obtained from the ratio of indoor/outdoor concentration when there are no outdoor sources (Bhangar et al., 2011; Wallace and Williams, 2005). Another way to estimate F_{in} is to regress the indoor $PM_{2.5}$ on outdoor values (Ott et al., 2000). However, this method has been shown to underestimate the infiltration factor while overestimating the indoor background (Wallace and Williams, 2005), or produce infiltration factors outside [0,1] ((Bi et al., 2021). Therefore, the ratio method was used for our analysis.

During the peak of cooking-like indoor particle release events, the indoor $PM_{2.5}$ resulting from cooking is much larger than the infiltrated smoke. When the indoor emission event is over, we assume the indoor source term becomes 0, and we have:

$$\frac{dC_{in}}{dt} = -(a + k_{loss})C_{in} \Rightarrow C_{in}(t - t_{peak}) = C_{in,peak}e^{-(a+k_{loss})(t-t_{peak})} \quad \text{(S8.4)}$$

Therefore, $(a+k_{loss})$ can be estimated by fitting the curve of $C_{in}(t)$ (Stephens and Siegel, 2012). We define $(a+k_{loss})$ as the total indoor particle loss rate constant (λ_t). A peak prominence of 30 μg m^{-3} (20 μg m^{-3} in the SC 2020 case to incorporate more peaks) was used as the threshold to find large indoor peaks that were subsequently used in the particle loss rate constant calculation. If windows were opened and then closed, the decay of resulted indoor $PM_{2.5}$ can also be described by Equation S4. Those peaks were also included because the decrease of indoor $PM_{2.5}$ under that circumstance can also be described by the exponential decay. The decay rate constant is also not substantially affected by the correction factor used because the correction factor affects C_{in} and $C_{in,\ peak}$ in the same way. To get total particle loss rate $\lambda_t = a+k_{loss}$, Equation S4 can be rewritten as:

$$-\ln\frac{C_{in}(t)}{C_{in}(t_{peak})}=\lambda_t(t-t_{peak}) \quad \text{(S8.5)}$$

We then linearly fitted this equation by least square method to get slope λ_t for the decay of each peak of indoor $PM_{2.5}$. In this part, we no longer require the width of the peak to be above 1 hour. In this way, indoor $PM_{2.5}$ peaks resulting from short-time window opening were also used to get λ_t. The 95% confidence interval of λ_t was also calculated. To ensure the exponential decay model is applicable, if the lower bound of the confidence interval of λ_t for a peak was below zero, this peak was not used as data for Figure 8.5.

The decrease of indoor $PM_{2.5}$ concentration can also be caused by the decrease of outdoor $PM_{2.5}$ concentration. In such cases, the assumption that incoming outdoor $PM_{2.5}$ source is stable no longer holds. Therefore, if the indoor $PM_{2.5}$ was decaying together with the outdoor $PM_{2.5}$ measured by the nearest sensor ($r^2 > 0.8$), this peak was excluded from the analysis. For the 1274 buildings considered in the NC 2020 case, we observed such decay peaks in 1000 buildings. On average, 4.7 decay peaks were captured in each building in the two-month period.

Uncertainty of the infiltration ratios and the decay rate constants

We roughly estimated the uncertainty of the infiltration ratios of individual sensor pairs, based on the idea that disagreement among any two paired sensors would lead to an uncertain estimate of the ratio of concentrations between those sensors. Thus, we gain a magnitude estimate of the uncertainty of the indoor/outdoor concentration ratio by examining the disagreement among a large number of paired nearby *outdoor* sensors across the PurpleAir dataset in our domain. We consider two timescales: (1) the uncertainty of the indoor/outdoor ratios of the 10-min data, reflecting the transient noise at short time scales, and (2) the uncertainty of the infiltration ratio for a building over the two-month period in the analysis, reflecting the possible range of persistent-sensor-to-sensor bias. To do so, we first found the outdoor sensors that were used to calculate indoor/outdoor ratios. Since it is possible that the nearest outdoor sensor of multiple indoor sensors is the same sensor, for the 1274 pairs of sensors, there are only 784 outdoor sensors used. For each sensor, we tried to find the nearest outdoor sensor within 1 km, which was successful for 775 sensors. For each pair of sensors i at time j, we calculate the ratios of $x_{i,i}/y_{i,j}$, where $x_{i,I}$ is the concentration of the i^{th} of the 775 used outdoor sensors at time t, and $y_{i,j}$ is the concentration of its nearest outdoor sensor. We make $\boldsymbol{R_i}$ as:

$$\boldsymbol{R_i}=\left[\frac{x_{i,1}}{y_{i,1}},\frac{x_{i,2}}{y_{i,2}},\ldots\ \frac{x_{i,n}}{y_{i,n}}\right]^T \quad \text{(S8.6)}$$

Then we concatenate the $\boldsymbol{R_i}$ array into $\boldsymbol{R_{all}}$ array by:

$$\boldsymbol{R_{all}}=\left[\boldsymbol{R}_1\ \boldsymbol{R}_2\ \ldots\ \boldsymbol{R}_n\right]^T \quad \text{(S8.7)}$$

The uncertainty of the indoor/outdoor ratio of 10-minute data is reflected by the variation of $\boldsymbol{R_{all}}$, which yields 0.886, 1.005, and 1.138 as 25^{th}, 50^{th}, and 75^{th} percentiles values, respectively.

The uncertainty of the infiltration ratio for a building over the two-month period can be roughly estimated by the statistics of $median(\boldsymbol{R}_i)$, which has 0.955, 1.035, and 1.131 as 25th, 50th, and 75th percentiles values, respectively. Therefore, we can conclude that the uncertainty of the infiltration ratio for a building over the two-month period is less than ±10%.

The decay rate calculation should have a very small uncertainty due to any bias in PA sensors because it uses measurements only from a single indoor sensor. We were fitting the decay curves of individual sensors by:

$$-\ln\frac{C_{in}(t)}{C_{in}(t_{peak})} = \lambda_t(t - t_{peak}) \quad \text{(S8.5)}$$

in which $C_{in}(t)$ ratios by the same sensor (especially in the same peak) should have very small uncertainty.

Given the reasons stated above, we expect the exposure reduction calculations have even lower uncertainties because we are averaging the exposure reduction of the 1274 buildings. Assume uncertainty of the infiltration ratio for a building over the two-month period is 10%, the average of infiltration ratios of all the buildings will have an uncertainty of $10\%/\sqrt{1274} = 0.28\%$ following central limit theorem. More conservatively, the median uncertainty of the infiltration ratio over two months, as reported for 774 sensor pairs above, was 1.035, or 3.5%. In either case, this uncertainty is quite small. We expect that the average exposure reduction would have a quantified uncertainty of similar or better magnitude to the I/O ratio, in other words, well less than 5%. Other unquantifiable uncertainties – e.g., differential or non-linear response of the PurpleAir to time-varying aerosol properties – add additional uncertainties that are more difficult to directly estimate, but we believe that these uncertainties do not fundamentally undermine the validity of our qualitative results.

Building information. Property data for PurpleAir Indoor-Outdoor comparison analysis were obtained by matching coordinates to addresses, verifying the addresses, looking up the addresses on publicly available property listing services, and finally quality control of the resulting data. The latitude-longitude coordinates were obtained from the publicly available PurpleAir database formally from a PurpleAir JSON file (purpleair.com/json – defunct as of December 2020), now available through the official PurpleAir API (api.purpleair.com). The coordinates contain 6 decimal places of precision and thus are accurate to under 10 meters, however, the placement is based on the available WiFi signal and can be edited by the sensor owner to be located anywhere on the map. As such, there is some uncertainty introduced into the reverse geocoding process, but since citizen scientists are interested in air quality within their own homes and research groups require spatial fidelity it can be assumed these coordinates are approximately correct.

After obtaining the list of coordinates, the Google and ArcGIS geocoding engines performed reverse geocoding scripted using the Python library OSMnx 1.0.1 (osmnx.readthedocs.io/en/stable/). About 38.5% of addresses in the SF Bay region disagreed between Google and ArcGIS lookups. The reasons for the disagreements are due to placement in homes leading to low confidence assigning addresses to lots such as on a street corner. The sensor

labels and manual searches on Google Maps were used to confirm the address. If the sensor label contains the address or a partial address or is obvious from the Google Map manual search, the confidence to the matched address is high. If the reverse geocoded searches match, then the confidence is medium, otherwise, it is assigned low confidence. From this analysis of valid addresses (n=1274), 13% were assigned high confidence, 73% were assigned medium confidence, and 14% were assigned low confidence. For low confidence addresses, the ArcGIS address was used.

The list of addresses was then manually inputted to Zillow, a publicly accessible website which offers data on homes and apartments using multiple listing services and county databases including building age, HVAC information, and livable area. Zillow furthermore uses existing publicly available information as well as a proprietary algorithm to derive an estimate of the current (as of December 2020) evaluation of the home or apartment (rent if a rental unit) termed a "Zestimate®." If the address matches an apartment complex, the first listed unit was then used to find the year of construction, HVAC information, and a bell-weather of the typical price and area of apartments since these can vary within complexes. From the 1274 address, 79.5% returned the year of construction, 83.6% returned HVAC data, 76.7% returned a price estimate, and 72.2% returned the area. Out of the 1274 buildings analyzed, 1112 (87%) buildings were found to be residential. Among these residential buildings, 80%, 13%, and 4% were matched to single-family houses, condominiums or multi-family buildings, and apartments, respectively.

As an additional sensitivity analysis, we restricted our dataset to the 87% of buildings that could unambiguously be ascertained to be residential. For this restricted dataset, the mean infiltration ratios on both fire days and non-fire days changed by less than 0.01.

8.4.2 Supplementary figures and tables

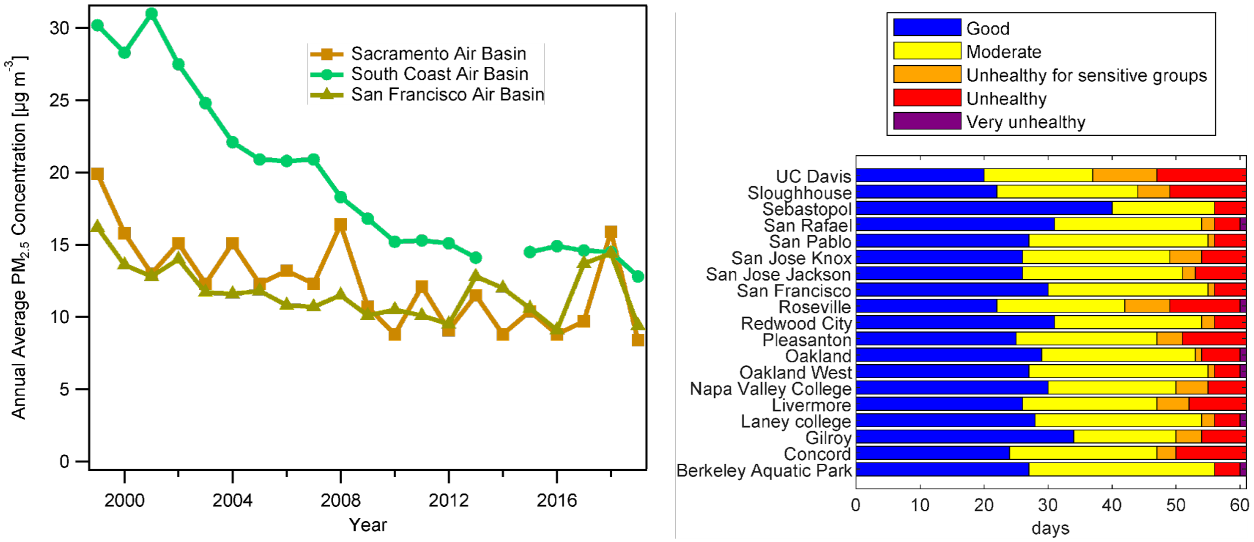

Figure S8.1 A. Annual average $PM_{2.5}$ concentrations in 3 Air Basins in California from 1999 to 2019 (Data retrieved from California Air Resource Board website https://www.arb.ca.gov/adam). The missing point is because of insufficient data available to determine the value. B. San Francisco Bay Area Air Quality Index (AQI) category in August and September 2020 based on 24-hour average level of $PM_{2.5}$ at each EPA Air Quality Measurement Station. 0 - 15.4 µg/m^3: Good; 15.5 - 35.4 µg/m^3: Moderate; 35.5 - 55.4 µg/m^3: Unhealthy for sensitive groups; 55.5 - 150.4 µg/m^3: Unhealthy; 150.5 - 250.4 µg/m^3: Very unhealthy.

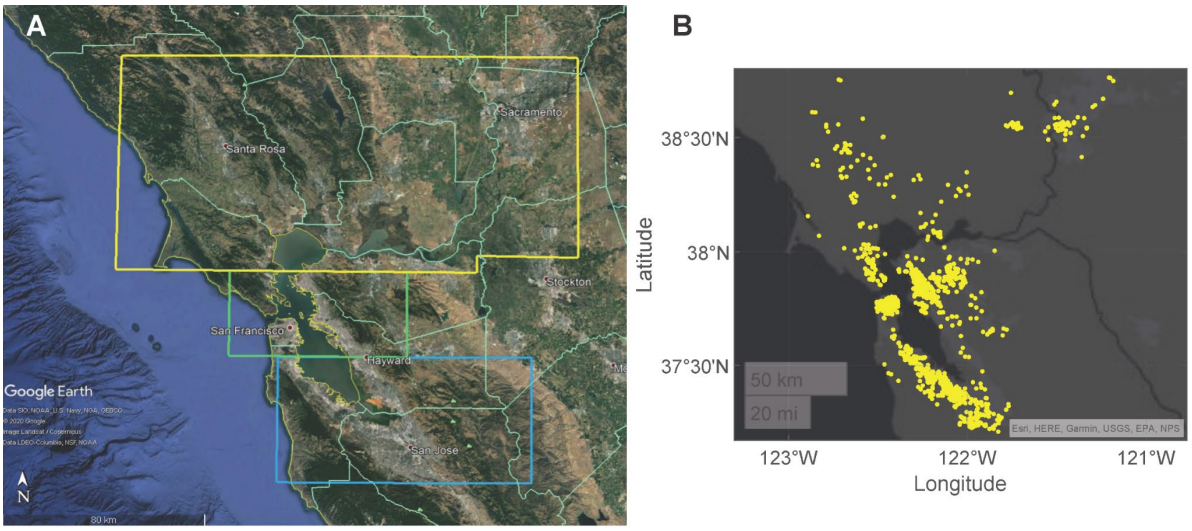

Figure S8.2 A. Study regions in the San Francisco Bay Area. Google Earth imagery © 2020 Google. PurpleAir sensors in the three boxes were analyzed together. B. Locations of all the indoor PurpleAir sensors included in the NC 2020 case.

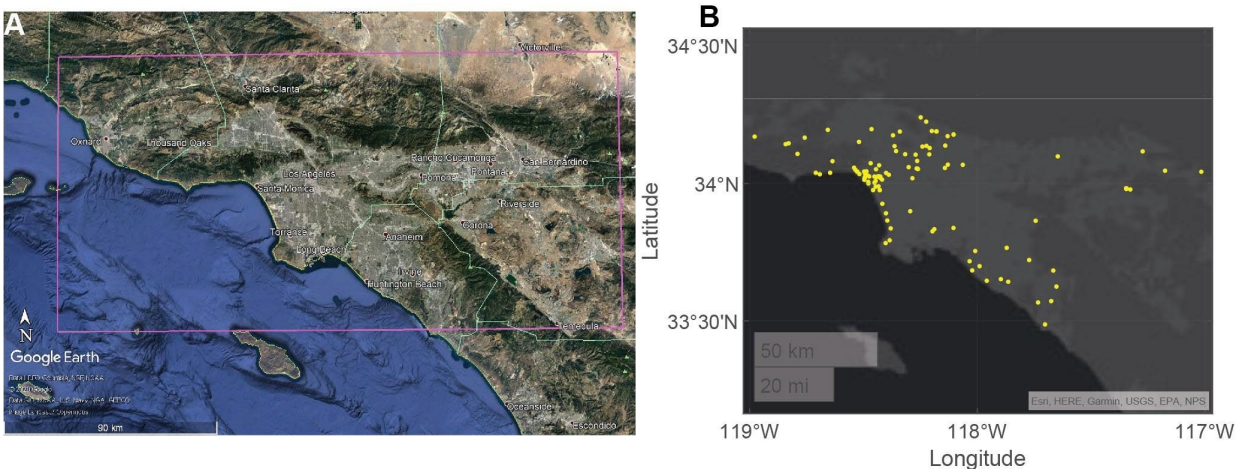

Figure S8.3 A. Study region in the Greater Los Angeles Area. Google Earth imagery © 2020 Google. B. Locations of all the indoor PurpleAir sensors included in the SC 2020 case.

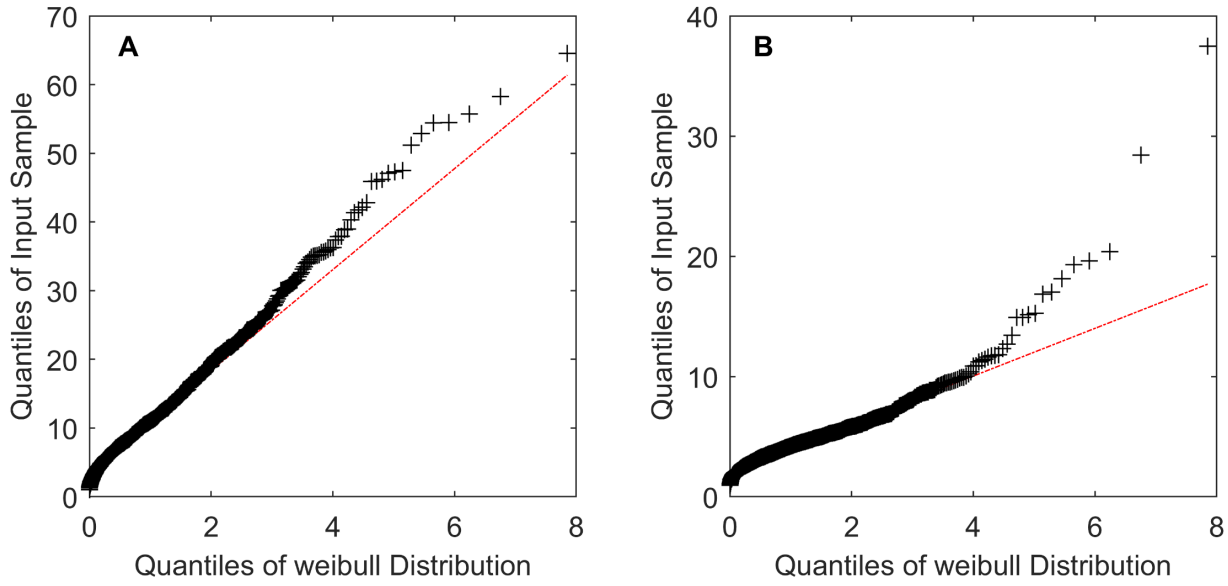

Figure S8.4 Quantile-quantile plots of mean indoor $PM_{2.5}$, on the fire days (A) and non-fire days (B) against Weibull distribution. The reference line represents the theoretical Weibull distribution.

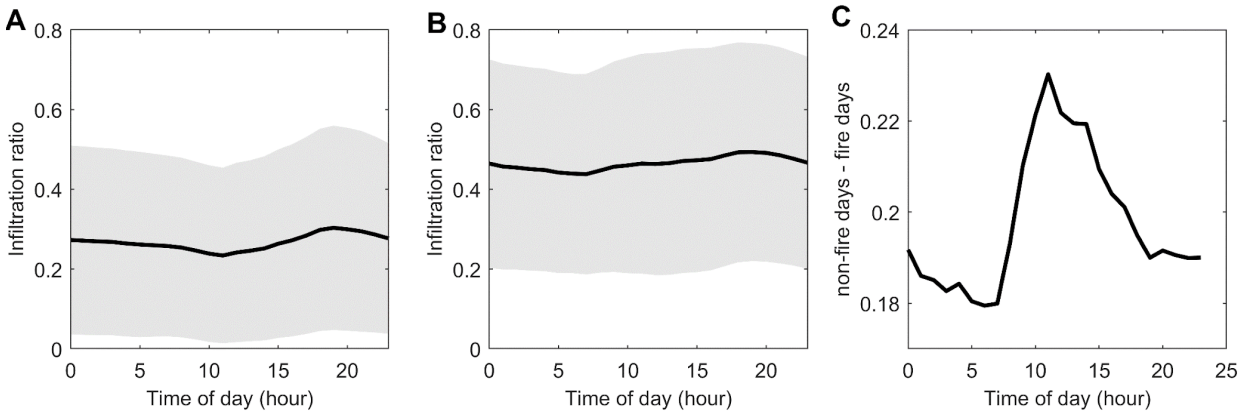

Figure S8.5 Diel plots (local time) A. Infiltrated $PM_{2.5}$ /outdoor $PM_{2.5}$ on fire days and B. Infiltrated $PM_{2.5}$ / outdoor $PM_{2.5}$ on non-fire days C. Diel plot of the difference in infiltrated $PM_{2.5}$ / outdoor $PM_{2.5}$ (non-fire days – fire days). Gray shading in A & B shows the standard deviation. Data are average of all the PurpleAir sensors in the NC 2020 case. The difference in mean infiltration ratio between fire days and non-fire days are most apparent in the daytime, consistent with more ventilation typically occurring during daytime.

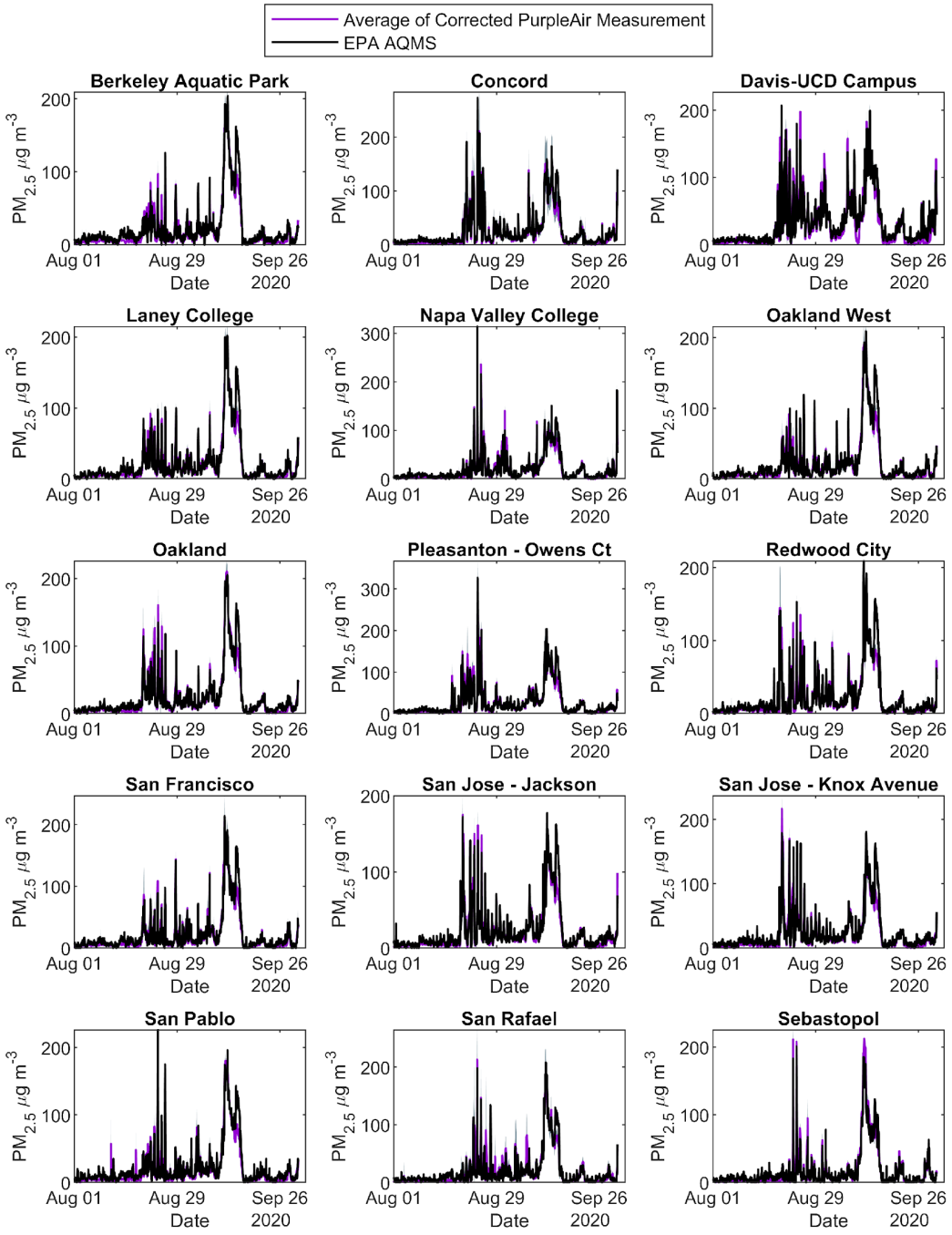

Figure S8.6 Hourly time profile of $PM_{2.5}$ concentration of the EPA monitors (black) and mean (purple) ± standard deviation (gray) of $PM_{2.5}$ (corrected) measured by nearby PurpleAir sensors in the San Francisco Bay Area in August and September 2020. The plots only include EPA monitoring stations having at least three outdoor PurpleAir sensors within 5 km of them. The EPA measurement and nearby PurpleAir sensors measurement agree reasonably well with each other.

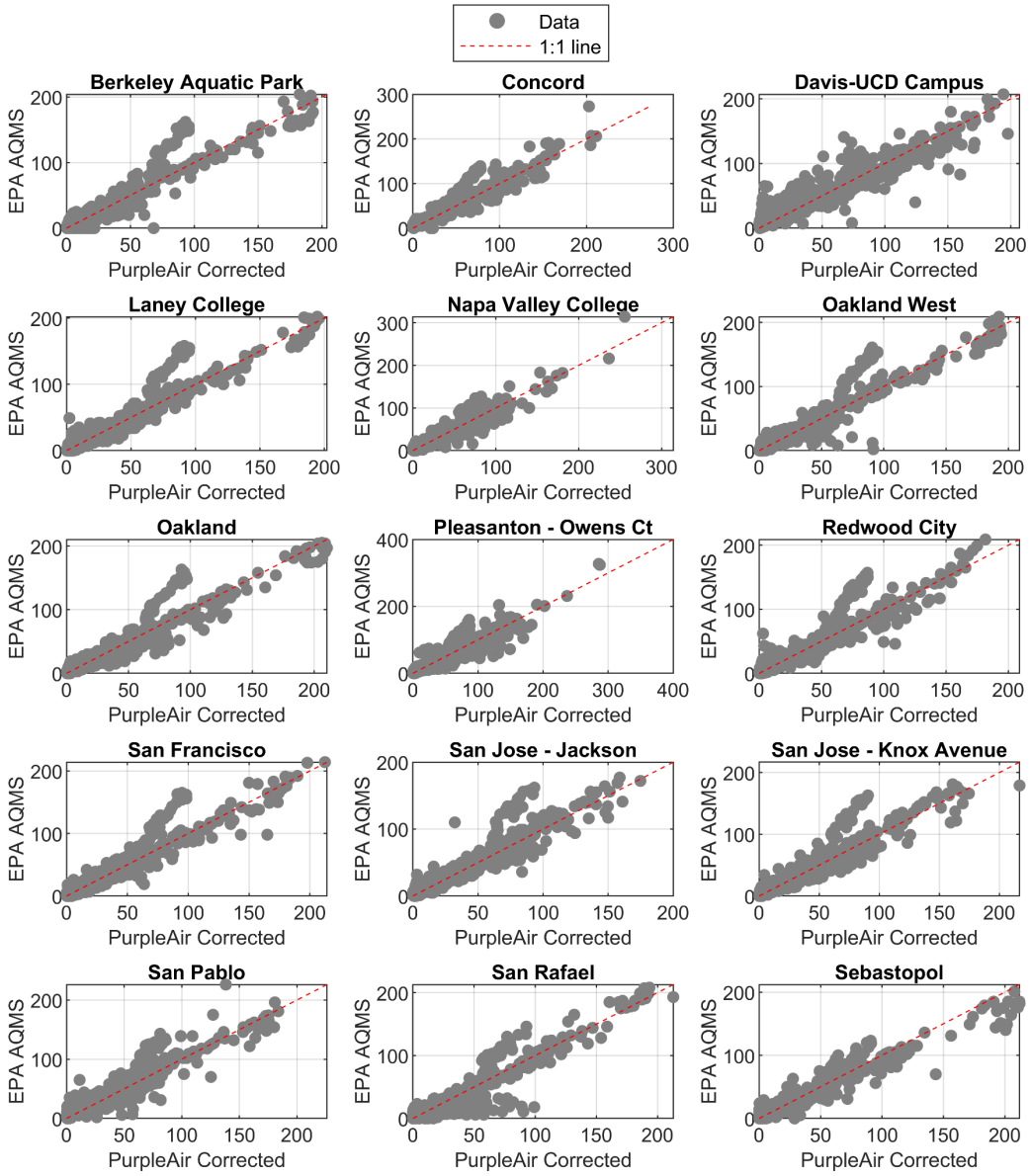

Figure S8.7 Scatter plot of $PM_{2.5}$ (μg m^{-3}) of the EPA monitors and mean $PM_{2.5}$ (corrected) measured by nearby PurpleAir sensors in the San Francisco Bay Area in August and September 2020.

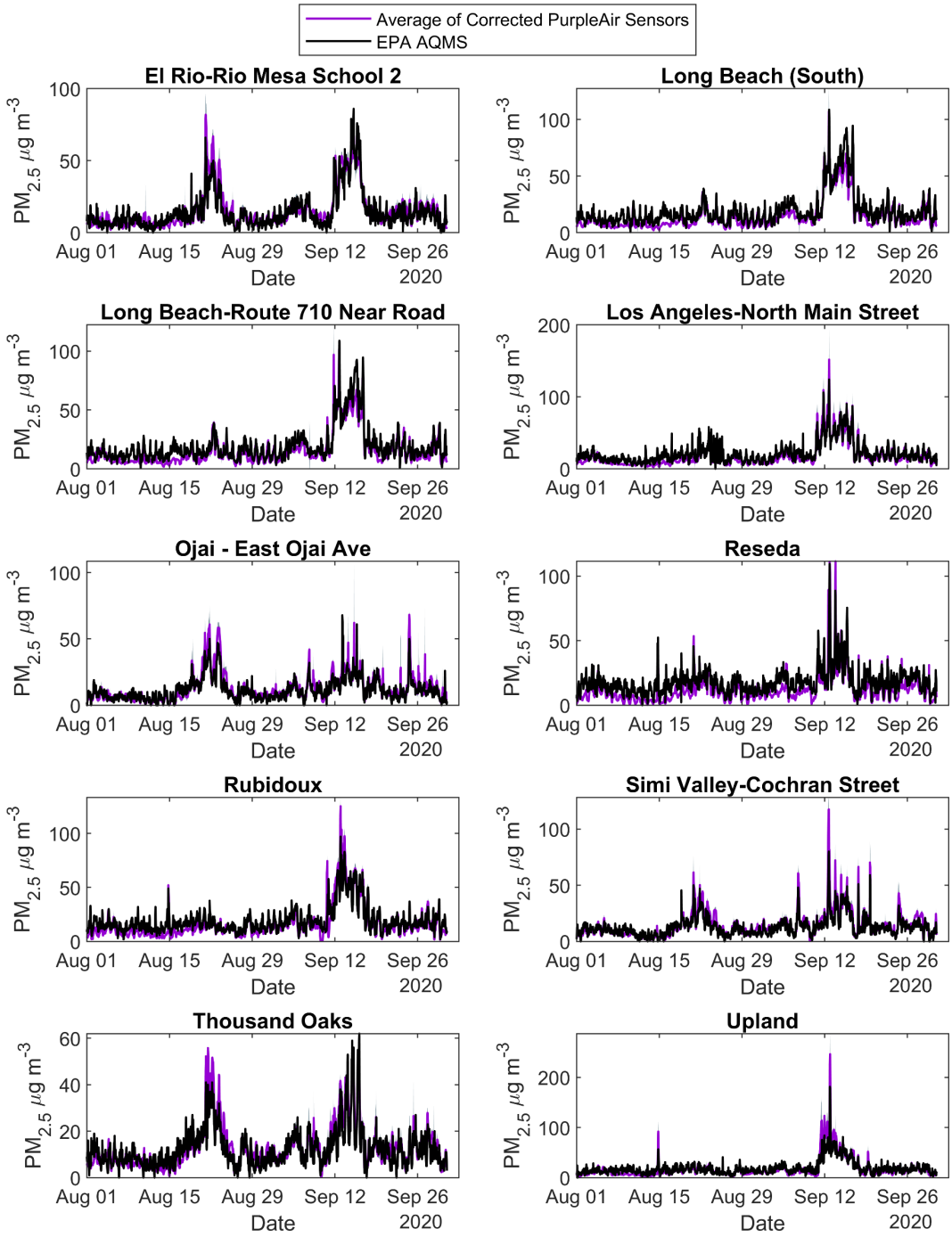

Figure S8.8 Hourly time profile of $PM_{2.5}$ concentration of the EPA monitors and mean (purple) ± standard deviation (gray) of $PM_{2.5}$ (corrected) measured by nearby PurpleAir sensors in the Greater Los Angeles Area in August and September 2020. The plots only include EPA monitoring stations having at least three outdoor PurpleAir sensors within 5 km of them.

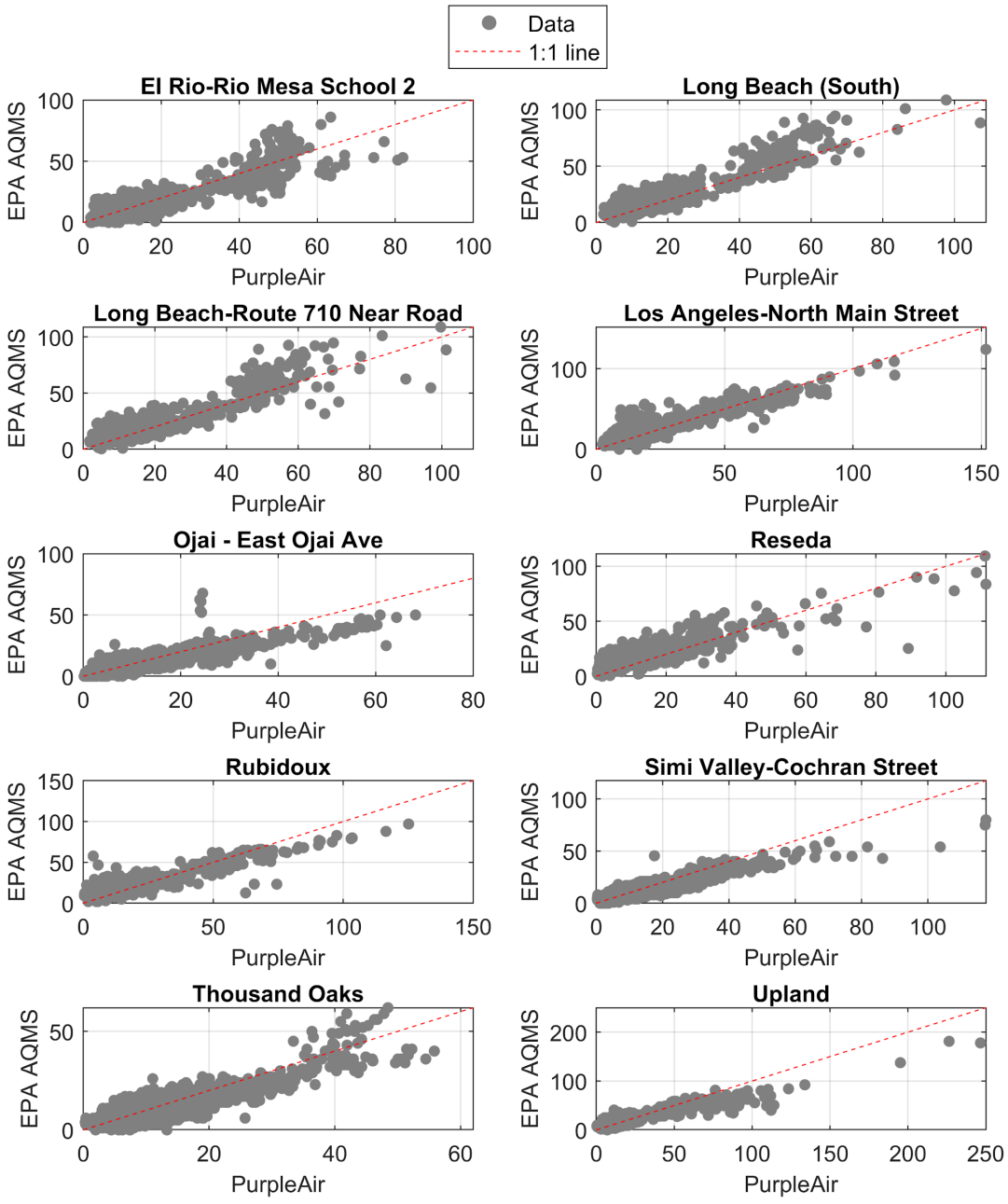

Figure S8.9 Scatter plot of $PM_{2.5}$ (μg m^{-3}) of the EPA monitors and $PM_{2.5}$ (corrected) measured by nearby PurpleAir sensors in the Greater Los Angeles Area in August and September 2020

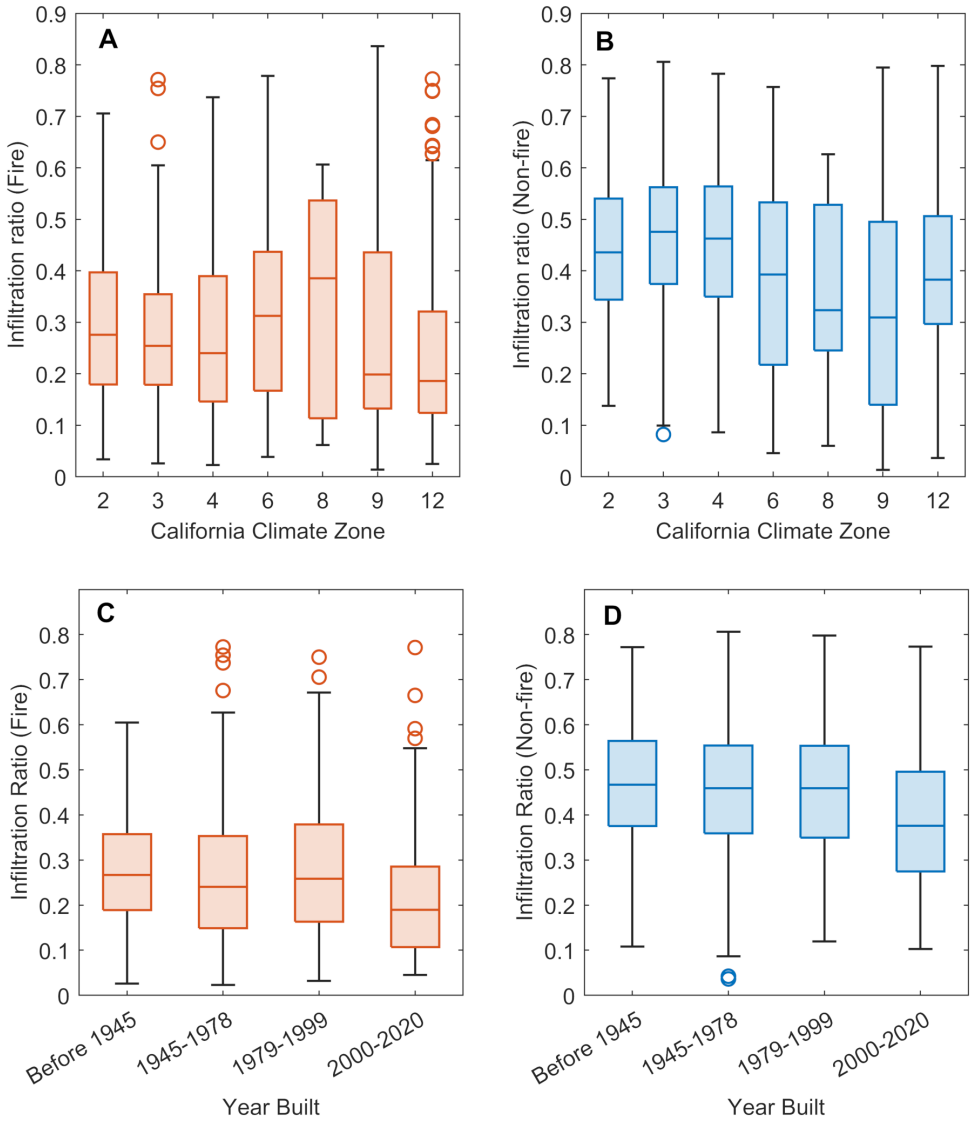

Figure S8.10 Infiltration ratio of buildings in different climate zones **A.** on fire days (ANOVA $p = 0.004$); **B.** non-fire days (ANOVA $p < 10^{-3}$) in August and September 2020. Only climate zones with at least 10 indoor sensors being analyzed are included in this figure. Reference cities for different climate zones (which were included in our study) are: Zone 2-Napa, Zone 3-San Francisco & Oakland, Zone 4-San Jose, Zone 6-Los Angeles (LAX), Zone 8-Long Beach, Zone 9-Los Angeles (Civic Center), Zone 12-Sacramento (California Energy Commission, 2018). Infiltration ratio of residential buildings (NC 2020 case) built in different periods **C**. on fire days (ANOVA $p = 0.004$); and **D.** on non-fire days (ANOVA $p < 10^{-3}$). Only residential buildings are considered in C and D. Buildings in Zone 12 had lower infiltration ratios than other Northern California climate zones considered.

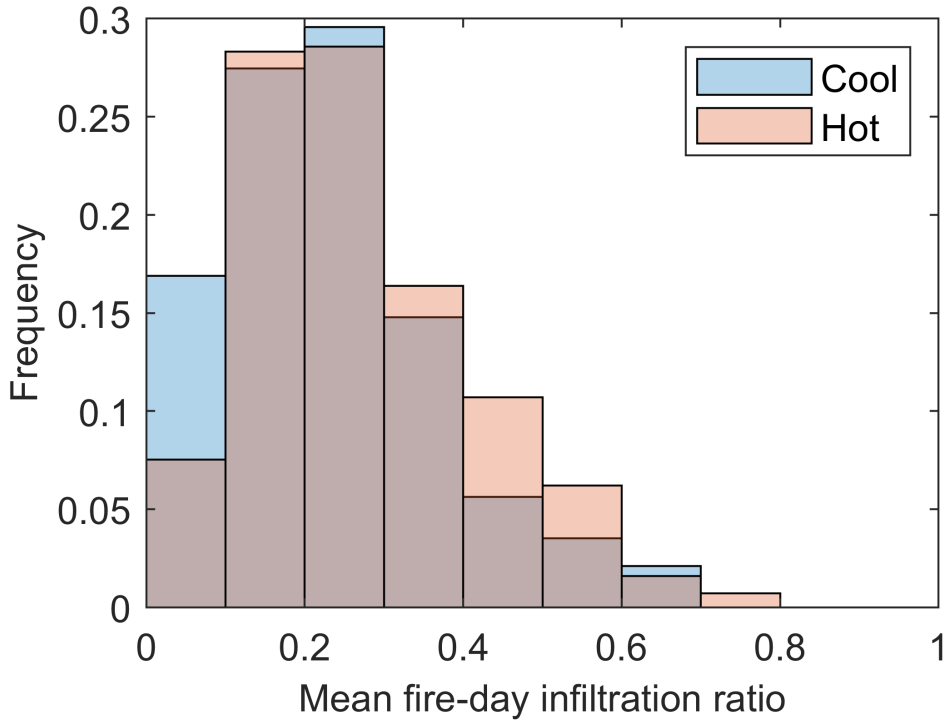

Figure S8.11 Infiltration ratio on fire days for cool buildings (95th percentile indoor temperature < 30ºC, N = 142) and hot buildings (95th percentile indoor temperature ≥ 30ºC, N = 1132) in the San Francisco Bay Area in August and September 2020. The cool buildings have significantly lower fire-day infiltration ratios than the hot ones ($p < 0.01$), and 17% of cool buildings had extremely low infiltration ratios (< 0.1).

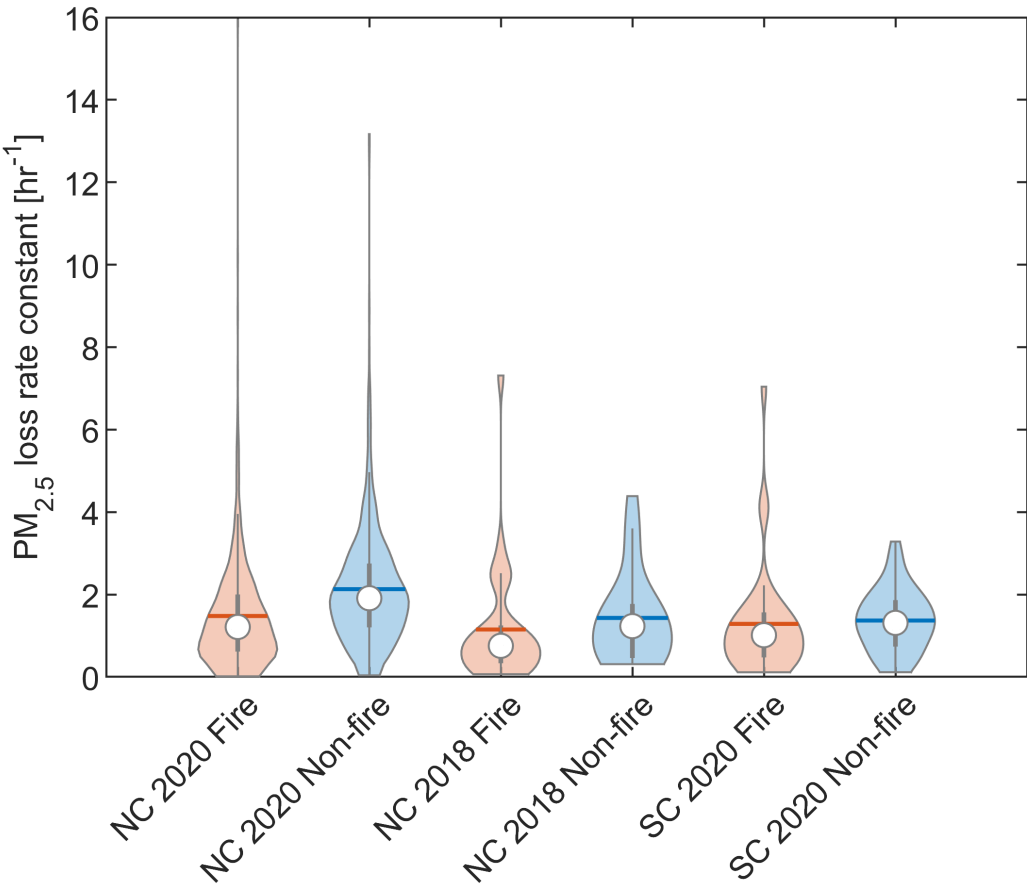

Figure S8.12 Violin plot of total particle loss rate constant in buildings in on the fire days and non-fire days. NC = San Francisco Bay Area, SC = Los Angeles Area. Each violin plot shows the probability density of the total $PM_{2.5}$ decay rate and a boxplot of interquartile range with whiskers extended to 1.5 times the interquartile range. Circles indicate the median, and horizontal lines indicate the mean.

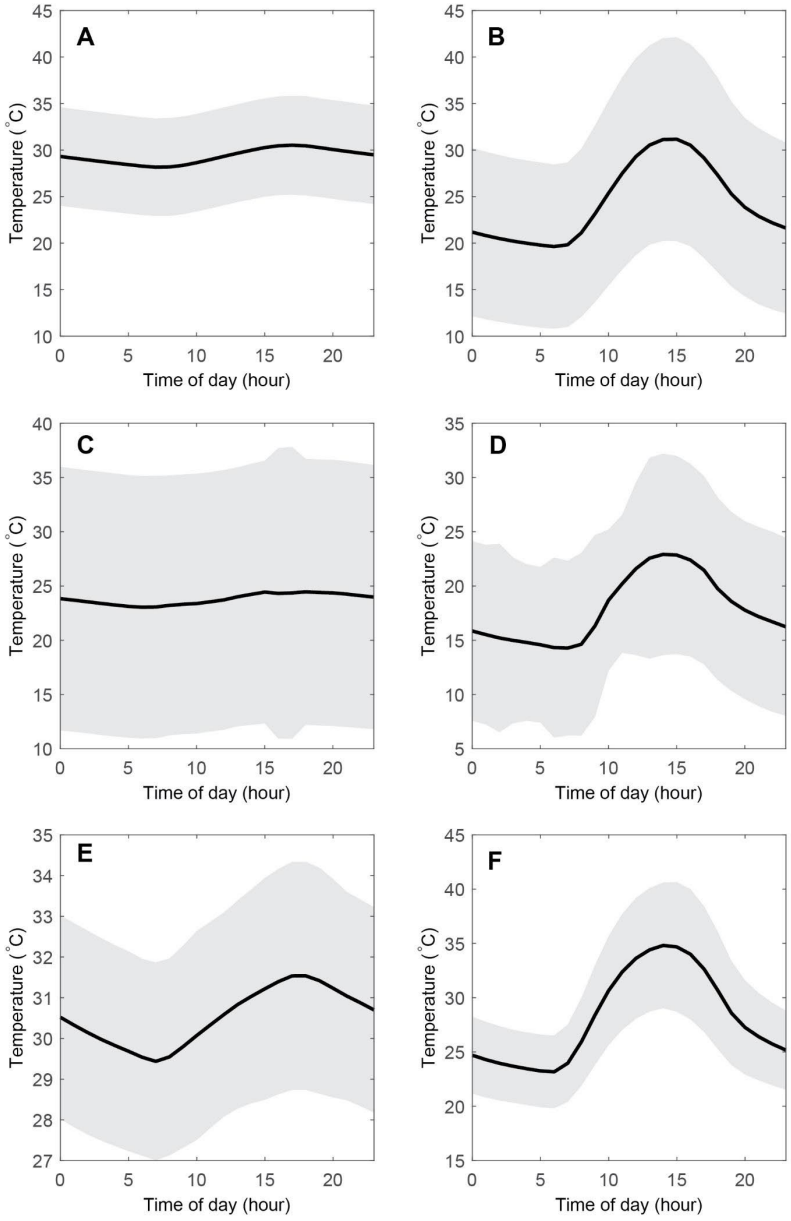

Figure S8.13 Diel plots (local time) of average temperature measured by PurpleAir sensors in the San Francisco Bay Area in August-September 2020 (**A**. Indoor **B**. Outdoor) and November 2018 (**C**. Indoor **D**. Outdoor); and in August-September 2020 in Greater Los Angeles Area (**E**. Indoor **F**. Outdoor). Gray shading shows the standard deviation. In the Summer 2020 cases, the difference in daytime indoor/outdoor temperature alternated between positive and negative values. In the NC November 2018 case, the indoor temperature was almost always higher than the outdoor temperature.

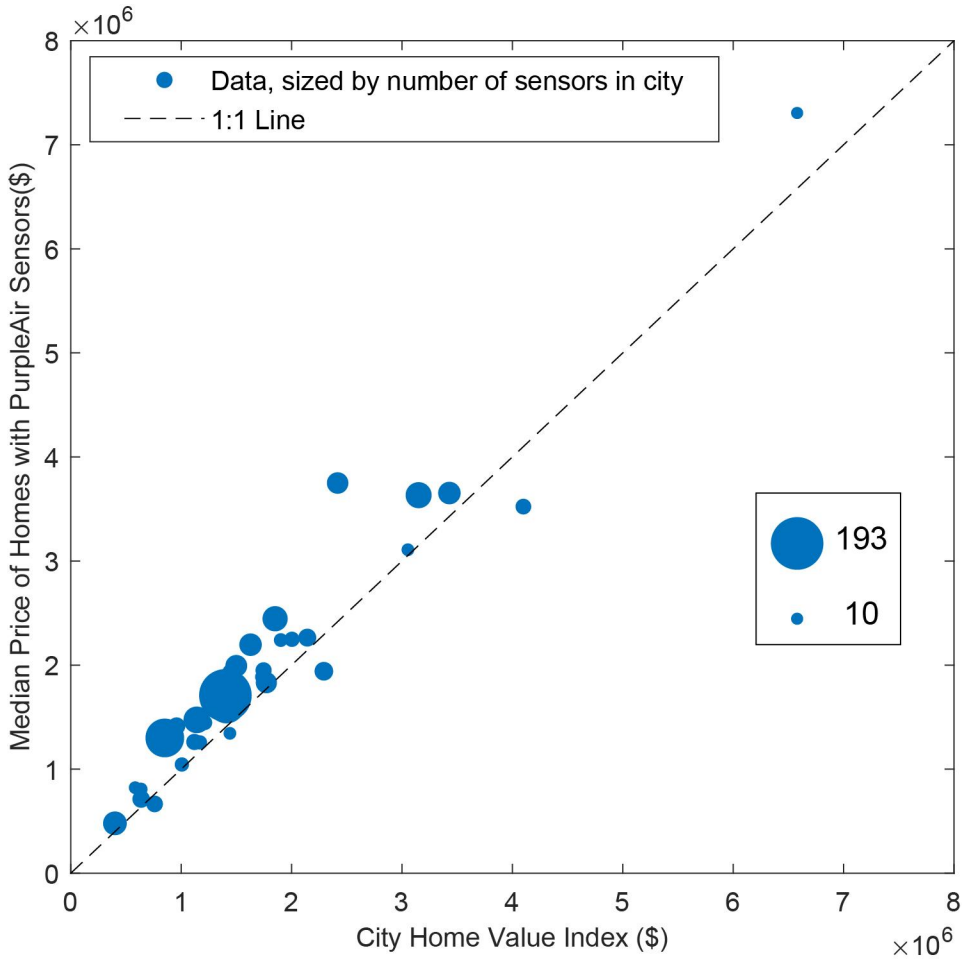

Figure S8.14 Median price of homes with indoor PurpleAir sensors vs. Median Housing Price in that city, sized by the number of indoor sensors in that city (only showing data from cities with at least 10 buildings with valid indoor sensors in the NC 2020 case). PurpleAir owners live in homes with estimated average property values 21% greater than the median property value for their cities.

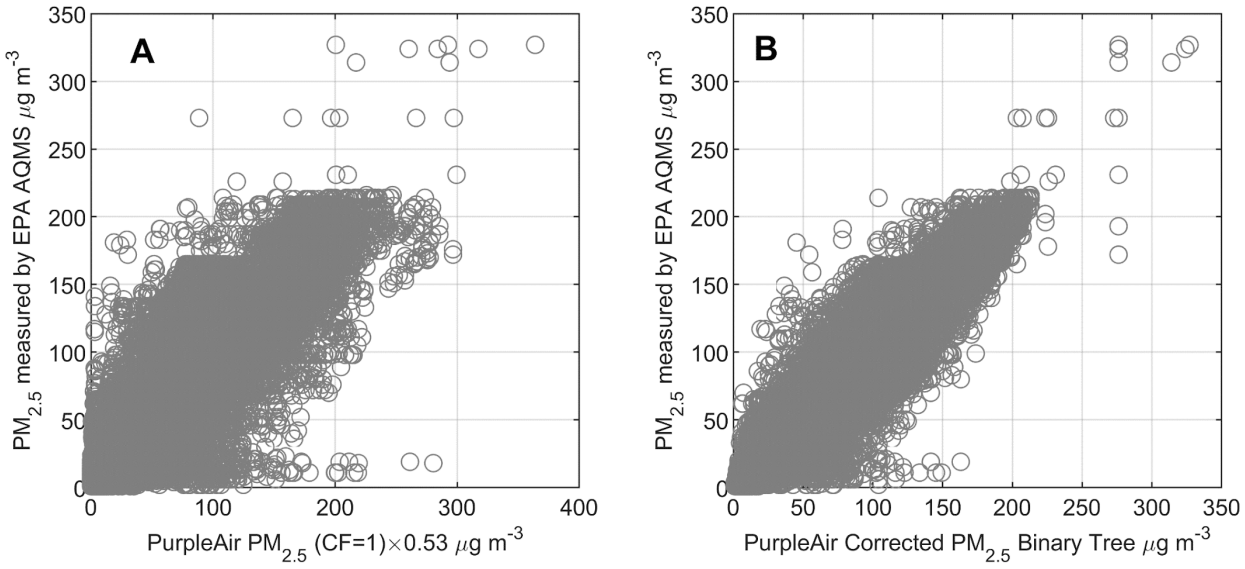

Figure S8.15 A. Hourly $PM_{2.5}$ measured by EPA AQMS against the linearly corrected (correction factor = 0.53) $PM_{2.5}$ data measured by nearby PurpleAir sensors; B. Hourly $PM_{2.5}$ measured by EPA AQMS against $PM_{2.5}$ measured by the PurpleAir sensors after the binary tree correction, both for data in San Francisco Bay Area in August and September 2020. This figure demonstrates the binary tree model can improve the precision and accuracy of the sensors.

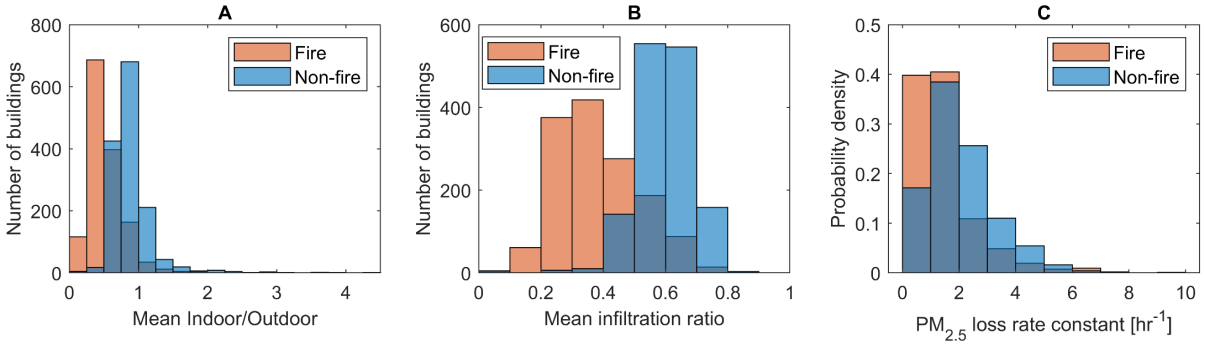

Figure S8.16 Binary tree $PM_{2.5}$ correction case. A. Distribution of mean Indoor/Outdoor $PM_{2.5}$ ratio during fire days and non-fire days for the buildings; B. Distribution of Infiltrated/Outdoor $PM_{2.5}$ ratio during fire days and non-fire days for the buildings. C. Probability density distribution of total indoor particle loss rate constants of $PM_{2.5}$ for the NC 2020 case. This figure demonstrates the binary tree correction does not meaningfully affect the fire day/non-fire day comparison.

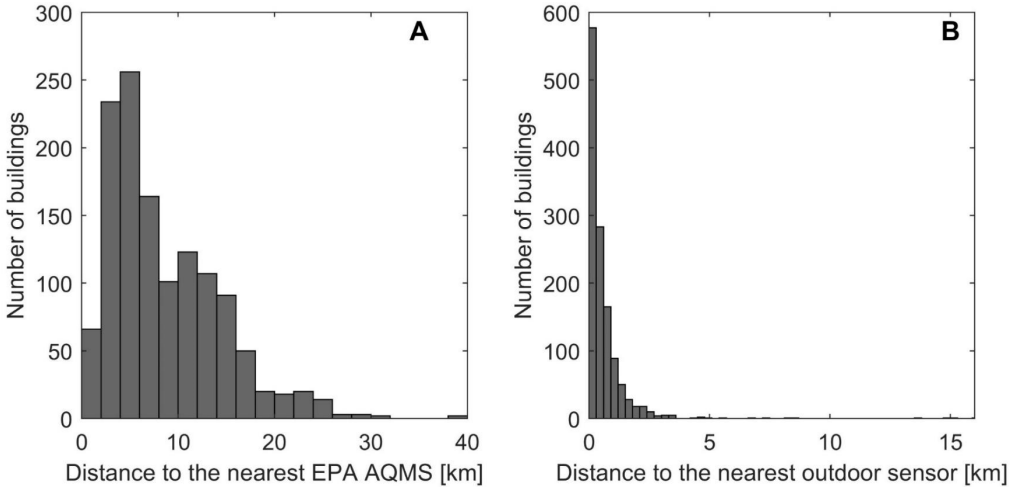

Figure S8.17 Distribution of distance from the indoor sensor to **A.** the nearest EPA air quality measurement station and **B.** the nearest outdoor PurpleAir sensor in the NC 2020 case. The geometric mean (GM) distance from an indoor sensor to the nearest AQMS is 6.7 km, but it is only 0.21 km to the nearest outdoor PurpleAir sensor.

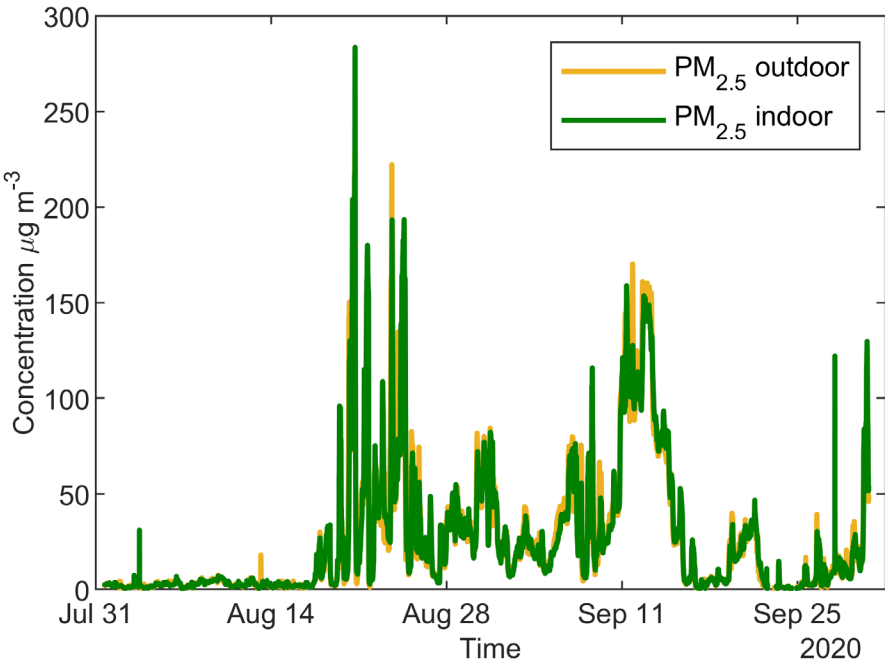

Figure S8.18 Concentration timelines of $PM_{2.5}$ reported by an "indoor" sensor and the nearest outdoor sensor. Because the indoor concentration measured is too close to and too well correlated with the outdoor concentration, this sensor might be placed outdoors. This node was therefore not used in this analysis.

Table S8.1 Parameters and performance of 7 correction methods for the outdoor sensors in the San Francisco Bay Area in August and September 2020 (NC 2020 case). Parameters are for the correction equation $PM_{2.5,corrected} = \beta_0 + \beta_1 PM_{CF1} + \beta_2 RH$. RH is between 0 and 1.

	Linear regression with intercept	**Linear regression no intercept**	**Linear regression no intercept (ODR)**	**Barkjohn et al. (2020b) US fire correction**	**Holder et al. (2020) wildfire correction**	**New fit incorporating RH**	**Binary decision tree with RH**
β_0 [µg m^{-3}]	3.52	n/a	n/a	5.60	-3.21	3.92	n/a
β_1	0.50	0.53	0.54	0.53	0.51	0.50	n/a
β_2	n/a	n/a	n/a	-0.084	n/a	-0.80	n/a
RMSE[a] [µg m^{-3}]	12.2	12.6	12.6	12.8	13.9	12.2	7.7
NRMSE[b]	0.48	0.50	0.50	0.51	0.55	0.48	0.39
Regression R^2	0.88	n/a	n/a	n/a	n/a	n/a	n/a
R^2 of calibrated data against EPA reference measurements	0.88	0.87	0.87	0.88	0.88	0.88	0.95

The root mean square error (RMSE, in [µg m^{-3}]) is calculated by

$$RMSE = \sqrt{\frac{1}{N}\sum_{h=1}^{N}(x_h - R_h)^2},$$

where N is the number of 1-hour $PM_{2.5}$ [µg m^{-3}] data points. x_h is hourly averaged sensor $PM_{2.5}$ concentration [µg m^{-3}] for hour h after correction. R_h is the hourly concentration of $PM_{2.5}$ [µg m^{-3}] measured by the EPA AQMS.

The root mean squared error normalized to the observed mean (NRMSE) is calculated by:

$$NRMSE = \frac{RMSE}{\overline{R_h}},$$

where R_h is the mean $PM_{2.5}$ [µg m^{-3}] observed by reference EPA AQMS.

Table S8.2 Corrections based on linear regression of EPA monitor $PM_{2.5}$ measurements with PurpleAir Sensors within a certain distance in the San Francisco Bay Area in August and September 2020 (NC 2020 case). Number of sensors refer to the total number of sensors near EPA monitoring sites that meet the requirements described in the "Selection of correction method" section in the SI Appendix. At most 50 sensors near each EPA site were included. Parameters are for the correction equation.

Distance (km)	**2**	**5**	**10**	**20**
Number of sensors	104	442	624	750
Intercept $\beta_0 \neq 0$				
β_0 **[µg m^{-3}]**	3.26	3.52	3.77	4.05
β_1	0.50	0.50	0.50	0.49
R^2	0.89	0.88	0.87	0.85
RMSE [µg m^{-3}]	11.5	12.2	12.7	13.5
NRMSE	0.46	0.49	0.51	0.53
No intercept ($\beta_0 = 0$)				
β_1	0.53	0.53	0.51	0.52
R^2	n/a	n/a	n/a	n/a
RMSE [µg m^{-3}]	11.8	12.6	13.1	13.9
NRMSE	0.47	0.50	0.52	0.55

Table S8.3 Median prices of homes with PurpleAir sensors compared to Home Value Index in cities with at least 10 buildings with valid indoor sensors in the NC 2020 case, as of December 2020. Prices were rounded to nearest thousand.

	Median price of homes with PurpleAir sensors	Number of buildings with PurpleAir sensors	Zillow Home Value Index of that city	Price Difference [a]
Alameda	$1,143,000	18	$1,119,000	2%
Albany	$1,257,000	14	$1,170,000	7%
Atherton	$7,306,000	10	$6,579,000	11%
Belmont	$2,240,000	13	$1,902,000	18%
Berkeley	$1,616,000	93	$1,411,000	14%
Campbell	$1,344,000	11	$1,441,000	-7%
Davis	$666,000	19	$759,000	-12%
El Cerrito	$1,045,000	14	$ 1,006,000	4%
Emeryville	$822,000	11	$ 583,000	41%
Lafayette	$1,992,000	33	$ 1,499,000	33%
Los Altos	$3,653,000	35	$ 3,429,000	7%
Los Gatos	$2,264,000	22	$ 2,142,000	6%
Menlo Park	$3,645,000	32	$2,417,000	51%
Mill Valley	$1,911,000	18	$1,746,000	9%
Moraga	$1,886,000	11	$1,726,000	9%
Mountain View	$2,317,000	44	$1,851,000	25%
Oakland	$1,300,000	104	$851,000	53%
Orinda	$1,941,000	24	$2,292,000	-15%
Palo Alto	$3,594,000	47	$3,151,000	14%
Portola Valley	$3,523,000	17	$4,099,000	-14%
Redwood City	$2,196,000	35	$1,628,000	35%
Richmond	$807,000	12	$635,000	27%
Sacramento	$469,000	39	$400,000	17%
San Carlos	$2,248,000	16	$2,003,000	12%
San Francisco	$1,696,000	193	$1,400,000	21%
San Jose	$1,460,000	49	$1,141,000	28%
San Mateo	$1,919,000	28	$1,461,000	31%
San Rafael	$1,447,000	15	$1,214,000	19%
Santa Rosa	$713,000	21	$637,000	12%
Saratoga	$3,109,000	11	$3,053,000	2%
Sunnyvale	$1,654,000	31	$1,771,000	-7%
Walnut Creek	$1,414,000	21	$958,000	48%

[a]Price difference = (Median price of homes with PurpleAir sensors - Median City Home Value)/ Median City Home Value

Table S8.4 Mean ± standard deviation of fire-day infiltration ratios and the number of buildings with fire-day infiltration ratios below 0.14 or above 0.40 in cities with at least 10 buildings with valid indoor sensors in the NC 2020 case.

City	Number of buildings with PurpleAir sensors	Mean ± SD of Fire-day infiltration ratio	No. of Buildings with Fire-day infiltration ratio < 0.14	No. of Buildings with Fire-day infiltration ratio > 0.40
Alameda	18	0.19±0.09	5	1
Albany	14	0.31±0.11	0	3
Atherton	10	0.31±0.12	1	3
Belmont	13	0.27±0.08	1	1
Berkeley	93	0.27±0.10	10	13
Campbell	11	0.24±0.13	0	2
Davis	19	0.17±0.16	11	2
El Cerrito	14	0.27±0.10	2	1
Emeryville	11	0.26±0.16	3	1
Lafayette	33	0.23±0.11	5	4
Los Altos	35	0.33±0.19	7	12
Los Gatos	22	0.34±0.15	2	7
Menlo Park	32	0.27±0.12	3	5
Mill Valley	18	0.36±0.18	1	6
Moraga	11	0.16±0.10	4	0
Mountain View	44	0.25±0.14	12	5
Oakland	104	0.25±0.12	14	11
Orinda	24	0.24±0.19	11	5
Palo Alto	47	0.28±0.17	12	15
Portola Valley	17	0.27±0.12	2	3
Redwood City	35	0.30±0.15	8	11
Richmond	12	0.25±0.16	4	2
Sacramento	39	0.29±0.19	10	10
San Carlos	16	0.20±0.10	5	1
San Francisco	193	0.28±0.12	24	35
San Jose	49	0.26±0.14	14	10
San Mateo	28	0.26±0.11	3	2
San Rafael	15	0.31±0.16	3	5
Santa Rosa	21	0.31±0.15	4	6
Saratoga	11	0.30±0.18	0	2
Sunnyvale	31	0.22±0.15	8	7
Walnut Creek	21	0.21±0.14	9	1

Table S8.5 Weibull parameters of the concentration indoor/outdoor ratios for buildings with PurpleAir sensors in August-September 2020 in the San Francisco Bay Area (35 μg m^{-3} daily average $PM_{2.5}$ concentration measured at the nearest EPA measurement site was used as the threshold for fire days and non-fire days). $N = 1274$. Unhealthy days are defined as days with daily average EPA $PM_{2.5}$ concentration above 55.4 μg/m^3.

	Mean indoor conc μg m^{-3}		**Indoor/outdoor ratio**		**Infiltration ratio**	
	γ	*β*	γ	*β*	γ	*β*
Non-fire days	4.65	1.82	1.00	1.35	1.00	1.35
Fire days	12.4	1.50	0.45	1.26	0.30	2.00
Unhealthy days	14.9	1.40	0.34	1.19	0.26	1.74

Quantile-quantile plots (*SI Appendix,* Figure S8.4) show the mean concentration of indoor $PM_{2.5}$ in all the buildings can be satisfactorily described by the Weibull distribution. The scale parameter and shape parameter of the Weibull fit are γ and *β,* respectively. The probability distribution function for x is $f(x) = \frac{\beta}{\gamma}(\frac{x}{\gamma})^{\beta-1} e^{-(x/\gamma)^{\beta}}$, where $x > 0$. Parameters of the SC 2020 and NC 2018 cases are not shown here due to the small sample sizes, which are less representative of all the buildings in these areas at that time.